UNIVERSITY OF CALIFORNIA, SAN DIEGO

Geophysical Constraints on Sediment Dispersal Systems

A dissertation submitted in partial satisfaction of the requirements for the degree

Doctor of Philosophy

in

Oceanography

by

Elizabeth Anne Carruthers Johnstone

Committee in charge:

Neal W. Driscoll, Chair
Christopher Charles
Graham M. Kent
Falko Kuester
David Sandwell

2012

ProQuest LLC.
789 East Eisenhower Parkway
P.O. Box 1346
Ann Arbor, MI 48106 - 1346

The Dissertation of Elizabeth Anne Carruthers Johnstone is approved, and it is acceptable in quality and form for publication on microfilm:

_____

_____

_____

_____

_____

Chair

University of California, San Diego

2012

To my mother, Judy Bird,
and my forever hero, Tim Johnstone

“Twenty years from now, you will be more disappointed by the things you didn’t do than those you did. So, throw off the bowlines, sail away from safe harbor. Catch the wind in your sails. Explore. Dream. Discover.”

- Mark Twain

Table of Contents

List of Figures

List of Tables

Acknowledgements

First and foremost, I am very grateful to my advisor, Neal Driscoll, for inspiring me and being a supportive mentor for many years. His enthusiasm for the processes at work on planet Earth is contagious and I have watched him spread curiosity to people of all ages. His ability to capture ones attention is magical and creative and allows others to have a glimpse of the unique perspective he has with genius powers of a four dimensional imagination.

I'd like to acknowledge and give thanks to my other committee members, Graham, Dave, Chris and Falko for their support and helpful guidance through the years. Traveling and conducting fieldwork with these professors has always been a wonderful learning experience and they have opened my eyes to different technologies and techniques for understanding science both theoretically and practically.

Paul Gayes deserves very special recognition in sparking my career in Marine Geology. He ignited a passion and curiosity in me for using technology to understand coastal and seafloor morphology. He not only helped pave the way for me to grow as a scientist, but showed me how fun and exciting the field of Geology can be. Other members in the professional Earth Science community that have inspired and taught me along the way include: John Milliman, Rudy Slingerland, Scott Ashford, Alistair Harding, Gordon Seitz, Jeffrey Babcock, William Schwab.

I want to thank my fellow mates in the Driscoll lab especially Jenna Hill, Kurt Schwehr, Jeff Dingler, Danny Brothers, Jessica Raymond, and Jillian Maloney for all their assistance and support during my tenure as a graduate student. There are others at SIO, mainly Warren Smith and Alex Hangsterfer, that deserve a huge thanks for all their help with acquiring and processing samples.

I could not have accomplished this achievement without the unwavering support of my family and friends. My mother, Judith Bird, always encouraged me to be curious about our planet and strive to always dig deeper into what is in front of you. My brother, Tim, has constantly inspired me to do great things, even when the going gets tough. Thank you both for your love and encoragement. To my dear friends, you know who you are, thank you enormously for all your support and care during the good and bad times that make up this beautiful thing called life. I look forward to the rest of the journey with many more smiles and laughs ahead!

Finally, I would like to express deep gratitude to the generous financial support from UC Regents, Poo Wyer, California Sea Grant, and the National Science Foundation. Cheryl Peach and Hubert Staudigel also deserves thanks for supporting me as a NSF GK-12 fellow for one year, where I was lucky enough to get wonderful hands-on teaching experience in the local San Diego school system.

The text and figures from chapter 4, in part of in full, is a reprint of the material as it appears in: Olsen, M.J., Johnstone, E., Driscoll, N., Ashford, S.A., and Kuester, F. (2009). Terrestrial laser scanning of extended cliff sections in dynamic environments: a parameter analysis, ASCE Journal of Surveying Engineering, 135(4), p. 161-169. This dissertation author was a co-author listed in this publication and provided significant contribution to the data acquisition and preparation of the manuscript.

Vita

1995-2000	Undergraduate Reserach Assistant Department of Marine Science Coastal Carolina University
2000	Bachelor of Science, Marine Science Bachelor of Science, Biology
2000-2004	Marine Technician Center for Marine and Wetland Studies Coastal Carolina University
2012	Doctor of Philosophy, Earth Sciences Geosciences Research Division Scripps Institution of Oceanography University of California, San Diego

Publications

Young, A.P., Olsen, M.J., Driscoll, N., Gutierrez, R., Guza, R.T., Flick, R, E., Johnstone, E., and Kuester, F., (2010). Mapping Seacliff Erosion with Terrestrial and Airborne LIDAR, ASPRS Journal of Photogrammetric Engineering and Remote Sensing 76(4), p. 421-427.

Olsen, M.J., Johnstone, E., Driscoll, N., Ashford, S.A., and Kuester, F. (2009). Terrestrial laser scanning of extended cliff sections in dynamic environments: a parameter analysis, ASCE Journal of Surveying Engineering, 135(4), p. 161-169.

Milliman, J.D., Xu, K.H., Slingerland, R. L, Driscoll, N. W. and Johnstone, E.A., Sediment mineralogy on the Gulf of Papua Clinoform: New insights into sediment source and redistribution, prepared for Geology.

Hill, J.C., Gayes, P.T., Driscoll, N.W., Johnstone, E.A., and Sedberry, G.R., Iceberg scours along the southern U.S. Atlantic margin. Geology, June 2008; 36: 447 - 450.

Olsen, M.J., Johnstone, E., Ashford, S.A., Driscoll, N., Young, A.P., Hsieh, T.J., and Kuester, F. (in press). Rapid Response to Seacliff Erosion in San Diego County, California using Terrestrial LIDAR, ASCE Solutions to Coastal Disasters Conference Proceedings, 2008, Oahu, Hawaii.

Slingerland, R., Johnstone, E., Milliman, J. , Scott R. Miller, Driscoll, N., Anatomy and Growth of a Holocene Clinothem in the Gulf of Papua, Journal of Geophysical Research, 2008.

Abstract of the Dissertation

Geophysical Constraints on Sediment Dispersal Systems

by

Elizabeth Anne Carruthers Johnstone

Doctor of Philosophy in Oceanography

University of California, San Diego, 2012

Neal W. Driscoll, Chair

Geophysical and geological approaches were employed to understand sediment dispersal systems and their response to various forcing functions (i.e., sea level fluctuations, tectonic deformation, sediment supply, and climate change). Two end member marine environments were studied; one with high precipitation and sediment discharge (Gulf of Papua, Papua New Guinea) and the other with low precipitation and sediment discharge (Oceanside Littoral Cell). The high-sedimentation rate in the Gulf of Papua (GoP) yields high-fidelity records of Earth history. As part of the NSF Margins Source-to-Sink (S2S) program, we acquired CHIRP and core data across the GoP continental shelf that complemented onshore and offshore research in the region. CHIRP seismic data imaged three Holocene sedimentary lobes. The older Central lobe is downlapped by two younger lobes to the north and south. Sediment analysis showed that the older Central lobe has an elemental signature similar to the younger Northern lobe with both sourced from the Purari River watershed and lobe migration appears to be climatically controlled. The Southern lobe has elemental signatures more consistent with the Fly River watershed. Our results suggest the northern rivers began depositing sediments on the shelf during the Holocene sea level rise in the central region of the GoP and migrated abruptly north at ~2 kybp. Conversely, during the early Holocene

transgression, sediments in the Fly drainage system were sequestered onshore infilling accommodation created in the large low-relief coastal plain during the sea level rise. Upon infilling the onshore accommodation, the Fly River delivered sediment to the ocean and formed the Southern lobe. Such differences in onshore storage capacity may introduce a lag between low-gradient rivers (Type I) with a large coastal plain versus high-gradient river systems (Type II) with small coastal plains.

The second study site is in the sediment-starved Oceanside Littoral Cell (OCL) of Southern California. Terrestrial Laser scanning was performed seasonally using Light Detection and Ranging (LiDAR) technology to perform time series modeling of sea cliff erosion. We established a repeatable and reliable protocol for efficiently conducting coastal sea cliff mapping. Changes in geomorphology were quantified to determine the forcing mechanisms controlling erosion. Results from our investigations provide insight into "hot spots" of erosion along the coast and the controlling processes. Subaerial and marine erosion are predominantly controlled by precipitation and wave energy, respectively. Beach elevation, a seasonally dependent variable, is the most important physical factor controlling whether a sea cliff is vulnerable to marine-based or subaerial erosion. Due to the heavy coastal development and important state revenue from beach tourism, it is critical to continue this type of time series research to understand fully these relationships. This study provides a baseline from which future change due to the rapid sea level rise (>3 mm/yr) and climate change can be assessed.

1

Introduction

1.1 SEDIMENT DISPERSAL SYSTEMS

Sediments are formed as larger rocks break down through the process of weathering, with gravity controlling where and how they are transported as part of a sediment dispersal system. Transport moves the liberated particles within the system and eventually they are deposited when energy levels drop low enough to allow them to fall from suspension. The amount of energy required to keep sediments entrained is based on a number of factors including: grain size, composition, and shape. By investigating the sediments in their present environment using stratigraphic relationships, one can decipher past environmental processes controlling deposition. This thesis document examines sediment dispersal systems in marine and coastal realms. Two different study sites are explored using geophysical techniques to quantitatively and qualitatively explore how the depositional environments change temporally over a regional spatial scale.

Weathering of geomorphic units through time is dependent on the characteristics of the parent rock and environmental factors to which it is exposed. Tectonically active regions on Earth often create relief in the form of mountainous areas as high as 7.2km high such as those as found in the Himalayas as well as the deepest oceanic features as found in the Marianas trench where the seafloor plunges to depths of 11km. Mechanical and chemical forcing conditions such as precipitation, freeze-thaw cycles and rock-type homogeneity play a role in the rate of erosional processes. For example, mountainous regions in tropical environments tend to decompose into smaller sediments more quickly than those in arid regions. Bioerosion also participates in the breakdown of parent rocks, especially in the marine and coastal environment. With over three-fourths of Earth's surface covered in sediments (Boggs 2001), understanding the products and patterns of erosion help us decode the history of our planet by reading the layers as if they were pages in a book telling us the story of the past.

Sequence stratigraphy is a relatively new geological method of analyzing the link between depositional sediment layers and the process by which they were placed. Deciphering stratal relationships between sediment packages provides insight about interplay between tectonics, sea level and sediment supply using sequence boundaries within a chronostratigraphic framework. The approach is increasingly popular in theoretical and applied science because it helps researchers understand major earth processes and is vitally important in the discovery of natural resources, such as petroleum, gas and minerals. Advanced acoustic, geospatial and imaging technologies recently available to scientists allow us to investigate regional areas in high resolution affording a four-dimensional view of landforms.

1.1.1 OVERVIEW OF STUDY

The first study region in this thesis is the mid-shelf clinoform in the Gulf of Papua (GOP, Figure 1), located southeast of the coast of Papua New Guinea. Several rivers drain the 4000m highlands of New Guinea into the semi-enclosed basin (Pickup, 1984; Walsh and Nittrouer, 2003), where most sediments are deposited on the shelf between 20-80m water depth (Febo et al., 2008; Goni et al., 2008; Slingerland et al., 2008a; Slingerland et al., 2008b; Walsh et al., 2004). Finer sediments may bypass the shelf system and escape to the deep sea fan environments through the Umuda Valley (Crockett et al., 2008) and the Pandora trough (Febo et al., 2008) located at the southwestern and northeastern edges of the shelf, respectively. Also, approximately 14% (Walsh and Nittrouer, 2004) of fluvial sediments are trapped in the estuarine mangrove environments along the coast, however, this mainly occurs in the Fly river system where flow velocity is less due to lower gradients in the topography (Walsh and Nittrouer, 2009b).

Subaqueous delta clinoform sediment systems exist in other regions where large rivers drain substantial volumes, at least 100Mt/yr, of sediments into the ocean

and large tidal ranges (Walsh and Nittrouer, 2009a). These sedimentary sequences provide an idealized sea-level record with information regarding the historical interplay between sediment supply, accommodation and tectonics (Figure 2). As sediment supply outpaces accommodation, the clinoform profile reveals a more progradational shape. When sediment supply equals the available accommodation, the profile becomes more aggradational. If accommodation outpaces sediment supply, the clinoform becomes more sigmoidal. Deciphering these patterns as they occur in various shelf setting around the world, is an important step in understanding interplay between sediment supply and creation of accommodation.

Using CHIRP subbottom profiling techniques (Figure 3), scientists can image the sedimentary sequences below the seafloor 50-70 meters deep with submeter resolution. This imaging technique provides information for multi-dimensional analysis. Sediment cores acquired along specific transects, provide groundtruthing information to understand the sediment characteristics and biogenic material for dating layers within the sequence. Through acquisition of several down-core radiocarbon dates, the rates of deposition can be estimated (Broecker et al., 1958). Our work discovered the clinoform sequences imaged in the GOP are mainly modern Holocene in origin and more complex than previously thought. The modern clinoform overlays an older clinoform partially eroded on top from a transgressive sequence, which is exposed at the surface in other offshore regions of our study area. We discovered multiple depocenters that have shifted over recent geologic history and the following chapters explain how that may have occurred.

The second study area is located along the coastline in the Oceanside Littoral Cell. Sea cliffs (25-100m high) abut the beaches in southern California and are prone to active erosion. The cliffs are mainly marine sandstone deposits of Eocene age (~45-50Mya), however some terrestrial units on top are as young as Pleistocene (~125Kya). Being sandstone with limited cementation, these formations are only semi-consolidated

and easily eroded providing ephemeral sand deposits to the beach. Certain factors (e.g., precipitation, dewatering, instability, ground movements) increase the erosion rates and cause large block or slump type failures.

Our group developed a survey assessment method to quantitatively analyze the amount of sediment liberated from the cliffs using a time-series laser scanning protocol. Every six months (or following large cliff failure events), we conducted geospatial modeling using Light Detection and Ranging (LiDAR) technology (Figure 5). The resultant, highly-resolved point cloud data (7cm resolution) were the foundation for creating georeferenced surface models. Each surface was compared to previous surveys to quantify cliff erosion. The information has been gathered since 2006 and provides insight about the processes that control cliff erosion in Southern California. This is especially important to understand because of ever-increasing manmade coastal development along with rising sea level.

The aim of this work is to answer the following overarching questions by investigating these two study areas:

What does the sediment record tell us about sea level fluctuations in the past?
Can we tease out climate or other signals from past environmental history?
What are the dominant and subordinate mechanisms controlling cliff erosion and shelf building?

1.1.2 Processes controlling Sediment Deposition

Tectonics

One of the most important scientific discoveries in the last century is the idea that the outer layer of planet earth is not stationary (Hess, 1965). Prior to this discovery, scientists believed the ocean basins were merely linear troughs, called geosynclines, where marine

deposits collected (Dietz, 1963). Today, scientists understand that the crust is actively deforming and this process controls many of the landforms by which we are surrounded. Tectonics create relief, while erosion breaks it down. The balance of space created or destroyed is accommodation (Vail, Posementier 1977). The slope and chemical makeup of earth's surface structures is predominantly based on the tectonic regime in which it was formed. Distance and impact from tectonic plate activity determines whether a continental margin is passive or active. After sediments erode from their parent rock, they travel through dispersal systems spreading out the smaller material as each unit breaks down over time. The rate of erosion and distance from the source depends on the inherent energy in the system. For example, Type I rivers on passive margins (e.g., Mississippi, Ganges-Brahmaputra, Fly; Milliman et al. 2011), tend to have high water output, yet predominantly transfer finer grain sediment due to the low gradient in the watershed. Alternatively, Type II rivers on tectonically active margins are characterized by steep gradients and fast, energetic flows capable of carrying larger sized rock material.

Climate and Sea Level

Oscillations in climate patterns are evident in sediment records worldwide (Bond et al., 1993; Charles and Fairbanks, 1992) and have been studied on a variety of scales from centennial (Macklin and Lewin, 2003) to interglacial cycles (Mcmanus et al., 1994). Climatic variation is analyzed in sediments by investigating isotopic changes in foraminifera incorporated in depositional units as oceanographic current, salinity and temperature conditions vary. Investigating lake sediment records can also be an effective method for understanding paleoclimate, especially on smaller timescales, as they often contain varved sequences documenting seasonal variation in processes such as precipitation and wind patterns (Finney and Johnson, 1991) without the complication of oceanic variables.

Eustatic sea level (ESL) fluctuations, from oscillating Milankovitch cycles, along with sediment supply and tectonics control the stratal patterns and facies distribution on the continental shelves (Posamentier and Vail et al 1977). Terrigenous sediments deposit on the shelf in a system of tracts depending on the space available. As relative sea level (RSL) oscillates with local tectonic conditions, the available accommodation adjusts either seaward or landward. Sediments fill the accommodation in predictable patterns based on the forcing functions discussed here (Figure 8). The resulting sedimentary packages and evolution, from changes in forcing functions, are three-dimensional and complex (Driscoll and Karner, 1999), yet are documented worldwide on a wide variety of continental shelves (Nittrouer 1986, Kuehl 1997, Liu 2007).

Sediment Supply

Sediment origin controls the genetic makeup of material in a dispersal system. Determining provenance is key to understanding the process, transport pathways and rate at which sediments may travel from source to sink. Supply is dependant on precipitation and geomorphological features of the landscape (e.g., slope and rivers, etc.) for the delivery of sediments. Certain regions, such as the Gulf of Papua, receive high sediment loads regularly because of the abundant source material and high rates of precipitation. This end-member provides an ideal scenario to read the layers of geological history and understand how sediment input has shifted based on climatic variation (Figure 7). The second study area in Southern California is an arid region with much lower levels of modern sediment supplied to the coast and is referred to as a “sediment-starved” area. Here, we are investigating the modern-day physical processes at work to “feed” the sediment system. Previous notions assumed the sediment on the beaches came from local rivers, however all rivers in the region are anthropogenically altered (e.g., dams, cementation, etc) and only episodic storm events provide enough flow to carry

sediments seaward. Our group, over the years, has revealed that the sea cliffs are crucial contributors to beach sands and are an important source in the coastal, nearshore and shelf system (Hass 2005; Young 2006).

1.1.3 OUTLINE OF DISSERTATION

This thesis begins with two chapters about the Papua New Guinea mid-shelf region. Chapter two focuses on the lobe switching that occurred during the Holocene on the mid-shelf clinoform. Chapter three is a more in-depth look into the sediments that make up the lobes and their provenance. The rest of the dissertation is focused on cliff erosion in Southern California and the methods that our group developed to quantify this regional phenomenon. Chapter four is a published manuscript that describes LiDAR technology and how our group conducted a time series analysis of the sea cliffs in the Oceanside Littoral cell. Chapter five investigates the processes controlling this type of erosion. The final chapter summarizes the concepts introduced within this dissertation. Three appendices are included with published manuscripts from these studies.

1.1.4 REFERENCES

Boggs, Sam Jr., Principles of Sedimentology and Stratigraphy (3rd ed.), 2001, 726 p.

Bond, G., Broecker, W., Johnsen, S., Mcmanus, J., Labeyrie, L., Jouzel, J., and Bonani, G., 1993, Correlations between Climate Records from North-Atlantic Sediments and Greenland Ice: Nature, v. 365, p. 143-147.

Broecker, W.S., Turekian, K.K., and Heezen, B.C., 1958, The Relation of Deep Sea Sedimentation Rates to Variations in Climate: American Journal of Science, v. 256, p. 503-517.

Charles, C.D., and Fairbanks, R.G., 1992, Evidence from Southern-Ocean Sediments for the Effect of North-Atlantic Deep-Water Flux on Climate: Nature, v. 355, p. 416-419.

Crockett, J.S., Nittrouer, C.A., Ogston, A.S., Naar, D.F., and Donahue, B.T., 2008, Morphology and filling of incised submarine valleys on the continental shelf near the mouth of the Fly River, Gulf of Papua: Journal of Geophysical Research-Earth Surface, v. 113, p. -.

Dietz, R.S., 1963, Collapsing Continental Rises: An Actualistic Concept of Geosynclines and Mountain Building: The Journal of Geology, v. 71, p. 314-333.

Driscoll, N.W., and Karner, G.D., 1999, Three-dimensional quantitative modeling of clinoform development: Marine Geology, v. 154, p. 383-398.

Febo, L.A., Bentley, S.J., Wrenn, J.H., Droxler, A.W., Dickens, G.R., Peterson, L.C., and Opdyke, B.N., 2008, Late Pleistocene and Holocene sedimentation, organic-carbon delivery, and paleoclimatic inferences on the continental slope of the northern Pandora Trough, Gulf of Papua: Journal of Geophysical Research-Earth Surface, v. 113.

Finney, B.P., and Johnson, T.C., 1991, Sedimentation in Lake Malawi (East Africa) during the past 10,000 years: a continuous paleoclimatic record from the southern tropics: Palaeogeography, Palaeoclimatology, Palaeoecology, v. 85, p. 351-366.

Goni, M.A., Monacci, N., Gisewhite, R., Crockett, J., Nittrouer, C., Ogston, A., Alin, S.R., and Aalto, R., 2008, Terrigenous organic matter in sediments from the Fly River delta-clinoform system (Papua New Guinea): Journal of Geophysical Research-Earth Surface, v. 113, p. -.

Hess, H.H.: Mid-ocean ridges and tectonics of the sea-floor. In: Submarine geology and geophysics, 17th Colston Research Symposium, Bristol, England, W. F. Whittard, R. Bradshaw, eds., p. 317-333. London: Butterworths 1965

Macklin, M.G., and Lewin, J., 2003, River sediments, great floods and centennial-scale Holocene climate change: Journal of Quaternary Science, v. 18, p. 101-105.

Mcmanus, J.F., Bond, G.C., Broecker, W.S., Johnsen, S., Labeyrie, L., and Higgins, S., 1994, High-Resolution Climate Records from the North-Atlantic during the Last Interglacial: Nature, v. 371, p. 326-329.

Pickup, G., 1984, Geomorphology of Tropical Rivers .1. Landforms, Hydrology and Sedimentation in the Fly and Lower Purari, Papua-New-Guinea: Catena, p. 1-17.

Slingerland, R., Driscoll, N.W., Milliman, J.D., Miller, S.R., and Johnstone, E.A., 2008a, Anatomy and growth of a Holocene clinothem in the Gulf of Papua: Journal of Geophysical Research-Earth Surface, v. 113.

Slingerland, R., Selover, R.W., Ogston, A.S., Keen, T.R., Driscoll, N.W., and Milliman, J.D., 2008b, Building the Holocene clinothem in the Gulf of Papua: An ocean circulation study: Journal of Geophysical Research-Earth Surface, v. 113.

Walsh, J.P., and Nittrouer, C.A., 2003, Contrasting styles of off-shelf sediment accumulation in New Guinea: Marine Geology, v. 196, p. 105-125.

—, 2004, Mangrove-bank sedimentation in a mesotidal environment with large sediment supply, Gulf of Papua: Marine Geology, v. 208, p. 225-248.

—, 2009a, Understanding fine-grained river-sediment dispersal on continental margins: Marine Geology, v. 263, p. 34-45.

—, 2009b, Understanding fine-grained river-sediment dispersal on continental margins: Marine Geology, v. 263, p. 34-45.

Walsh, J.P., Nittrouer, C.A., Palinkas, C.M., Ogston, A.S., Sternberg, R.W., and Brunskill, G.J., 2004, Clinoform mechanics in the Gulf of Papua, New Guinea: Continental Shelf Research, v. 24, p. 2487-2510.

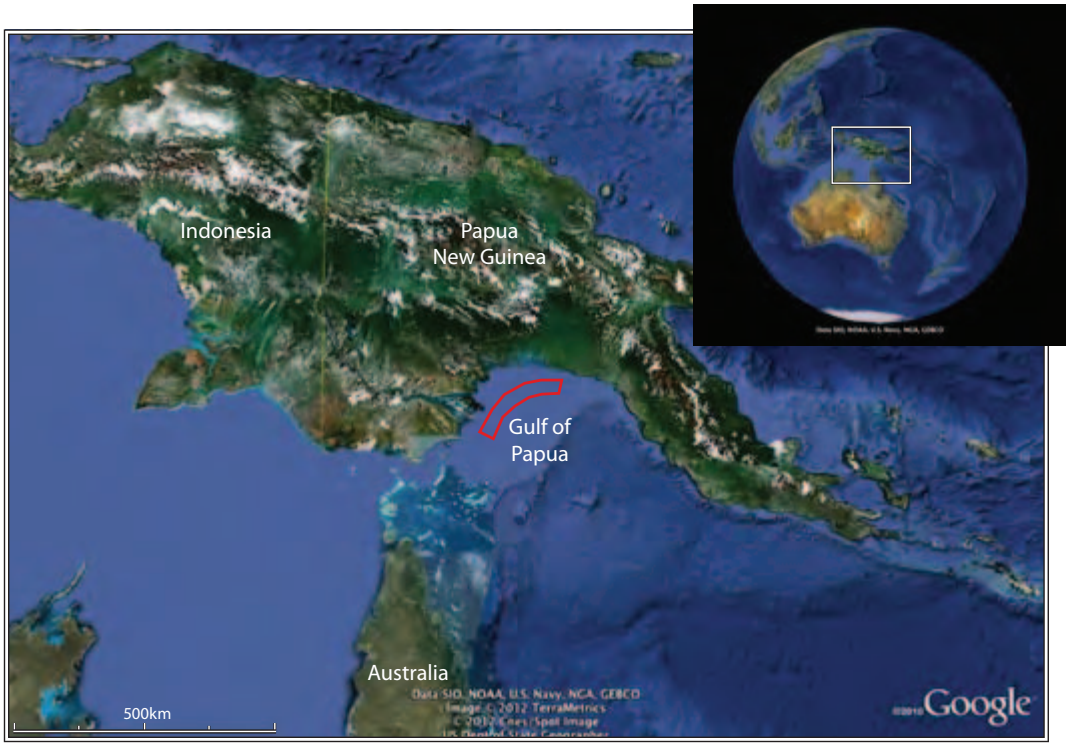

Figure 1-1: Location map of study site on the mid-shelf clinoform in the Gulf of Papua.

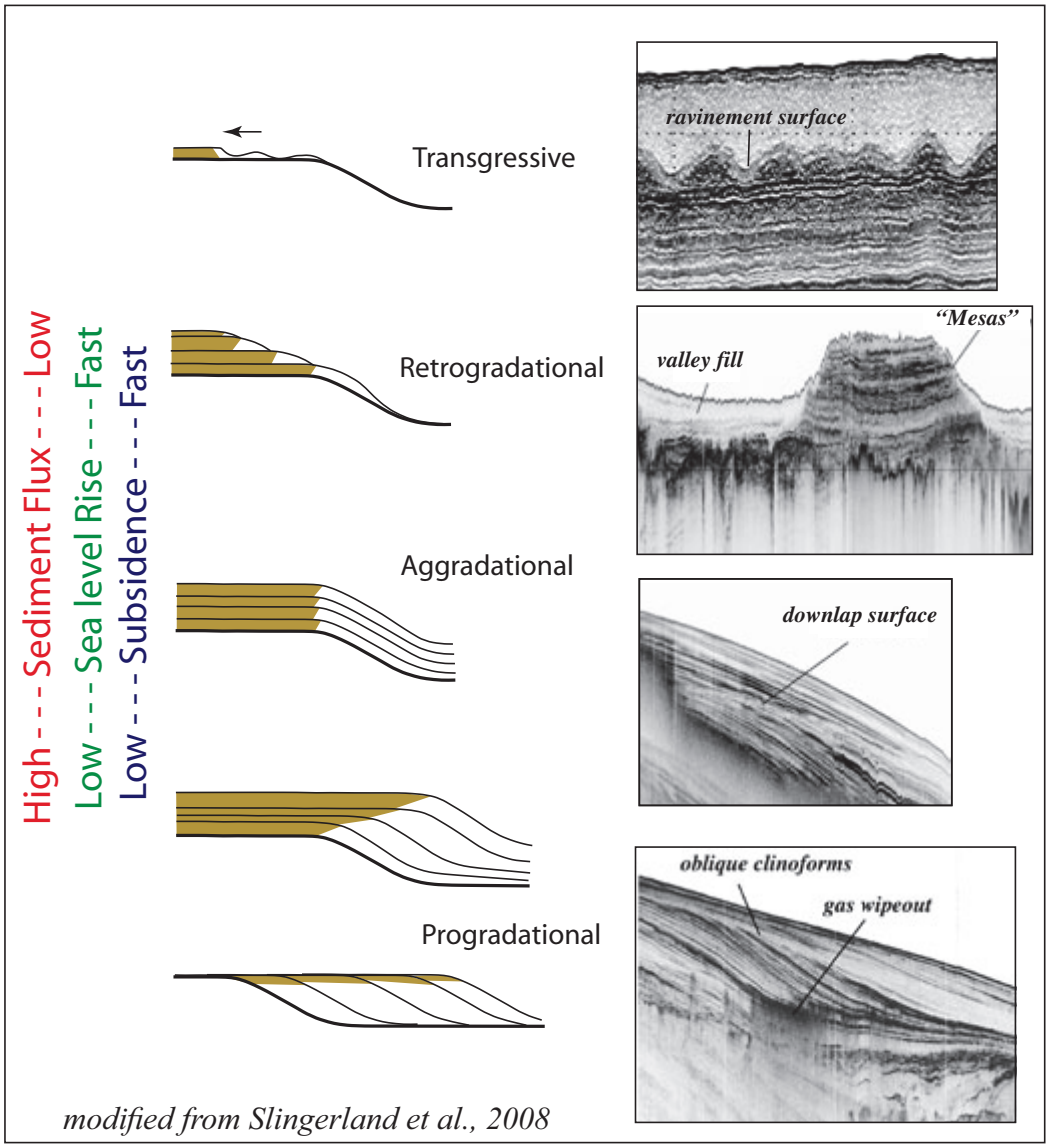

Figure 1-2: Diagram illustrating the interplay between tectonics (subsidence), sea level change and sediment supply and the effect on stratal geometry in stratigraphic units. CHIRP data (right) show examples of patterns imaged in the Gulf of Papua's mid-shelf clinoform.

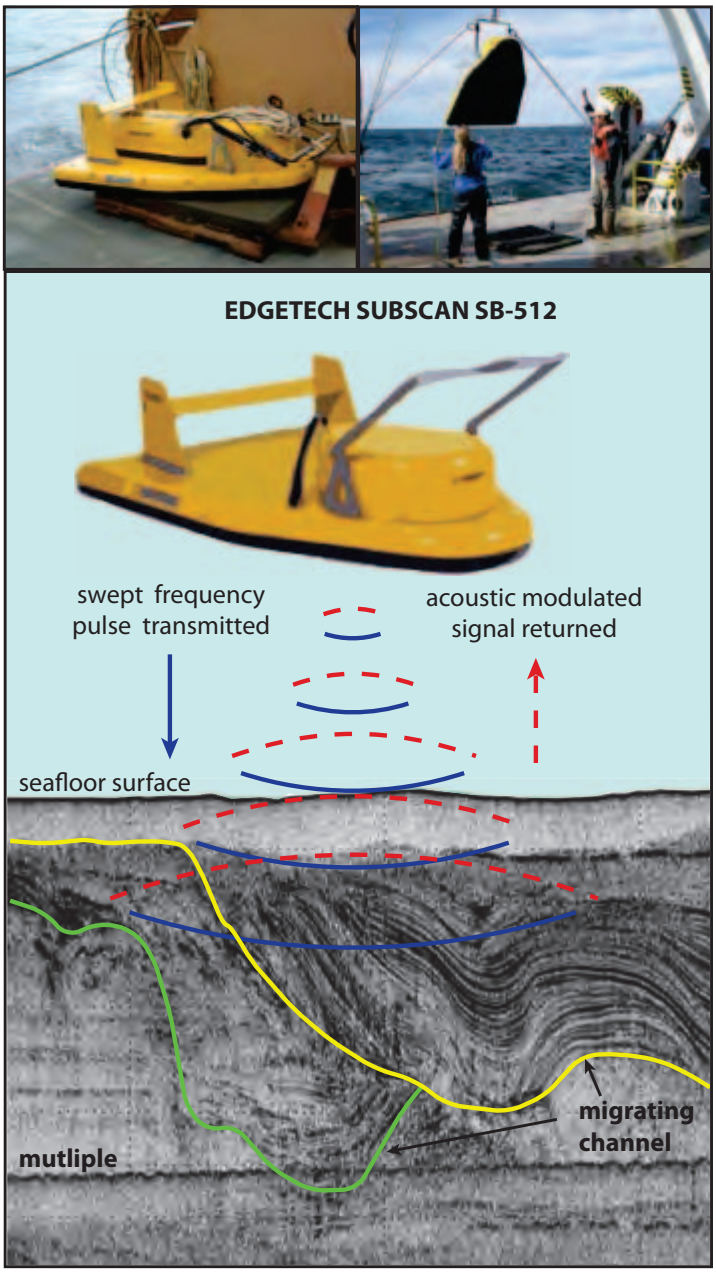

Figure 1-3: Photographs of Edgetech CHIRP SB-512 on deck (top left) and being deployed (top right) off the stern of a research vessel. Lower diagram illustrates how a multi-frequency pulse is transmitted and penetrates through the seafloor and reflects off of reflective lenses with different impedience. Upon return to the towfish, a match filter is applied to the signal before being digitally transferred by coaxial cable to the ship. Note the high- fidelity imaging resulting in sub-meter resolution.

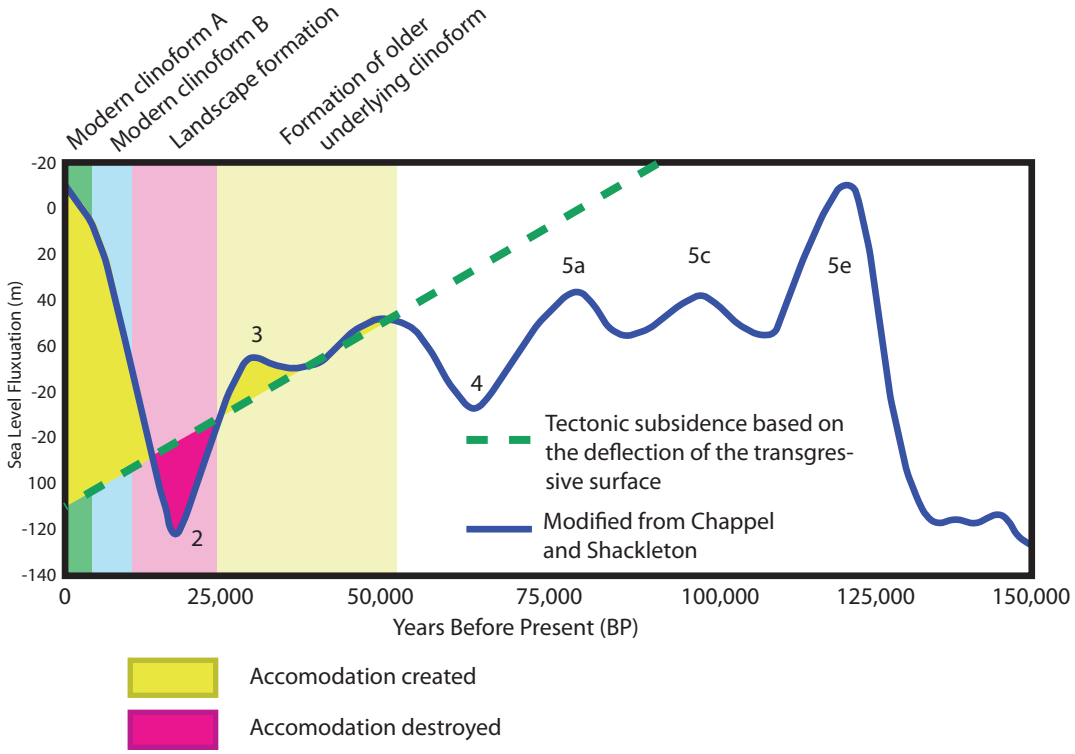

Figure 1-4: Idealized sea level curve (modified from Chappel and Shackleton 1986) with isotope stages and local GOP basn subsidence rate overlain. Note where curve is above the subsidence rate, accomodation is created and is destroyed where the curve falls below the rate of subsidence.

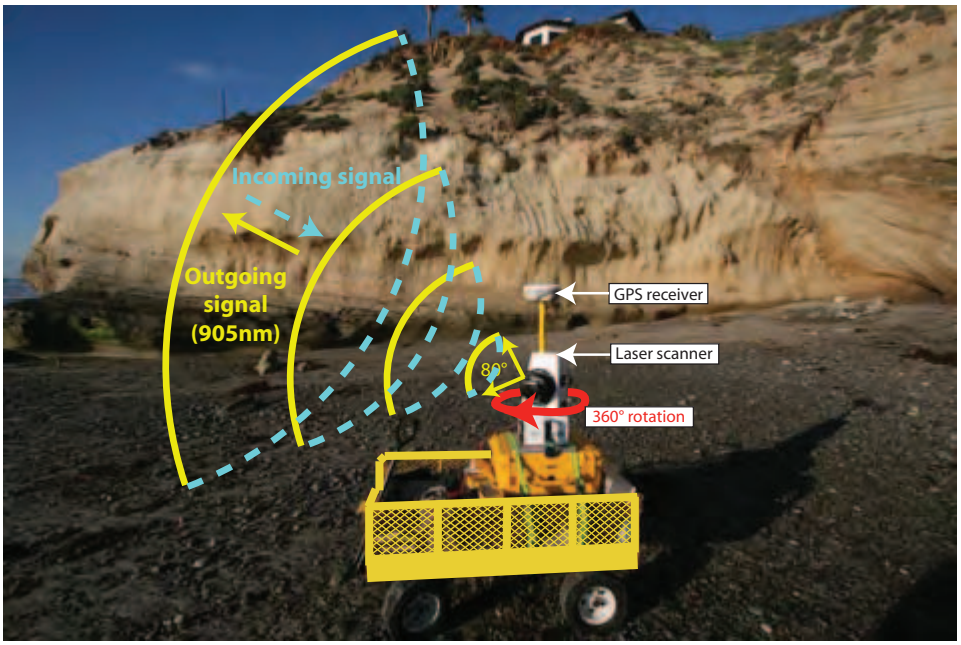

Figure 1-5: Image of I-Site 4400 terrestrial scanner field setup with diagram of laser pulse function and head rotation. Scanner emits infrared wavelength laser pulses (905nm) that radiate in a 360 degree rotational scan field with a vertical look angle of 80 degrees. The signal is returned and distance is calculated based on time of return. Data clouds are georeferenced based on the real-time kinematic (RTK) GPS survey origin of the receiver.

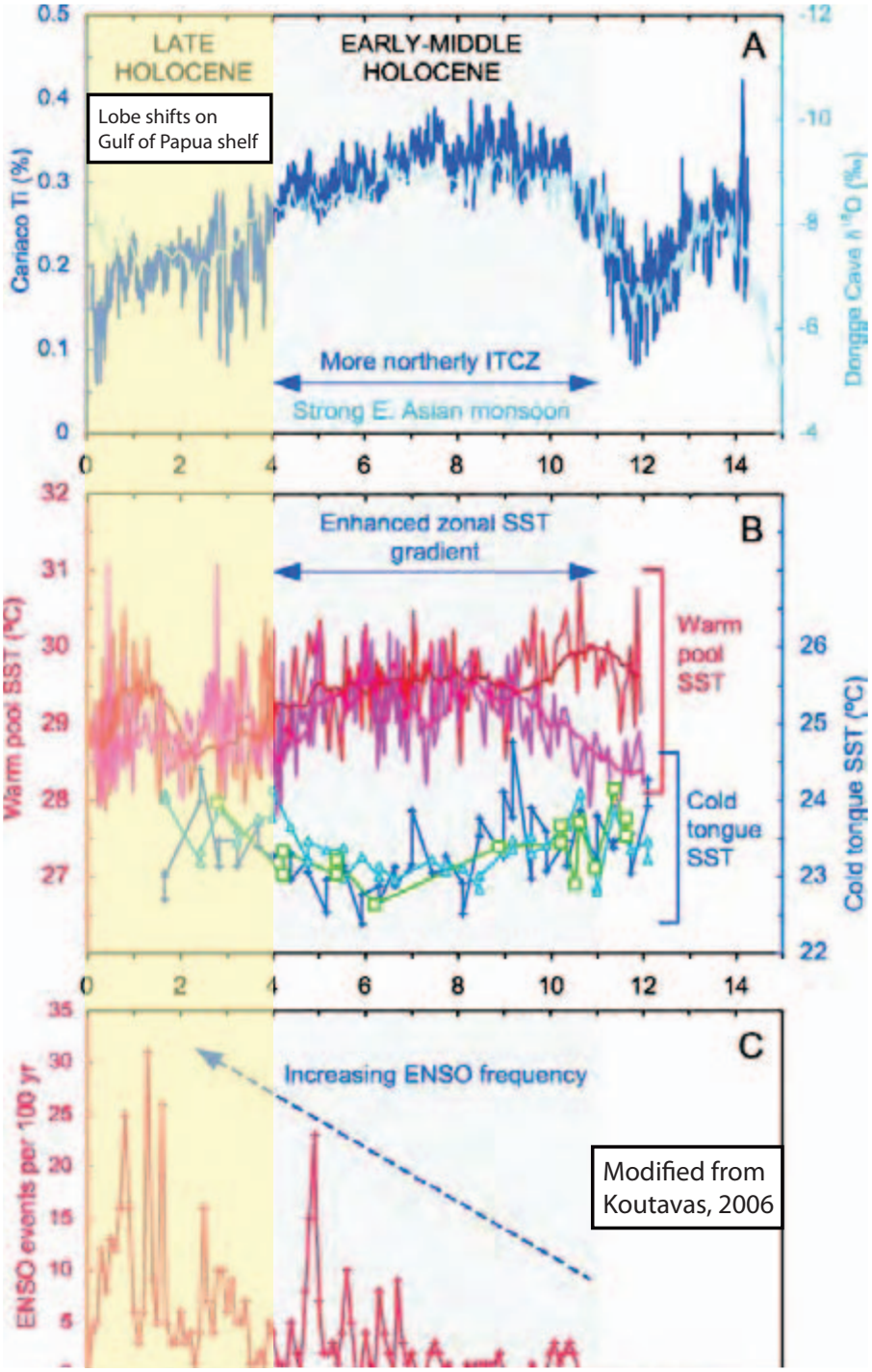

Figure 1-6: Sea surface temperature signals (modified from Koutavas, 2006) from present to 15Kya. Note shifts in ITCZ and change in ENSO frequency beginning approximately 4kya. The yellow box shows the timing of the presented hypothesis regarding the PNG lobe shifting events (see Chapter 2 and 3).

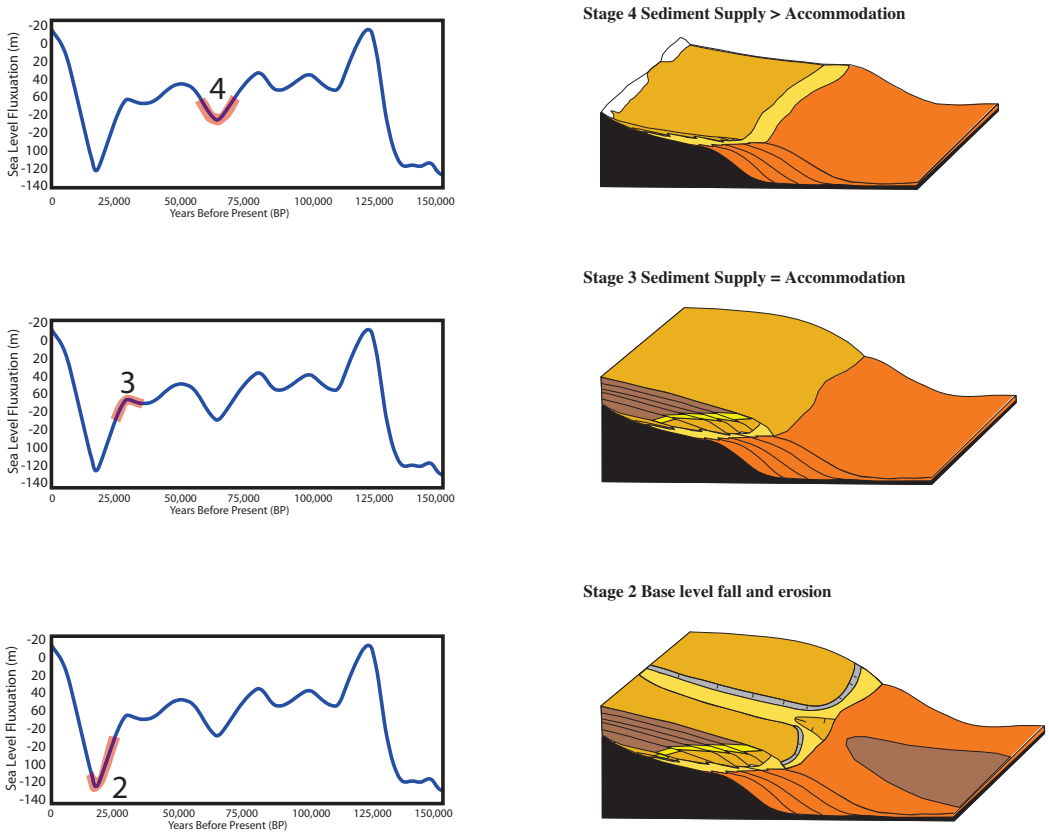

Figure 1-7: Illustration of sea level curve (left) at highlight period during the last interglacial with associated stratal package behavior based on relationship between sea level and accommodation.

Figure 1-8: Diagram (modified from Walsh et. al. 2009) illustrating the various sediment accumulation patterns and the forcing conditions with respect to sediment supply, tidal and wave conditions.

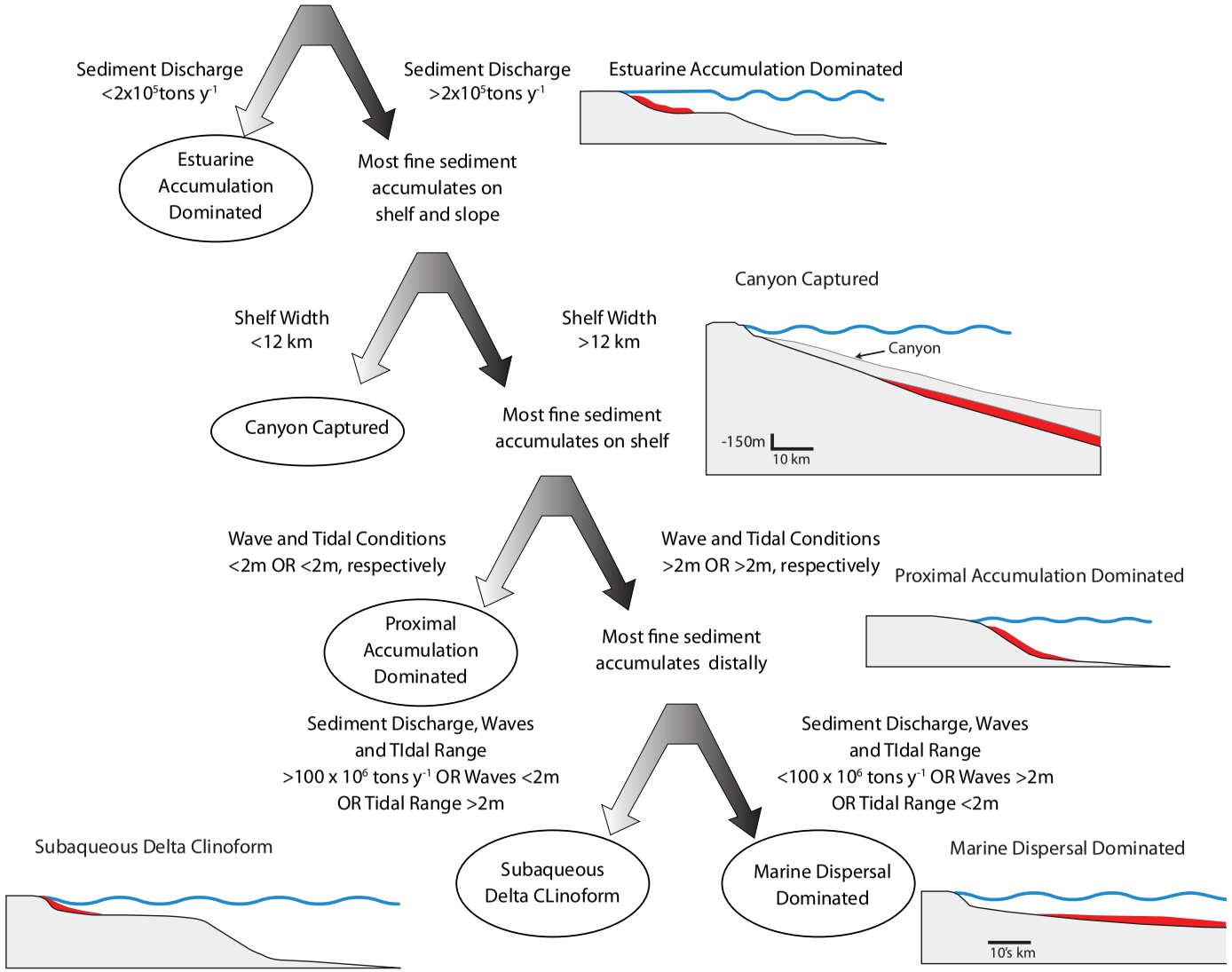
Sediment Discharge
<2x10^5tons y^-1
Sediment Discharge
>2x10^5tons y^-1
Estuarine Accumulation Dominated
Estuarine Accumulation Dominated
Most fine sediment accumulates on shelf and slope
Shelf Width
<12 km
Shelf Width
>12 km
Canyon Captured
Canyon
-150m
10 km
Canyon Captured
Most fine sediment accumulates on shelf
Wave and Tidal Conditions
<2m OR <2m, respectively
Wave and Tidal Conditions
>2m OR >2m, respectively
Proximal Accumulation Dominated
Proximal Accumulation Dominated
Most fine sediment accumulates distally
Sediment Discharge, Waves and TIdal Range
>100 x 10^6 tons y^-1 OR Waves <2m
OR Tidal Range >2m
Sediment Discharge, Waves and TIdal Range
<100 x 10^6 tons y^-1 OR Waves >2m
OR Tidal Range <2m
Subaqueous Delta Clinoform
Subaqueous Delta CLinoform
Marine Dispersal Dominated
Marine Dispersal Dominated
10's km

Figure 1-9: Cliff sediments actively eroding at Torrey Pines State Park on August 4, 2007.

2

Three-Dimensional Clinoform Architecture in the Gulf of Papua: Interplay Between Sediment Supply and Dispersal.

2.1 ABSTRACT

CHIRP seismic data acquired in the Gulf of Papua (GoP) reveal that the modern mid-shelf clinothem consists of three depositional lobes, a central lobe downlapped by younger northern and southern lobes. Defining the three-dimensional architecture of this clinothem provides the ideal opportunity to examine the evolution of a sediment dispersal system, and thus gain insight into the role of sea level, sediment supply, and climate on annual to millennial timescales. The depocenter shift and infilling of available accommodation within the central lobe appear to be predominantly controlled by depositional processes and stacking patterns (autocyclic forces). Conversely, the marked shift in deposition away from the central lobe to the northern and southern lobes (~60-80 km), which bypassed adjacent accommodation, is difficult to explain by depositional processes alone and likely is controlled by fluctuations in the intensity and frequency of regional climate cycles. Radiocarbon dates show that the marked shift in deposition away from the central lobe occurred after 2 ka, approximately 5 ka after the last rapid eustatic sea-level rise. The timing of this abrupt shift is roughly coincident with millennial scale changes observed in climate proxy data from the region. As it is unlikely that sediment flux from the various contributing rivers (e.g., Fly, Purari, Kikori, etc.) changed appreciably, we speculate that lobe shifting reflects a change in coastal circulation, perhaps the result of fluctuations in the location of the Intertropical Convergence Zone (ITCZ).

2.2 INTRODUCTION

Clinothems are heterolithic, coarsening-upwards sequences containing chronostratigraphic horizons (clinoforms) that cut obliquely through them (Mitchum et al., 1977, Slingerland et al., 2008). Clinothems have a three-part morphology defined by two prominent breaks in slope: a gently sloping nearshore topset, a steeper foreset, and a gently sloping offshore bottomset (Nittrouer et al., 1986). Clinothems constitute a significant building block on many present-day continental shelves, including those off major rivers such as the Amazon (Nittrouer et al., 1986, 1995; Kuehl et al., 1986), Ganges-Brahmaputra (Kuehl et al., 1997; Michels et al., 1998), Yangtze (Liu et al., 2007), and Ebro (Diaz et al., 1996). Clinothem architecture and morphology record the interplay between relative sea-level fluctuations, changes in sediment supply, and climate (Driscoll and Karner, 1995). Despite intense study, understanding how these processes control the three-dimensional character of clinothems remains unresolved.

To investigate the formation of the Gulf of Papua (GoP) clinothem, we have employed a three-pronged approach: 1) computational and physical modeling to illuminate mechanisms of clinothem formation under various controls; 2) field investigation of clinothem morphology and internal architecture; and 3) stratigraphic documentation at appropriate spatial scales to provide desired temporal resolution (Slingerland et al., 2008). Here we present new data from the GoP that place lithologic and chronological constraints on the packages, thereby allowing us to understand the causes of shifting loci of deposition.

The Gulf of Papua Holocene clinothem, located off the southeastern coast of Papua New Guinea, is fed by two principal rivers systems – the Fly to the south and a series of rivers to the north, principally the Purari and Kikori that drain the Finesterre Range (Fig. 1), with maximum elevations exceeding 4000 m. Assuming average runoff of 2000mm/yr (Milliman and Farnsworth, unpublished data), collective freshwater

discharge is estimated to be ~300 km^3/yr with less than ~50% seasonal or interannual variation. Largely unaffected by typhoons, GoP rivers seldom experience catastrophic floods, 100-yr floods discharging only about twice the runoff of 2-year floods (Pickup, 1984). Despite their hydrological similarities, the Fly River and the northern rivers are quite different. The northern watersheds are more mountainous, the ratio of elevations >1000 m (source) to elevations <100 (sink) ranging from 5 to 15. Moreover, northern rivers drain primarily lithoclastic and pyroclastic Jurassic strata and Quaternary volcanics (D'Addario, 1975). In contrast, the Fly River drainage basin is dominated by elevations <100 m (>1000m to <100 being ~0.5), and the headwaters drain primarily Mesozoic limestone. As such, the northern rivers discharge relatively immature sediments, with a cumulative volume at least twice that of the Fly (Milliman et al., 2006; unpublished data.).

The GoP also experiences strong climate forcing caused by seasonal variation between the SE trades and NW monsoon, the Coral Sea Current, and meso- to macro-tides, resulting in both across- and along-shore sediment transport (Harris, 1990; Wolanski, et al., 1984, 1995; Slingerland et al., 2008). Because of strong forcing functions and the distinctly different sediment sources, the mid-shelf clinothem in the Gulf of Papua provides an ideal location to study the evolution of these sedimentary bodies.

While annual climate forcing associated with the trades and monsoon creates large seasonal changes in sediment supply and dispersal within the GoP, the proximity of the Gulf of Papua to the Indo-Pacific Warm Pool (IPWP) makes it susceptible to millennial scale climate shifts associated with shifts in the ITCZ. Climate proxies reveal decadal to millennial time scale fluctuations in meridonal location of the ITCZ (Partin, Cobb 2007), which may control the three-dimensional clinothem architecture and lobe-switching. For example, during NW Monsoons when the ITCZ is farther south, the

ocenaic currents support mid-shelf deposition to the southwest of the northern rivers. Conversely, during the SE trades the Coral Sea current becomes stronger and forces deposition to the east (Slingerland, et. al, 2008).

2.3 METHODS

As part of the NSF-funded MARGINS Source to Sink program (S2S), we acquired 2300 km of Compressed High-Intensity Radar Pulse (CHIRP) data and an additional 4500 km of hull-mounted Knudsen subbottom data onboard the R/V Melville in 2004. The CHIRP is a towed subbottom system with a 1-5.5 kHz pulse and 50-ms sweep that yields sub-meter vertical resolution data. A differential global positioning system (DGPS) was used to georeference all data. A total of 50 piston and gravity cores (cumulative length 432 m) were obtained during the cruise, their locations based on CHIRP subbottom data. Correlation of CHIRP profiles with the core data and combined with radiocarbon dating established a chronostratigraphic framework for the region.

2.4 RESULTS

The grid of high-resolution CHIRP seismic data highlights the three-dimensional geometry of the mid-shelf clinothem (Fig. 1). The modern mid-shelf clinothem obscures and infills an underlying 30-40 meter thick clinothem with sub-horizontal, concordant reflectors exhibiting minimal thickness variation. The older clinothem appears to have been formed during Oxygen Isotope stages 3 and 4 and subsequently eroded during stage 2 (Slingerland et al., 2008); this erosional landscape is exposed as a corrugated surface seaward of the modern clinothem (Fig. 2). The modern GoP mid-shelf clinothem contains three main lobes, a central lobe downlapped by two younger lobes to the north and south with no evidence of interfingering between the lobes (Fig. 2). Below we describe the internal architecture and morphology of the central lobe and then its relationship to the northern and southern lobes.

The central lobe consists of three units, an oblique progradational basal sequence (Yellow unit) overlain by a sigmoidal progradation package (Orange unit) that is mantled by a draping sequence (Red unit). A fence diagram delineates the northeast trend of the depocenter within the Yellow unit, which is coincident with the oblique clinforms observed on dip lines T15 and STR1 (Fig 2). The Orange and Red units downlap onto the oblique prograding Yellow unit, such an observation requires the generation of new accommodation (Slingerland et al., 2008).

Above the Yellow unit, the depocenter for the Orange unit is systematically displaced to the southeast, infilling the adjacent accommodation (Fig. 2). The depocenter for the Orange unit is located where the Yellow unit is thinnest along the distal portion of Line 15. Furthermore, the Orange unit systematically thins and onlaps onto the underlying Yellow unit toward the northeast along strike line STR1. Two younger lobes colored in Blue/Purple and Turquoise/Green oriented to the north-northeast and south-

southwest, respectively, downlap onto the central lobe (Fig. 3). To the north of the central lobe, the Blue unit downlaps onto the Red unit, and in the south the Turquoise unit downlaps the Red unit, while both lobes prograde offshore. Where the southern and northern lobes downlap onto the central lobe, there is no observed interfingering of the acoustic reflectors. Moreover, the region where the downlap is observed is a bathymetric low. The depocenter for both the northern and southern lobes have bypassed this region of accommodation adjacent to the central lobe. The intervening lows between the three depocenters are not controlled by the antecedent erosional terrain formed during Stage 2 (Slingerland et al., 2008); rather it records differential deposition across the mid-shelf related to the development of the modern mid-shelf clinothem.

Core Data

Sedimentological analysis of gravity and piston cores allows us to correlate the CHIRP seismic data to the lithostratigraphy. AMS-^{14}C radiocarbon dates of hand-picked mollusk shells, foraminifera tests, and ooids were dated at NOAMS/Woods Hole Oceanographic Institution, to establish a chronostratigraphic framework (see supplemental Figures and Table 1 CH.3). Cores from the promontories of the central lobe recovered homogenous fine-grained clays/muds, beneath which are intermittent laminations of alternating clay and sand couplets. Cores acquired in the embayments adjacent to the promontories recovered coarser sediments, correlating with high-amplitude reflectors imaged in the CHIRP seismic data (Fig. 2). Additionally, cores (e.g., JPC 13; Fig. 1) collected seaward of the modern clinothem reveal laminated sediments with coarse-grained lag deposits and abundant ooids, underlain by discontinuous sand and clay lenses. Radiocarbon dates from organic material in the lag deposit yield ages greater than 34 ka. Dated materials from cores in the northern and southern lobes were all younger than 2000 years old, while dated material from the red and orange units of the

central lobe was deposited in the last 6000 years (see supplemental Figures and Table).

Lithostratigraphy of mid-shelf cores

Three distinct lobes exist (Figure 1) within our study region with sediments sampled from the High Stand systems tract (HST) and part of the older Transgressive systems tract (TST). Within each lobe, four distinct zones are mapped: topset, foreset, bottomset and relict surface and these components of each clinothem are labeled 1-4, respectively. Each lobe has been classified by relative location as Southern (S1-4), Central (C1-4), Northern (N1-4). Core samples were acquired within the clinoform package and offshore relict deposits in water depths of 20-80 meters. Three lithostratigraphic zones are part of the modern clinoform, while the offshore zone is differentiated by relatively older and coarser material.

The southernmost zone (S1-4) is part of the lobe extending from 20-80m water depth offshore from the Fly river delta. Cores from this region exhibited mostly fine, homogenous brownish, gray clay with limited bioturbation. The cohesive muds are interbedded with increasing terrigenous sand laminations in topset section of each clinothem. Sediments sampled from the foreset consist of homogenous muds and very little to no bioturbation. No cores sampled the bottomset of the southern lobe. The two cores from the southern-most extent, JPC53 and JPC54 penetrated a sandy terrigenous layer at 650cm, with some mud clasts present.

Within the Central region, cores were collected ranging from 22m to 70m water depth. Sediment collected from the Central lobe (C1-4) consists mainly fine homeogenous clay with some interbedded structures within the topset region of the clinothem. Several cores were acquired along the foreset and exhibit fine grain, homogenous clay. Cores acquired offshore from the clinoform bottomset sampled older transgressive lag deposits including abundant ooids and foraminifera.

Cores acquired from the Northern region (N1-4) sampled the clinothem only and

no samples were obtained offshore. However, one core did penetrate the relict surface underlying the modern sedimentary deposit.

2.5 DISCUSSION

The mid-shelf clinothem in the Gulf of Papua consists of two stacked clinothems representing late Pleistocene and Holocene progradational phases. The two clinothems are separated by an erosional surface that formed during the Stage 2 sea-level regression (Slingerland et al., 2008). Based on its stratal geometry, the older clinothem prograded two-thirds of the way across the pre-existing shelf prior to modern deposition. The modern clinothem is composed of three main lobes: an older central lobe downlapped by northern and southern lobes. Within the central lobe, three packages are identified on the basis of stratal geometry. The basal Yellow unit builds relief with oblique clinoforms prograding seaward (Fig. 2). The depocenter has a northeast-southwest trend along the GoP mid-shelf. The formation of oblique clinoforms in the Yellow unit with no aggradation indicates no new accommodation was generated during this time (Christie-Blick and Driscoll, 1995). Mantling the Yellow unit is the Orange unit that thins distally by downlap, laterally by onlap onto the underlying depocenter, and proximally by offlap.

Within the underlying Stage 4 clinothem, we observe geometry that suggests the rate of sediment supply filled the available accommodation. The obliquely stacked sediments must have been deposited during the sea level regression between ~55,000- 75,000 years BP since we detected no aggradation during the progradational phase of construction. Eustatic sea level would have been falling faster than subsidence. Febo et al. 2008 also observed a major siliclastic pulse on the slope between 60,000 – 100,000 years BP. As sediment supply came into equilibrium with accommodation, during Stage 3 before the major regression associated with the LGM, topsets were formed with consistant age dates

from core samples (Harris et al. 1996).

The lateral shift of the Orange depocenter to southeast fills the adjacent accommodation and the clinothem shingles off the constructional high. Unlike the underlying Yellow unit, the Orange unit exhibits both aggradation and progradation. Despite the increase in accommodation required to explain the shift from oblique (Yellow unit) to sigmoidal clinoforms (Orange unit), the locus of deposition remained within the central lobe, which suggests only a minor shift in the sediment dispersal patterns along the GoP mid-shelf. This depocenter shift and infilling of available accommodation within the central lobe from the Yellow to Orange unit appear to be predominantly controlled by depositional processes and stacking patterns (autocyclic forces). The uppermost Red unit is predominantly a drape deposit as it mimics the underlying morphology and is regionally distributed.

Depocenters of the northern and southern lobes migrate away from the central lobe by at least 60 km and then infill the intervening accommodation space through time. The younger lobes downlap onto the central lobe with no evidence of interfingering. All radiocarbon age dates from the Northern and Southern lobes are younger than 2 ka, indicating that the switch in deposition occurred long after the last rapid sea-level rise (Liu et al., 2004). An abrupt shift away from the central lobe to both the north and south is difficult to explain by stochastic processes alone because both lobes bypassed adjacent accommodation that was subsequently infilled without any major eustatic change. If the cause of the lobe shift were autocyclic due to an avulsion or flow diversion associated with inner shelf deposition, one would expect migration away from the underlying depocenter with infilling of adjacent accommodation, as is observed within the central lobe between the Yellow and Orange units.

It is difficult to explain why sediment dispersal migrated ~60 km away from the previous depocenter only to systematically infill the adjacent accommodation as

the new lobes prograded both seaward and laterally through time (Fig. 3). We suggest that oceanographic processes, perhaps associated with the fluctuations in intensity and location of the Coral Sea Current, caused the abrupt shift in deposition away from the central lobe. Based on oceanographic modeling and sediment provenance studies, a convergence in flow exists to the north of the Fly River (Fig. 1; Slingerland et al., 2008; Milliman et al., 2006). At the zone of convergence, along-shelf flow is diverted toward the southeast and flows off the GoP shelf. The boundary between the southern lobe and the central lobe is spatially coincident with this zone of convergence, which is also defined by a change in sand and clay mineralogy (Fig. 1). At present, along-shelf current patterns and the resulting zone of offshore flow appear to favor the development of a northern and southern depocenter. If this convergence zone had been previously displaced southward, it could have lead to the development of a central lobe with sediment sourced predominantly from the northern rivers. Such a prediction for the central lobe is consistent with the results from our sediment provenance study (Milliman et al., 2006). Finally, it is difficult to explain the observed lobe switching by changes in river discharge alone, given the headwater regions for these rivers are sourced from the same geographic area (Fig. 1). In the GoP S2S system, we propose that oceanographic processes and sediment dispersal are the dominant processes controlling the lobe switching. Present-day rainfall and wind shear in the region of PNG are strongly influenced by the location of the Intertropical Convergence Zone (ITCZ) and seasonal shifts cause monsoonal conditions. The frequency and extent of the shifts may have varied over the last sea level cycle (Partin, Cobb et al. 2007). Further modeling and recovery of long cores are required to test these preliminary predictions.

The presence of multiple lobes (Figure 3) confirms that clinothem evolution is indeed three-dimensional (e.g., Driscoll and Karner, 1999), with significant along-shelf and cross-shelf transport. Previous authors (Walsh et al., 2004, Fulthorpe and Austin,

1999) have suggested that subaqueous clinothems shaped by oceanographic circulation should exhibit a predominantly two-dimensional architecture with minimal along-strike variability. The high-resolution CHIRP data in the GoP indicate that clinothems are inherently three-dimensional across a variety of scales. In fact, much of the sediment in the GoP appears to be sourced from the northern rivers and transported south obliquely across the shelf by the Coral Sea current; despite being shaped by oceanographic circulation, the clinothem still exhibits much along-strike variability.

2.6 CONCLUSIONS

Modern clinothem development in the GoP is a complex three-dimensional process that appears to be driven by seasonal to millennial tropical climate variability. The tropical ocean-atmosphere system regulates precipitation and consequent sediment yield to the GoP margin. Based on climate proxies from the tropical Pacific, the onset of modern ENSO periodicities began approximately 5 ka, with an abrupt increase in the intensity about 3 ka (Gagan et al, 2004). This marked increase in intensity results from the enhanced interaction between the Southern Oscillation and the Pacific Intertropical Convergence Zone (ITCZ). We postulate this regional interaction affected the Coral Sea Current and caused a northward shift in the along-shelf convergence within the GoP to the present position (Figs. 1 and 2). In our conceptual model the migration of the convergence zone controls the sediment dispersal and location of lobe development.

Numerous studies using climate proxies provide evidence of millennial scale oscillation in the location of the ITCZ during the Holocene (Partin, Cobb, 2007). More recently, speleothem proxy records indicate millennial scale oscillation exist in the strength of the East Asian Monsoon over the last two glacial-interglacial cycles (Wang et al., 2008). Perhaps the observed long-term changes in the meridonal location of ITCZ or regional monsoon conditions may account for the lobe switching in the GoP. Future

data collection in this region, including longer sediment cores and additional geophysical coverage, will allow us to sample the oldest material in the northern and southern lobe above the downlap surface (Fig. 3) as well as the youngest material of the central lobe beneath the downlap surface. In so doing, we can constrain the age of the downlap surface and determine if the shift in deposition from the central lobe to the northern and southern lobe is coincident with the regional observed changes in ocean circulation conditions.

2.7 ACKNOWLEDGEMENTS

Funding for this research was through a grant from the NSF MARGINS Program. We also would like to thank the crew of the R/V Melville, Scripps Institution of Oceanography, that made the data acquisition in the GoP possible. J.P. Walsh, D. Walsh, J.C. Hill, and R. Fenwick participated in the cruise and provided valuable feedback.

2.8 REFERENCES

Christie-Blick, N and Driscoll, N.W., 1995, Sequence Stratigraphy, Annual Review of Earth and Planetary Sciences, 23, 451-478

D'Addario, G.W., Dow, D.B., Swoboda, R., 1975, Geology of Papua New Guinea, 1:2,500,000, Canberra, Bureau of Mineral Resources, Australia

Diaz, J.I., Palanques, A., Nelson, C.H., Guillen, J., 1996, Morpho-structure and sedimentology of the Holocene Ebro prodelta mud belt (northwestern Mediterranean Sea), Continental Shelf Research, 16, 435-456

Driscoll, N. W. and G. D. Karner, 1999, Three-dimensional quantitative modeling of clinoform development, Marine Geology, 154, 383-398.

Fairbanks, R., Mortlock, R.A., Chiu, T., Cao, L., Kaplan, A., Guilderson, T.P., Fairbanks, T.W., Bloom, A.L., Grootes, P.M., Nadeau, M., (2005), Radiocarbon calibration curve spanning 0 to 50,000 years BP based on paired $^{230}Th/^{234}U/^{238}U$ and ^{14}C dates on pristine corals, Quaternary Science Reviews, 24, 1781-1796

Fulthorpe, C.S., and Austin, J.A., 1999, Buried fluvial channels off New Jersey; did sea-level lowstands expose the entire shelf during the Miocene?, Geology, 27(3), 203-206

Gagan, M. K., Hendy, E. J., Haberle, S. G., Hantoro, W. S., 2004, Post-Glacial evolution of the Indo-Pacific Warm Pool and El Nino-Southern Oscillation, Quaternary International, 118-119, 127-143

Harris, P. T., 1990, Sedimentation at the Junction of the Fly River and the Northern Great Barrier Reef, in Torres Strait Baseline Study Conference, edited by D. Lawrence and T. Cansfield-Smith, pp. 59-85, Queensland, Australia.

Kuehl, S. A., D. J. DeMaster, and C. A. Nittrouer,1986, Nature of sediment accumulation on the Amazon continental shelf, Continental Shelf Research, 6, 209-225.

Kuehl, S.A., Levy, B.M., Moore, W.S. and Allison, M.A., 1997, Subaqueous delta of the Ganges-Brahmaputra river system. Marine Geology, 144, 81-96.Liu, J.P. et al., 2007, Flux and fate of Yangtze River sediment delivered to the East China Sea. Geomorphology, 85, 208-224.

Michels, K.H., Suckow, A., Breitzke, M., Kudrass, H.R., Kottke, B., 1998, Sediment transport in the shelf canyon "Swatch of No Ground" Bay of Bengal, 50, 1003-1022

Milliman, J. D., K. Xu, G. J. Brunskill, R. Slingerland, and N. W. Driscoll, 2006, Sediment mineralogy on the Gulf of Papua Clinoform: New insights into sediment sources and redistribution processes, Eos Trans. AGU, Ocean Sci. Meet. Suppl., 87, Abstract OS16A-25

Nittrouer, C. A., et al. 1986, The deltaic nature of Amazon shelf sedimentation, Geological Society of America Bulletin, 97, 444-458

Partin, J. W., K. M. Cobb, et al. (2007). "Millennial-scale trends in west Pacific warm pool hydrology since the Last Glacial Maximum." Nature 449(7161): 452-U453.

Ogston, A.S., R. W. Sternberg, C.A. Nittrouer, D.P. Martin, M.A. Goñi, and J.S. Crockett, 2008, Sediment Delivery from the the Fly River tidally dominated delta to the nearshoremarine environment and the impact of El Niño, J. Geophys, Res, 113, doi:10.1029/2006JF000669

Pickup, G., 1984, Geomorphology of tropical rivers; I, Landforms, hydrology and sedimentation in the Fly and Lower Purari, Papua New Guinea, Catena Supplement, 5, 1-17.

Slingerland, R., N. W. Driscoll, J. D. Milliman, S. R. Miller, and E. A. Johnstone (2008), Anatomy and growth of a Holocene clinothem in the Gulf of Papua, J. Geophys. Res., 113, F01S13, doi:101029/2006JF000628

Tudhope, A. W., et al. Variability in the El Nino - Southern oscillation through a glacial-interglacial cycle. Science 291(5508): 1511-1517, 2001.

Walsh, J. P., C. A. Nittrouer, C. M. Palinkas, A. S. Ogston, R. W. Sternberg, and G. J. Brunskill, 2004, Clinoform mechanics in the Gulf of Papua, New Guinea, Continental Shelf Research, 24, 2487-2510.

Wang, Y., Cheng, H., Edwards, R. L., Kong, X., Shao, X., Chen, S., Wu, J., Jiang, X., Wang, X., An, Z., 2008, Millennial- and orbital-scale changes in the East Asian monsoon over the past 224,000 years, Nature, 451, 1090-1093

Wolanski, E., G. L. Pickard, and D. L. B. Jupp, 1984, River plumes, coral reefs and mixing in the Gulf of Papua and the northern Great Barrier Reef, Estuarine Coastal and Shelf Science, 18(3), 291-314.

Wolanski, E., and D. M. Alongi, 1995, A hypothesis for the formation of a mud bank in the Gulf of Papua, Geo-Marine Letters, 15, 166-171.

Wolanski, E., A. Norro, and B. King, 1995, Water Circulation in the Gulf of Papua, Continental Shelf Research, 15, 185-212.

Figure 2-1: Location map for the GoP shows the extent of the Northern, Central and Southern lobes. Location of the CHIRP survey lines and sediment cores are shown. Red lines are CHIRP data shown in the fence diagrams in Figures 2 and 3. Note the boundary between the Central and Southern lobes is coincident with the zone of convergence just north of the Fly River.

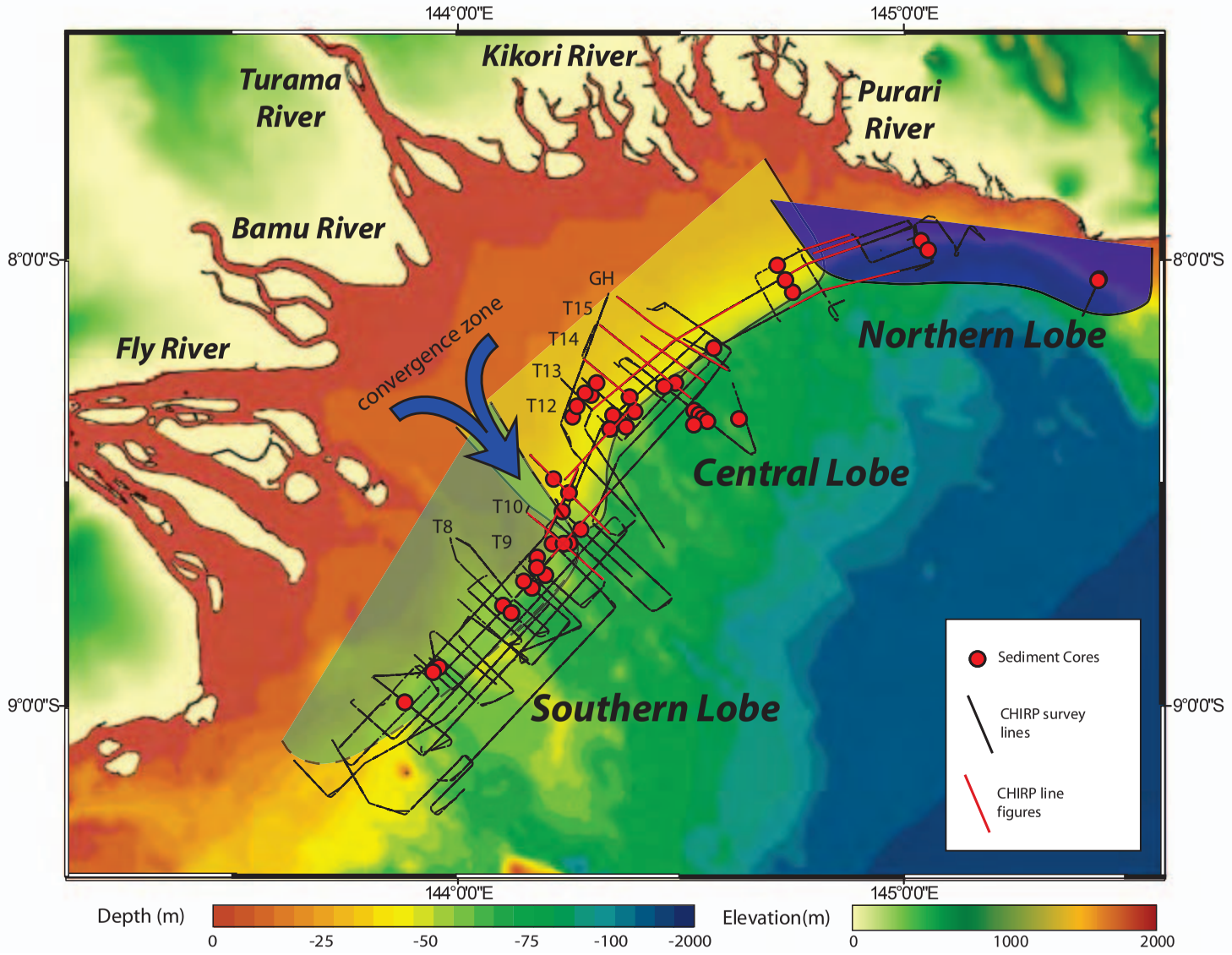
144°0'0"E
145°0'0"E
8°0'0"S
9°0'0"S
Kikori River
Turama River
Purari River
Bamu River
Fly River
convergence zone
GH
T15
T14
T13
T12
T10
T8
T9
Northern Lobe
Central Lobe
Southern Lobe
Sediment Cores
CHIRP survey lines
CHIRP line figures
Depth (m)
0
-25
-50
-75
-100
-2000
Elevation(m)
0
1000
2000

Figure 2-2: a) Isopach map and seismic lines overlain on bathymetry map (5m intervals) with seismic line in (b) highlighted in red. b) CHIRP seismic strike line STR2 (uninterpreted-top and interpreted-bottom) across foreset of Central lobe. Note the high amplitude reflector (HAR) in the trough and thickening of sediments on the promontories. c) Three-dimensional fence diagram of Central lobe with inset from seismic line T15 illustrating the oblique to sigmoidal progradation pattern of the clinoform. Note the southeasterly shift on line STR1 in the depocenter from the underlying Yellow unit to the younger Orange unit. The youngest unit (Red) drapes the entire Central lobe. Jumbo piston core locations are shown in white.

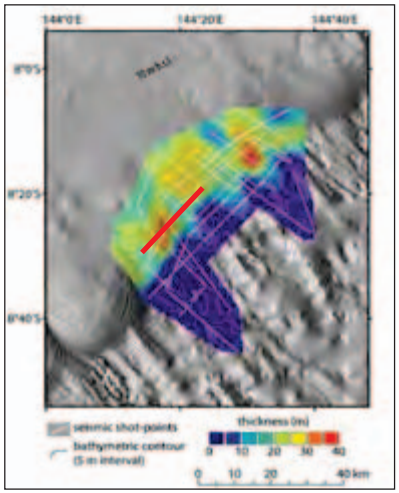
seismic shot-points
bathymetric contour
(5 m interval)
thickness (m)
0 10 20 30 40
0 10 20 40 km

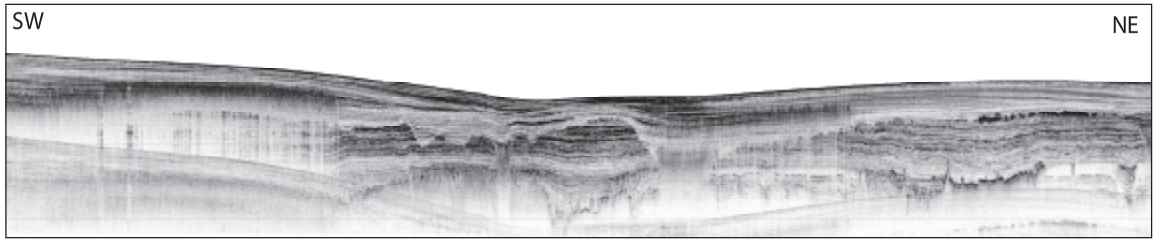
SW
NE

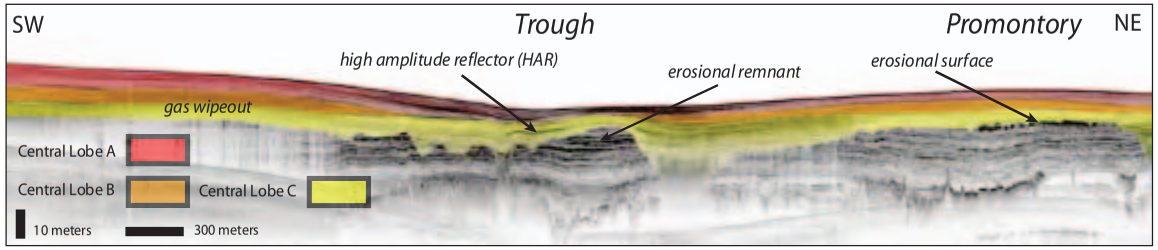
SW
Trough
Promontory
NE
high amplitude reflector (HAR)
erosional remnant
erosional surface
gas wipeout
Central Lobe A
Central Lobe B
Central Lobe C
10 meters
300 meters

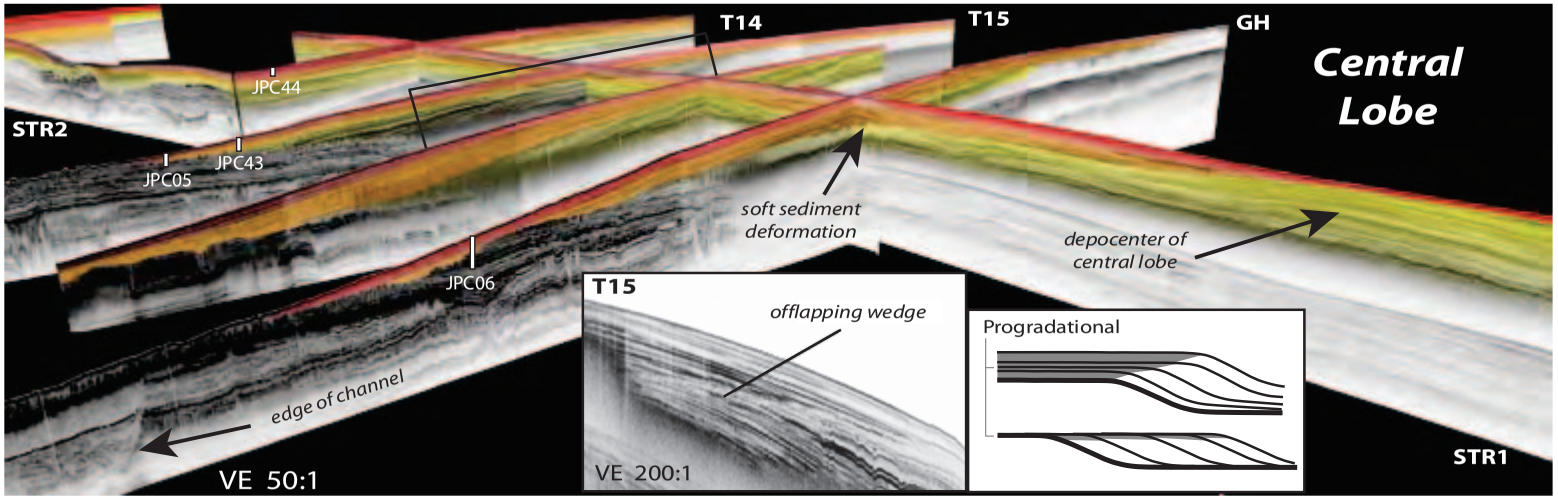
T14
T15
GH
Central Lobe
JPC44
STR2
JPC43
JPC05
soft sediment deformation
depocenter of central lobe
JPC06
edge of channel
VE 50:1
T15
offlapping wedge
VE 200:1
Progradational
STR1

Figure 2-3: Chirp fence diagrams showing the northern lobe downlapping the central lobe (above) and the southern lobe downlapping the central lobe (below). The downlapping stratal geometry of the northern and southern lobes onto the central lobe suggests an abrupt shift in the loci of deposition away from the central lobe. Note the shift in the depocenter is approximately 60 km (see Fig. 1). Sediment rerouting or oceanographic changes may account for this dramatic shift in the depositional lobes. Observing the three dimensional development of this shelf building system provides insight into the succession of sediment dispersal systems during recent geologic history. Note the three-dimensional downlap observed in the southern lobe

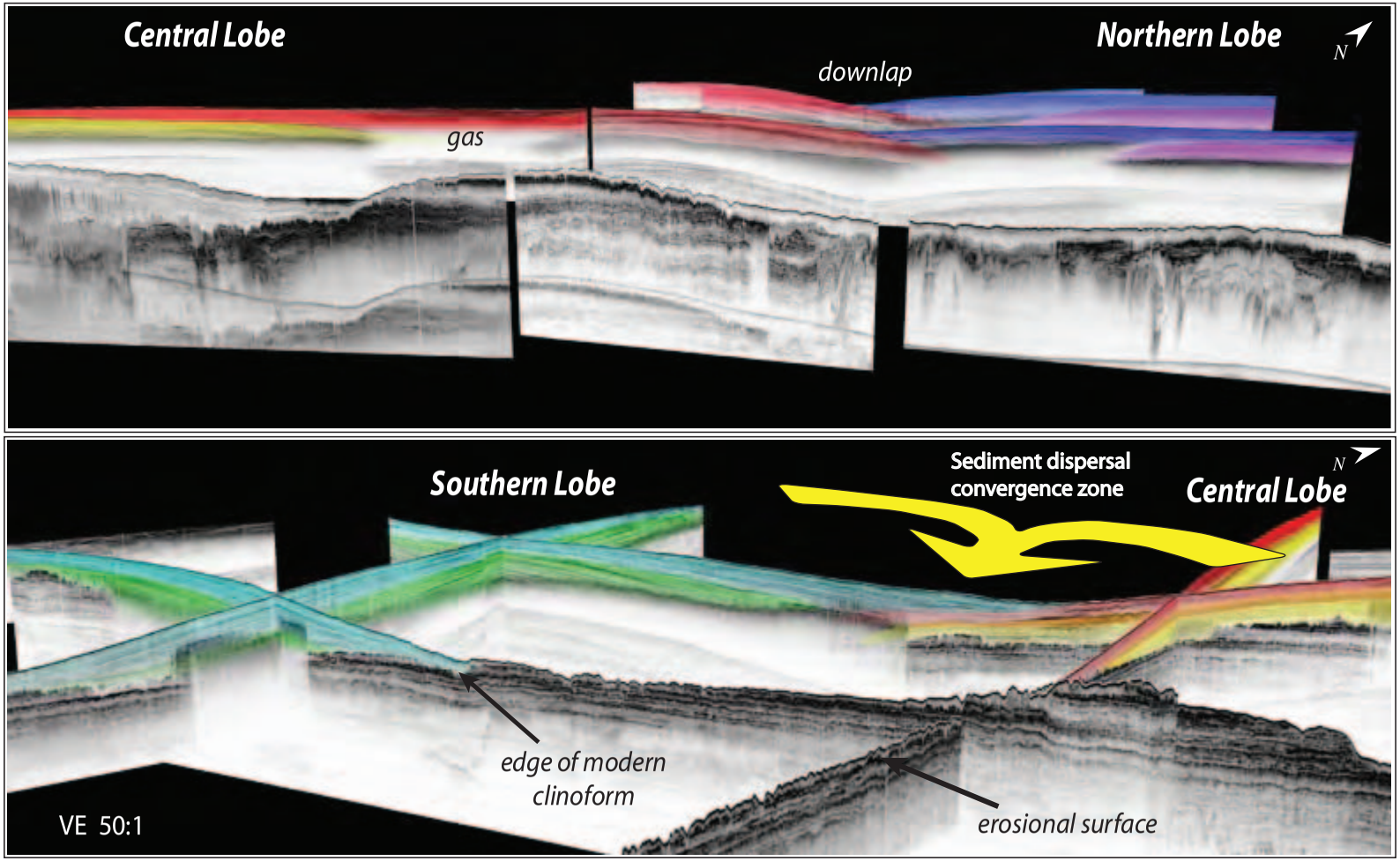
Central Lobe
Northern Lobe
N
downlap
gas
Southern Lobe
Sediment dispersal
convergence zone
N
Central Lobe
edge of modern
clinoform
erosional surface
VE 50:1

3

Clinoform Development and Sediment Dispersal in the Gulf of Papua

3.1 ABSTRACT

A suite of geophysical and analytical tools was used to map sediment packages and investigate depositional layers in the mid-shelf clinoform of the Gulf of Papua (GoP) off Papua New Guinea. As part of the NSF Margins Source-to-Sink (S2S) program, this study was an interdisciplinary effort to study sediment dispersal from two types of river systems draining onto the same margin. CHIRP seismic data imaged three Holocene sedimentary lobes. The older central lobe is downlapped by two younger lobes to the north and south. Sediment analysis was performed on cores using a MultiSensor Track (MST) and X-ray Fluorescence (XRF) instruments. Elemental ratio analysis provides insight into the sediment provenance of the deposits, while Carbon-14 dating yields age constraints, which allows us to determine the importance of the various river systems through time. The older central lobe has an elemental signature similar to the younger northern lobe and both appear to be sourced from the Purari watershed. In contrast, the southern lobe has elemental signatures more consistent with the Fly watershed. Our results suggest the northern rivers began depositing sediments on the shelf during the Holocene sea level rise in the central region of the GoP. Conversely, during the early Holocene transgression, sediments in the Fly drainage system were sequestered onshore infilling the accommodation created in the large low-relief coastal plain. Such differences in onshore storage capacity may introduce a lag between low-gradient rivers with a large coastal plain versus high-gradient river systems with small coastal plains. As onshore accommodation was filled (~2kya), sediments sourced from the Fly system prograded across the shelf forming the southern lobe. In addition, the central lobe migrated abruptly to the north and may reflect oceanographic changes. Whether these changes are due to regional climate oscillations and/or changes in the oceanic current regime is not well-understood, but future efforts with deeper core samples could help define the processes controlling the changes in sediment dispersal.

INTRODUCTION

3.1.1 Gulf of Papua, its Rivers and Shelf Stratigraphy: An Overview

The Gulf of Papua Holocene clinoform, located off the southeastern coast of Papua New Guinea, has particular interest because of its location in a marine foreland basin in mid-life (Figure 1; Davies et al., 1989). Loading of the Australian plate by New Guinea creates accommodation that is being filled by clastic sediment delivered by rivers draining central mountains. The Fly and Purari are the two principle rivers that supply sediment to the GoP, with four smaller rivers entering the Gulf (Bamu, Turama, Kikori, and Vaidala; Figure 2). Collective freshwater discharge is estimated at 450 km3/yr (Wolanski et al., 1995) spread evenly both seasonally and interannually such that 100-yr floods are only about twice the magnitude of two-year floods (Pickup, 1984). Because they are unaffected by typhoons, GoP rivers seldom experience catastrophic floods observed in other rivers, such as in Taiwan rivers (e.g., Milliman et al., 2008). One marked difference between the Fly River to the south and multiple-source rivers in the north (Purari, Kikori, Turama, Vaidala and several unnamed smaller rivers) is the Fly's extensive flood plain, where some (perhaps much) of the river's sediment is deposited. Collective sediment discharge to the entire GoP has been estimated at 380 MT/yr (Milliman, 1992), but the amount of fluvial sediment discharged to the clinoform itself is more likely somewhere between 175 and 265 Mt/yr, in large part depending on the amount discharged by the Fly. The Fly River is large low–gradient river (Type 1) and the northern rivers are small, steep gradient rivers (Type 2; Figure 3).

The GoP shelf between 143˚ and 145.5˚ E is characterized by two distinct morphological "treads" separated by a "riser" (Harris, 1990; Slingerland et al., 2008). The upper tread is a smooth and gently seaward-sloping surface extending seaward as much as 60 km from the mangrove-fringed shoreline to water depths of 30 m. The riser – the clinoform's foreset - lies between the 30 and 60 m isobaths, where seafloor

gradients increase to 0.8°. The gentle bottom tread (gradients 0.2-0.3°) extends to the shelf edge at 120 m water depth. Unlike the smooth upper tread, the riser and lower tread are corrugated with NW-SE-trending lineations, a surface expression of an older, eroded clinoform (Slingerland et al., 2008). The southern edge of the clinoform abuts sharply against the northern extension of the Great Barrier Reef and extends eastward along the entire GoP inner shelf, narrowing at about 145˚ E (Figure 2). North of 9.5˚ S surface sediments are predominantly terrigenous, to the south they are mostly carbonate (Harris et al., 1996). Sediments at the seaward edge of the clinoform are characterized (≥70 m) by a marked increase in carbonate, from less than 10% landward to more than 80% offshore (Harris et al., 1996).

The overarching objective of our GoP research is to understand sediment dispersal and clinoform formation, and, in particular, determine how clinoform morphology and internal geometry vary as a function of relative sea-level fluctuations, changes in sediment flux to the shelf, and oceanographic processes. In our study of the GoP clinoform, we have used a three-pronged approach: 1) modeling of the coastal ocean to illuminate potential sediment transport processes and pathways; 2) field investigation of clinoform morphology and internal architecture and accumulation rates; and 3) stratigraphic documentation at appropriate spatial scales to provide desired temporal resolution. In 2004, we collected more than 6800 km of high-resolution seismic data and 50 piston and gravity cores whose locations were largely determined by the seismic data. Combined with the 1500 km of multi-electrode sparker profiles collected on previous cruises and the sediment and oceanographic data collected by other MARGINS projects in the focus area and earlier Australian studies (e.g., Harris et al., 1996; Brunskill, 1995), the GoP study area has perhaps the densest data grid of any modern clinoform (Figure 2).

3.1.2 Flux and Fate of River-Derived Sediment

Rivers discharging directly onto the GoP clinoform drain more than 160,000 km2. Although the Fly River's basin area is more than twice that of the Purari River (75,000 vs. 33,000 km2), measured sediment loads of the two rivers are equal (~85-90 Mt/yr; Pickup, 1983) because the Purari watershed, as well as other northern rivers, has a greater potential source area (>1000-m elevations) and drains a more volcanic and siliciclastic-dominated terrain (Figure 3; Brunskill, 2004). Moreover, northern rivers generally lack low-lying flood plains; the Purari River, for instance, has only 2000 km2 of watershed <100 m in elevation, compared to 22,000 km2 in the Fly Basin.

The Fly River and the northern rivers are markedly different with respect to their sediment source region. The headwaters of the Fly River predominantly drain uplifted Mesozoic limestone from the Papuan Fold Belt with limited additional input of quaternary volcanics from the eastern portion of the watershed (Harris, Baker et al. 1993). In the Fly estuary, the sediments are composed mainly of weathered clays with lithic fragments including quartz sand, plagioclase, hornblende and diopside (Blake and Loffler 1971). Sediment deposits on the distal delta are mainly clays, which are illite- and kaolinite-dominated, with some chlorite and smectite, reflecting significant weathering. Interbedded sands in the Fly Delta are generally clear angular and iron-stained quartz with some amphibole and shell fragments (Harris, 1993). In contrast, the Purari River drains primarily lithoclastic and pyroclastic Jurassic strata and Quaternary volcanics (D'Addario, 1975). As such, the northern rivers discharge relatively immature sediments, with a cumulative volume at least twice that of the Fly (Milliman, Farnsworth et al. 2008). Composition of the Purari River sediments is diagnostic of their provenance, where high elevation sediments liberated from the Mount Hagen region are sourced from granodiorite and low-grade schist, with some gabbro and limestone originating from the Kubor Range. Sediments contributed to the Purari River at lower elevations consist

mainly of greywacke, shale, some tuff and basalt (Petr 1976; Gaillardet, DuprÈ et al. 1999).

The different bedrock and storage time in the drainage basins provides a distinct signal to determine sediment provenance of the shelf sediments. Northern river clays, for example, have illite/smectite ratios of ~2-3, whereas Fly River clays have I/S ratios between 6 and 16. Here we will present high-resolution CHIRP data together with down-core stratigraphy and mineralogy to define the sediment source for the modern clinoform as well as its evolution in the GoP. The GoP is an ideal locale to compare how sediment dispersal from these two types of river systems varies throughout a sea level cycle and associated climate fluctuations.

3.2.3 GoP Oceanographic conditions

The GoP experiences strong climate forcing caused by seasonal variation between the SE trades and NW monsoon, the Coral Sea Current, and meso- to macro-tides, resulting in both across- and along-shore sediment transport (Harris and Milner 1990; Slingerland et al., 2008). While annual climate forcing associated with the trades and monsoon creates large seasonal changes in sediment supply and dispersal within the GoP, the proximity of the Gulf of Papua to the Indo-Pacific Warm Pool (IPWP) makes it susceptible to millennial scale climate shifts associated with shifts in the ITCZ. Climate proxies reveal decadal to millennial time scale fluctuations in meridonal location of the ITCZ (Partin, Cobb 2007), which may control the three-dimensional clinothem architecture and lobe-switching. For example, during NW Monsoons when the ITCZ is farther south, the ocenaic currents support mid-shelf deposition to the southwest of the northern rivers. Conversely, during the SE trades the Coral Sea current becomes stronger and forces deposition to the east (Slingerland, et. al, 2008).

3.2 METHODS

As part of the NSF-funded MARGINS Source to Sink program (S2S), we acquired 2300 km of Compressed High-Intensity Radar Pulse (CHIRP) data and an additional 4500 km of hull-mounted Knudsen subbottom data onboard the R/V Melville in 2004. The CHIRP is a towed subbottom system with a 1 - 5.5 kHz pulse and 50-ms sweep that yields sub-meter vertical resolution. A differential global positioning system (DGPS) was used to georeference all data. A total of 50 piston and gravity cores (cumulative length 432 m) were obtained during the cruise with locations based on CHIRP data. Correlation of CHIRP profiles with the core data and combined with radiocarbon dating established a chronostratigraphic framework for the region. In addition, all cores were imaged lengthwise with a multiSensor Track (MST) meter and select cores have been analyzed for geochemical ratios using X-ray fluorescence (XRF). Select sediment samples were processed for mineralogy signals including illite/smectite ratios, quartz feldspar ratios. Downcore depth of radiocarbon dates is reported in Table 1.

3.3 RESULTS

3.3.1 Seismic Stratigraphy

A grid of high-resolution CHIRP seismic data highlights the three-dimensional geometry of the mid-shelf clinoform (Figure 2). The modern mid-shelf clinoform obscures and infills an underlying 30-40 meter thick clinoform with sub-horizontal, concordant reflectors exhibiting minimal thickness variation. The older clinoform appears to have been formed during Oxygen Isotope stages 3 and 4 and subsequently eroded during stage 2 (Slingerland, Driscoll et al. 2008); this erosional landscape is exposed as a corrugated surface seaward of the modern clinoform (Figure 4).

3.3.2 Depositional units and sedimentary facies

The modern (Holocene) GoP mid-shelf clinoform contains three main lobes, a central lobe downlapped by two younger lobes to the north and south with no evidence of interfingering between the lobes (e.g., Figure 5). Furthermore, the lobes do not appear to mimic the antecedent erosional character.of the underlying reflectors (Figure 6). Rather, the sequences were deposited as seaward prograding packages that exhibit sedimentary architecture predominantly dependent on supply and accommodation. Below we describe the internal architecture and morphology of the central lobe (Figure 6) and then its relationship to the northern (Figure 7) and southern lobes (Figure 5).

Three stacked units make up the modern clinoform architecture of the Central lobe. The basal unit is an oblique progradational sequence (Yellow, Figure 6) overlain by a sigmoidal progradational package (Orange, Figure 6) and draped by a veneer of the youngest sediment (Red, Figure 6). The three-dimensional fence diagram in Figure 6 images the evolving clinoform as the maximum deposition region oscillates first to the northeast of Line GH (Figure 4) in the yellow unit. Deposition of the orange unit then shifts southwestward over time requiring new accommodation (Slingerland 2008). This is obvious as the thickest part of the orange unit overlies the thinnest part of the yellow in Line 15 and the orange thins and onlaps the yellow toward the northeast.

The Southern Lobe lies southwest of the Central Lobe and consists of two main packages shown in Turquoise/Green (Figures 4 and 5) that prograded offshore and downlap the Red unit of the Central lobe. Where the downlapping occurs there is no apparent interfingering of sedimentary layers (Figure 5) and there is a bathymetric low at the junction between lobes.

To the northeast of the central and southern lobes, a Northern modern lobe exists (Figure 6). This lobe is also comprised of two distinct packages that downlap the Central

lobe. Similarly to the Southern lobe, there is no observed interfingering between the Northern and Central lobe (Figure 9) and the intersection exhibits a relative low in the bathymetry. The depocenter has therefore bypassed this region of accommodation.

3.3.3 Core Data

Fifty cores comprised of jumbo piston cores and gravity cores were acquired within the study region. The cores targets were co-located with the CHIRP seismic data transects and provide insight regarding the mineralogical variation between depositional units and the respective provenance. The dominant sediment type sampled consists of fine-grained brown clay with little or no bioturbation. Cores sampled in the shallower areas displayed laminations of sand-size sediment interbedded in the clays (Figure 10). Samples acquired seaward of the clinoform consisted of coarser-grain lag deposits and abundant ooid-rich layers. Magnetic susceptibility measured by the MST and XRF data reveal the relative elemental chemistry and composition of the downcore sediments as described in the following section.

3.3.4 Chronostratigraphy

Velocity information and potential impedance contrasts measured by the MST allow us to correlate the lithostratigraphy with the seismic stratigraphy. AMS-14C radiocarbon dates obtained from mollusk shells, foraminifera tests, and ooids were dated at NOAMS/Woods Hole Oceanographic Institution, to establish a chronostratigraphic framework (Table 1). Cores from the promontories of the Central lobe recovered homogenous fine-grained clays/muds, beneath which are intermittent laminations of alternating clay and sand couplets (Figure 10). Cores acquired in the embayments, or bathymetric lows, adjacent to the promontories recovered coarser sediments, correlating with High-Amplitude Reflectors (HARs) imaged in the CHIRP seismic data (Figure

11). Additionally, cores (e.g., JPC 13; Figure 12) collected seaward of the modern clinoform reveal laminated sediments with coarse-grained lag deposits and abundant ooids, underlain by discontinuous sand and clay lenses. Radiocarbon dates from organic material in the lag deposit yield ages greater than 34 ka. Dated materials from cores in the Northern and Southern lobes were all younger than 2ky bp, while dated material from the red and orange units of the Central lobe was deposited in the last 6ka years (Table 1).

3.3.5 Mineralogy

A marked variation in mineralogy was observed in the cores recovered from the Northern and Southern lobes. X-ray diffraction was performed on select surficial core samples (Figure 13). The samples revealed distinct signals depending on the sediment provenance as described below.

Clay size (<2μm)

Cores from the region were dominated by clay size sediment. Surface samples fell within two classes for illite/smectite ratios. Sediment samples from southern cores had distinctly higher illite to smectite ratios (Figure 13). The values were highest (9-10) in the delta region of the Fly River. Illite/Smectite ratios were lower levels for samples acquired from the central lobe and were lowest (1-4) in the samples from the Purari River system. A mixing zone is observed north of the Southern and Central lobe boundary and correlates with an embayment where HARs are observed (Figure 11).

Sand Size (2 μm - 2mm)

Surficial sediment samples had two discrete quartz/feldspar ratio signals (Figure 13). Surface sands collected in the southern region were dominated by quartz with ratio values ranging from 1.61-4.18. Whereas surface samples from the northern rivers

had lower quartz/feldspar ratios ranging from 0.34-1.60. The highest ratios were from samples located in the Fly River Delta, in the shallow, nearshore region to the northeast and offshore on the shelf near the Southern lobe boundary. The lower ratios (<1.60) were located in surficial sediments co-located on the Central and Northern lobes, including the nearshore and delta area of the northern rivers. In the area where the Central lobe is downlapped by the Southern lobe, the ratio data shows a distinct shift in values.

3.3.6 Lithostratigraphy of mid-shelf cores

Three distinct lobes exist (Figure 3) within our study region with sediments sampled from the Highstand Systems Tract (HST) and part of the older Transgressive Systems Tract (TST). Each lobe has been classified by relative location as Southern, Central, and Northern. Core samples were acquired within the clinoform package and offshore relict deposits in water depths ranging from 20-80 meters. Three main lithostratigraphic zones are part of the modern clinoform, while the offshore zone is differentiated by relatively older and coarser material.

The southernmost zone is part of the lobe extending from 20-80m waterdepth offshore from the Fly River Delta (Figures 5, 8). There were 18 cores collected in this zone ranging from water depths of 23m to 64m. Cores from this region exhibited mostly fine, homogenous brownish, gray clay with limited bioturbation. XRF data (Sr/Ca ratio, in particular) reveals distinct spikes in value coinciding with a coarse calcareous fraction of the sediments (Figure 14). Cohesive muds are interbedded with increasing terrigenous sand laminations in topset section of the clinoform. Sediments sampled from the foreset consist of homogenous muds with very little to no bioturbation. No cores recovered the bottomset of the southern lobe based on the seismics. The two cores from the southern-most extent of the Southern lobe, JPC52 and JPC53, penetrated a highly mafic, sand layer at 560 cm and 650cm (water depth 53.5m and 51.5m), respectively, with some mud clasts

present.

Within the Central region, cores were collected in water depths ranging from 22m to 70m. Sediments collected from the Central lobe consist mainly of fine homeogenous clay with some interbedded sand/clay couplets within the topset region of the clinoform. Cores acquired along the foreset exhibit fine grain, homogenous clay. Cores acquired offshore from the clinoform bottomset sampled older transgressive lag deposits including abundant ooids and foraminifera (Figure 12).

Cores acquired from the Northern region sampled the clinoform only and no samples were obtained offshore. However, one core, JPC02, did penetrate a relict surface underlying the modern sedimentary deposit (Figure 14) characterized by sediment waves. The clinoform consists of a homogenous mud enriched in heavy elements (e.g., Fe, Mn, etc), and are distinctly lower in carbonates (Figure 14). Depositional rates for the modern clinoform (upper package) are 1-1.4 cm/year based on radiocarbon-14 dating. A significant ooid-rich layer exists 4-5.5m downcore in JPC02 with an age of approximately 10kya.

3.3.7 XRF data

XRF analysis is non-destructive so cores are preserved and can be used for further methods of analysis. XRF core scanning rapidly delivers high-resolution data of the chemical composition of cut sediment cores (Richter et al., 2006). The atomic mass range that can be resolved by the scanner extends from Al to Ba. For this project, the XRF data were used to make a correlation between cores, investigating terrigenous sediment input patterns from the different river systems and compare the downcore variation with the surficial sediment analysis (Figures 13 and 14).

A number of inter-elemental ratios or element integrals were selected to identify characteristic sedimentation features and geochemistry of the various units (Figure 14).

Even though we acknowledge that the measured XRF element data from the scanner do not have a perfectly constant relationship with the actual element concentration in varying sediment types, a combination of element integrals and ratios can provide substantial information, useful for geochemical interpretation. These include Ba, Ti, Fe, Ca, Al, S, Sr, and their ratios. It is important to note that the sediments in the cores have not experienced diagenesis from deep burial and heating, therefore post-depositional chemical changes should be minimal.

Titanium

Titanium is the ninth most abundant element in the Earth's crust and is present in igneous rocks and sediments derived from them. It is a good proxy for the presence of terrestrial material and has no biological source. Cores from the ODP site 1002, from the Cariaco Basin on the northern shelf of Venezuela, were analyzed with an x-ray fluorescence scanner for iron and titanium and can be used to infer variations in the hydrological cycles with a subdecadal resolution (Haug et al., 2001). Iron variations could be attributed to redox variations in the sediments, while titanium is insensitive to such changes. Variations in titanium can thus be used as a proxy for terrigenous sediment input and can provide a measure for river runoff.

Barium and Ba/Ti ratio

Barium is often used as a geochemical proxy for past and present productivity in the photic zone. The amount of biogenic barium is estimated by subtracting terrigenous barium from the total barium content present in the sample. Terrigenous barium values are obtained from the amount of aluminum present in the sample and the Ba/Al ratio. The applicability of this proxy to different settings is, however, still unresolved. Several studies have described the link between Barium accumulation in sediments and primary

productivity in the photic zone (Arrhenius, 1958; Paytan and Kastner, 1996; Pfeifer et al. 2001; etc). The main carrier of Ba in the water column has been identified to be barite. The formation of barite is thought to be associated with the decay of organic material in the oxygen minimum zone. As a result, a typical water column profile of particulate Barium decreases with depth, having a maximum concentration in the euphotic zone. Other mechanisms responsible for the formation of barite have been discussed in the literature: decaying organic sulfur components, precipitation of organisms that possess skeletons made of barite. The main advantage of using biogenic Barium as a proxy for productivity is the fact that barite is well preserved in sediments. Paytan and Kastner (1996) and Dymond et al. (1992) have conducted studies investigating the preservation of barite in sediments. Their results point to an average preservation factor of 30 percent. Our results show a distinct signal difference between the downcore Ba/Ti ratio for the Southern lobe with higher values (average 0.35), while the Central and Northern lobe have lower (average <0.1).

Iron and Fe/Ti ratio

Concentration of iron in surface waters is extremely low (Martin, 1989). The main input of iron into sediments is from terrigenous sources. Fe is prone to diagenic remobilization so normalizing Fe to Ti will highlight the difference between iron that is of terrigenous origin from that associated with redox-related diagenesis. Maximums in Fe/Ti ratio correspond to the precipitation of pyrite and other sulfate phases. Pyrite (FeS2, reduced sulfur) has been shown to have a strong positive correlation with organic carbon in modern sediments. The oxidation of organic matter results in bacterial sulfate reduction in anoxic sediments. This produces H2S, which reacts with detrital iron minerals, to form pyrite (Berner and Hood, 1983). Downcore XRF data from the Central and Northern lobes have Fe/Ti ratios ten times higher than the Southern lobe (Figure 14). The Northern

lobe also has large spikes in the Fe/Ti ratio that coincide with increases in the grain size size (lag deposits) imaged in the seismics below the modern clinoform.

Calcium and Ca/Si ratio

Calcium is a good element to analyze using XRF methods, along with Si, because both elements have high detection. The Ca/Si ratio can be used to determine if sand layers are biogenic versus terrigenous. Calcium carbonate is the greatest source of sediments, other than river input of eroded material. Some calcium in the Fly River system may be associated with the eroded material from the carbonate formation from the Western PNG highlands. Peaks in the Ca/Si ratio are mainly associated with the presence of foraminifera and shells and may represent marine or freshwater biogenic activity. Our results show low ratios of Ca/Si in all lobes with significant spikes associated with the older, underlying stratigraphy in the Northern lobe. In the Southern lobe, a small increase in the ratio is present in the top two meters of sediment.

Silica and Si/Ti ratio

The main sources of silica in sediments are the weathering of rocks and diatoms, and thus indicates either be a terrigenous or productivity source. The Si/Ti ratio can show the relative contributions of terrigenous-derived silica compared to a biogenic source. Since the sensitivity of the XRF to titanium is strong, the Si/Ti ratio should result in reliable data signals. The Southern lobe Si/Ti ratio was three times lower (~1) than the Central and Northern lobes (~3) and was relatively stable downcore (Figure 14). The variability did increase slightly with depth in the Northern lobe.

Strontium and the Strontium/Calcium ratio

Most strontium in the sea is derived from carbonate rocks on continents, while calcium

is usually biogenic in source, but can also be non-biogenically precipitated in seawater. High ratios would suggest a terrestrial source for areas draining limestone deposits, as is the case for GoP. XRF data from all three lobes is highly variable downcore. The Southern lobe has ratios that peak near the top 2 meters of the core and have minimal variability from 2.5-5.5 meters. Another set of peaks is observed from 5.5 – 8 meters. In this core, the high variability is associated with the clays and finer grain material, while the low variability is correlated with the coarser laminations. The Central lobe appears relatively stable downcore with some variation, but no major peaks. Downcore data from the Northern lobe is also relatively stable, but has slightly higher values that decrease with depth.

Titanium/Calcium ratio

The titanium/calcium ratio is a useful indicator of terrestrial versus marine deposition and may indicate variation in precipitation or sediment supply and subsequent sedimentation. Mountainous terrain of PNG highlands is high in heavy metals and there is no natural source for titanium in the marine environment. Our results for Ti/Ca ratio indicate a relatively stable downcore variation for the Central and Northern lobe with a slight decrease downcore in the Northern lobe. The Southern lobe shows more variability with a spike in Ti/Ca around 2meters depth (Figure 14) and another increase in variability from 6-8 meters depth.

3.4 DISCUSSION

3.4.1 Depsositional History

The mid-shelf clinoform in the Gulf of Papua consists of two stacked clinoforms representing late Pleistocene aggradation and progradation and Holocene progradational phases. The two clinoforms are separated by an erosional surface that formed during Isotope Stage 2 sea-level regression (Slingerland et al., 2008). Based on its stratal geometry, the older clinoform prograded two-thirds of the way across the pre-existing shelf prior to modern deposition. The modern clinoform is composed of three main lobes: an older Central lobe downlapped by Northern and Southern lobes. Within the Central lobe, three packages are identified on the basis of stratal geometry. The basal Yellow unit builds relief with oblique clinoforms prograding seaward (Figure 6). The depocenter has a northeast-southwest trend along the GoP mid-shelf. The formation of oblique clinoforms in the Yellow unit with no aggradation indicates no new accommodation was generated during this time (Christie-Blick and Driscoll, 1995). Mantling the Yellow unit is the Orange unit that thins distally by downlap, laterally by onlap onto the underlying depocenter, and proximally by offlap.

Within the underlying Stage 4 clinoform, we observe geometry that suggests the rate of sediment supply filled the available accommodation. The obliquely stacked sediments must have been deposited during the sea level regression between ~55,000-75,000 years BP since we detected no aggradation during the progradational phase of construction (Figure 4). To generate such stratal geometry, eustatic sea level must have been falling faster than subsidence. Febo (2008) also observed a major siliclastic pulse on the slope between 60,000 – 100,000 years BP. As the rate of sediment supply was roughly equal to the generation rate of new accommodation, during Stage 3 before the major regression associated with the LGM, topsets were formed with consistent age dates from core samples (Harris et al. 1996).

3.4.2 Central Lobe

The lateral shift of the Orange depocenter to southeast fills the adjacent accommodation and the clinoform shingles off the constructional high. Unlike the underlying Yellow unit, the Orange unit exhibits both aggradation and progradation (Figure 6). Despite the increase in accommodation required to explain the shift from oblique (Yellow unit) to sigmoidal clinoforms (Orange unit), the locus of deposition remained within the central lobe, which suggests only a minor shift in the sediment dispersal patterns along the GoP mid-shelf. This depocenter shift and infilling of available accommodation within the central lobe from the Yellow to Orange unit appear to be predominantly controlled by depositional processes and stacking patterns (autocyclic forces). The uppermost Red unit is predominantly a drape deposit as it mimics the underlying morphology and is regionally distributed. However, this unit does appear to shift towards the north in a gradual mantling process before an abrupt depocenter shift occurred. One possible explanation for the repositioning of deposition is a marked shift in the oceanographic current conditions. Keen (2006) and Slingerland et al. (2008b) examined the variation in seasonal currents through modeling efforts using NCOM lagrangian drifter data. The surface and bottom currents are predominantly controlled by wind, which changes seasonally throughout the year during the NW monsoon and SE trades. During the normal SE trade season (April-Sept), the forcing conditions cause WSW sediment transport (Slingerland et al., 2008b). Monsoonal conditions cause a prominent decrease in the strength of the SE tradewinds (Prentice and Hope, 2007). Climate studies have documented a sudden significant shifts in the meridonal location of the ITCZ (Partin, Cobb, 2007). Shifts in the ITCZ, where the SE trade conditions were more frequent or intense would likely cause the Coral Sea Current to play a dominant role in transporting sediments from the northern rivers to the northeast of the Central lobe.

This timing is correlative with the age of the lobe shift and may explain why the sediment deposition from the Purari River was displaced to the northeast rather abruptly.

3.4.3 Southern Lobe

The southern lobe extends eastward onto the shelf from the Fly River. This tidally dominated delta is highly energetic and provides some storage for sediments (Walsh and Nittrouer, 2004). Most modern sediments (<2kya) are transported offshore and deposited on the mid-shelf (Walsh, Nittrouer et al. 2004; Walsh and Nittrouer 2009). The question remains regarding the location for deposition during the early to mid Holocene (>2kya). We propose that the sediment is sequestered in the large, low-gradient coastal plain. As sea level rises, onshore accommodation is created in the low relief of the coastal plain. Therefore, larger the coastal plains create more accommodation. Sediments will be deposited onshore until the system regrades to the sea level rise. Rivers with smaller coastal plains (e.g., the northern rivers) will have less of a lag between sea level rise and and supplying sediments to the ocean. In summary, we believe the southern Type I river has a longer lag time before supplying sediment to the ocean and subsequent shelf progradation than the northern Type II rivers.

3.4.4 Northern Lobe

The northern lobe downlaps the central lobe (Figure 2D n/c lobe) and carbon-14 dates suggest that the age of this unit is younger than 2kya. Sedimentological characteristics of the surficial sediments (Figure 13) and at depth (Figure 14) are similar to the central lobe suggesting the sediment provenance is the same for both lobes. The strong correlation between the mineralogy of the Central and Northern lobes suggest the northern rivers were draining the eastern portion of the PNG highlands during the early to mid- Holocene and the depocenter abruptly shifted to the North approximately 2kya.

3.4.5 Mineralogical signals

Distinct lithologic signatures from the two types of rivers (Type I and II) are present in both fine grain-clays and sand-size surficial sediments providing insight regarding the provenance of the mid-shelf clinoform lobes. The sediments sourced from the Fly River system in the southernmost lobe reveal mineralogy that is characteristic of more weathered sands and clays with higher quartz/feldspar ratios. Further evidence from XRF analysis downcore point towards a siliclastic origin in the western part of the PNG highlands (Figures 13 and 14) and appear to be distinct signals from the Fly River. Relatively higher Ba/Ti signals in the Southern lobe indicate higher biogenic sediment deposition. This may be due to sediment spending more time in the expansive coastal plain and estuarine environment. Aller et al. (2008) disseminates the diagenic processing that occurs on the GoP nearshore and shelf and shows extensive remineralization in the shelf environment. This is consistent with our results off the Fly River where the Fe levels are lower because of diagensis. Additionally, the lower Fe and higher Si near the Fly depocenter are consistent with the surficial Illite/Smectite ratios (Figure 13) because Illite composed mostly of Al and Si, while smectite is composed mostly of Fe and Mg. The spikes in Ti/Ca that are roughly coincident with the Sr/Ca spikes could record time of increased sediment discharge from the Fly River system, which we estimate to be approximately 2.5-3k BP.

The Central and Northern Rivers have higher levels of Fe/Ti likely because of fast burial from higher sedimentation from volcanic origins (Figure 3) and the sediments spending less time in the watershed. The Si/Ti ratio also indicates more terrestrial silica is supplied to the shelf in the Central and Northern lobes, which is consistent with drainage from more volcanic regions. Surficial and downcore sediments offshore from the Purari river (Type II) river system are characterized by a distinct volcanoclastic origin

and elemental ratios suggestive of immature sediments with less time spent in transport (less weathered). Considering the high slope of the drainage terrain, this observation is consistent with the tectonically controlled environment. Sediment elemental ratio signals from the Central lobe are more closely aligned with those of the Northern lobe, suggesting the Purari River sediments were first transported in a southwesterly direction.

Our age data reveals an abrupt shift occurred during the recent Holocene (~2kya), when the depocenter shifted northward to the narrow shelf region just offshore the Purari Delta. What may have caused this shift is not well understood, however climate studies by Moy et al. (2002) and Donnelly and Woodruff (2007) indicate a change in intensity and frequency of El Nino conditions beginning approximately 2kya. This climate pattern would alter the location of the Coral Sea Current and dominant current conditions in the GOP. Specifically, during El Nino conditions, the SE trade winds slacken and reduce current flow towards the west - southwest. This would provide the necessary environment for the abrupt shift of the Purari River sediment depocenter to the northeast part of the shelf.

3.5 CONCLUSIONS

Sediment deposition in the GoP is a complex, three-dimensional process forming stratal patterns based on the input of several variables including sediment supply, relative sea level, and climate. The sediment yield that actually reaches the ocean is highly dependant on the geomorphology of the watershed of origin as elucidated in the our work comparing the higher gradient northern river deposits with the lower gradient southern sediment lobe architecture and evolution in the GoP. Moreover, once sediments reach the coast and offshore environment a different set of variables become dominant and the oceanic current direction and velocity play an important role in the location of lobe development and evolution.

Our work investigating the mid-shelf clinoform in the GoP suggests that low-gradient onshore morphology in the Fly watershed provided for large onshore accommodation to be created during the late Pleistocene/early Holocene sea level rise. This large onshore accommodation introduces a lag between the sea level rise and sediment delivery to the ocean for Type I rivers. Concurrently, sediments from the steep-gradient northern river watersheds that are Type II rivers (e.g., Purari, Kikori) were delivered offshore and deposited in the central region of the GoP shelf (Figure 14). Based on age dates from our core data (Figure 14), approximately 2-4kya, we postulate there was an abrupt shift in the oceanic current regime, causing the Northern river sediments to be emplaced farther north on the shelf. Regional climate studies indicate a shift in the East Asian monsoon (Wang, Cheng et al. 2008) and changes in ITCZ locations and we suggest this oscillation may account for the shift in deposition around 2-4kya. Perhaps, the increased frequency and intensity of ITCZ shifts changed the distance and velocity of currents that are responsible for transporting sediments. A shift of the convergence zone to the north, as during the SE trades could be important in altering the oceanographic current regime enough to change sediment transport and deposition. Slingerland et al. (2008) and Keen (2006) document the importance of the SE trades in moving sediment from the Northern rivers to the northeast. Without this wind-driven forcing, the sediments would likely follow the more southwesterly route to the Central lobe.

We postulate the larger coastal plain of the Fly provides ample onshore storage of sediments until approximately 5,000 years ago when the onshore accommodation created by the sea level rise was infilled and sediment delivery to the ocean formed the Southern lobe of the GOP mid-shelf clinoform.

In summary our research in the GoP highlights the following:

1. **Clinoforms are inherently three-dimensional (e.g., Driscoll and Karner, 1999).**

2. **Type I rivers have a longer lag after a sea level rise before delivering sediment to the ocean and margin progradation than Type II rivers because of onshore accommodation.**

3. **Oceanographic conditions play an important role in clinoform architecture and migration.**

3.6 ACKNOWLEDGEMENTS

Funding for this research was through a grant from the NSF MARGINS Program. We also would like to thank the crew of the R/V Melville, Scripps Institution of Oceanography, which made the data acquisition in the GoP possible. J.P. Walsh, D. Walsh, J.C. Hill, and R. Fenwick participated in the cruise and provided valuable feedback.

3.7 REFERENCES

Alexander, C. R., C. A. Nittrouer, et al. (1986). "High-Resolution Seismic Stratigraphy and Its Sedimentological Interpretation on the Amazon Continental-Shelf." Continental Shelf Research 6(1-2): 337-357.

Aller, R. C., N. E. Blair, et al. (2008). "Early diagenetic cycling, incineration, and burial of sedimentary organic carbon in the central Gulf of Papua (Papua New Guinea)." Journal of Geophysical Research-Earth Surface 113(F1).

Arrhenius, G., N. M. Bramlette, et al. (1958). "Localisation Des Elements Radioactifs Dans Les Sediments Oceaniques Recents." Geochimica Et Cosmochimica Acta 14(1-2): 150-151.

Berner, L. A. and L. F. Hood (1983). "Iron-Binding by Sodium Alginate." Journal of Food Science 48(3): 755-758.

Blake, D. H. and E. Loffler (1971). "Volcanic and Glacial Landforms on Mount Giluwe, Territory of Papua and New Guinea." Geological Society of America Bulletin 82(6): 1605-&.

Brunskill, G. J., I. Zagorskis, et al. (2004). "Sediment and trace element depositional history from the Ajkwa River estuarine mangroves of Irian Jaya (West Papua), Indonesia." Continental Shelf Research 24(19): 2535-2551.

Christie-Blick, N. and N. W. Driscoll (1995). "Sequence Stratigraphy." Annual Review of Earth and Planetary Sciences 23(1): 451-478.

D'Addario, G.W., Dow, D.B., Swoboda, R., 1975, Geology of Papua New Guinea, 1:2,500,000, Canberra, Bureau of Mineral Resources, Australia

Dymond, J., E. Suess, et al. (1992). "Barium in Deep-Sea Sediment: A Geochemical Proxy for Paleoproductivity." Paleoceanography 7(2): 163-181.

Gagan, M. K., E. J. Hendy, et al. (2004). "Post-glacial evolution of the Indo-Pacific Warm Pool and El Nino-Southern Oscillation." Quaternary International 118: 127-143.

Gaillardet, J., B. Dupre, et al. (1999). “Geochemistry of large river suspended sediments: Silicate weathering or recycling tracer?” Geochimica Et Cosmochimica Acta 63(23-24): 4037-4051.

Gaillardet, J., B. DuprÈ, et al. (1999). “Global silicate weathering and CO2 consumption rates deduced from the chemistry of large rivers.” Chemical Geology 159(1-4): 3-30.

Harris, D. J. and E. Milner (1990). “The Measurement of Rainfall in Papua-New-Guinea, and Its Effect on Microwave Propagation.” International Journal of Satellite Communications 8(3): 173-180.

Harris, P. T., E. K. Baker, et al. (1993). “A Preliminary-Study of Sedimentation in the Tidally Dominated Fly River Delta, Gulf of Papua.” Continental Shelf Research 13(4): 441-472.

Harris, P.T. C.B. Pattiaratchi, J.B. Keene, R.W. Dalyrmple, J.V. Bardner, E.K. Baker, A.R. Cole, D. Mitchell, P. Gibbs, and W.E. Schroeder. 1996. Late Quaternary deltaic and carbonate sedimentation in the Gulf of Papua foreland basin: Response to sea-level change. Journal of Sedimentary Research, 66:801-819.

Haug, G. H., K. A. Hughen, et al. (2001). “Southward migration of the intertropical convergence zone through the Holocene.” Science 293(5533): 1304-1308.

Keen, T. R., D. S. Ko, et al. (2006). “Potential transport pathways of terrigenous material in the Gulf of Papua.” Geophysical Research Letters 33(4).

Liu, J. T. and H. L. Lin (2004). “Sediment dynamics in a submarine canyon: a case of river-sea interaction.” Marine Geology 207(1-4): 55-81.

Martin, J. H., R. M. Gordon, et al. (1989). “Vertex - Phytoplankton Iron Studies in the Gulf of Alaska.” Deep-Sea Research Part a-Oceanographic Research Papers 36(5): 649-&.

Milliman, J. D., K. L. Farnsworth, et al. (2008). “Climatic and anthropogenic factors affecting river discharge to the global ocean, 1951-2000.” Global and Planetary Change 62(3-4): 187-194.

Milliman, J. D. and J. P. M. Syvitski (1992). “Geomorphic Tectonic Control of Sediment Discharge to the Ocean - the Importance of Small Mountainous Rivers.” Journal of Geology 100(5): 525-544.

Partin, J. W., K. M. Cobb, et al. (2007). “Millennial-scale trends in west Pacific warm pool hydrology since the Last Glacial Maximum.” Nature 449(7161): 452-U453.

Petr, T. (1976). “Some chemical features of two Papuan fresh waters (Papua New Guinea).” Marine and Freshwater Research 27(3): 467-474.

Pfeifer, K., S. Kasten, et al. (2001). “Reconstruction of primary productivity from the barium contents in surface sediments of the South Atlantic Ocean.” Marine Geology 177(1-2): 13-24.

Pickup, G. and R. J. Higgins (1979). “Estimating sediment transport in a braided gravel channel ‚Äî The Kawerong River, Bougainville, Papua New Guinea.” Journal of Hydrology 40(3‚Äì4): 283-297.

Pickup, G. 1984. Geomorphology of tropical rivers: I. Landforms, hydrology, and sedimentation in the Fly and lower Purari, Papua New Guinea. Catena Suppl. 5:18-41.

Prentice, M. and Hope, G.S. (2007). Climate of Papua Pp 177-195 in A. J. Marshall and B. M. Beehler, (Eds.), The Ecology of Papua. Singapore, Periplus Editions.

Richter, T O. (2006). The Avaatech XRF Core Scanner: technical description and applications to NE Atlantic sediments. Special publication - Geological Society of London, 267(1), 39-.

Ruxton, B. P.; Bleeker, P.; Leach, B. J. , Lands of the Kerema-Vailala Area, Territory of Papua and New Guinea.1969 pp. 158 pp.Land Research Series, No.23

Slingerland, R., N. W. Driscoll, et al. (2008). “Anatomy and growth of a Holocene clinothem in the Gulf of Papua.” Journal of Geophysical Research-Earth Surface 113(F1).

Slingerland, R., R. W. Selover, et al. (2008). “Building the Holocene clinothem in the Gulf of Papua: An ocean circulation study.” Journal of Geophysical Research-

Earth Surface 113(F1).

Swanson, K. M., E. Watson, et al. (2008). “Sediment load and floodplain deposition rates: Comparison of the fly and Strickland rivers, Papua New Guinea.” Journal of Geophysical Research-Earth Surface 113(F1).

Tudhope, A. W., C. P. Chilcott, et al. (2001). “Variability in the El Nino - Southern oscillation through a glacial-interglacial cycle.” Science 291(5508): 1511-1517.

Vail, P.R., Mitchum, R. M. and Thompson III, S. (1977) Seismic Stratigraphy and the global changes of sea-level, part 4: gloal cycles of relative changes of sea level. In:Seismic Stratigraphy – Applications to Hydrocarbon Exploration (Ed. By C.E. Payton), Am. Assoc. Petrol. Geol. Mem., 26, 83-97.

Walsh, J. P. and C. A. Nittrouer (2004). “Mangrove-bank sedimentation in a mesotidal environment with large sediment supply, Gulf of Papua.” Marine Geology 208(2-4): 225-248.

Walsh, J. P. and C. A. Nittrouer (2009). “Understanding fine-grained river-sediment dispersal on continental margins.” Marine Geology 263(1,Äì4): 34-45.

Walsh, J. P., C. A. Nittrouer, et al. (2004). “Clinoform mechanics in the Gulf of Papua, New Guinea.” Continental Shelf Research 24(19): 2487-2510.

Wang, Y. J., H. Cheng, et al. (2008). “Millennial- and orbital-scale changes in the East Asian monsoon over the past 224,000 years.” Nature 451(7182): 1090-1093.

Wolanski, E. and R. J. Gibbs (1995). “Flocculation of Suspended Sediment in the Fly River Estuary, Papua-New-Guinea.” Journal of Coastal Research 11(3): 754-762.

Table 3-1: Radiocarbon data from selected core samples. All samples were analyzed at the Woods Hole AMS facility and were calibrated using Radiocarbon Calibration Program CALIB 5.0.2 (http://calib.qub.ac.uk/calib/).

Core	Core Depth (m)	Water Depth (m)	Actual Depth (m)	Calender Age (+/-100years)	14-C age	Location	Material
JPC02	1	62	63	920	1320	Northern Lobe	bivalves
JPC02	1.5		63.5	1470	1870	Northern Lobe	mollusks
JPC02	2.5		64.5	1790	2190	Northern Lobe	mollusks
JPC02	3.5		65.5	3090	3490	Northern Lobe	Asterorotalia
JPC02	4		65.5	2850	3250	Northern Lobe	gastropod
JPC02	4.1		66	6650	7050	Northern Lobe	mollusk
JPC02	4		66	9290	9690	Northern Lobe	ooids
JPC02	4.5		66.5	9030	9430	Northern Lobe	ooids
JPC02	5		67	9070	9470	Northern Lobe	ooids
JPC02	5.1		67	10000	10400	Northern Lobe	mollusk
JPC02	5.7		68	8850	9250	Northern Lobe	mollusk
JPC02	7.5		69.5	9590	9990	Northern Lobe	gastropod
JPC02	7.5		69.5	9470	9870	Northern Lobe	ooids
JPC02	8		70	9650	10050	Northern Lobe	gastropod
JPC02	8		70	10350	10750	Northern Lobe	ooids
JPC02	8.2		70	9240	9640	Northern Lobe	pteropoods
JPC02	8.5		70.5	10500	10900	Northern Lobe	ooids
JPC02	9.5		71.5	10400	10800	Northern Lobe	ooids
JPC14	1	48.3	49.3	961	1050	Northern Lobe	Foraminifera
JPC14	4		52.3	1348	1450	Northern Lobe	Foraminifera
JPC14	5		53.3	1438	1550	Northern Lobe	Foraminifera
JPC14	5		53.3	1097	1180	Northern Lobe	Bulk Carbonate
JPC14	7.5		55.8	1252	1330	Northern Lobe	Foraminifera
JPC14	11		59.3	3367	3150	Northern Lobe	Bulk Carbonate
JPC15	0.5	34	34.5	1604	1700	Northern Lobe	Foraminifera
JPC15	2		36	1604	1700	Northern Lobe	Foraminifera
JPC15	3		37	1438	1550	Northern Lobe	Foraminifera
JPC15	5		39	1512	1620	Northern Lobe	Mollusk
JPC15	1		35	1418	1530	Northern Lobe	Bivalve
JPC15	3		37	1252	1330	Northern Lobe	Foraminifera
JPC15	3		37	830	915	Northern Lobe	Gastropod
GC16	0.66	26	26.66	380	325	Northern Lobe	Plant macrodetritus
GC16	1.13		27.13	474	430	Northern Lobe	Plant macrodetritus
GC16	2		28	2330	2310	Northern Lobe	Plant macrodetritus

Figure 3-1: Location map of Study area (red polygon) along the mid-shelf clinoform in the Gulf of Papua overlain on regional map with main geological features. Inset is of regional map of Oceana.

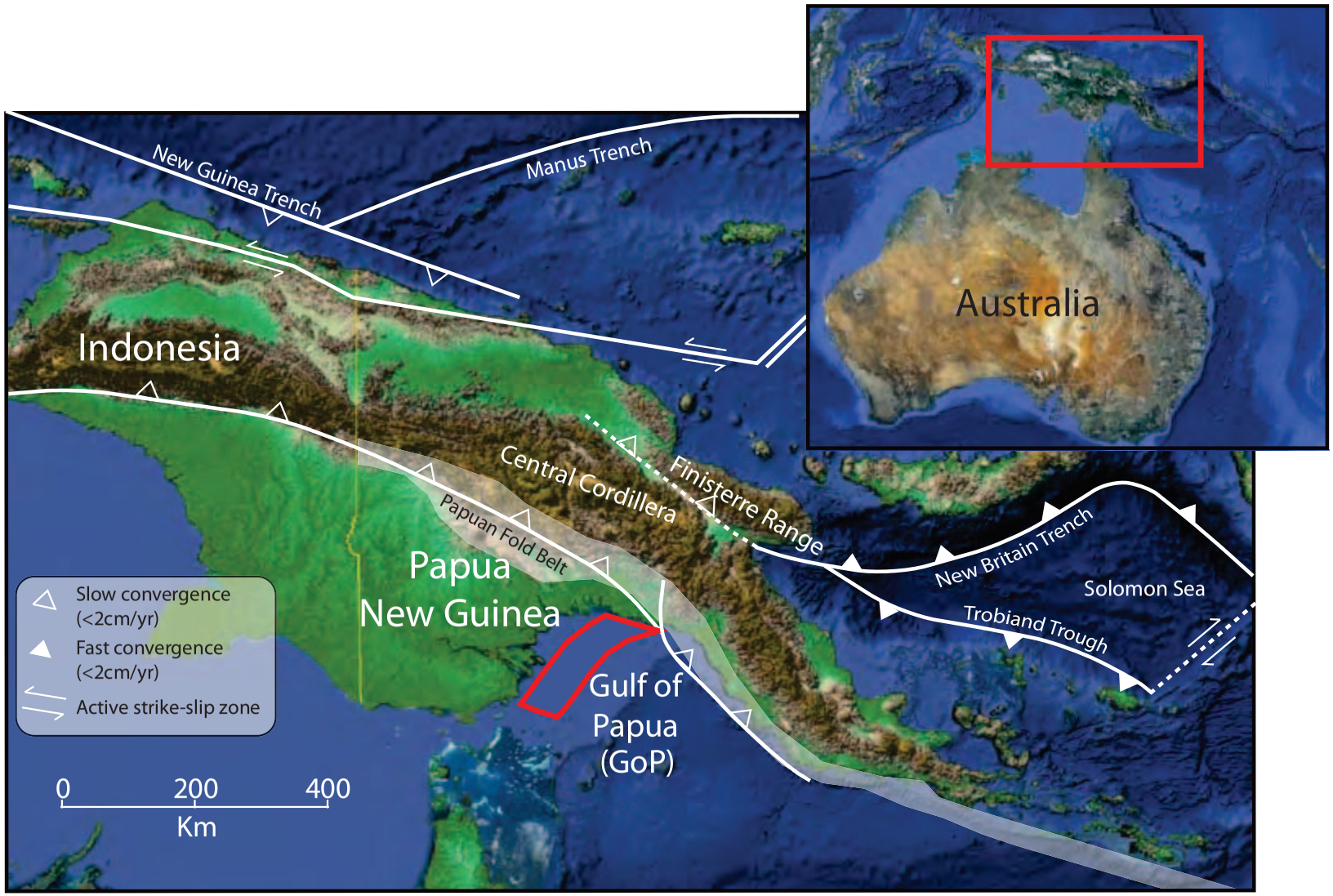
New Guinea Trench
Manus Trench
Indonesia
Australia
Central Cordillera
Finisterre Range
Papuan Fold Belt
Papua
New Guinea
New Britain Trench
Solomon Sea
Trobiand Trough
Gulf of
Papua
(GoP)
Slow convergence
(<2cm/yr)
Fast convergence
(<2cm/yr)
Active strike-slip zone
0
200
400
Km

Figure 3-2: Location map for the GoP shows the location of the CHIRP survey lines and sediment cores. Red lines are CHIRP data shown in the fence diagrams in figures 3, 4 and 5. Bathymetry was gridded from Harris (1995).

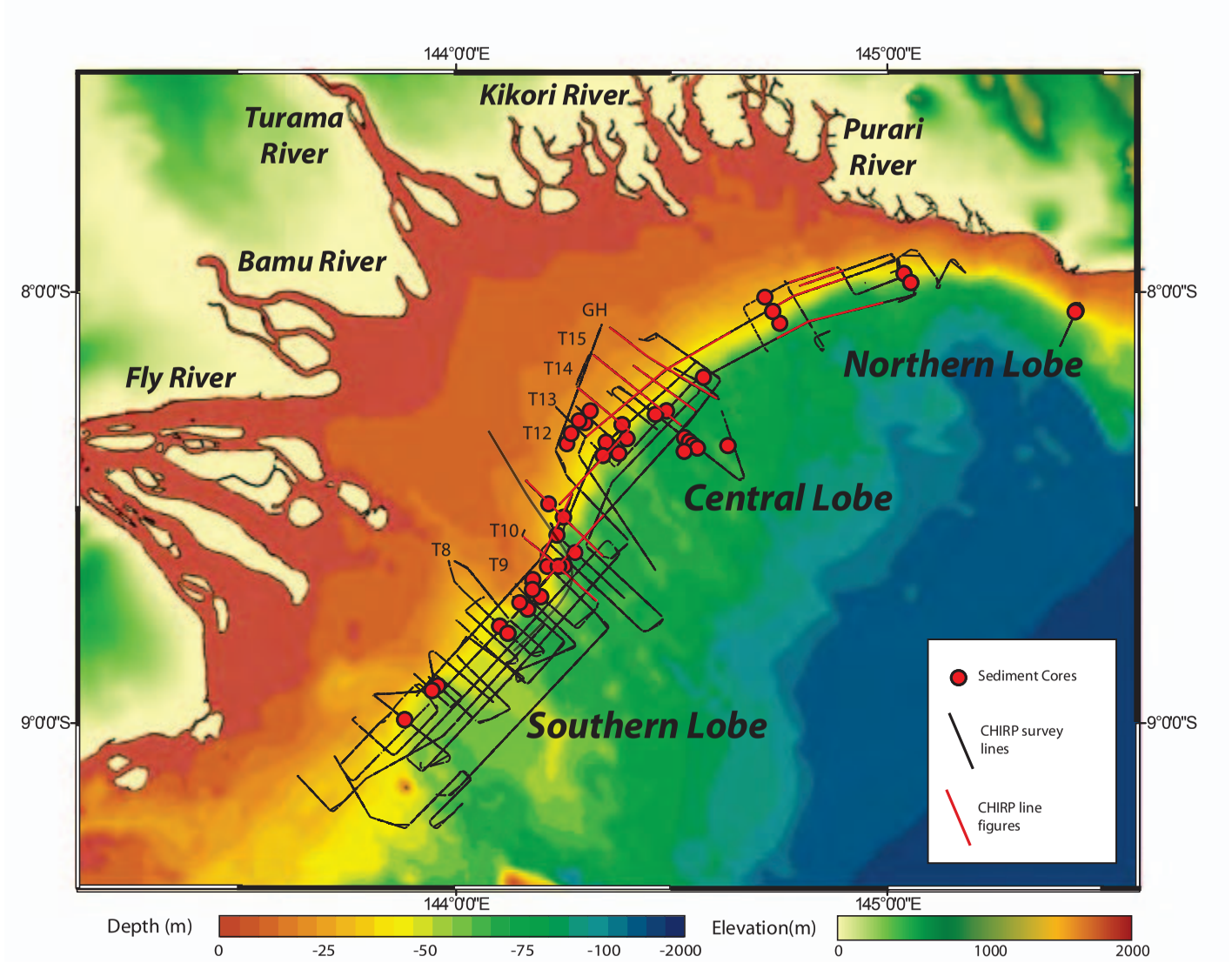
144°0'0"E
145°0'0"E
8°0'0"S
9°0'0"S
Turama River
Kikori River
Purari River
Bamu River
Fly River
GH
T15
T14
T13
T12
T10
T9
T8
Northern Lobe
Central Lobe
Southern Lobe
Sediment Cores
CHIRP survey lines
CHIRP line figures
Depth (m)
0
-25
-50
-75
-100
-2000
Elevation(m)
0
1000
2000

Figure 3-3: Three-dimensional map of the study area from source to sink. Geological map (source) of Papua New Guinea is draped on the digital elevation model (Sandwell)¬¬ distinguishes the sediment provenance between dominantly carbonate rocks to the west and highly mafic volcanics to the east. Onshore, enclosed red line is the boundary of the Fly River watershed (Type I river system) and Yellow enclosed line (Type II river system) is the Purari watershed. Bathymetric data grid (Harris, 1995) from shoreline to the shelf. Offshore red, blue and yellow semi-enclosed areas represent the boundaries of the Southern, Central and Northern lobes, respectively. Gray arrows approximate generalized sediment transport direction from river mouths to shelf depositional area. Note: Sediment from the Purari river system deposited as the Central lobe earlier in the Holocene and more recently shifted the depocenter to the northern part of the shelf.

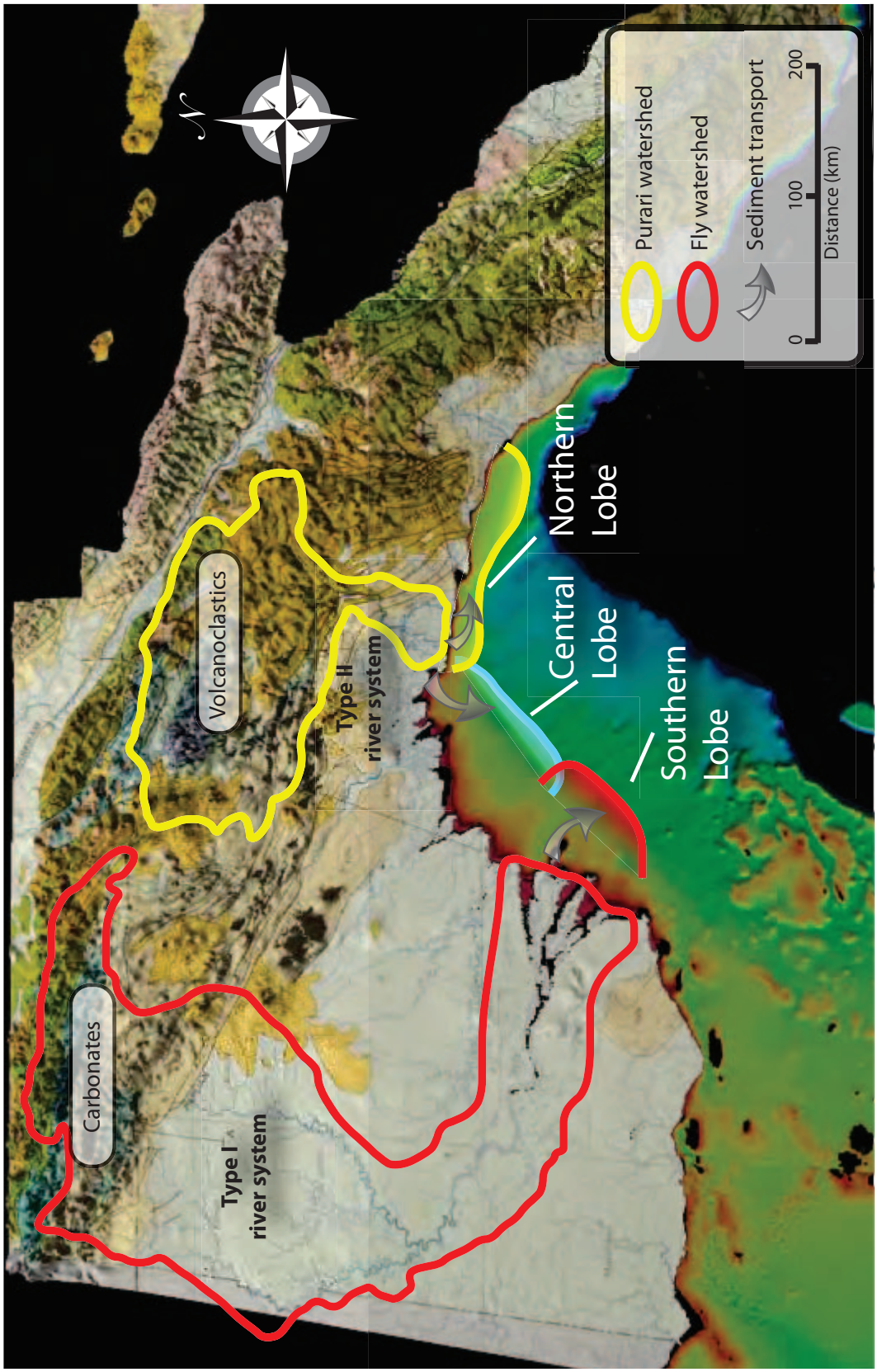
Carbonates
Volcanoclastics
Type I
river system
Type II
river system
Northern
Lobe
Central
Lobe
Southern
Lobe
Purari watershed
Fly watershed
Sediment transport
0
100
200
Distance (km)

Figure 3-4: Chirp seismic line imaged from the southern portion of the study area. The modern clinoform (blue and green units) drape the erosive surface separating older underlying clinoform. Note the change from progradation in the oldest unit (purple) to aggradation in the beige unit above.

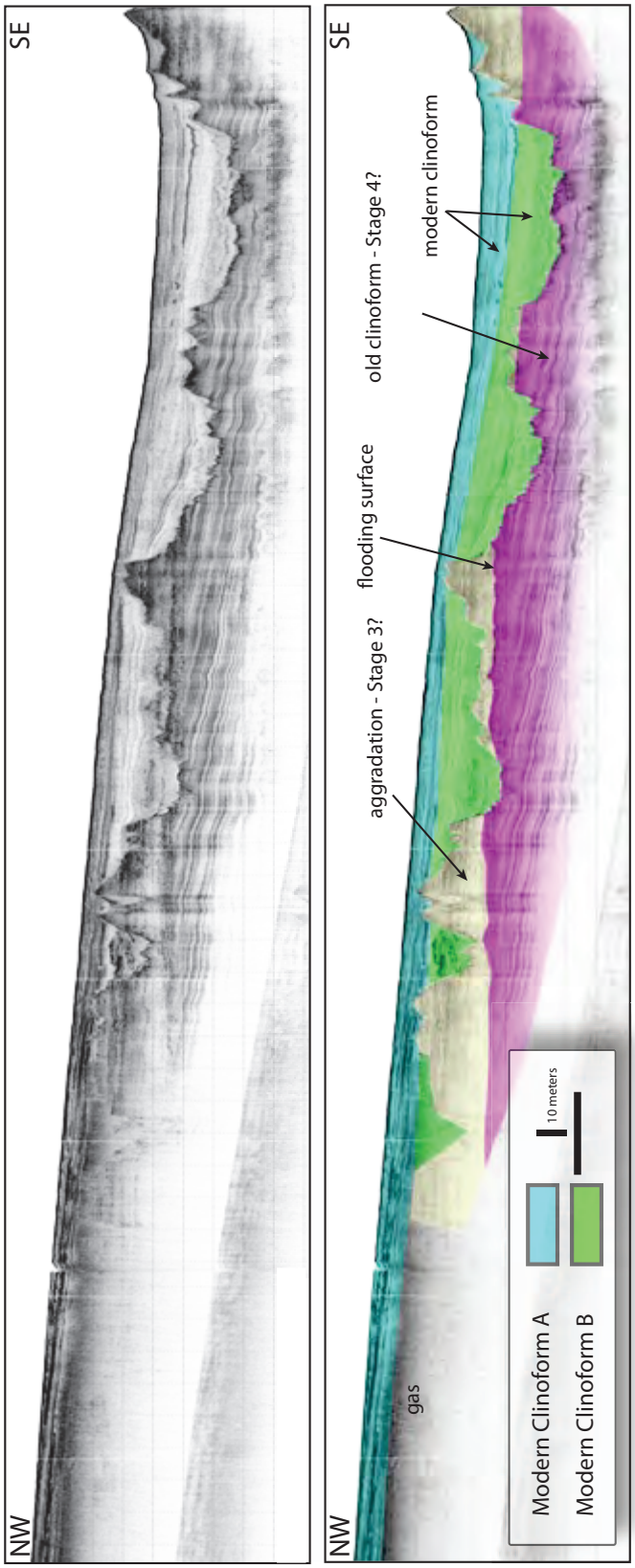
SE
NW
SE
NW
aggradation - Stage 3?
flooding surface
old clinoform - Stage 4?
modern clinoform
gas
Modern Clinoform A
Modern Clinoform B
10 meters

Figure 3-5: Chirp fence diagram showing the southern lobe downlapping the central lobe between dip lines T-18 and T-20. the southern lobe is displayed in two distinct blue and green packages, while the central lobe is represented in red, orange and yellow packages. Both lobes are overlying an older erosional surface.

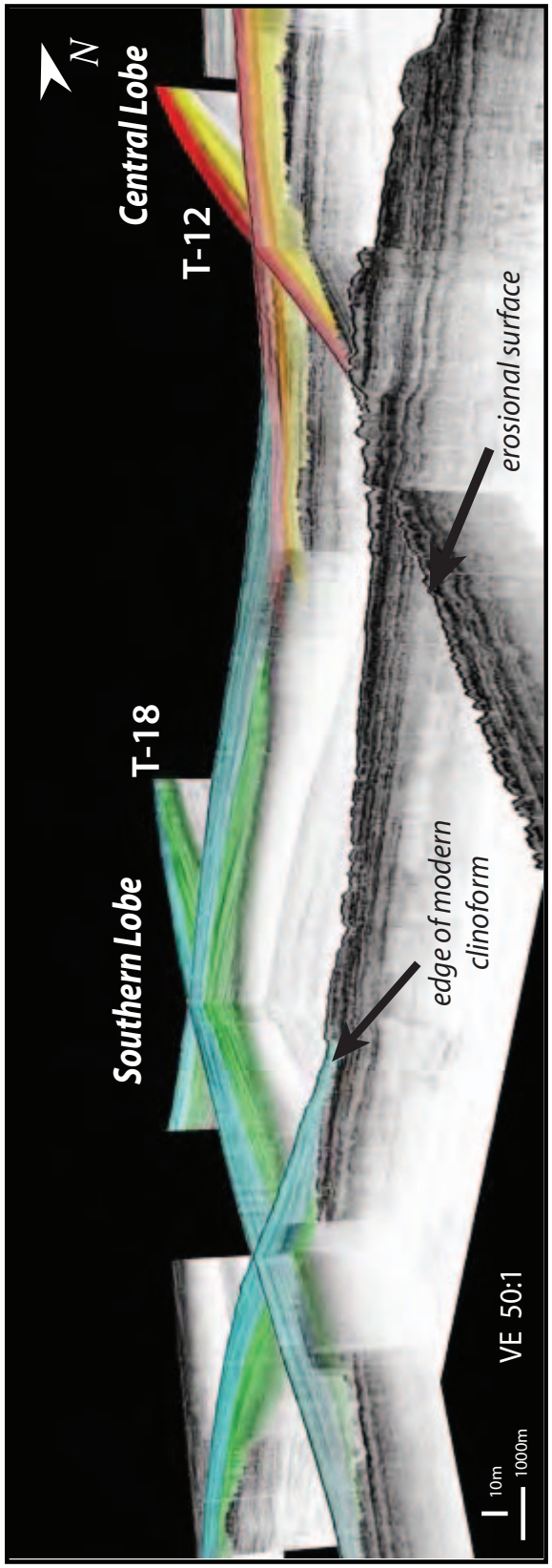
N
Central Lobe
T-12
T-18
Southern Lobe
erosional surface
edge of modern
clinoform
10m
1000m
VE 50:1

Figure 3-6: Three-dimensional fence diagram of Central lobe with inset from seismic line T15 illustrating the oblique to sigmoidal progradation pattern of the clinoform. Note the southerly shift on line STR1 in the depocenter from the underlying Yellow unit to the younger Orange unit. The youngest unit (Red) drapes the entire Central lobe with modern sediment. Location of jumbo piston cores are shown in white.

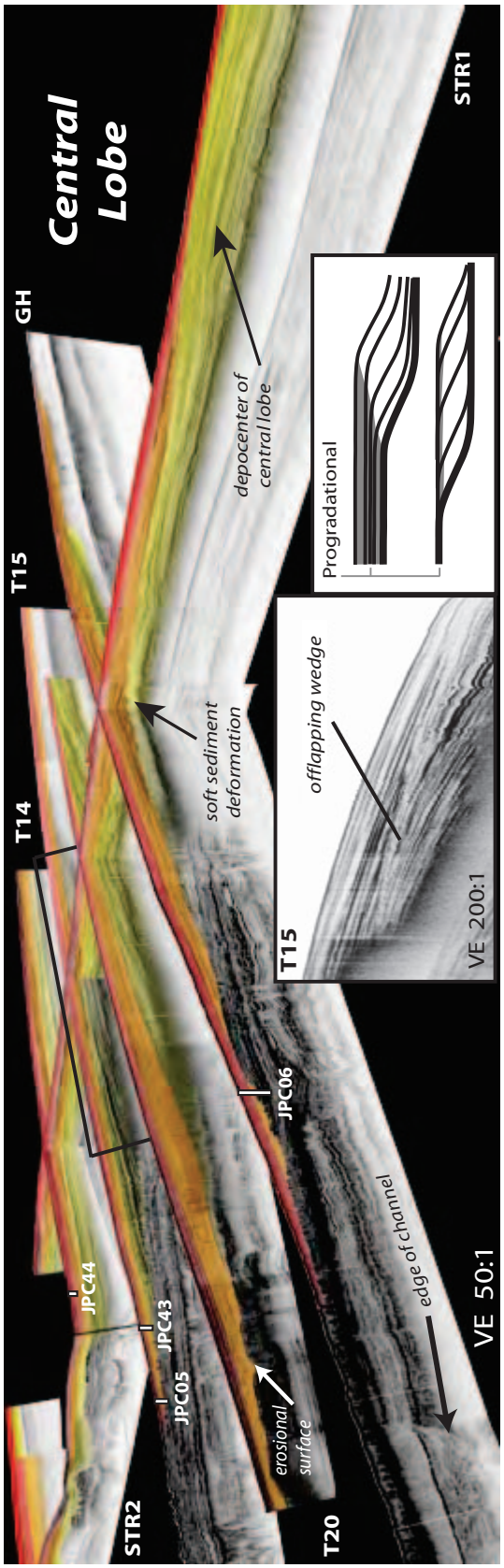
Central Lobe
GH
T15
T14
T20
STR2
STR1
JPC44
JPC43
JPC05
JPC06
soft sediment deformation
depocenter of central lobe
erosional surface
edge of channel
VE 50:1
T15
offlapping wedge
VE 200:1
Progradational

Figure 3-7: Chirp fence diagram showing the northern lobe downlapping the central lobe. The northern lobe is displayed in two distinct blue and purple packages, while the central lobe is represented in red, orange and yellow packages. Both lobes are overlying an older erosional surface with incised channels trending in a NW-SE direction towards the shelf edge.

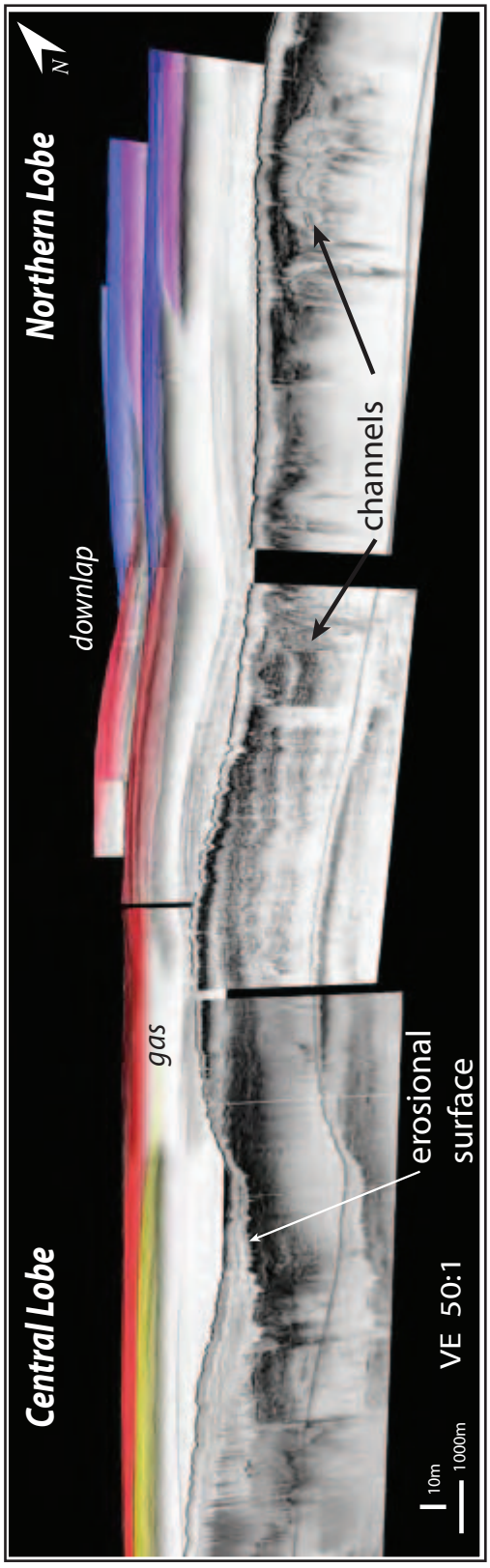
Central Lobe
Northern Lobe
N
downlap
gas
channels
erosional surface
10m
1000m
VE 50:1

Figure 3-8: Two-dimensional uninterpreted (top) and interpreted (bottom) Chirp seismic line of southern lobe (blue/turquoise) downlapping onto the central lobe (red). Note lack of interfingering between lobes and marked bathymetric low where lobes intersect.

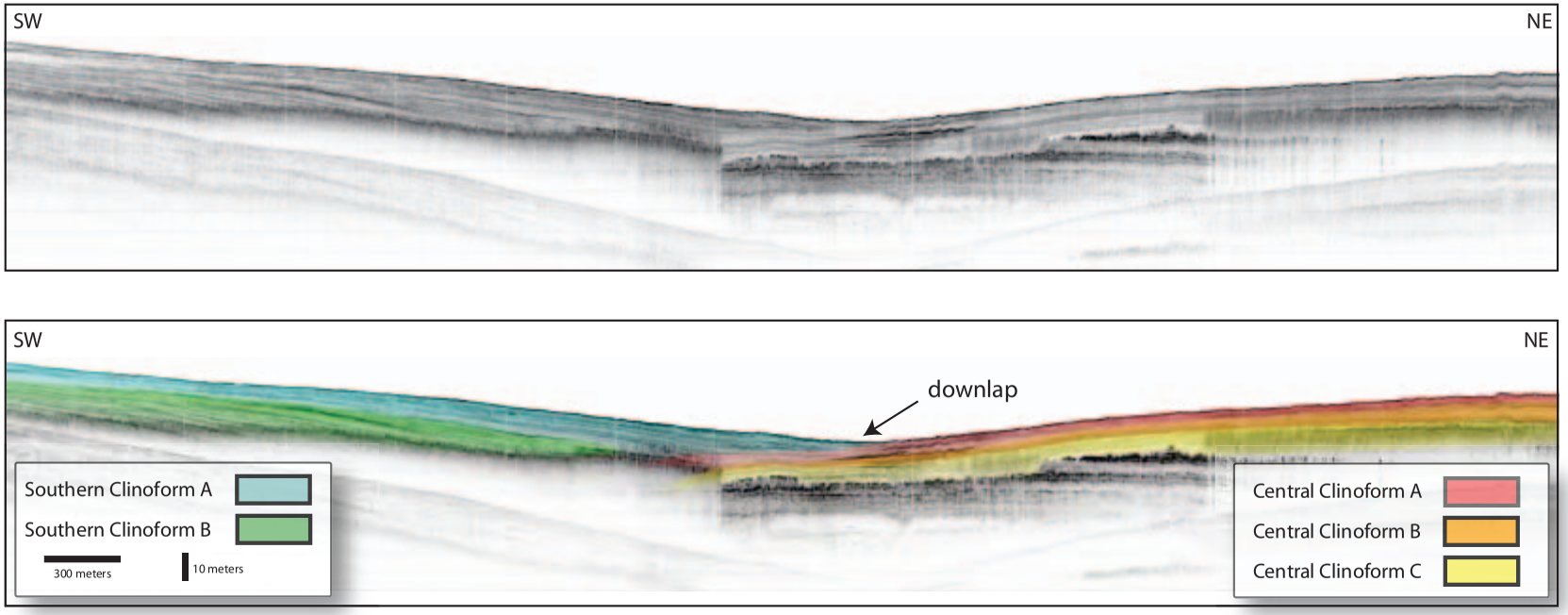
SW
NE
SW
NE
downlap
Southern Clinoform A
Southern Clinoform B
300 meters
10 meters
Central Clinoform A
Central Clinoform B
Central Clinoform C

Figure 3-9: Two-dimensional uninterpreted (top) and interpreted (bottom) Chirp seismic line of northern lobe (blue/purple) downlapping onto the central lobe (red). Note lack of interfingering between lobes and marked bathymetric low where lobes meet.

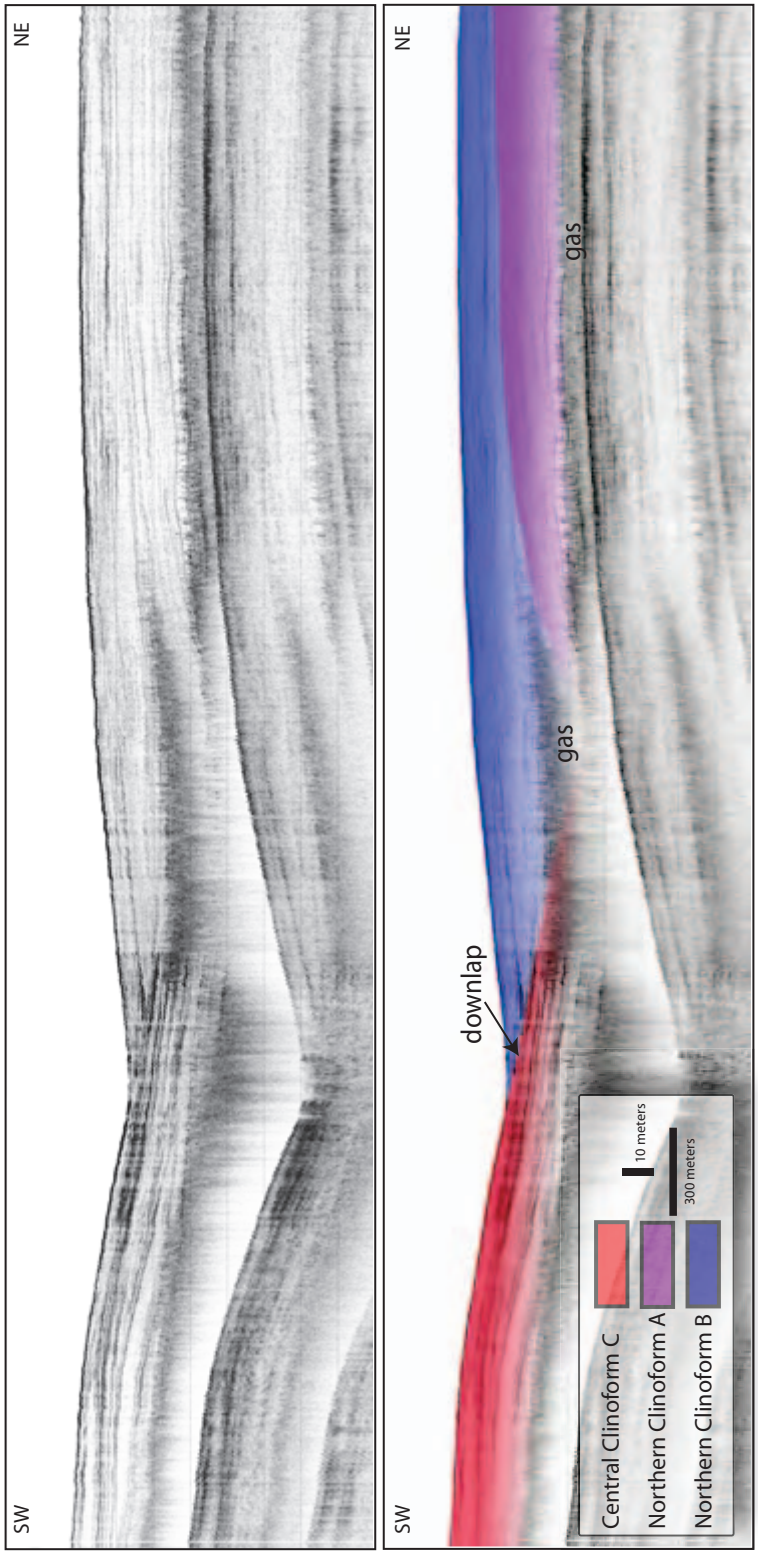
NE
SW
NE
SW
downlap
gas
gas
Central Clinoform C
Northern Clinoform A
Northern Clinoform B
10 meters
300 meters

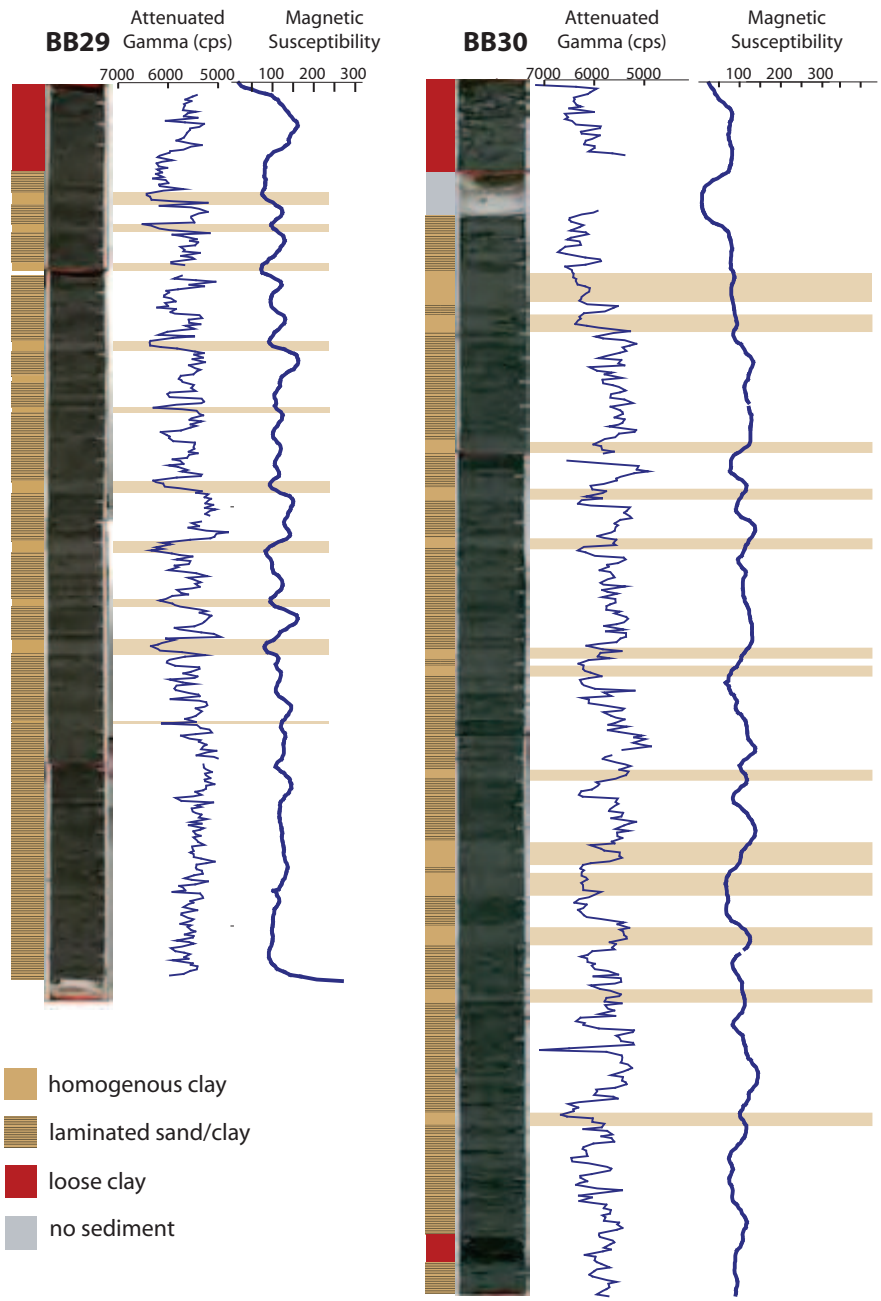

Figure 3-10: Two cores (BB29 & BB30) with alternating sand and clay couplets acquired in the topset portion of the central lobe. Colored side bar represents lithological description of core sample adjecent to photograph. Attenuated Gamma (cps) and magnetic susceptibility also are shown downcore.

Figure 3-11: A) Isopach map and seismic lines overlaid on bathymetry map (5m intervals) with seimic line in Figure 6 highlighted in red. B) CHIRP seismic strike line STR2 (uninterpreted-top and interpreted-bottom) across foreset of Central lobe. Note the high amplitude reflector (HAR) in the trough and thickening of sediments on the promontory. Note the poor correlation between the modern promontory and the underlying erosional surface.

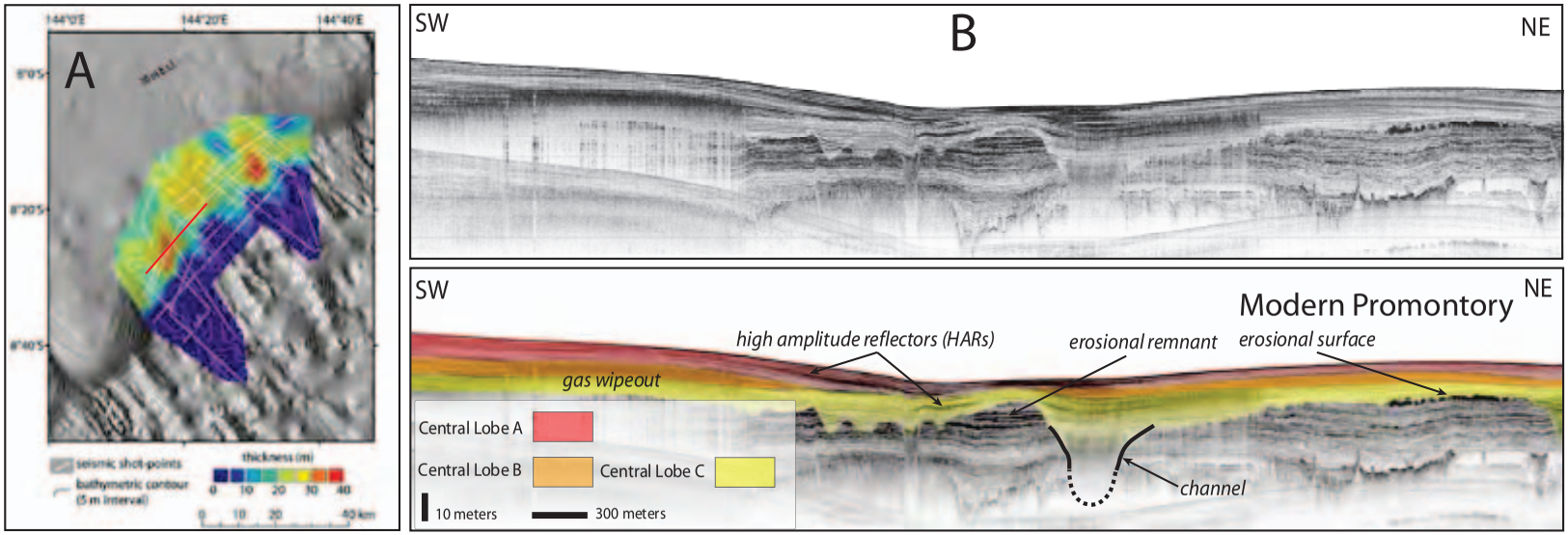
A
B
SW
NE
SW
NE
Modern Promontory
high amplitude reflectors (HARs)
erosional remnant
erosional surface
gas wipeout
channel
Central Lobe A
Central Lobe B
Central Lobe C
10 meters
300 meters
seismic shot-points
bathymetric contour
(5 m interval)
thickness (m)
0 10 20 30 40
0 10 20 40 km

Figure 3-12: CHIRP seismic line (dip) imaging offshore edge of Central lobe and underlying erosional corrugated surface. Location of Jumbo Piston Core (JPC13) co-located on line (inset) with core image (right) and associated magnetic susceptibilty data downcore. Note: laminations of layered sand/clay couplets in upper section of core.

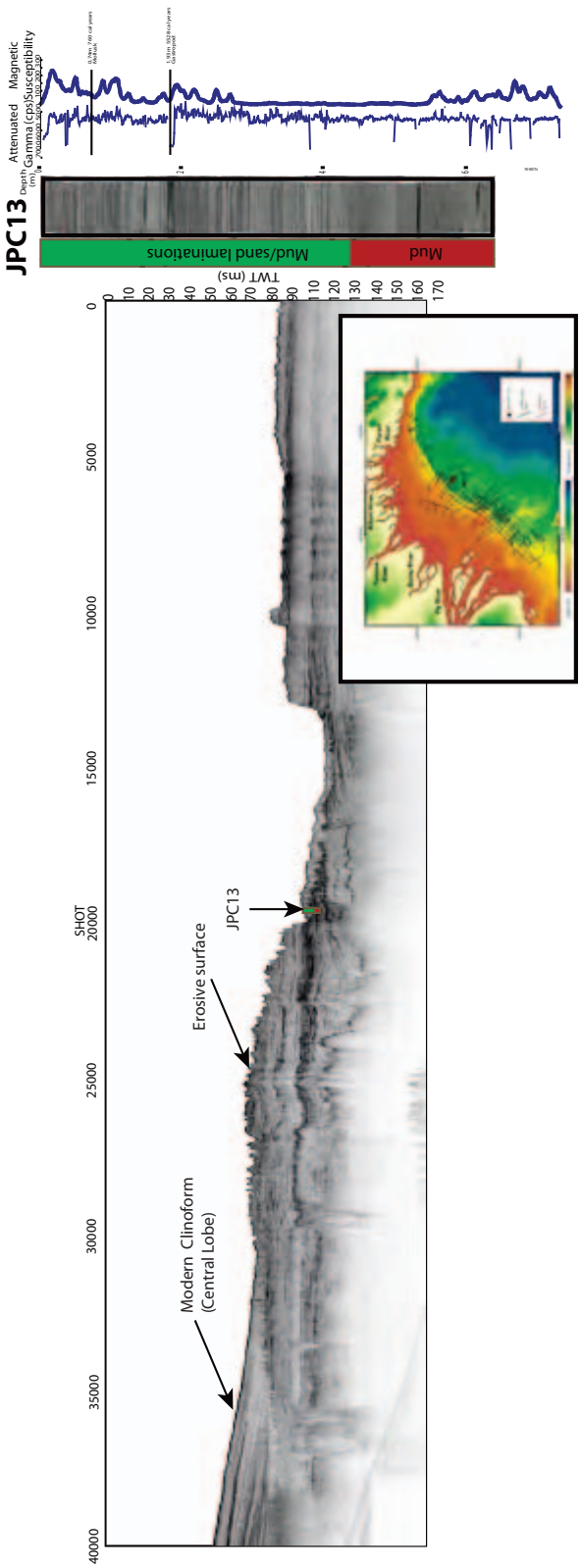
JPC13
Depth (m)
Attenuated Gamma (cps)
Magnetic Susceptibility
Mud
Mud/sand laminations
TWT (ms)
SHOT
JPC13
Erosive surface
Modern Clinoform
(Central Lobe)

Figure 3-13: A. Illite/Smectite ratios of surficial sediment samples in the clay-size range. Two color classifications reveal signal from Fly River system (Type I - red) and Purari River system (Type II - blue). Higher values of these ratios suggest increased weathering and transport time in the system. B. Quartz/ Feldspar ratios of sand size grains from surficial sediment samples. Higher ratios are sourced from the Fly River watershed.

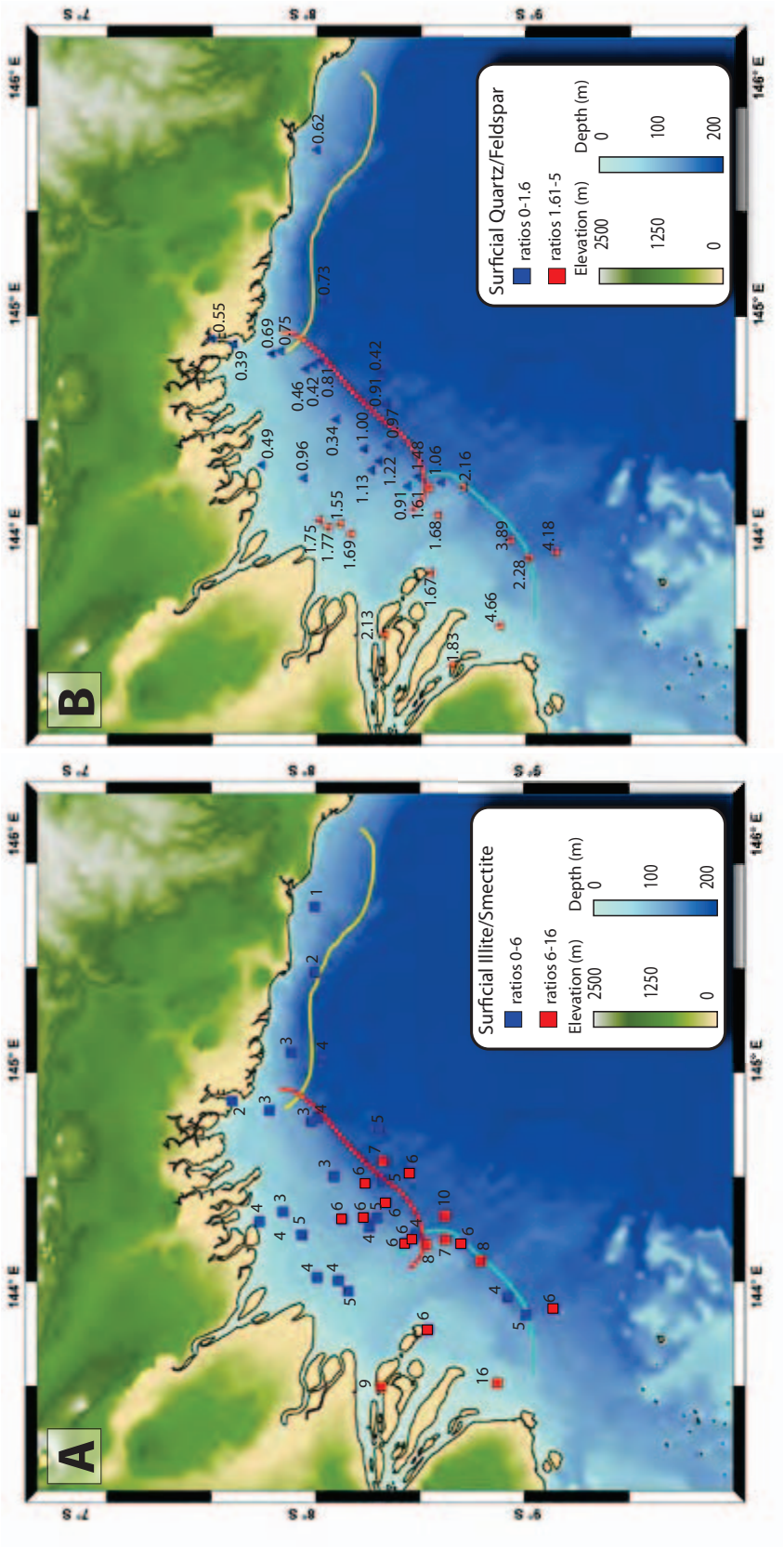
A
Surficial Illite/Smectite
ratios 0-6
ratios 6-16
Elevation (m)
2500
1250
0
Depth (m)
0
100
200
B
Surficial Quartz/Feldspar
ratios 0-1.6
ratios 1.61-5
Elevation (m)
2500
1250
0
Depth (m)
0
100
200
7° S
8° S
9° S
144° E
145° E
146° E

Figure 3-14: Downcore ratios of selected elements (2mm sampling resolution) from cores acquired in the Gulf of Papua. One core from each lobe (Southern-Top, Central-Middle, Northern-Bottom). Signature ratios from the two distinct provenances, Fly Watershed in red and Purari Watershed in blue are apparent in the fine grain homogenous clay lithology. Elemental ratios are more erratic in the coarser sediment and are co-registered with the CHIRP seismic data to the right side of the figure. Color codes are shown next to the core photograph and are based on detailed core descriptions.

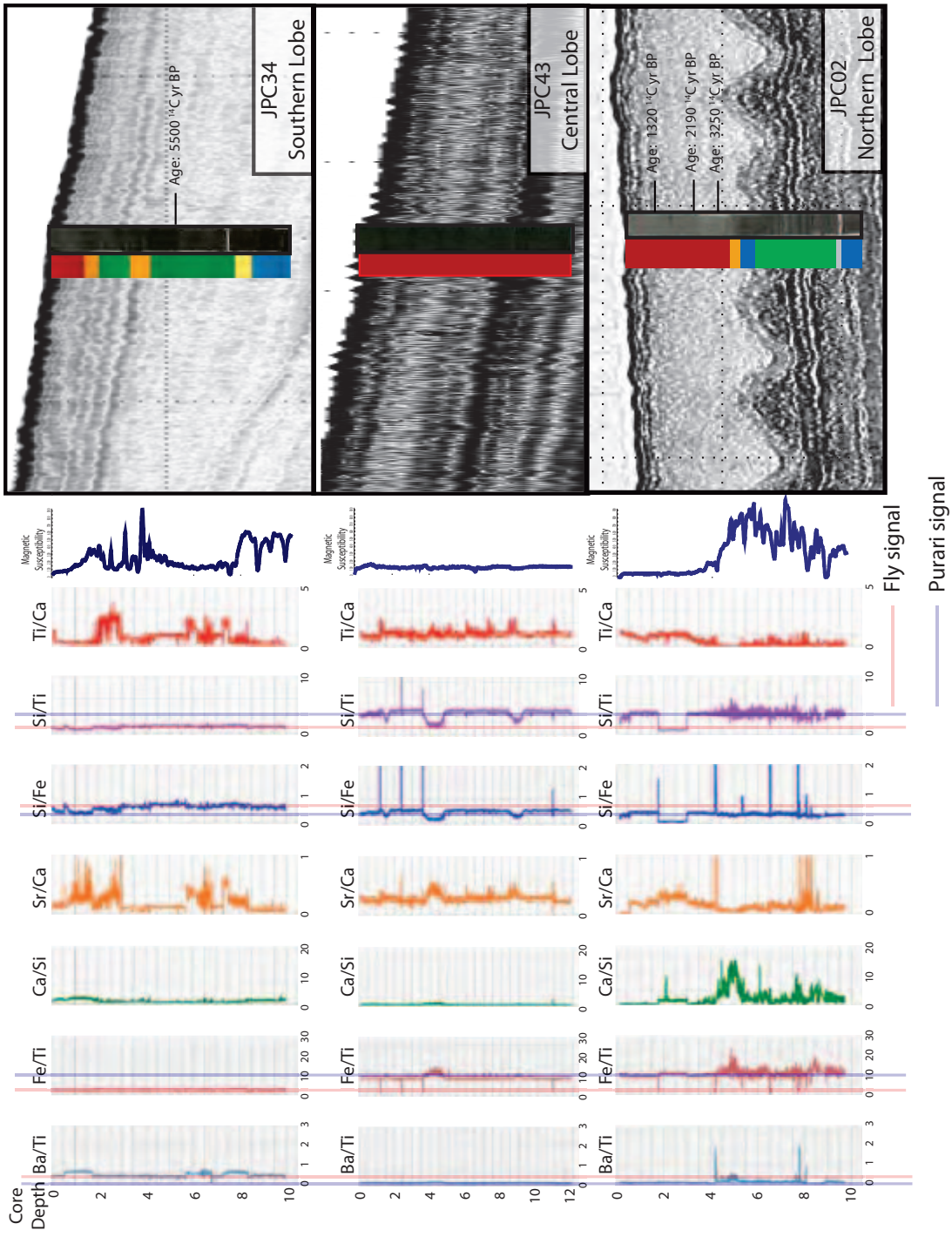
JPC34
Southern Lobe
Age: 5500 ¹⁴C yr BP
JPC43
Central Lobe
JPC02
Northern Lobe
Age: 1320 ¹⁴C yr BP
Age: 2190 ¹⁴C yr BP
Age: 3250 ¹⁴C yr BP
Magnetic Susceptibility
Ti/Ca
Si/Ti
Si/Fe
Sr/Ca
Ca/Si
Fe/Ti
Ba/Ti
Core Depth
Fly signal
Purari signal

4

Terrestral Laser Scanning of Extended Cliff Environments: Parameter Analysis

Terrestrial Laser Scanning of Extended Cliff Sections in Dynamic Environments: Parameter Analysis

Michael J. Olsen[1]; Elizabeth Johnstone[2]; Neal Driscoll[3]; Scott A. Ashford[4]; and Falko Kuester[5]

J. Surv. Eng. 2009.135:161-169.

Abstract: Substantial erosion of the unstable seacliffs along the economically important coastline of San Diego County, California, threatens existing developments and public safety. Time-series mapping of the seacliffs and beaches provides valuable information about seasonal and rapid-event erosion. With high resolution terrestrial laser scanning (TLS) georeferenced using real-time-kinematic global positioning systems, it is possible to establish reliable comparisons of time-series surveys for quantitative change analysis of seacliff morphology. This paper introduces new field survey methods for georeferencing TLS surveys collected in dynamic environments where conventional control methods cannot be effectively implemented for large-scale mapping. Specifically, the quality control of scan alignment and the identification of optimal surveying parameters of point separation/density, distance from target, setup spacing, and efficiency are discussed for long cliff sections. These TLS surveys, performed several times along an approximately 17-km segment of seacliffs in San Diego County show an average root-mean-square uncertainty of 7.9 cm between adjacent scans approaching the nominal 7.2 cm accuracy of the survey equipment.

DOI: 10.1061/(ASCE)0733-9453(2009)135:4(161)

CE Database subject headings: Mapping; Terrain; Topographic surveys; Erosion; Cliffs; Lasers; Parameters.

Introduction

New procedures for terrestrial laser scanning (TLS) with real-time-kinematic (RTK) global positioning systems (GPS) are presented for regional mapping of cliff topography that markedly reduce manual processing and eliminate reliance on previous data sets for data alignment. Procedures are also presented to determine optimal surveying parameters for TLS. For clarity, a consistent nomenclature is used to describe these parameters. Spacing, s, refers to the distance between scan setup locations. Distance, d, refers to the horizontal distance from the scanner to the cliff. Finally, the scanner sampling ratio (γ) represents the resolution at which a scan is performed relative to the maximum resolution capabilities of the scanner. This ratio influences the point separation (distance between points on the target surface) and likewise the point density (number of points on the target surface). It should be noted that the final point density on the target is always higher because of overlap between multiple scans. The TLS surveys for this study repeatedly imaged 17 km of seacliffs in San Diego County, from La Jolla to Encinitas, to understand better the processes governing seacliff retreat. The region was divided into sections based on natural breaks in the seacliffs from lagoons or points of limited beach access, as shown in Fig. 1. While the project involved regional mapping of seacliffs, the new approaches can be applied to a variety of similar mapping projects using TLS.

Seacliff erosion occurs through both marine and subaerial processes (Sunamura 1992). Marine processes include wave erosion of the cliff base, often creating notches and unstable, cantilever cliff sections. Subaerial processes include erosion from precipitation and surface runoff from cliff tops forming gullies and canyons, eroding the upper slope. Seacliff erosion tends to happen as episodic events where large sections of the cliffs fail on to the beach. In San Diego County, these failures often threaten developed structures and public safety in this highly used and economically important coastal region (Griggs et al. 2005). Additionally, the seacliffs can provide much needed sediment to the beaches (Haas 2005; Young and Ashford 2006), which are vital resource to the economy of Southern California. Furthermore, the heavy municipal development on the cliff tops along the coastline in this region requires accurate quantification of aggregate retreat rates for effective coastal management solutions. To gain a broader understanding of the processes that occur, quantitative analysis of the stability of seacliffs and erosional trends is essential. Such information can only be obtained by establishing a reference baseline model of the cliff location and geometry for future comparisons. Methods of data collection such as digital photogrammetry (i.e., Moore et al. 1999; Hapke and Richmond 2000), aerial light detection and ranging (LIDAR) (Young and Ashford 2006) and oblique helicopter LIDAR (Rosser et al. 2008) are not generally feasible for repeated coastal cliff surveys due to greater

[1]Assistant Professor, School of Civil and Construction Engineering, Oregon State Univ., 220 Owen Hall, Corvallis, OR 97331 (corresponding author). E-mail: michael.olsen@oregonstate.edu

[2]Ph.D. Candidate, Scripps Institution of Oceanography, Univ. of California San Diego, 9500 Gilman Dr, MC 0244, La Jolla, CA 92093. E-mail: eajohnst@ucsd.edu

[3]Professor, Scripps Institution of Oceanography, Univ. of California San Diego, 9500 Gilman Dr, MC 0244, La Jolla, CA 92093. E-mail: ndriscoll@ucsd.edu

[4]School Head, School of Civil and Construction Engineering, Oregon State Univ., 220 Owen Hall, Corvallis, OR 97331. E-mail: scott.ashford@oregonstate.edu

[5]Professor, Dept. of Structural Engineering, Univ. of California San Diego, 9500 Gilman Dr, MC 0085, La Jolla, CA 92093. E-mail: fkuester@ucsd.edu

Note. This manuscript was submitted on April 21, 2008; approved on March 11, 2009; published online on October 15, 2009. Discussion period open until April 1, 2010; separate discussions must be submitted for individual papers. This paper is part of the ***Journal of Surveying Engineering***, Vol. 135, No. 4, November 1, 2009. ©ASCE, ISSN 0733-9453/2009/4-161–169/$25.00.

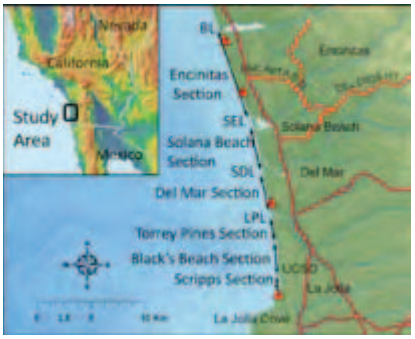

Fig. 1. Map of study region showing individualized sections. Lagoons are abbreviated on the map and are as follows: BL=Batiquitos Lagoon; SEL=San Elijo Lagoon; SDL=San Dieguito Lagoon; and LPL=Los Penasquitos Lagoon. Triangles represent survey monuments used for calibration.

expense, difficult logistics, lower resolution, and/or the ability to capture the cliff face topography (including complex sea caves) in sufficient detail. As substantial change from seacliff failures greater than 30 m^3 can be observed monthly throughout the study area, such information must be obtained on a regular basis before becoming overprinted by subsequent natural processes or anthropogenic control efforts.

TLS Background

TLS (also called terrestrial LIDAR) a line-of-sight remote sensing technique, rapidly transmits a light source to a target which subsequently reflects the light back to the scanner, producing a 3D point cloud model. High-speed phase-based scanners compare phase differences between a modulated laser beam to determine distance to a target at close ranges (typically $<$80 m). Time-of-flight scanners measure the laser pulse travel time to determine the coordinates of the survey scene relative to the scanner. Time-of-flight scanners are more suitable for longer range applications ($>$50 m) such as this study where data needs to be acquired on a large scale (Fig. 2).

The ability to capture centimeter accuracy data at high-resolution and the rapid response capability afforded by TLS makes it the ideal tool for quantitative mapping of seacliff erosion. TLS has various applications in civil and survey engineering and has proven to be an effective tool to study topography for coastal studies (Collins and Sitar 2004; Lim et al. 2005; Rosser et al. 2005; Collins et al. 2007; Young and Ashford 2007). While these studies show the effectiveness of TLS for studying seacliff geomorphology, they required time-intensive processes for data alignment and thus were only performed on small segments of the coast (typically less than 1 km). This study builds upon their efforts to produce a method applicable for large sections (several kilometers) of seacliffs, which presents new challenges to be addressed because the typical control methods cannot be efficiently applied.

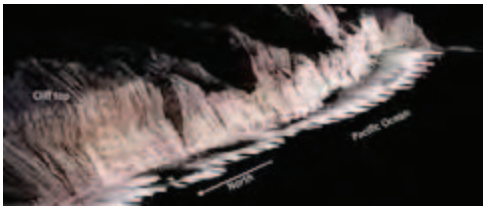

Fig. 2. Georeferenced point clouds for regional mapping of Torrey Pines, Calif. (September 2007). Black semicircles represent scan setup locations spaced at approximately 50 m.

Several scans must be linked together and georeferenced in order to map regional features. Collins and Sitar (2004; Collins et al. 2007) discuss several methods to commonly used to georeference TLS for localized studies of cliff failures and landslides. One method locates the scanner using known control monuments. While feasible in a static urban environment, dynamic factors of coastal environments including seasonal beach height fluctuation, and daily beach width changes from tides render this method unrealistic for large-scale mapping. Another method places target reflectors as control points at locations that have been surveyed that can be used to georeference the data with at least three control targets per scan. This method provides repeatable results between surveys provided the target locations remain fixed or are resurveyed during each scan. A difficulty mentioned by Collins and Sitar (2004) is some targets or target locations placed on the cliff can be lost during cliff collapses and new targets need to be introduced in subsequent surveys. In addition, placement of targets can be difficult and dangerous on near-vertical seacliffs such as those of San Diego County. Also, there is substantial public resistance to any alterations to the natural beach environment.

A common practice used for site surveying uses temporary reflector targets spread throughout the scan scene that are subsequently coregistered between scans. The use of such targets is possible in regional mapping, however, either substantial numbers of targets are required or the targets need to be repositioned as the mapping progresses, which can be very time and labor intensive. Also, in coastal locations with unconsolidated sediment, the targets can sink or be disturbed by wind or waves during scanning, creating increased uncertainty in the alignment during data processing.

Lim et al. (2005) and Rosser et al. (2005) used a total station to obtain control points on the cliff, which are manually matched to comparative points in the point clouds to georeference the TLS surveys. Limitations of this method for large-scale application in sandy beach environments include requiring substantial field and manual user processing time, difficulty in maintaining survey control on a sandy beach environment [Lim et al. (2005) and Rosser et al. (2005) were both performed on hard, rocky coasts], potential safety hazards, and requiring very high resolution scans to adequately find matching tie points in the point cloud. Young and Ashford (2007) performed TLS for a portion of the study area from 2004–2005. The data was georeferenced during post processing using common baseline features (e.g., seawalls, buildings, etc.) between surveys, limiting application to developed areas of the coast. Such a technique also requires substantial processing time to manually register surveys together. Thus, new methods are requisite to efficiently and accurately survey large sections of coastline.

Fig. 3. TLS and RTK GPS field equipment

Error Sources in Terrestrial Laser Scanning

Error sources in TLS depend on the laser characteristics, target characteristics, the scanner setup, and the alignment of scans. Lichti et al. (2005) discuss an error budget for the direct georeferencing of TLS and common artifacts from laser scanning. Direct georeferencing errors occur in the ability to resolve coordinates for the scanner origin, leveling, and backsighting. An important error source to consider for topographical mapping is the increasing spot size of the laser beam with range which reduces accuracy, removes the ability to model small variability which is averaged over the spot size, and creates artifacts in the point cloud. Scaoini (2004) discusses the theoretical increase in error from the spot size with distance from the target using simulated data.

While TLS may be able to produce a high accuracy model from a single setup, improper alignments can produce much larger error when attempting to globally align several scans. For example, a small rotation from an incorrect alignment between scans or unlevel setup can have a minimal effect on a localized area. However, in regional mapping, a small rotation during post processing alignment in software can be amplified as scans are merged together leading to an increasing offset with distance and can be several meters in magnitude over a 1 km range. These large alignment errors can be reduced by adequate data collection through the selection of appropriate parameters in the data collection to avoid error propagation.

Approach: Field Procedure for Regional Surveys

The field survey equipment (Fig. 3) used for this study combines an I-Site 4400 laser scanner, a tablet PC controller, a survey-grade Trimble 5800 RTK GPS unit, and a cell phone, all transported on a rugged wagon. The scanner is nominally accurate to 2 cm at 50 m in a controlled lab test environment and 5 cm for general topographical scanning in the field for its range of 5–500 m (I-Site 2008). The RTK GPS is nominally accurate to 2.2 cm (Trimble 2008). Overall, this amounts to a worst case potential of 7.2 cm of uncertainty for each point measurement. This scanner is not the most accurate scanner available; however, several features such as optical backsight capability, a wide range level/tilt compensator, internal 37 megapixel scan-line camera, a calibrated GPS receiver connection directly above the scanner origin, and long range capability of 500 m made it an appropriate scanner for coastal studies where surveys need to be completed rapidly and repeatedly in a dynamic environment. The scanner requires 6 minutes to perform a 180-degree scan at its highest resolution (9.4-cm point separation at 50 m), which typically captures a cloud of approximately 0.5 million *X*-, *Y*-, and *Z*-points. The level/tilt compensator of the scanner determines the angle (maximum range of 3°, detectable within 20″ increments) at which the scanner is unlevel by performing a 360° preview rotation before the scan is acquired and adjusts the data so that they are appropriately leveled. The self leveling markedly reduces field setup time because the scan does not have to be manually leveled at each new origin.

To properly georeference TLS data, each point cloud must be appropriately constrained along six degrees-of-freedom (DOF) including translation in the *X*-, *Y*-, and *Z*-directions and rotation about the *X*-, *Y*-, and *Z*-axes. The objective of this field procedure is to constrain as many DOFs in the field as possible to minimize data alignment processing. The field procedure builds upon the procedures developed by I-Site (2008) and other scanner manufacturers and involves

- Surveying using the optimal scanning parameters of point separation (i.e., γ), scan spacing (s), and target distance (d).
- Using a virtual reference station (VRS) network or establishing a GPS Base Station as a reference point for RTK GPS surveying.
- Occupying fixed control monuments with the RTK GPS receiver for calibration.
- Performing TLS surveying by obtaining RTK GPS points at each scan origin to translate the scanner origin to its real-world *X*-, *Y*-, and *Z*-coordinates, leveling the scanner via a level compensator to constrain rotation about the *X*- and *Y*-axes, and backsighting the scanner to an estimated (cannot be accurately marked in dynamic environments) previous location or reference point to constrain rotation about the *Z*-axis.
- Perform a multiscan software alignment to correct for backsight error.
- Use quality control methods to verify accuracy of point cloud alignments.

Determining Optimal Scanning Parameters from a Calibration Survey

Choosing the appropriate spacing between scan setups, distance from the target, and sampling ratios for TLS is a delicate balance between collecting enough information to capture the topography and avoiding excess redundant data, which can overload data processing. The spacing of the scans can be highly variable, as relatively flat cliff surfaces allow for increased spacing, whereas complex cliff topography requires closely spaced scans to avoid data gaps from shadowing. A simple rule for maximum scan spacing can be obtained from the following equation based on the Pythagorean theorem:

$$s_{\max} = \sqrt{r_{\max}^2 - d^2 - h^2} \tag{1}$$

where $s_{\max}$=maximum scan setup spacing; $r_{\max}$=maximum scanner or filtered data range; d=typical cliff distance; and h=average cliff height.

The scanner used for this study has low, medium, and high resolution settings (Table 1) which are based on an angular separation between scan lines, not the actual sampling ratio on the target surface. At the highest sampling ratio, the angular separation between points is 0.108°. The point separation for any scanner is a function of distance from the target (and thus will vary across the scan scene) and can be calculated by:

Table 1. Resolution Settings and Corresponding Point Densities Available for the I-Site 4400 Scanner

Resolution setting	Scanner sampling ratio, γ	Angular separation, θ	Point separation, ρ, at 50 m (cm)
LOW	1/16	0.432°	37.7
MED	1/4	0.216°	18.8
HIGH	1/1	0.108°	9.4

$$\rho = d \cdot \tan \theta \quad (2)$$

Where ρ=point separation on the target; d=distance from the target; and θ=angular separation.

Some scanners allow the user to specify a desired resolution at a particular range but are still limited by a minimum possible angular separation and accuracy limitations. Scanning near the target at close spacings increases point density at the expense of broad data coverage. The reverse is true for scanning at far distances from the target at far spacings. To understand the effects of these variables in field data collection and the repeatability of the survey method described previously, several calibration surveys were performed. Fig. 4 shows a typical setup for a calibration survey where scans were performed at a 20 m spacing at distances (d) of 20, 40, and 50 m from the cliff. From these surveys, scan spacings (s) at 20, 40, 60, 80, and 100 m (and 120 m for the surveys 40 m from the cliff) apart were aligned separately to illustrate their effects on scan alignments. The scans were performed at the highest sampling ratio (Table 1) and then filtered to include only points on every 2nd, 3rd, and 4th, scan line and row to simulate 1/4, 1/9, and 1/16 sampling ratios (γ), respectively. All data sets were filtered to 200 m from the scanner origin to remove distant sections of lower point density and less accuracy from a larger spot size.

Using a Virtual Reference Station

This study utilizes the CALVRS (California Virtual Reference Station 2008) system to provide the necessary correction factors transmitted from a base station for RTK GPS. A VRS system links data from several different base stations on a network accessible through a cell phone to interpolate the correction values between base stations. Although any form of RTK GPS could be used, a virtual reference station eliminates the need to set up a dedicated base station at the site, provided the site has sufficient cell phone signal strength. Thus, the VRS network requires less equipment, reduces setup time, and provides more quality control (i.e., multiple base stations providing correction factors) than conventional RTK GPS surveying.

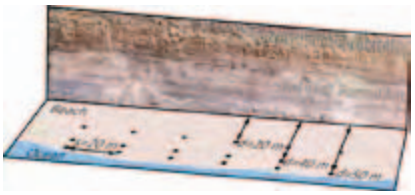

Fig. 4. Calibration survey setup locations spaced 20 m apart at distances of 20, 40, and 50 m from the cliff consisting of the Torrey Pines and Del Mar formations

Occupying Fixed Control Monuments for Calibration

Each section surveyed (Fig. 1) is calibrated using RTK GPS on fixed control monuments so the data are consistent between surveys in areas that are repeatedly scanned. Two monuments (preferably one at each end of the scan region) are employed because the coast is essentially linear along a NW-SE axis. In areas where the region expands along two axes, a third monument should be used to calibrate the scans in and out of the plane.

Terrestrial Laser Scanning Surveying

The coordinates of the scanner origin are obtained during the scan via RTK GPS centered directly over the scan origin. Laser scan data for each setup are in positions relative to the scanner origin, so a coordinate for the origin allows the data to be correctly translated in the X-, Y-, and Z-directions, constraining three DOF in the alignment process. Because of the extreme difficulty in identifying and reoccupying the exact same position (to cm accuracy) on the beach, real time survey methods must be used, with RTK GPS providing the most efficient solution. Temporary or permanent markers are ineffective when on a mobile platform because there is no downward optical site to identify the exact setup location and markers are easily disturbed by waves or people on the beach. The dual axis/tilt compensator of the scanner (±3° determined within 20″ for the scanner in this study) constrains the DOF associated with rotation about the X- and Y-axes. Generally laser scanners do not have such a wide range for level compensation, and thus, would need to be leveled manually. Because the beach sand elevations can be highly variable, leveling the scanner mounted on a wagon is a generally a tedious and difficult task; hence, a wide-range level compensator is valuable.

Aligning the scanner to a known location (e.g., backsighting) can remove the DOF associated with rotation about the Z-axis by calculating a bearing between the scanner origin and the backsight coordinates. Typically a previous scan location provides a convenient backsight. Unfortunately, because the there are no monuments and the previous position cannot be determined using markers to centimeter accuracy when using a mobile platform on the sandy beach, it must be approximated. Estimating the backsight without a fixed reference point typically places the scan within 0.25° of rotation about the Z-axis of its correct position. As most scanners do not have backsighting capabilities, the Z-axis rotation angle can also be estimated by a digital compass (within 0.1°, if calibrated with the scanner). Alternatively, the scanner can be aligned approximately northward and a fictitious point due north can be used as the backsight coordinates. The scan can then be manually rotated about the Z-axis (centered at the scanner origin) in software to a rough alignment (quickly within 1°–2°).

Multiscan Software Alignment

Because the final DOF with rotation about the Z-axis is not completely resolved in the field, a software alignment is required for proper alignment. The scan origins are first translated to the RTK GPS coordinates obtained for their origins and level corrections are applied. The backsight estimate is then used to approximate the rotation about the Z-axis. A scan point cloud alignment algorithm should then be implemented using the leveling and

origin coordinate constraints from the field procedure to find the optimal rotation for a scan about the *Z*-axis at its origin based to eliminate the backsighting error. The point cloud alignment algorithm must have several capabilities to avoid detrimental global error propagation. First, the algorithm must not depend on one scan being completely fixed because all of the scans probably have some backsighting error that must be eliminated because of the difficulty in marking a backsight target on the beach. In addition, aligning adjacent scans to a single fixed scan can lead to the propagation of misalignments because of warping effects in scans. Second, the algorithm must constrain five of the six DOF's (translation *X*, *Y*, *Z* and rotation *X*, *Y*) and only allow for rotation about the *Z*-axis (centered at the scanner origin) to avoid misalignments. Third, points should only be compared in areas where both scans have dense point coverage. Finally, it is important that the alignment be performed using neighboring scans on each side of every scan because pairwise point cloud registrations can misalign the scan with its other neighbor, whereas a multineighbor alignment better distributes the error between neighboring scans. These requirements are not met in most available software packages. An automated algorithm, developed by the writers, will be publicly available at http://lidarweb.ucsd.edu/coastalstudy/softwaretools.html, which incorporates these requirements. This algorithm determines neighboring scans by searching through the survey database of GPS coordinates (*X*, *Y*, *Z*, scan ID, and backsight ID), and batch processes the scan alignment procedure. The algorithm simultaneously rotates adjacent scans about the *Z*-axis at their origins and compares the distance from the points in one scan to planes formed by neighboring points in the adjacent scans to determine the optimal rotational angles for each of the scans producing the lowest root-mean-square (RMS) distance.

Quality Control of Scan Alignments

To ensure the accuracy of the scans, several methods of quality control can be employed. Scans can be compared to their neighboring scans to evaluate the RMS distance between the points in one scan and the plane formed by the nearest three neighbors in the second scan. Sometimes results can appear adequate mathematically because a localized minimum can be obtained in software alignments. By viewing two-dimensional cross sections of the cliff from neighboring scans simultaneously, misalignments become apparent that can be indiscernible in three-dimension. To ensure misalignments do not propagate globally through the aligned scans, annual RTK GPS surveys can be performed on "fixed" structures such as stairwells, seawalls, and fences. Certainly these objects will move over time as waves disturb them, but during short time periods, they can be assumed to be fixed, especially during the calmer summer months. Obtaining RTK GPS points on features of highest curvature are easy to quickly visually compare to the TLS data. This also provides more tie points in georeferencing data sets from different sources. These surveys can be rapidly completed and do not have the constraint of requiring low tides. Because of possible movements of the fixed structures with time, it is recommended to repeat these surveys annually after the winter season. After obtaining repeat surveys of an area, surveys can be compared in areas with minimal change to ensure a successful alignment. This study used all of these methods to verify the accuracy of the TLS surveys.

Results and Discussion

Calibration Study Results

For each scan spacing and cliff distance during the calibration experiments performed on the Torrey Pines section, the alignment uncertainty was evaluated by calculating the RMS uncertainty between neighboring scans. The RMS uncertainty metric used in this study compares distances of the points of one scan to a plane formed by their nearest neighbors in another scan to predict where the scans should be relative to one another. Fig. 5 shows the relationship between scanning distance (d), setup spacing (s), and the sampling ratio (γ). The three curves in Fig. 5 drawn for (a) full; (b) quarter; (c) ninth; and (d) sixteenth resolution represent the distances from the cliff (20, 40, and 50 m) at which the scans were performed. For a given sampling ratio, there are three zones. First, at close spacings (<40 m for $\gamma=1$) between setups, the RMS uncertainty is mostly dependent on the accuracy of the equipment. While the RMS is lowest in this region, it requires the most time. At large spacings (>60 m for $\gamma=1$), the RMS is heavily dependent on the poorer point overlap and shadowing effects of the topography, causing data gaps. Additionally, at this spacing, scans are performed more obliquely to the cliff surface. In between, is the optimal zone (40–60 m for $\gamma=1$) for efficiency (provided it meets the desired accuracy of the project) where the distance curves converge and the RMS is optimized.

Comparing the distance curves for different sampling ratios shows that resolution is more critical at higher spacings, and lower sampling ratios increases the RMS. The spacing where these curves pivot (s_p) tends to increase with decreasing sampling ratio. The curves also become more linear with increasing distance from the cliff. Additionally, Fig. 6 shows that at close distances, the RMS is heavily dependent on the setup spacing, whereas, at far distances, the curves converge, showing that the RMS is more a function of the sampling ratio than scan spacing for long-distance scans. Curves for closer spacings increase at higher distances, whereas curves for higher spacings decrease with higher distances. These curves show a sharp dropoff between $\gamma=1/16$, $\gamma=1/9$, and $\gamma=1/4$, but less of a drop between $\gamma=1/4$ and $\gamma=1$. This shows that the lower sampling ratios do not adequately resolve features on the topography, which are mostly resolved for $\gamma=1/4$ and better resolved at $\gamma=1$. While the scanner cannot sample more than this, the flattening of the curves suggests that the highest sampling ratio sufficiently resolves the topographical features within its accuracy limits.

Sample results of the calibration experiment with various scanner spacing and distance from the cliffs with $\gamma=1$ are shown in Fig. 7. Fig. 7(a) shows scans spaced at 80 m with a distance of 20 m from the cliff. The scans show high point density on the cliff; however, they have several large shadow zones, including at the cliff top, as a consequence of being too close to the cliff. Fig. 7(b) shows scans at the same spacing (80 m) but at a distance of 40 m from the cliff. Note there is less shadowing at a 40 m distance but also a lower point density. Fig. 7(c) shows scans at the same spacing (80 m) that are 50 m from the cliff, showing less point density than the 40 m curves. Fig. 7(d) illustrates scanning near the optimal spacing of 60 m with a distance of 40 m from the cliff where shadowing problems are eliminated and a sufficient point separation is maintained.

When working in a dynamic coastal setting, the survey team often has minimal flexibility in determining the scanning distance from the cliff because of tide cycles and resulting limited beach width. Thus, a closer spacing is required when the tide forces

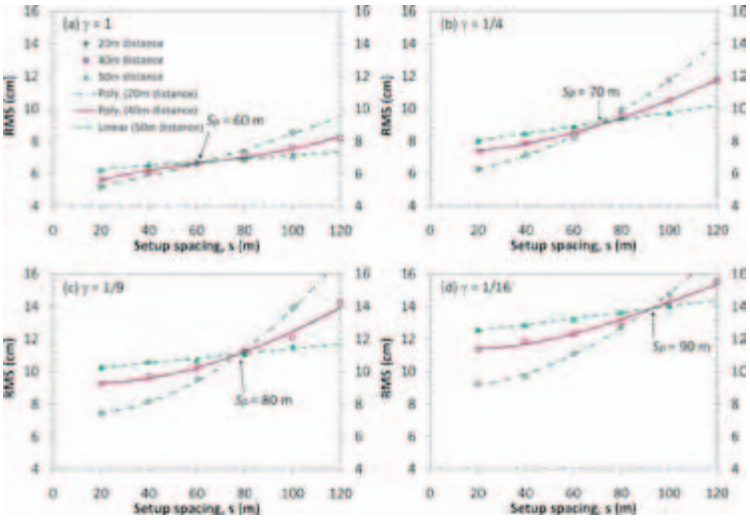

Fig. 5. RMS uncertainty of adjacent scans at varying scan setup spacings (s) for (a) full; (b) quarter; (c) ninth; and (d) sixteenth scanner sampling ratios (γ). Setup spacing pivot points (s_p) indicate where closer distances from the cliff produce higher RMS uncertainty.

scanning to be performed closer to the seacliffs. Fortunately, the distance from the cliff (within 20–50 m) appears to have the largest increase in RMS at large scan spacings, so if the survey team works within the optimal zone, the data quality should not be compromised. As shown in Fig. 5, for this particular scanner, the optimal spacing for the highest sampling ratio would be from 50–70 m to limit the RMS to below 7.2 cm (5 cm error from the scanner and 2.2 cm error from the RTK GPS). Above this, the RMS tends to steepen rapidly with increased spacing. Scans should be performed about 30–40 m from the cliff, if possible, to allow the scan window to capture the cliff top (up to 70 m) and minimize topographic shadowing from being too close to the cliff.

While the optimal range of parameters for scanning for a location is illustrated by the calibration survey, there are times when a different spacing should be employed. Areas of complex topography such as sea caves will require closer spaced scans at different angles to capture occluded features. Also, care should also be taken to scan with a tighter spacing around acute angle corners where the scanning direction switches considerably to ensure sufficient overlap for alignment of the point cloud data sets. Finally, if increased morphological resolution is desired, the scanning should be performed closer to the cliff and at closer intervals. However, this will increase the time cost associated with scanning.

Further, to use the calibration scans to assess the repeatability between surveys, two sets of four scans of the same section were aligned separately with the near-optimal scanning parameters ($\gamma = 1$, $d = 40$ m, $s = 40$ m) to simulate two independent surveys. The RMS difference between these two data sets was 6.2 cm, which agrees with the RMS the calibration curves. This shows that the survey method not only reduces alignment uncertainty between neighboring scans but between surveys, as well.

Results of Repeat Large-Scale Field Surveys

Table 2 shows the results of the RMS uncertainty between neighboring scans calculated from the alignment of several regional seacliff studies. The overall average RMS uncertainty of 7.9 cm approaches the limitations of the equipment for field conditions (7.2 cm). Fig. 8 shows a comparison RMS uncertainty of the individual scans from the field data sets to the calibration curves [Fig. 5(a)]. Data from the Torrey Pines section where the calibration survey was performed are shown as plus marks; whereas all field data from the entire study area are shown as gray circles. The field data shows the same general trends as the calibration data, however, the RMS values are higher and show much more spread. While the trendline for the Torrey Pines field data are slightly higher than the calibration curves, there is a larger difference when compared to the entire survey region showing that there are morphological effects that contribute to the RMS uncertainty in other sections. The topography can have very complex features, which increases error from shadowing and less consistency between data sets for alignment.

There are several other reasons why these RMS difference values are higher than results from the calibration survey. First, some of these surveys include areas of heavy vegetation, which can move during scans. Also, points can be collected on varying parts of the vegetation, making correspondence between scans difficult. Where possible, these points were eliminated from the data set, however, this also reduces the number of points available for the alignment process. The maximum RMS values in Table 2 occur from scans in these vegetated areas; 10% of the field scans have an RMS larger than 10 cm with their neighboring scans, and 68% of those were in areas of dense vegetation covering the majority of the cliff face, so less data were available for alignment. Second, some areas required scanning far from the cliff to obtain data on the entire cliff face [Fig. 8(f)], which results in a

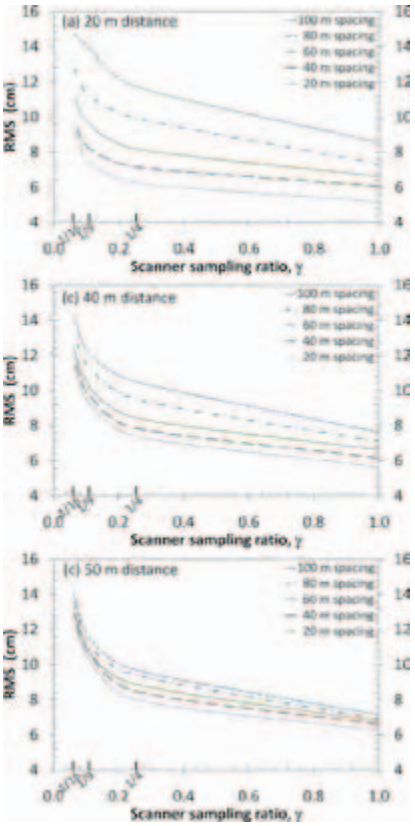

Fig. 6. Influence of scan sampling ratio (γ) on alignment RMS uncertainty at (a) 20 m; (b) 40 m; and (c) 50 m distance, d, from the target during the calibration surveys

lower point density; 28% of the scans with an RMS greater than 10 cm were in areas of tall cliffs (>100 m), so they were performed at a far distance from the cliff for complete coverage, which resulted in a lower point density. Third, the calibration surveys were carefully controlled and the scan spacings were measured, which was not done during the field surveys where scan spacing is often estimated during scanning. Fourth, there is always some possible equipment error such as high interference for the RTK GPS readings or atmospheric conditions affecting the laser time measurements. Finally, the scanner platform can settle slightly as the scan is being performed in the wet loose sand.

Verification of Field Data

The field data was verified through the procedures discussed in the approach section. By comparing scans to RTK GPS surveys performed on fixed structures, the RTK GPS points were generally found to be within 10 cm of the scan points for those structures. Because of a typical point separation of 10 cm on the structures, their equivalent location in the point cloud could not be better resolved. Using the RTK GPS points as a check to

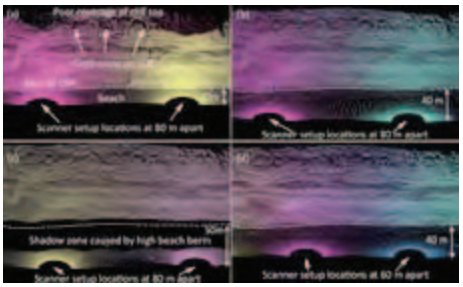

Fig. 7. Aligned point clouds (γ=1) for scans spaced at (a) 80 m at a 20 m distance; (b) 80 m at a 40 m distance; (c) 80 m at a 50 m distance; and (d) 40 m at a 40 m distance. Note the missing cliff top and several occlusions on the cliff in (a); that points appear less bright because of decreased point density at the farther distance in (c); and the optimal coverage of the cliff in (d).

ensure there was not any large global propagation of misalignments proved effective. Examination of cross sections throughout the entire span of each data set showed much less than 10 cm error between adjacent scans (typically undetectable), except in approximately 10% of the field scans where the RMS was slightly larger than 10 cm and occurred in areas of heavy vegetation or areas with extremely tall cliffs forcing the survey team to scan far from the target.

The repeatability was verified by comparing the results of points representing structures from the four surveys of the Del Mar section. The results shown in Table 3 show that the RMS between surveys is very similar to the RMS between adjacent scans during a survey so that comparison analysis can be performed without alignment biases between surveys.

Conclusions

By using consistent methods which minimize data alignment processing to perform field work, regional TLS surveys can be efficiently georeferenced for comparative studies and mapping. The methods outlined in this paper show how to perform TLS for large, dynamic sections and how to ensure the data are accurately georeferenced both between adjacent scans in a survey and between surveys without requiring time-intensive control surveys, which may not be possible in such environments. Accurately georeferenced data are essential to compare time series data sets to observe real change as opposed to apparent change from misaligned data. Data acquired with such techniques provide a reliable baseline for subsequent erosion monitoring and analyses.

Furthermore, understanding the influence of scan setup spacing (s), cliff distance (d), and sampling ratio (γ) on alignment RMS through calibration surveys ensures that quality data are collected consistently and efficiently so that features are adequately resolved in the data. Additionally, it provides a simple test to assess the repeatability between surveys. The optimal parameters presented in this study are a function of seacliff morphology and the type of scanner used; thus, it is recommended that researchers implement these calibration methods on test sections of their study areas to determine the optimal parameters based on their equipment and the seacliff morphology. While trends will be similar, the scanner characteristics and seacliff mor-

Table 2. Survey Data Set Properties and RMS Uncertainty between Adjacent Scans (March 2007–March 2008)

Segment	Survey date	Length (km)	No. scans	Average scan spacing (m)	No. points (millions)	RMS ave. (cm)	RMS max (cm)	RMS min (cm)	RMS std. dev. (cm)
Encinitas	May 08	4.3	67	64	19.004	8.6	12.3	6.4	1.3
	Oct. 07	4.9	89	55	22.374	8.6	13.8	5.6	1.7
Solana Beach	Feb. 08	2.9	66	44	17.948	8.2	10.0	5.4	1.0
	Mar. 07	2.9	117	25	38.635	6.9	10.4	4.0	1.2
Del Mar	Apr. 08	2.6	39	67	12.273	8.8	12.6	6.1	1.8
	Jan. 08	2.8	46	61	7.645	8.3	13.6	5.7	2.0
	Aug. 07	2.5	60	42	14.965	7.3	10.4	4.9	1.5
	Mar. 07	2.5	66	38	16.321	7.8	12.3	4.8	1.8
Torrey Pines	Apr. 08	1.8	47	38	17.662	7.1	9.8	4.6	1.1
	Mar. 08	1.8	42	43	13.364	7.3	11.4	5.9	0.9
	Sep. 07	1.7	79	22	33.515	6.4	8.7	4.7	1.0
	Apr. 07	1.5	36	42	13.428	6.6	10.6	4.6	1.4
Black's Beach	Feb. 08	4.4	81	54	19.346	9.7	13.5	6.0	1.6
	May 07	3.3	54	61	13.500	8.8	12.7	5.5	2.2
Scripps	Mar. 08	0.6	14	43	4.530	7.5	9.2	6.3	0.9
	Sep. 07	0.6	12	50	5.441	7.7	9.0	6.0	1.2
	May 07	0.4	11	36	4.420	7.5	8.8	6.2	0.9
Totals	—	41.5	926	—	274	—	—	—	—
Overall	—	—	—	45	—	7.9	13.8	4.0	1.4

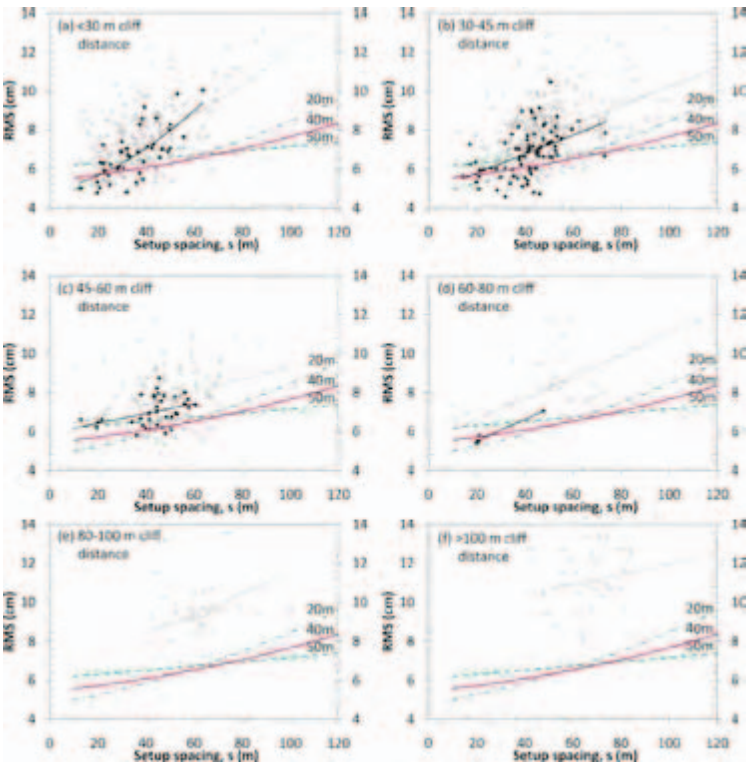

Fig. 8. Comparison of RMS uncertainty for field surveys performed at varying distances with results of calibration surveys [Fig. 5(a)] at 20, 40, and 50 m distances at full resolution ($\gamma=1$). Black+represents scans performed in the same section (Torrey Pines section) as the calibration survey with best fit lines shown as dark lines. Gray dots represent data from the entire study area, with best fit lines shown as gray dotted lines.

Table 3. RMS (cm) of Static Structures in Del Mar from Four Surveys Showing the Repeatability of the Survey Method

Jan. 08	7.2	—	8.5
Aug. 07	8.6	8.5	—
Mar. 07	7.0	6.7	8.4
Survey date	Apr. 08	Jan. 08	Aug. 07

phology will produce different RMS values than those presented herein. Fortunately, the described calibration survey is simple to implement and can be performed quickly. Because of additional factors and complexities possible in typical field scanning, the optimal parameters should be used as an upper limit for spacing, s, and distance, d, and a lower limit for the scanner sampling ratio, γ, to ensure adequate field data collection.

Acknowledgments

This research was funded via a grant from California Seagrant (Grant No. R/OE-39) and the Coastal Environmental Quality Initiative (CEQI) under Grant No. 04-T-CEQI-06-0046. Pat Rentz and Jessica Raymond of Scripps Institution of Oceanography assisted in the TLS surveys. Scott Schiele and John Dolan from I-Site provided technical assistance for this work. Travis Thompson of CALVRS assisted in using the CALVRS network. The writers would also like to thank the reviewers and editorial staff whose valuable comments and insights enhanced the paper.

References

California Virtual Reference Station. (2008). "CALVRS: A real-time California cooperative." ⟨http://www.calvrs.net⟩ (August 7, 2008).

Collins, B., Kayen, R., Reiss, T., and Sitar, N. (2007). "Terrestrial LIDAR investigation of the December 2003 and January 2007 activations of the Northridge Bluff Landslide, Daly City, California." *Rep. No. 2007-1079*, U.S. Geological Survey, Menlo Park, Calif.

Collins, B., and Sitar, N. (2004). "Application of high resolution 3D laser scanning to slope stability studies." *Proc., 39th Annual Symp. on Engineering Geology and Geotechnical Eng.*, Butte, Mont., 79–92.

Griggs, G. B., Patsch, K., and Savoy, L. E. (2005). *Living with the changing California coast*, University of California Press, Berkeley, Calif.

Haas, J. (2005). "Grain size and mineralogical characteristics of beach sand with implications for sediment provenance in the Oceanside Littoral Cell." MS thesis, Univ. of California, San Diego, 126.

Hapke, C., and Richmond, B. (2000). "Monitoring beach morphology changes using small-format aerial photography and digital softcopy photogrammetry." *Envir. Geosciences*, 7(1), 32–37.

I-Site. (2008). "Maptek I-Site 3D laser scanning." ⟨http://www.isite 3d.com⟩ (Aug. 7, 2008).

Lichti, D. D., Gordon, S. J., and Tipdecho, T. (2005). "Error models and propagation in directly georeferenced terrestrial laser scanner networks." *J. Surv. Eng.*, 131(4), 135–142.

Lim, M., Petley, D. N., Rosser, N. J., Allison, R. J., and Long, A. J. (2005). "Combined digital photogrammetry and time-of-flight laser scanning for monitoring cliff evolution." *Photogramm. Rec.*, 20(110), 109–129.

Moore, L. J., Benumof, B., and Griggs, G. B. (1999). "Coastal erosion hazards in Santa Cruz and San Diego Counties, California." *J. Coastal Res.*, 28, 121–139.

Rosser, N. J., Lim, M., Norman, E., and Petley, D. N. (2008). "Exploring variations in and controls upon cliff, platform and coastline geometry." *Geophysical research abstracts*, Vol. 10, European Geosciences Union, Copernicus Publications, Gottingen, Germany.

Rosser, N. J., Petlety, D. N., Lim, M., Dunning, S. A., and Allison, R. J. (2005). "Terrestrial laser scanning for monitoring the process of hard rock coastal cliff erosion." *Q. J. Eng. Geol.*, 38, 363–375.

Scaoini, M. (2004). "Direct georeferencing of TLS in surveying of complex sites." *Proc., 3D-ARCH, Virtual Reconstruction and Visualization of Complex Architectures, Int. Society of Photogrammetry and Remote Sensing*, ISPRS, Mestre-Venice, Italy.

Sunamura, T. (1992). *Geomorphology of rocky coasts*, Wiley, New York.

Trimble. (2008). "Trimble 5800 GPS receiver." ⟨http://www.trimble.com/ 5800.shtml⟩ (Sept. 24, 2008).

Young, A. P., and Ashford, S. A. (2006). "Application of airborne LIDAR for seacliff volumetric change and beach sediment budget contributions." *J. Coastal Res.*, 22(2), 307–318.

Young, A. P., and Ashford, S. A. (2007). "Quantifying sub-regional seacliff erosion using mobile terrestrial LIDAR." *Shore Beach*, 75(3), 38–43.

5

Styles of Cliff Erosion in the Oceanside Littoral Cell, Southern California.

5.1 ABSTRACT

High-resolution, terrestrial Light Detection And Ranging (LiDAR) data have been acquired since 2006 to measure the rate and style of sea cliffs erosion along the southern 20km of the Oceanside Littoral Cell (OLC). Twelve cliff failures were mapped repeatedly using an Isite 4400 terrestrial laser scanning system to examine how failures propagate along and across the cliffs as well as feedbacks between the liberated material and subsequent cliff failures. Grain size analysis of the failed material (retention cutoff) was performed to estimate the contribution to the beach sand inventory. Even with a relatively short time series (only six years), a quantitative baseline has been established from which future change can be assessed. In addition, the results are providing new insight into the different processes controlling cliff erosion in the OCL. Both lithological and environmental conditions are known to play a major role in governing the rate of cliff erosion, however other factors such as beach width, elevation and precipitation also exert control on rates and styles of cliff failures. Cliff erosion is subaerial dominated where the beaches are wider and elevation is higher. Alternatively, erosion is marine dominated where the beaches are narrow and have lower average elevation. Feedbacks exist between beach elevation and undercutting and erosion along the failure edges and thus might provide a mechanism to create the observed linear retreat of the cliffs in the OLC rather than the formation of promontories and embayments. This time series is useful to document seasonal and short-term erosional patterns as well as establish a baseline to understand cliff erosion in response to the rapid sea level rise (>3mm/yr).

5.2 INTRODUCTION

Beaches in San Diego County are an important natural resource. Economic studies indicate that beach related tourism and associated services contribute more than $200 million a year to the local economy (Figure 1; CDBW, 2002). Currently, concern is growing that this resource is at risk. The damming of local rivers (Inman and Jenkins, 1999), urbanization (Warrick and Rubin, 2007), and armoring of the bluffs (Haas, 2005; Runyan and Griggs, 2003) are reducing the natural sand supply to the beach. Recent studies suggest that bluff erosion currently contributes more to the beach sand supply than previously thought (Haas, 2005; Young and Ashford, 2006). Young et al., (2010b) and Raymond (2010) determined that the OCL sea cliffs are composed of over 75% sand content throughout much of the study area. Furthermore, there is much debate on whether or not seawalls contribute to active erosion (i.e., increased beach erosion due to the presence of the seawall). A better understanding of the relationship between bluff erosion and beach sand supply is necessary for proper management of this valuable resource. Researchers have quantified regional erosion rates for San Diego County using long term averaging methods (Hapke et al., 2009; Griggs and Patsch, 2004). While this technique provides a valuable estimate for average erosion rates in a region, it is often difficult to assess accurately the processes controlling cliff erosion. Quantitative mapping of cliff erosion on temporal and spatial scales similar to the operative processes provide insights into the mechanisms that control cliff erosion and our results complement longer-term studies that yield average erosion rates (Figure 2).

Three-dimensional change modeling using LiDAR, when combined with grain size information, allow us to determine what percentage of the cliff failure is likely to remain on the beach given the average grain size population of sand on the beach and the wave climate (Runyan and Griggs, 2003; Young et al., 2010a). Based on sediment

provenance Hass (2005) and airborne LiDAR data, (Young and Ashford, 2006; Young et al., 2009) 50% or more of the sand supplied to the beach is sourced from the sea cliffs. This estimate is in marked contrast to the established paradigm that rivers in the OLC supply the majority of sand to the beach system with the cliffs being a minor source (Inman and Jenkins, 1999; Brownlie and Taylor, 1981).

Human development, including extensive cliff-top construction, plays a major role in the erosive nature of seacliffs. Armoring of cliffs in the study region alters the natural process of sediment liberation from the cliff face and local inputs of sand supply. This in turn, lowers the beach elevation and width, which then diminishes the ability of the beach to act as a natural barrier to wave energy. Within our study area, beach width and height is greatest in areas without cliff armoring (e.g., Torrey Pines south to La Jolla Cove; Hass et. al. 2005, Young et al., 2010a). Approximately 30% of the sea cliffs within OLC have been altered in some manner. In addition, with heightened development from coastal properties and golf courses in close proximity to the coast, water runoff and groundwater seepage has increased along the cliffs. This accumulation and drainage of water simulates increased precipitation creating zones where sapping, which used to be seasonal, now occurs year-round. As the rate of sea level rise increases, it is important to understand how the coastal cliffs and beaches will be impacted.

5.2.1 California cliff formation and geologic history

Southern Califonia's coastal sea cliffs are formed from the active erosion of tectonically uplifted marine terraces (Kuhn and Shepard, 1984). The OCL located in the San Diego County region, spans a 77-kilometer stretch of coastline from Dana Point to La Jolla (Figure 1; Inman and Frautschy, 1966). Narrow sand and cobble beaches backed by steep sea cliffs cutting into uplifted marine terraces characterize much of the OCL. The study area is dominated by residential and commercial development. Steep cliffs are

present in approximately 70% of the study area with occasional alternating lowlands at coastal river mouths and lagoons. Seacliff elevations range from 2 to 110 meters high, with the majority being greater than 25 meters (Benumof, Storlazzi et al. 2000, Young et al., 2010).

Most of the cliffs in the OLC study area are composed of sedimentary rocks from the Eocene classified as part of the La Jolla Group (Kennedy, 1975) and are mantled by thin veneers of Pleistocene marine terrace (i.e., Linda Vista and Bay Point formations) and alluvium deposits. The basal unit making contact with the beach in the northernmost areas is the clay-rich Del Mar Formation. The Del Mar Formation is overlain by the Torrey Sandstone Formation, which is interpreted as an ancient beach deposit consisting of mostly semi-consolidated sandstone with very little organic and fossil material. The sandstone in this formation consists of medium- to coarse-grained lithified quartz sediments. The Bay Point Formation, a terrestrial Pleistocene deposit cap with poorly lithified, fine- to medium-grain sandstone (Kennedy, 2005), mantles an unconformity made of beach cobbles. The lower unit, Delmar Formation, is stronger and more resistant to erosion, however, the Torrey and Bay Point formations, are both highly susceptible to erosion, with long-term erosion rates of 8 to 43 cm/yr (Benumof and Griggs, 1999; Young and Ashford, 2006).

5.2.2 Sediment Sources

Based on airborne LiDAR data between 2001 and 2004, it was estimated that seacliffs and gullies yielded 76,900 m3/yr and 20,000 m3/yr of sediment, respectively (Young and Ashford, 2006). The average annual sediment flux estimated from the coastal rivers for the study period was 15,700 m3/yr. The volumetric rate of sediment yield per length of shoreline ranged from 0.47 (Carlsbad) to 3.61 (San Onofre) m3/m-yr with a weighted average of 1.80 m3/m-yr for the Oceanside Littoral Cell. Based on these data,

linear rates of seacliff retreat ranged from 3.1 to 13.2 cm/yr with a weighted average for the littoral cell of 8.0 cm/yr. The highest retreat rates were observed in the Del Mar, Solana Beach, and San Onofre sections - all of which were greater than 10 cm/yr. Hapke et al. (2009) reported erosion rates of ~20 cm/yr on average for sea cliffs in the OLC. Due to the complex nature of the cliffs and forcing functions controlling the erosion, it is difficult to assign one regional erosion rate that captures the local variability. Overall styles of erosion within southern California are highly dependent on localized factors such as geological composition, wave dynamics and regional climate patterns. Here we examine the various styles of cliff erosion observed in the OLC (Figure 2), the controlling parameters, and potential contribution to the beach sand budget.

To date, given the relatively short duration of this study and the episodic nature of cliff failures, it is difficult to make any long-term conclusions about contributions to the beach sand budget. Our quantitative baseline dataset for the sea cliffs in the OLC with repeat LiDAR scans allows us to measure the failures associated with different processes (e.g., wave undercutting versus subaerial processes) and how the failures vary from pristine environments to developed landscapes. Further, sediment contributions from the erosion of sea cliffs may become a larger percentage of the sediment source as the effects of damming (Willis and Griggs, 2003) and urbanization of the coastal watershed continue to increase (Warrick and Rubin, 2007). Finally, it is important to understand how sea cliff erosion will be impacted by the rapid sea level rise as well as changes from climate shifts, such as the Pacific Decadal Oscillation (PDO) and El Nino- Southern Oscillation (ENSO). As we enter a negative phase of PDO (Figure 3), local precipitation is expected to decrease (Higgins et al., 1998; Inman and Jenkins, 1999; Milliman et al., 2008) and how this modern climate regime will impact coastal erosion is not well understood.

The two dominant modes of cliff erosion in the OCL are wave cutting (Figure 4) and subaerial erosion (Figure 5). Additionally, the tectonic nature of Southern

California leads to extensive jointing and faulting along the coastal cliffs. Wave-based erosion occurs when the wave-runup, as described in Ruggerio (2001) is above the beach elevation and therefore the wave energy makes contact and scours the base of the cliffs acting from bottom up. Subaerial erosion occurs above the wave impact zone (Benemouf, 2000) and generally occurs from the top downwards. Faults and joints exist as zones of weakness and provide conduits for groundwater seepage and further destabilize the sea cliffs. Here we describe how these processes are controlling regional sea cliff erosion and quantify the rates of erosion in the OCL.

5.3 METHODS

To date, we have acquired continuous terrestrial LiDAR scans between La Jolla and Encinitas during a six-year period to establish a quantitative topographic baseline from which future change can be assessed. We have developed new TLS survey approaches and algorithms for aligning LiDAR scans to minimize uncertainty for sea cliff erosion studies (Olsen et al., 2009; Olsen et al., 2011). These advances in processing LiDAR data increase the resolution and reliability of TLS surveys, which allows quantitative mapping of cliff failures with centimeter accuracy in all azimuths.

In conjunction with this effort, we have been systematically mapping large portions of the southern Oceanside Littoral cell (Figure 1). Given the current >3 mm/ year eustatic sea level rise measured by tide gauges and satellite altimetry in response to thermal expansion as well as accelerated glacial retreat, it is imperative to establish a baseline from which future cliff erosion can be assessed Rahmstorf, 2007; 2009. In addition to establishing this baseline, we have been tracking a number of failures (Table 1) to determine how quickly the liberated material is reworked by wave-based erosion.

We resurveyed these failures sites at least every few months or after large storm events to determine the rate of sediment reworking.

Field surveys were conducted using an I-Site 4400 laser scanner. The scanner emits light pulses at a wavelength of 905 nanometers that radiate in 360 degrees around the origin and 80 degrees in the Z-axis (Figure 6). The laser signal is transmitted to the cliff face and returned to an internal receiver, which sends point cloud information to a PC computer running proprietary software. Each signal is assigned to an X, Y, Z point that is based on two-way time travel from the scan origin. All data is georeferenced to GPS data collected concurrently with scan acquisition. The scanner also records signal intensity along with color information (Red, Green, Blue values) for each data point in the cloud. Scan time varies based on the resolution and rotational swath of each survey. Our study mainly consisted of 180 degree scans oriented orthogonal to the cliffs. This method required an interscan distance of 40-50 meters to obtain adequate point cloud overlap and complete coverage along the coast. Olsen et al. (2009) demonstrated optimal scan protocol for beaches backed by high seacliffs and equipment limitations (Figure 7).

The ISITE 4400 laser scanner has several scanning parameters including high, medium and low resolution. These settings enable users to find an appropriate balance to maximize scan effort to data ratio because of the labor-intensive nature of terrestrial laser scanning, especially in dynamic coastal areas (Olsen et al, 2009). Successful data collection was highly dependent on weather and tidal conditions. Negative low tides were an environmental requirement for most of our survey sections. The extended exposed beach width provided an adequate space with optimal distance from the cliff so the laser beam angle would reach the cliff tops.

Scanning efficiency (survey coverage area/time) was taken into consideration during survey planning and acquisition. Calibration surveys were completed in order to determine the optimal scanning parameters. Most scans in our surveys were done

on medium resolution and spaced 40-50 meters apart. High-resolution scans were performed along sections with large failures or other features of interest.

Georeferencing was conducted throughout our study using a Trimble Real-Time Kinematic GPS (RTK-GPS) system with a vertical and horizontal accuracy of +/-2 cm. Combined with the +/-5 cm resolution of the scanner, a resultant resolution of +/-7cm was achieved. GPS data recorded an X, Y, Z values with a measured offset above the origin of the laser scanner. A "backsighting" technique was used during surveys to increase the efficiency of inter-scan alignment. Control points (USACE survey markers) were measured and used for calibration to ensure quality and precision of point cloud data.

Post collection data processing and analysis was performed using ISITE software. Each scan was imported with the corresponding GPS data and aligned with neighboring scans within a region (Figure 7). Olsen et al. (2009) developed an alignment protocol and software to maximize horizontal and vertical matching of surface data.

Grain size analysis was performed on ten sediment samples (Table 2), from each formation (upper and lower), acquired at Sites A, B, C in Figure 8. Sand percentage was calculated using a Littoral Cutoff Diameter (LCD) limit of 125μm based on the grain size results of Haas (2005).

5.4 RESULTS

Use of the ground-based LiDAR has yielded quantitative estimates of cliff erosion and placed important constraints on the volume of sediment liberated by each geologic layer within the cliffs. Systematic mapping of the sea cliffs and calculated rates of erosion are critical to understand the importance of the sea cliffs as a sediment source to the beach. Furthermore, the LiDAR data are being used to calculate erosion rates from areas adjacent to new seawalls.

Twelve sea cliff failures in our study region were monitored since 2006 (Figure 1). Environment conditions varied and probable cause of each failure is listed in Table 1. These classifications are based on whether wave-runup, as described by Ruggerio (2001, 2008), reached the base of the cliff face or if there was local precipitation in the region near the time of the failure. The presence of groundwater was also used to determine the failure mechanism in select sites. If a potential triggering mechanism could not be observed, then a failure was deemed to have occurred from general instability. Due to the difficulty of accessing the beach and tidal constraints, not all failures in the study area were scanned on a regular basis and thus were not included in the analysis, particularly if they were relatively small volumes of sediment.

Wave undercutting was more prevalent during periods with extreme wave-runup from tidal conditions or large storm systems. Sites most impacted tended to have lower beach elevations and talus debris piles were quickly reworked (Figure 8). Subaerial failures were generally initiated along aquatards where increased sapping was documented (Figure 9) and often occurred after large precipitation events. Groundwater failure sites tend to be zones where the lithologic bedding plane is saturated along free surfaces where concentrated fluid flows toward the coast.

5.4.1 Cliff Failures by region

Encinitas

Failures in Encinitas, EN1 & EN2, initially occurred on June 6, 2007 and February 8th, 2007, respectively (Figure 10). At site EN1, a follow-up failure occurred on September 1, 2007 , and it was noted to be a retrogressive failure, presumably from the

instability created by over steepening after the first failure in June (Figure 10).

Del Mar

Two failures sites were documented in the Del Mar region during the summer of 2007 (Figure 11). 88 cubic meters of blocky sediment failed in a gully at DM1where there was significant groundwater sapping observed. DM2 was a smaller event, releasing only 28 cubic meters.

Torrey Pines State Park

A relatively small failure occurred in Torrey Pines State reserve on August 4th, 2007 when 31cubic meters dislocated from the Torrey sandstone formation (Figure 12). Site TP2 initially failed during our study on August 23rd, 2007 when 79 cubic meters was liberated from the cliff face (Figures 13 and 14). Additional failures occurred throughout the study period with a maximum mass failure occurring in September 2008, where 595 cubic meters eroded overnight. The talus pile on the beach was reworked relatively quickly as high tides and storm waves caused higher wave runup. After the initial failure, the instability propagated vertically upwards until the top of the cliff was recessed and a new profile established (Figure 14).

Failures initiated during periods of high precipitation occurred at sites TP4 and TP5 in October 2007 and January 2008, respectively. Storm events increased the groundwater flow and sapping was evident where the block-style cliff erosion occurred. TP4 liberated 168 cubic meters of sediments from the Torrey sandstone formation. Failure TP6 and TP7 (Figure 5) occurred in close proximity to one another near the northern extent of the park. TP6 initially released 77 cubic meters of sandstone to the beach below in June 2008 with an additional failure event placing 233 cubic meters on the beach. TP7 had a major failure during December 2008 with 678 cubic meters of

sediment from the Torrey Formation eroding off the cliff face. TP8 occurred on the northern side of a headland within the Torrey Pines State Park (Figure 12). This failure released 141 cubic meters of sediments and occurred on the north side of the headland discussed in regard to TP2.

Scripps

At Scripps beach, in September 2007, 30 cubic meters of material eroded and deposited a talus pile on top of an elevated rock platform (Figure 15). The sediments originated from the Scripps Formation and initiated near a zone of groundwater discharge.

Average cumulative frequency grain size distribution was determined for the formations in our study area (Figure 16) to determine the littoral sediment contribution. Sediment yields from each site are listed in Table 2, where sediments above the cuttoff diameter (125m) are assumed to remain on the beach and sediments below are transported offshore from wave energy.

5.5 DISCUSSION

The five-year, repetitive LiDAR study conducted in the Oceanside littoral cell produced high-resolution spatial data used for quantifying sea cliff erosion. This work provides insight into the short-term mechanisms that control cliff failures along a tectonically active coastline. The erosion patterns observed are controlled by the lithological composition of sedimentary units and the physical forces acting upon them. Subaerial and marine based erosion were both present along the entire study site; however, the degree to which each end-member played a role was highly dependent on the intrinsic character of the cliff face and local beach width and elevation. The next

section discusses the details each failure study site.

Encinitas

Two failures were investigated in Encinitas (Figure 10). Both of these failures nucleated within the Delmar Formation and were initiated by wave undercutting in zones that also were exhibiting heavy groundwater sapping at the time. The sea cliffs in this region of Encinitas are topped with high population density and development. Low intensity returns in LiDAR data and visual observation suggest that groundwater seepage is occurring regularly at numerous expulsion sites along the cliff face.

Del Mar

General instability from over-steepened cliff faces appears to have initiated the failures documented at Del Mar (Figure 11). An interesting note on this location is the presence of active train tracks directly above the failure site DM2 as shown in Figure 11. Whether the vibrations from train activity may have contributed to the cliff instability is unclear from this study. However, future work with seismic measurement devices along this beach area may help determine the amount of vibration in the cliffs from the train activity.

Torrey Pines

Failure TP1 occurred where over steepened slopes were present; however, no potential triggers were identified for this failure. TP2 was the site of numerous retrogressive failures (Figure 13) that were originally caused by wave undercutting at the base of the cliff (Figure 12). After the original bluff collapsed, the cliff face angle was over steepened and most likely retrogressive instability caused the following series of failures observed. Figure 14 shows the evolution of the nucleation point elevation migrating

upward through time. The pattern of beach erosion during the Winter 2008-09 confirms the talus from this failure did not remain on the beach long, but rather was reworked quickly by waves. Moreover, this site exists on part of a south facing natural headland created where relict, highly cemented lagoonal deposits from the Del Mar Formation intersect the beach because of the southward dip of the formation. These lithofied hard grounds are resistant to erosion and cause the cliffs to jut seaward with increased exposure to waves. A small failure at site TP3 occurred in September 2007 and was initiated by wave undercutting. The winter precipitation during the Winter 2007-08 may have initiated failures at TP4 and TP5, where the dislocation of 120 cubic meters occurred close to one another from the Torrey Formation (Figure 12). Failure sites, TP6 and TP7, appear to be the result of bioersoion from root swelling and general instability (Figure 5). Both failures occurred near the cliff tops where root material was burrowing through the sediment and are exposed on the cliff face. TP8 appears to be a result of general instability from over steepening of the cliff. Plant material (roots) exists above the failure zone. Furthermore, most material was liberated from the upper part of the cliff in the Torrey Formation (Figure 12) where a significant overhang was located prior to the failure event.

Scripps

The SC1 (Figure 15) failure occurred just below the Institute of Geophysics and Planetary Physics (IGPP) building where groundwater seepage is observed in the Scripps Formation. It appears the sapping zone, with concentrated groundwater discharge, is an aquatard developed along the lower lens of relict channel fill conglomerate. This stratigraphic low point likely focused the water transport causing the increased moisture to destabilize the cliff.

5.4.1 Local Controls on Cliff Erosion

Wave run-up

Rates of cliff erosion are highly dependent on the exposure to wave energy (Figure 2). The hydraulic pressure forces of compression, shear, and tension exerted by breaking waves is the most dominant erosive force for most sea cliffs (Sunamura, 1977). Abrasive forces from mobile sand and cobbles tend to scour the base of the cliffs and create smoothed notches (Figure 4) at the cliff base (Emery and Kuhn, 1980). Pneumatic pressure from trapped air forced in weakened substrate also contributes to significant erosion in these environments (Woodruffe, 2002). The dynamic regime set up by wave energy is complex and is highly dependent on the angle of exposure in relation to incident wave angle, wave height and tidal conditions. Erosional conditions exist only when the total water level (TWL), the sum of the tides and the vertical height of wave run-up, is above beach elevation (Ruggiero et al., 2001). This condition exists most often during the Northern Hemisphere winter season when the beach sands are shifted seaward to an offshore bar (Guza and Thornton, 1981) and wave energy often reaches the base of the cliffs during high tidal events (Collins and Sitar, 2008).

The wave climate within the Oceanside Littoral Cell is highly variable and seasonally dependent on three dominant conditions: the Northern Hemisphere swell, the Southern Hemisphere swell and local wind-driven swell. Northern swell tends to impact local coastal regions in southern California during the Fall and Winter months (Benumof et al., 2000). Due to the directional nature of the wave energy, the impacts on cliff erosion are directly dependent on the angle of exposure (Sunamura, 1977).

Strength & Lithology

Two main lithological units make up the cliffs in the OCL. Fine grain clays and muds with numerous sand layers and cross-bedding make up much of the basal Del Mar

Formation that is exposed along the northern study sites (Figure 1). The negatively charged ionic nature of the clay tends to exhibit fissility, due to the pressure from gravitational forces, and erosion occurs as platy blocks crumble into talus piles typically during shifts in wet-dry cyclical conditions. The other dominant lithology is sandstone in the Torrey Formation, which exhibits high permeability and is highly susceptible to erosion when over saturated. Cliff failures occurring in sandstone may erode in large block detachments, slumps or slides depending on the erosional processes and sediment composition. The sandstones also exhibit a honeycomb erosional character due to the interplay of wind, meteoric waters, and salts (e.g., Figure 8c).

Overall strength of semi-consolidated cliffs may also be reduced from local seismicity. Seismic events in the OCL have been limited in magnitude and frequency by distance to the active zones of the San Andreas and San Jacinto faults, however there are several faults (e.g. Elsinore, Rose Canyon) in closer proximity exhibiting less intense seismic activity in modern geologic history. Nonetheless, several large failure events from central and northern California have been attributed to earthquake activity (Keefer, 2002; Collins and Sitar, 2011), and the OCL is susceptible to considerable seismicity.

Permeability & Aquatards

Slope stability is highly dependent on the permeability structure of the stratigraphic units (Jones et al., 1993; Komar and Shih, 1993). For example, when porous sandstone is overlain on less permeable claystone, an aquatard may develop at the boundary (Figure 9). Southern California cliffs exhibit this type of composite layering, predominantly with permeable sandstone layers intercalated with less permeable mudstones. If an aquatard develops at these boundary layers, it focuses drainage to the free surface. Groundwater moves orthogonal to the free surface and, particularly in this region, discharges groundwater toward the coast, where sapping occurs on the cliff

face. Pore pressure in the sediments is controlled by overburden and permeability (Fei and Ugai, 2004), which also can contribute to the instability of cliff systems. For this reason, subaerial cliff erosion is considerably more active during episodes of increased precipitation (Collins & Sitar, 2008) as the increased weight of the sediment and sapping increases pressure and destabilizes the sediment matrix along aquatards.

Thermal expansion & Contraction

Due to the semi-arid environment of southern California, the temperature ranges fluctuate significantly on daily and seasonal cycles. Clay-rich sediments are most vulnerable to changes in temperature, especially from the montmorillonite/smectite group (Mitchell, 1976). As sediments get wet/dry and hot/cold, expansion and contraction may increase the tendency for instability. The positive charge of the water molecules reacts with the negative charge of the platy clay to change the pore space dynamics. This dynamic causes platy/blocky erosion patterns, mainly in the lagoonal deposits of the Del Mar Formation (Kennedy, 1975).

Salt precipitation & Wind Erosion

Exposure to the salted sea spray also contributes to the weathering patterns of OLC sea cliffs. Patterns of honeycombing are dominant in sandstones, in direct contact with salt laden air, then blasted by wind (Turkington, 1998). An example of this erosion pattern is imaged in Figure 5, where daily wind, salt spray and occasional meteoric discharge have sculpted complex tafoni in the sandstone of the Torrey Formation. On the leeward side of the same sedimentological unit that is exposed at a road cut, the dominant pattern of subaerial erosion is rilling, rather than honeycombing.

Human induced

Over 80% of human populations live within 30 miles of the coast. As population density increases along the coastline, so does the development of utilities and infrastructure. In one region of our study, Solana Beach, the cliffs are approximately 90% armored with human engineered structures (Figure 18). Additionally, human development has increased the groundwater supply, which naturally drains seaward due to local elevation and the free surface. Aquatards made of less-permeable clay-rich sediments funnel groundwater toward the coast. Sapping on the cliff face occurs year-round from heavy irrigation practices of local communities (Figure 9). This unnatural introduction of groundwater to a semi-arid system increases the pore pressure of sediments causing instability and may accelerate the erosion processes (Griggs and Patsch, 2004).

5.4.2 Styles of Erosion

Subaerial Erosion

Weathering of sediments from above the waterline is a common form of erosion in Southern California due to the semi-consolidated paleo-sedimentary deposits. Erosion is activated by various processes including wind, precipitation, bioerosion, and mass-wasting (Figure 2). Cliff retreat from subaerial processes can be gradual in step fashion, as seen with TP2 (Figure 13) or event-driven as seen with DM1 (Figure 11). Benumof (2000) suggests that lithology is a more important control on cliff erosion than the wave climate in California. However, certain climatological conditions such as increased storminess also may cause higher rates of cliff erosion (Storlazzi and Griggs, 2000). Jointing and faulting is observed in the cliffs such as in southern Torrey Pines and Solana Beach and provides nucleation sites for increased cliff erosion.

Marine Erosion

Oceanographic conditions, such as swell direction and amplitude, play an important role in the stability of sea cliffs, but unfortunately the ability to model or quantify the direct impact of these conditions is limited because of lack of current in-situ data. Offshore buoys have been used to model wave-runup conditions, but due to the complexity of the bathymetry associated with the canyons in the coastal zone of southern California, these models do not accurately represent actual wave runup along the beach and cliffs (Raymond 2010). Offshore topography and coastal headlands refract wave energy (Inman and Frautschy, 1966; Guza and Thompson, 1981) complicating the resultant conditions reaching and acting on the coast. In addition, the beach elevation in southern California exhibits seasonal inflation and deflation, (Figure 19) both based on the precursor wave climate and also where offshore sand bodies are positioned. During boreal winter, Northern Hemisphere swells dominate, keeping the sand bars in deeper waters. During the summer, the Southern Hemisphere swells transport sand to shallower depths attaching a sand bar to land, inflating the regional beach elevations. This landward shift of additional sand onshore provides increased protection for the cliffs from marine erosion. Moreover, the summer wave energy is lower and thus is typically less erosive than winter swells (Inman and Jenkins, 1991). If the actual wave runup exceeds the beach elevation, the base of the cliff is exposed to the hydraulic energy of the waves and then the sediment resistance to erosion controls the rate of basal notching (Figure 4).

Jointing and Faulting

Southern California is historically a tectonically active region (Le Dantec et al., 2010). Antecedent jointing and faulting is pervasive within the OLC and trends in a northeast oblique pattern along the coast (Figure 18). Joints are zones of weakness in the

seacliffs that are more vulnerable to attack by waves and create permeability pathways for groundwater discharge. Once established, the erosion is exacerbated by wave funneling and focused hydraulic action creating caves (Trenhaile, 1987). Hydrostatic pressure is exerted on the base of the cliffs causing cavitation and pneumatic forcing that can abrade rock surfaces. The increased hydraulic energy also allows the water to entrain cobbles and sand size grains that cause mechanical erosion within the undercut structures. Eventually, the weight and pressure of the overhang creates instability with lack of support and large angular blocks may fail. Jointing angles are fundamentally important in shaping the regional coastline. Abundant low angle (nearly parallel to the beach) faulting exists in San Diego.

5.5.1 Feedback

Beach elevation was shown to play a major role in the dominant style of erosion at a particular site (Figure 8). Lower elevations allow wave energy to reach the base of the cliffs and actively erode semi-consolidated sediments (Figure 4). In addition, the beach elevation controlled the rate of sediment reworking once a failure was emplaced on the beach. Failure sites, such as TP2, that were initiated by wave undercutting, exhibit a lower beach elevation and over steepened cliff profile. Over time, the instability created from the initial failure, migrates upward along the cliff face and causes subsequent retrogressive failure events (Figures 13 and 14). After the cliff has experienced a failure, the rugosity is reduced (Figure 5) and the profile exhibits a nearly vertical slope angle, essentially “resetting” the stability until wave action reaches the cliff toe and undercuts the base.

A feedback cycle exists between the amount of sediment eroded and the beach sand levels. As sediment from the cliffs adds to the volume of material on the beach, it may provide additional buffering from the wave energy. Beaches backed by cliffs with

consistent talus piles at their base (e.g., Site A, B; Figure 8.) also exhibited higher average beach elevations and the cliffs in these areas were dominated by subaerial erosion rather than marine erosion. Conversely, narrow beaches with lower elevations (e.g., Site C; Figure 8) were dominated by wave-cut erosion and consistently had notching at the base of the cliff, unless armoring was present.

Regions that are dominated by jointing and faulting focus the groundwater drainage and create sections (e.g., Southern Torrey, Solana Beach) with distinct serration patterns along the coastline (Figure 18). Wave erosion is enhanced in these locations because the cliff-face angles become more oblique and exposed to directional swell wave energy. In addition, the persistent groundwater drainage along the zones of weakness increase the upslope erosion and large block failures tend to exist at these locations.

Results from grain size analysis shown in Figure 16 and Table 2 reveal the contribution of cliff material to the littoral cell. Using techniques described in Hapke 2009 and Young 2010, we set a range of grain size that would likely remain on the beach based on existing sediments and energy conditions. According to our analysis, approximately 75% of eroded sediments from the cliffs should be retained on the beach. While higher energy conditions, such as northern winter swells, may be effective at removing the sand from the beach (Figure 13 and 14), the sand size grains probably remain in the littoral cell and are recycled as beach sand within the system during favorable conditions, such as the boreal summer.

5.6 CONCLUSIONS

Our study area is dominated by two modes of cliff erosion: wave-undercutting and subaerial weathering (Figures 5 and 6, Table 2). These two end-members play an important role in controlling how the seacliffs contribute sediments to

the OCL, while the composition of the cliffs (grain size) is a factor in whether the failed material will remain on the beach. This research, along with current findings by others (Haas, 2005; Young, 2006), illustrates the significance of these geological features for coastal resource management.

Subaerial weathering is the predominant style of erosion in areas where the beaches are wider and tend to dominate in the southern portion of our study area. Our results are consistent with previous research on grain size (Haas, 2005) analysis revealing that the cliffs are contributing significant amount of sand to the beaches, particularly in the southern study area where the highest sea cliffs occur (Figure 17). The sandstone-rich formations that make up the upper portion of much of the Oceanside littoral cell's composite sea cliffs, provide an abundant source of sand to the local beaches and this, in turn, creates an elevated beach platform (Figure 16, Table 2). The increase in topological structure acts as a physical barrier against the energetic erosive nature of waves. Moreover, the addition of sand to the beach acts as nourishment to moderate the effect of seasonal inflation and deflation (Figure 19). Profiles of the bluffs in sections that are controlled mainly by subaerial processes tend to exhibit a more relaxed angle as the sediments move toward the angle of repose (Figure 17). This angle is dependent on the grain size and structure, but intrinsic sediment strength characteristics may vary based on the level of cementation and lithology.

Sea cliffs in the study area that are dominated by wave-cut dynamics tend to back narrower beaches with lower elevations and have more hard grounds (basement rock) exposed (Figure 17). These regions are also zones where development and human population density are higher, although it is difficult to assess directly how anthropomorphic factors affect erosion rates. Human development leads to increased irrigation and runoff, causing year-round groundwater sapping along aquatards (Figure 9) that may only have a seasonal signal in undisturbed settings. The increased erosion

in these highly developed sections has lead to artificial alteration to the cliff face and armoring may also decrease the natural sediment supply to the beaches, therefore it is unclear whether armoring is a reasonable method for protecting the coast. The lack of sediment to the system allows deflation of the beach elevation that bottoms out when basement rock is exposed. Areas with the highest percentage of seawalls have the narrowest and lowest elevation beaches (Figure 17). An erosional feedback loop initiates and increases the amount of wave energy reaching the base of the cliffs, which subsequently increases marine-based cliff erosion.

Jointing and faulting are intrinsic elements of the tectonically active region of southern California. These geological features are present throughout the study area (Figure 18) and play a key role in the shape of the coastline. Sawtooth shaped patterns exist where there are abundant fault and/or jointing structures exposed at the coast, which in turn, modifies the angle of exposure to wave energy of the sea cliffs. The dominant NNW trending oblique angle of the fault structures controls the angle of exposure of the weakened substrate to the wave climate. Exposure is mainly toward the south and is impacted more by the Southern Hemisphere swells generated during the boreal summer.

High-resolution terrestrial LiDAR is an effective tool to quantify volumes of sediment eroded from sea cliffs. These techniques also provide valuable modeling information in order to understand the mechanisms forcing erosive patterns along a geologically complex and variable coastline. Longer-term studies are needed to measure quantitatively change through climatological oscillations to gain insight on how Southern California sea cliffs will be impacted by sea-level rise, ENSO and PDO cycles.

Sediments liberated from the OCL sea cliffs are an important source for beach sand supply, especially considering the modern rate of sea level rise (>3 mm/yr; IPCC, 2007; Pfeffer et al., 2008; Rahmstorf, 2007) and increased erosion along southern California's coastline. It is imperative to consider the significant contribution of a

natural source of sand when making decisions regarding coastal management, especially as southern California enters a drier climatic cycle and sediment input from fluvial systems is likely to be further reduced. At the same time, our understanding of the beach sand budget and the relative importance of the different sources are evolving (Haas, 2005). Longer time series data are required to adequately document impacts from climate change and population increase (coastal development) in the OCL. Our research provides valuable information regarding the processes that control the different styles of cliff erosion in Southern California and a baseline from which future change can be evaluated.

5.7 ACKNOWLEDGEMENTS

Funding for this research was through a grant from the California Sea Grant Program. We also would like to thank Gary Samad for his helpful updates .

5.8 REFERENCES

Benumof, B.T., Griggs, G.B., 1999. The dependence of seacliff erosion rates on cliff material properties and physical processes: San Diego County, California. Shore and Beach 67 (4), 29–41.

Benumof, B. T., C. D. Storlazzi, R. J. Seymour, and G. B. Griggs (2000), The relationship between incident wave energy and seacliff erosion rates: San Diego County, California, J Coastal Res, *16*(4), 1162-1178.

Brownlie, W.R., and Taylor, B.D., 1981, Sediment management for southern California mountains, coastal plains and shoreline; Part C, Coastal sediment delivery by major rivers in southern California: Pasadena, California Institute of Technology, Environmental Quality Laboratory Report 17-C, 314 p.

Change, I P O C. (2007). Climate change 2007: The physical science basis. Agenda, 6, 07.

Collins, B. D., and N. Sitar (2008), Processes of coastal bluff erosion in weakly lithified sands, Pacifica, California, USA, *Geomorphology*, *97*(3-4), 483-501.

Collins, B. D., and N. Sitar (2011), Stability of Steep Slopes in Cemented Sands, *J Geotech Geoenviron*, *137*(1), 43-51.

Emery, K. O., and G. G. Kuhn (1980), Erosion of Rock Shores at La-Jolla, California, *Mar Geol*, *37*(3-4), 197-208.

Fei, C., and K. Ugai (2004), Numerical Analysis of Rainfall Effects on Slope Stability, *International Journal of Geomechanics*, *4*(2), 69-78.

Griggs, G. B., and K. Patsch (2004), Cliff erosion and bluff retreat along the California coast - Coast of California caught between increasing numbers of people and ongoing process of shoreline retreat, *Sea Technol*, *45*(9), 36-40.

Guza, R. T., and E. B. Thornton (1981), Wave Set-up on a Natural Beach, *J Geophys Res-Oc Atm*, *86*(Nc5), 4133-4137.

Hapke, C. J., D. Reid, and B. Richmond (2009), Rates and Trends of Coastal Change in California and the Regional Behavior of the Beach and Cliff System, *J Coastal Res*, *25*(3), 603-615.

Haas, J.K., 2005. Grain Size and Mineralogical Characteristics of Beach Sand in the Oceanside Littoral Cell: Implications of Sediment Provenance. San Diego, California: University of California, San Diego, Master's thesis, 41p.

Higgins, R. W., K. C. Mo, and Y. Yao (1998), Interannual variability of the US summer precipitation regime with emphasis on the southwestern monsoon, *Journal of Climate*, *11*(10), 2582-2606.

Inman, D.L. and Frautschy, J.D., 1966. Littoral processes and the development of shorelines. Proceedings Coastal Engineering Specialty Conference, American Society of Civil Engineers, pp. 511–536.

Inman, D. L., and S. A. Jenkins (1999), Climate change and the episodicity of sediment flux of small California rivers, *J Geol*, *107*(3), 251-270.

Jones, J. R., B. Cameron, and J. J. Fisher (1993), Analysis of Cliff Retreat and Shoreline Erosion - Thompson Island, Massachusetts, USA, *J Coastal Res*, *9*(1), 87-96.

Keefer, D. K. (2002), Investigating landslides caused by earthquakes - A historical review, *Surv Geophys*, *23*(6), 473-510.

Kennedy, M.P., 1975.Geology of the SanDiego metropolitan area,western area. California Division of Mines and Geology Bulletin, 200, 56p.

Kennedy, M.P. and Tan, S.S., 2007. Geologic map of the Oceanside 309 3 609 quadrangle, California, California Department of Conservation, Division of Mines and Geology, scale 1:100,000, 1 plate.

Kern, J. P. (1977), Origin and History of Upper Pleistocene Marine Terraces, San Diego, California, *Geol Soc Am Bull*, *88*(11), 1553-1566.

Komar, P. D., and S. M. Shih (1993), Cliff Erosion Along the Oregon Coast - a Tectonic-Sea Level Imprint Plus Local Controls by Beach Processes, *J Coastal Res*, *9*(3), 747-765.

Kuhn, G.G. and Shepard, F.P., 1984. Sea Cliffs, Beaches, and Coastal Valleys of San Diego County: Some Amazing Histories and Some Horrifying Implications. Berkeley, California: University of California Press, 193p.

Le Dantec, L., G. Cardinet, J. Bonet, M. Fouche, K. Boudehri, A. Monfort, J. L. Poessel, A. Moing, and E. Dirlewanger (2010), Development and mapping of peach candidate genes involved in fruit quality and their transferability and potential use in other Rosaceae species, *Tree Genet Genomes*, *6*(6), 995-1012.

Mitchell, J K. (1976). Fundamentals of soil behavior.

Olsen, M. J., E. Johnstone, N. Driscoll, S. A. Ashford, and F. Kuester (2009), Terrestrial Laser Scanning of Extended Cliff Sections in Dynamic Environments: Parameter Analysis, *J Surv Eng-Asce*, *135*(4), 161-169.

Olsen, M. J., E. Johnstone, F. Kuester, N. Driscoll, and S. A. Ashford (2011), New Automated Point-Cloud Alignment for Ground-Based Light Detection and Ranging Data of Long Coastal Sections, *J Surv Eng-Asce*, *137*(1), 14-25.

Pfeffer, W. T., J. T. Harper, and S. O'Neel (2008), Kinematic constraints on glacier contributions to 21st-century sea-level rise, *Science*, *321*(5894), 1340-1343.

Rahmstorf, S. (2007), Response to comments on "A semi-empirical approach to projecting future sea-level rise", *Science*, *317*(5846).

Raymond, J. H., 2010. New Constraints on the Processes that Control Cliff Erosion and Sediment Dispersal Using Ground-Based LIDAR. San Diego, California: University of California, San Diego, Master's thesis, 73p.

Ruggiero, P., P. D. Komar, W. G. McDougal, J. J. Marra, and R. A. Beach (2001), Wave runup, extreme water levels and the erosion of properties backing beaches, *J Coastal Res*, *17*(2), 407-419.

Runyan, K., and G. B. Griggs (2003), The effects of armoring seacliffs on the natural sand supply to the beaches of California, *J Coastal Res*, *19*(2), 336-347.

Storlazzi, C. D., and G. B. Griggs (2000), Influence of El Nino-Southern Oscillation (ENSO) events on the evolution of central California's shoreline, *Geol Soc Am Bull*, *112*(2), 236-249.

Sunamura, T. (1977), Relationship between Wave-Induced Cliff Erosion and Erosive Force of Waves, *J Geol*, *85*(5), 613-618.

Trenhaile, A S. The geomorphology of rock coasts. (1987).

Turkington, A. V. (1998), Cavernous weathering in sandstone: lessons to be learned from natural exposure, *Q J Eng Geol*, *31*, 375-383.

Warrick, J. A., and J. D. Milliman (2003), Hyperpycnal sediment discharge from semiarid southern California rivers: Implications for coastal sediment budgets, *Geology*, *31*(9), 781-784.

Warrick, J. A., and D. M. Rubin (2007), Suspended-sediment rating curve response to urbanization and wildfire, Santa Ana River, California, *J Geophys Res-Earth*, *112*(F2).

Willis, C. M., and G. B. Griggs (2003), Reductions in fluvial sediment discharge by coastal dams in California and implications for beach sustainability, *J Geol*, *111*(2), 167-182.

Young, A. P., R. E. Flick, R. Gutierrez, and R. T. Guza (2009), Comparison of short-term seacliff retreat measurement methods in Del Mar, California, *Geomorphology*, *112*(3-4), 318-323.

Young, A. P., J. H. Raymond, J. Sorenson, E. A. Johnstone, N. W. Driscoll, R. E. Flick, and R. T. Guza (2010a), Coarse Sediment Yields from Seacliff Erosion in the Oceanside Littoral Cell, *J Coastal Res*, *26*(3), 580-585.

Young, A. P., M. J. Olsen, N. Driscoll, R. E. Flick, R. Gutierrez, R. T. Guza, E. Johnstone, and F. Kuester (2010b), Comparison of Airborne and Terrestrial Lidar Estimates of Seacliff Erosion in Southern California, *Photogramm Eng Rem S*, *76*(4), 421-427.

Young, A.P. and Ashford, S.A., 2006a. Application of airborne LIDAR for seacliff volumetric change and beach-sediment budget contri- butions. Journal of Coastal Research, 22(2), 307–318.

Table 1. Large failures occurring between 2007 and 2010 within the study region.

X	Y	Geologic Unit	Location	Failure Mecahnism	Failure Date	First Survey	Failure Volume (m^3)
472340	3655625	DM	EN1a	Undercutting/ Groundwater	6/6/07	6/7/07	139
472340	3655625	TS	EN1b	Retrogressive Failure	9/1/07	9/10/07	30
472315	3655718	DM	EN2	Undercutting/ Groundwater	Feb-08	3/7/08	177
475776	3642506	TS	TP1a	General Instablity	8/4/07	8/6/07	31
475842	3641779	TS	TP2a	Wave undercutting	8/23/07	8/24/07	79
475842	3641779	TS	TP2b	Wave undercutting	2/10/08	2/17/08	50
475842	3641779	TS	TP2c	Wave undercutting	9/22/08	9/23/08	445
475957	3641547	TS	TP3	Wave undercutting	9/30/07	10/5/07	28
475767	3642888	TS	TP4	Precipitation	10/20/07	10/29/07	168
475776	3642320	TS	TP5	Precipitation	1/28/08	1/31/08	120
475768	3642677	TS	TP6a	General Instablity/ Roots	6/16/08	6/18/08	77
475768	3642677	TS	TP6b	General Instablity/ Roots	9/2/09	9/4/09	335
475764	3642676	TS	TP7	General Instablity/ Roots	Dec-08	12/26/08	678
475832	3641794	TS	TP8	General Instablity/ Roots	8/15/09	8/17/09	141
475134	3645947	DM	DM1	Groundwater	8/21/07	8/28/07	88
474973	3646577	DM	DM2	General Instablity	Summer 2007	8/28/07	24
476266	3636734	SF	SIO1	Groundwater	9/2/07	9/12/07	30

Marine Eroison

Subaerial Eroison

Table 2. Summary of the cliff sediment yield (m3) and littoral sediment yield (m3) using an LCD of 125 µm for each the upper and lower geological units as well as alluvium.

Site	Qcliff Lower	% LCD Lower	Qsand Lower	Qcliff Upper	% LCD Upper	Qsand Upper	Cliff Sediment Yield	Littoral Sediment Yield
A	1,073.0	59.0	**633.1**	1,096.0	91.0	**997.4**	2,169.0	**1,630.5**
B	625.0	86.0	**537.5**	272.0	92.0	**250.2**	897.0	**787.7**
C	925.0	32.0	**296.0**	706.0	73.0	**515.4**	1,631.0	**811.4**
Total	2,623.0		**1,466.6**	2,074.0		**1,763.0**	4,697.0	**3,229.6**

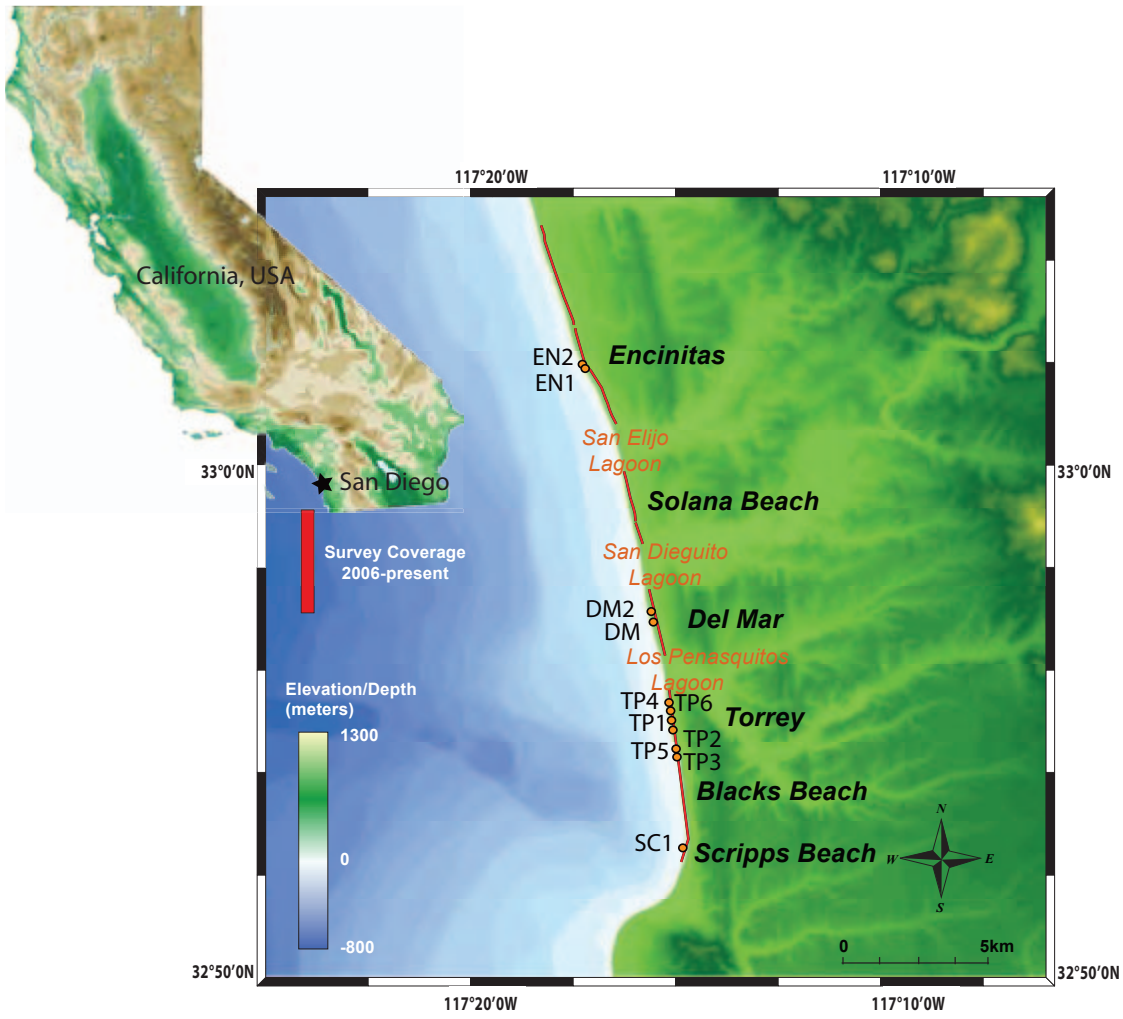

Figure 5-1: Location map of LiDAR study sites in the Oceanside Littoral Cell, southern California and select failure sites are labeled (orange circles) where repeat rapid response and seasonal surveys (red lines) were conducted.

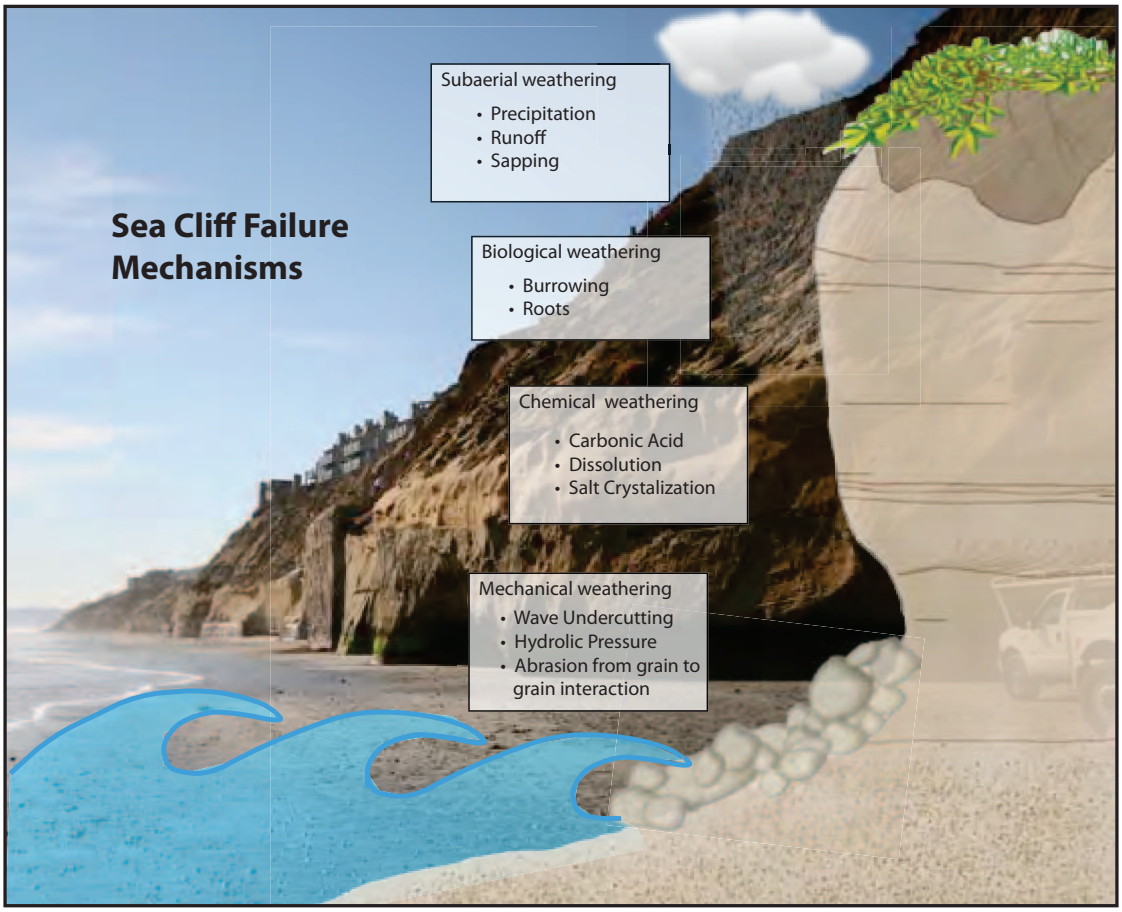

Figure 5-2: Schematic illustrating the dominant mechanisms and associated forcing functions controlling sea cliff erosion.

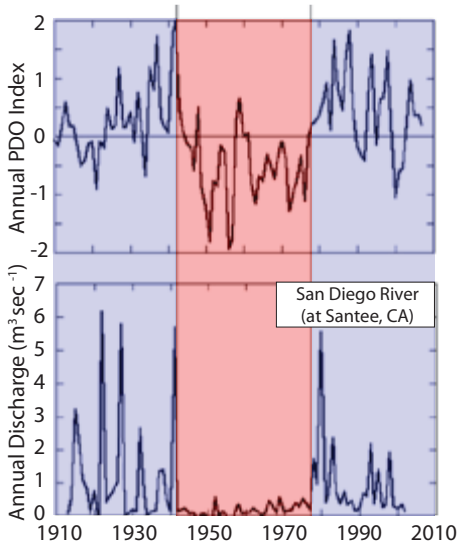

Figure 5-3: Annual Discharge for the San Diego River shown in relationship to the annual PDO index. This correlation suggests that high discharge in Southern California rivers predominantly occurs in El Nino years with a positive PDO index (modified from Milliman et al., 2008). Areas shaded in blue are positive PDO and areas in red are negative PDO.

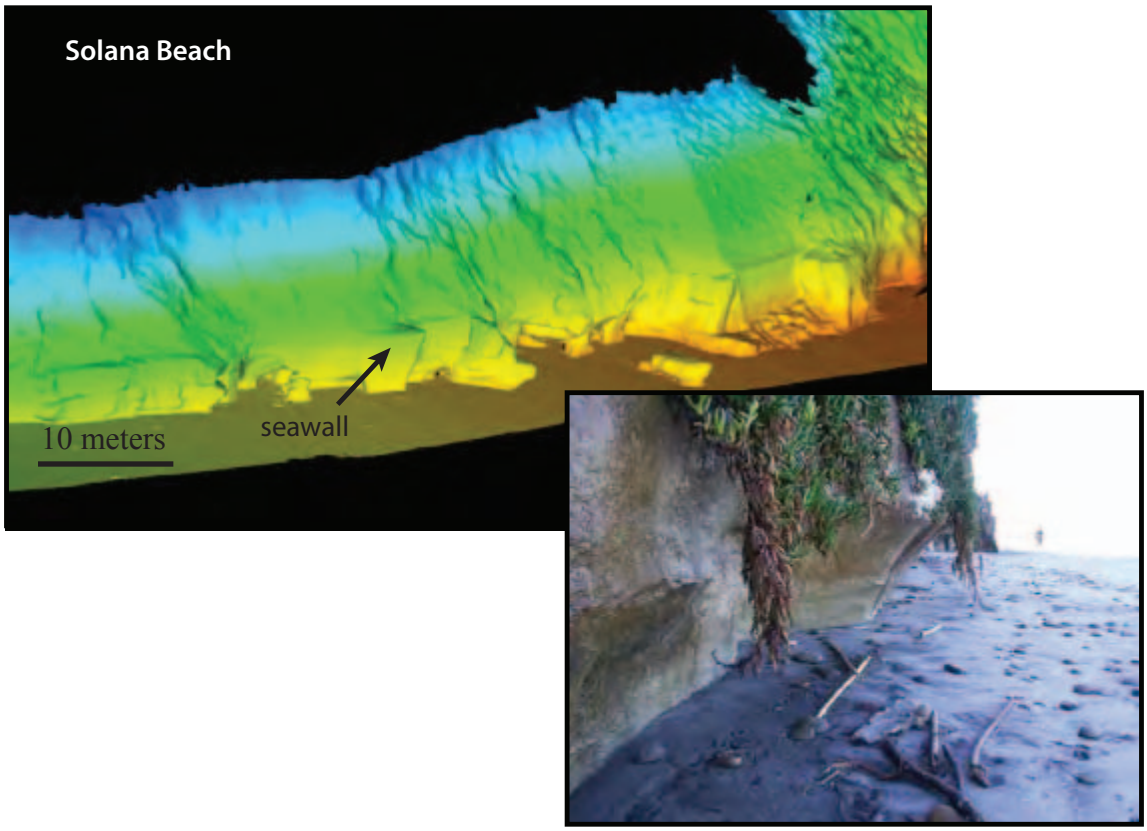

Figure 5-4: a) Three-dimensional LiDAR model of seacliffs in Solana Beach imaging the wave-cut notching at base of cliffs. b) lower image is close-up photograph of wave-cut notching in this region. Note cobbles on beach that act as tools to enhance erosion rates.

Figure 5-5: A) Topographic triangulation of northern Torrey Pines study region. Survey was conducted on 11/13/2008 and images the pre-failure sites TP6 and TP7. B) Topographic triangulation of northern Torrey Pines study region. Survey was conducted on 05/13/2009 and images the post-failure sites TP6 and TP7. C) Gridded surface of TP6 before the cliff failure (cell size 0.04m). D) Gridded surface of TP6 after the cliff failure (cell size 0.04m). E) Gridded surface of TP7 before the cliff failure (cell size 0.04m). F) Gridded surface of TP7 after the cliff failure (cell size 0.04m). Root mean square values are indication of surface roughness. Note the surface roughness decreases on failure surfaces.

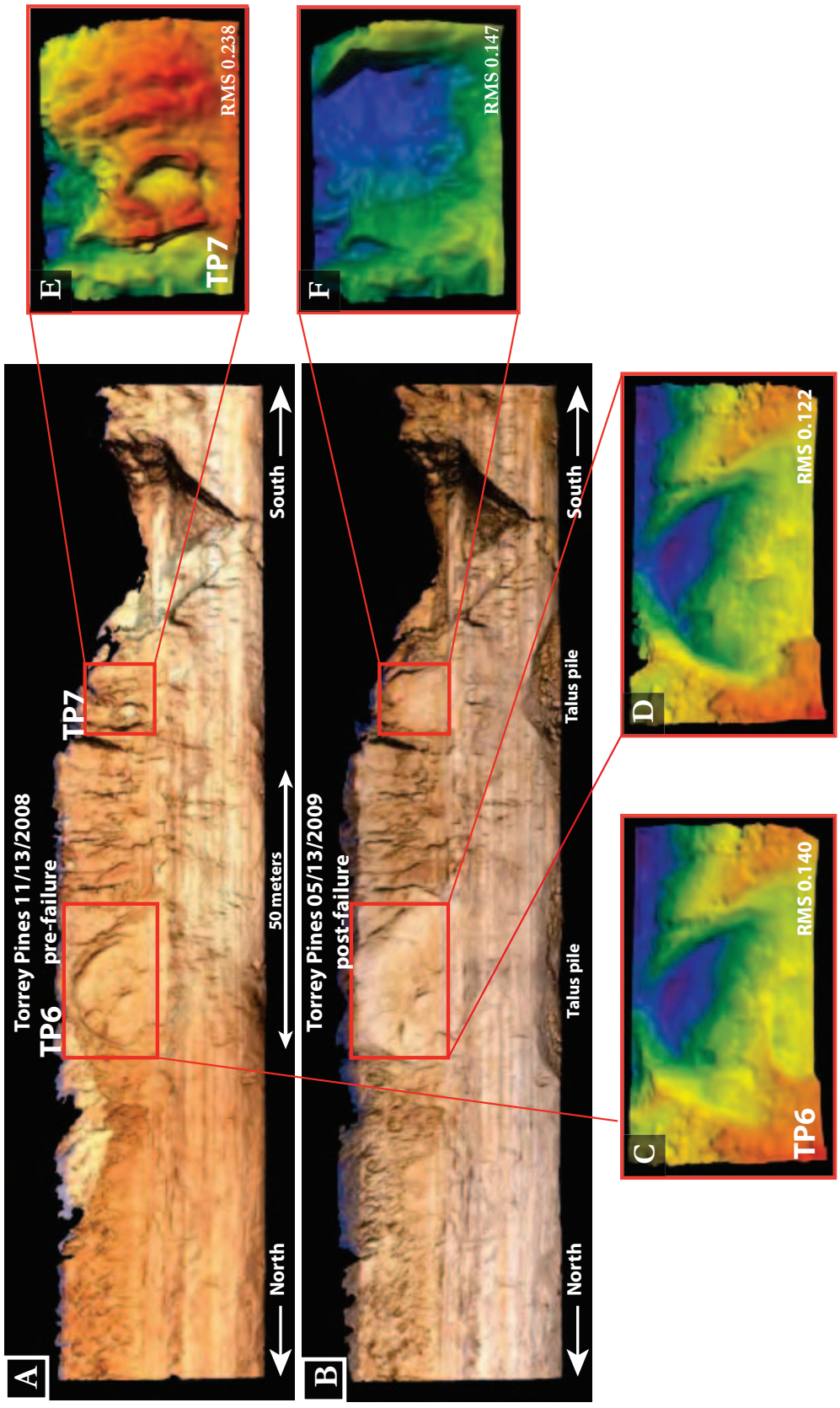
A
Torrey Pines 11/13/2008
pre-failure
TP6
TP7
South
50 meters
North
B
Torrey Pines 05/13/2009
post-failure
Talus pile
Talus pile
South
North
C
RMS 0.140
TP6
D
RMS 0.122
E
RMS 0.238
TP7
F
RMS 0.147

Figure 5-6: Image of I-Site 4400 terrestrial scanner field setup with diagram of laser pulse function and head rotation. Scanner emits infrared wavelength laser pulses (905nm) that radiate in a 360 degree rotational scan field with a vertical look angle of 80 degrees. The signal is returned and distance is calculated based on time of return. Data clouds are georeferenced based on the real-time kinematic (RTK) GPS survey origin of the receiver.

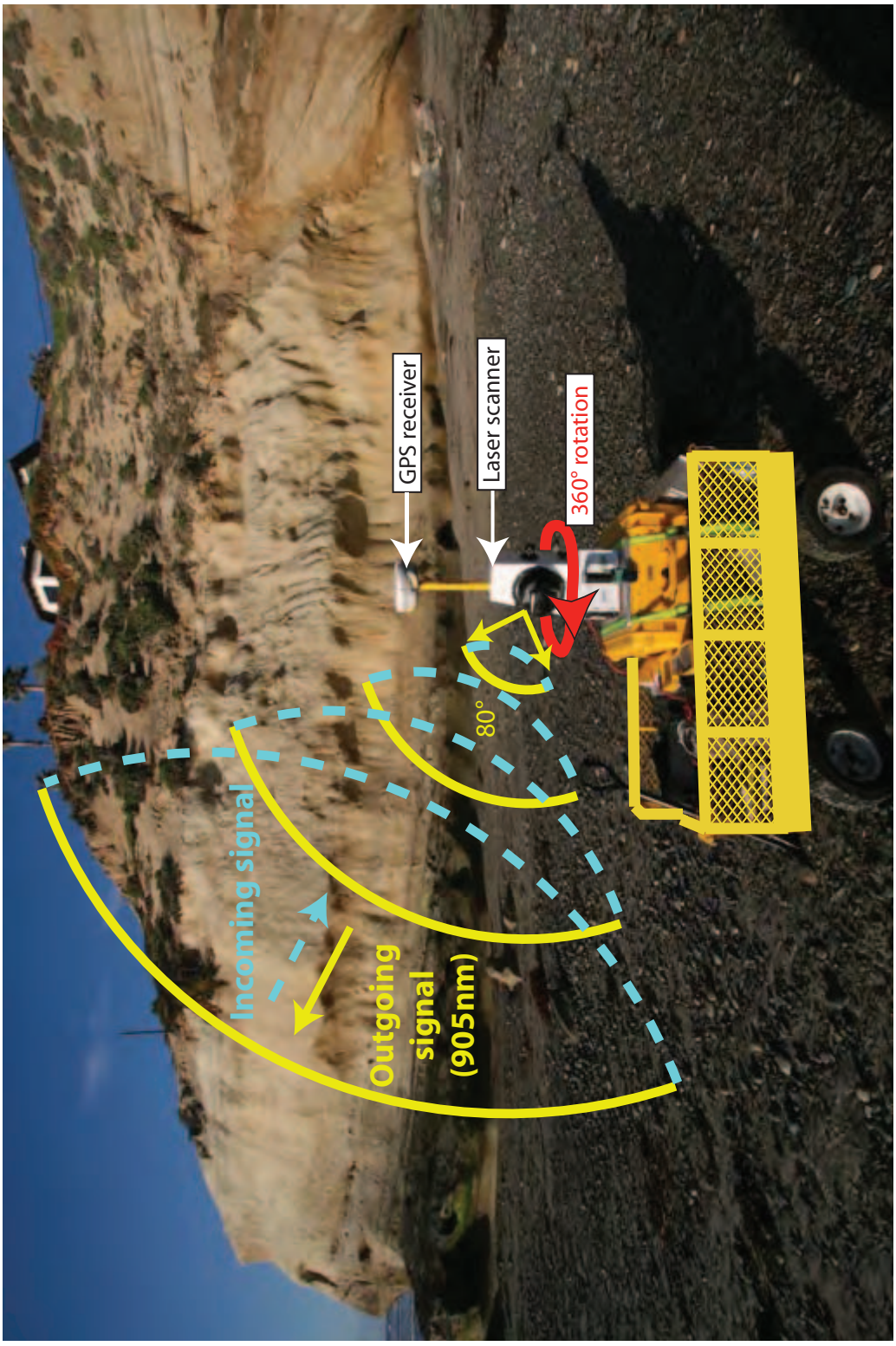
GPS receiver
Laser scanner
360° rotation
80°
Incoming signal
Outgoing signal (905nm)

Figure 5-7: Georeferenced point cloud data (approximately 50million points) of Torrey Pines study area. Semi-circles on beach represent the scan origins with approximately 40 meters spacing.E) Gridded surface of TP7 before the cliff failure (cell size 0.04m). F) Gridded surface of TP7 after the cliff failure (cell size 0.04m). Root mean square values are indication of surface roughness. Note: values decrease on failure surface sites.

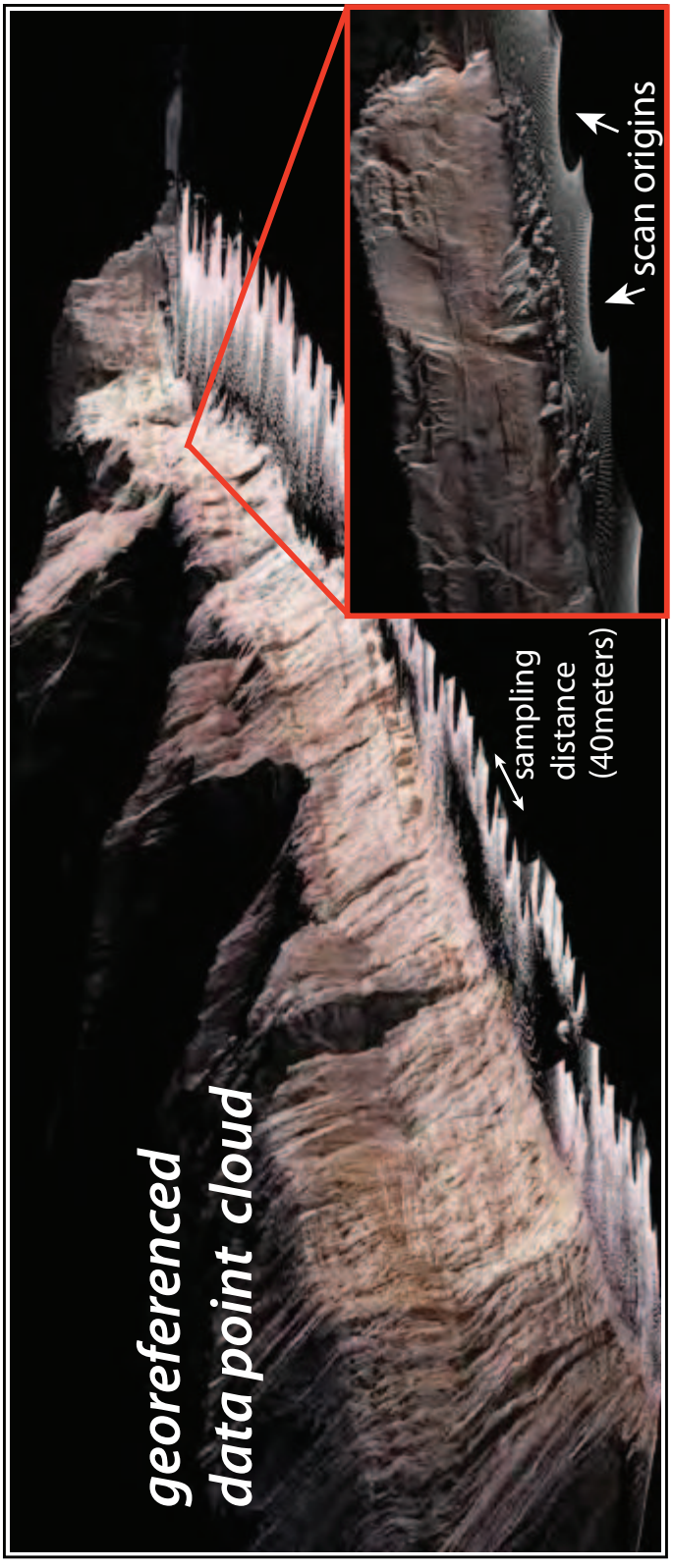
georeferenced
data point cloud
sampling
distance
(40meters)
scan origins

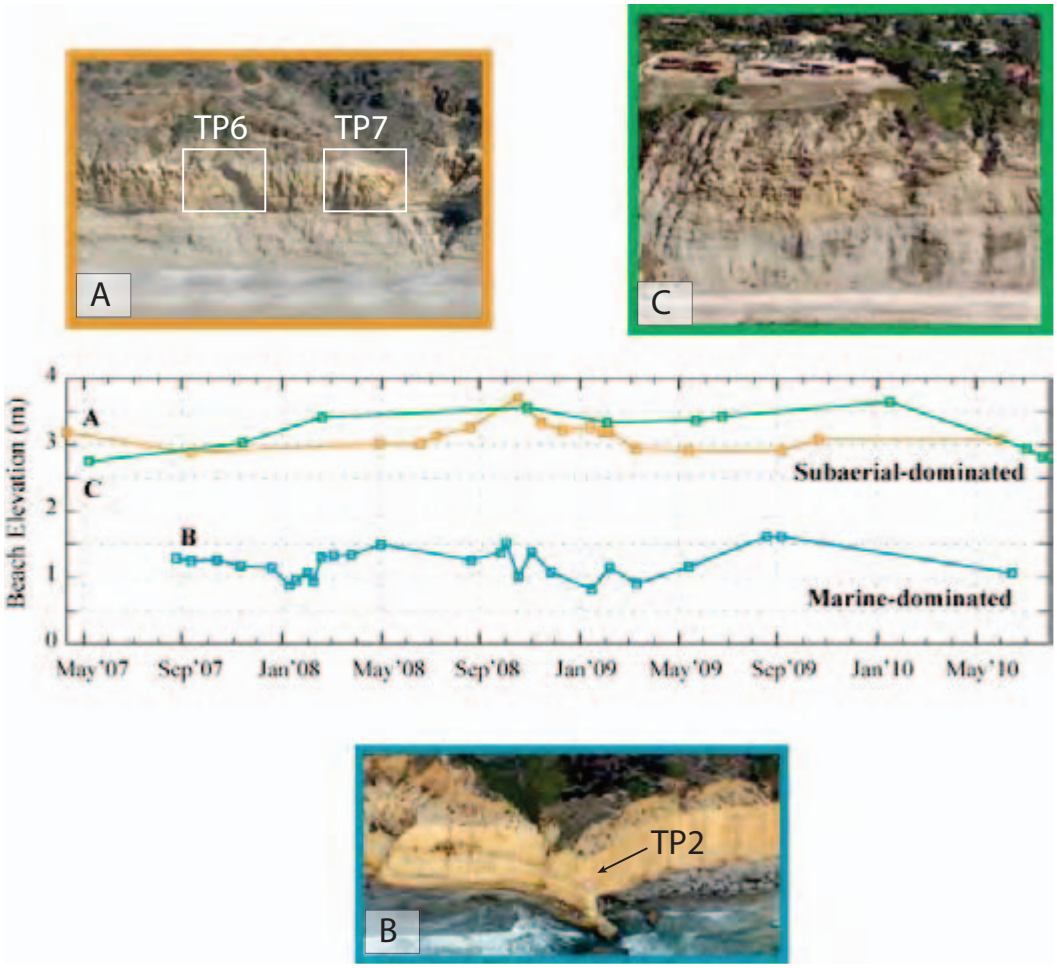

Figure 5-8: Images of three failure sites (A, B, C) within the study area and graphical representation of beach elevations at each site over time. Site A is the location of failures TP6 and TP7. Site B is located just south of the "Flat Rock" in Torrey Pines State Park where failure TP2 occurred. Site C is located just north of the Blacks beach ramp.

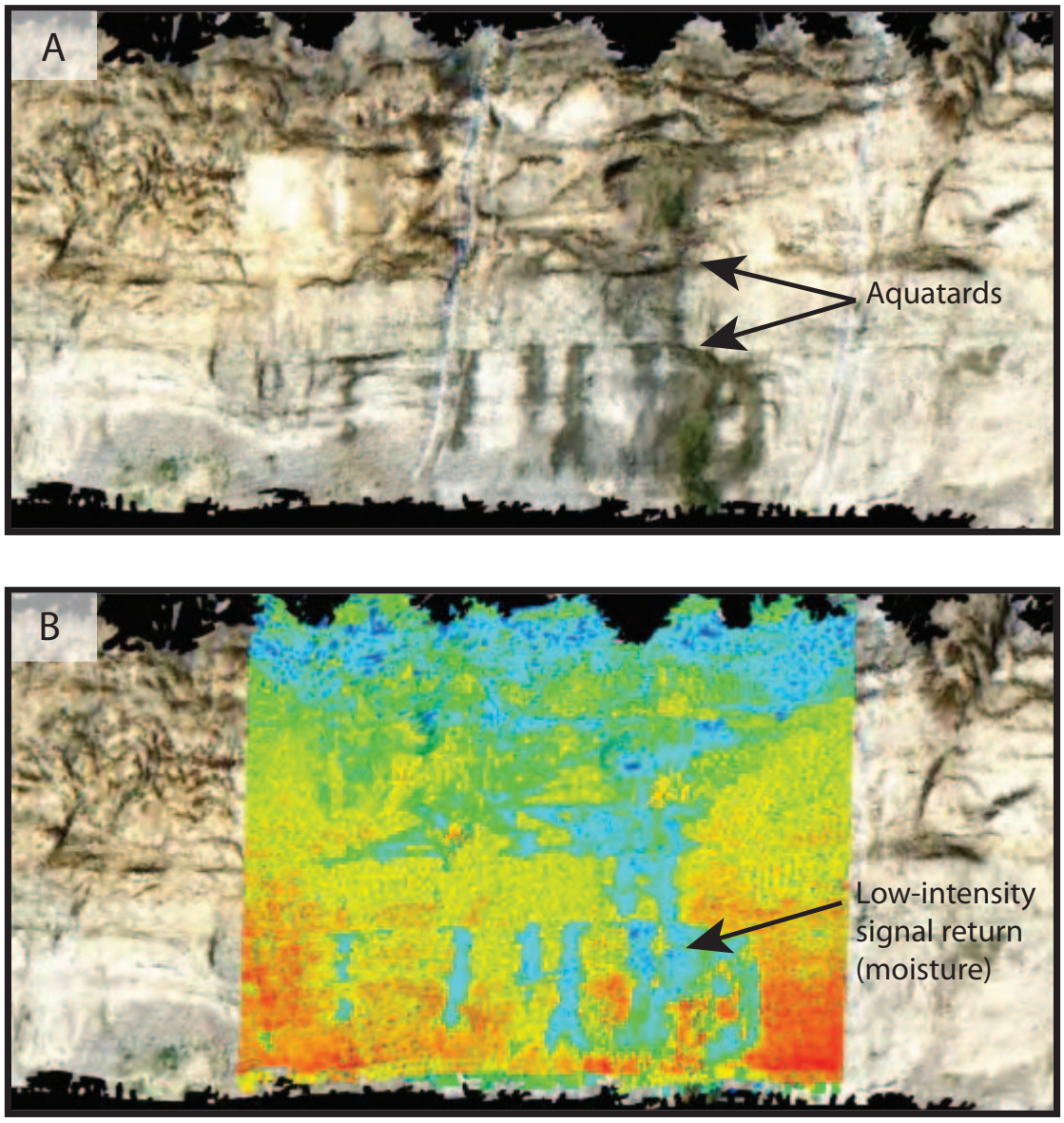

Figure 5-9: A) LiDAR scan model of Blacks Beach with points colored in photographic color data (RGB) values. B) Intensity return values draped on surface of same region. Note the red color indicates high signal return and blue color indicates lower return signals.

Figure 5-10: Photographs of cliff failures surveyed using Terrestrial Laser Scanning in Encinitas.

Figure 5-11: Photographs of cliff failures surveyed using Terrestrial Laser Scanning in Del Mar.

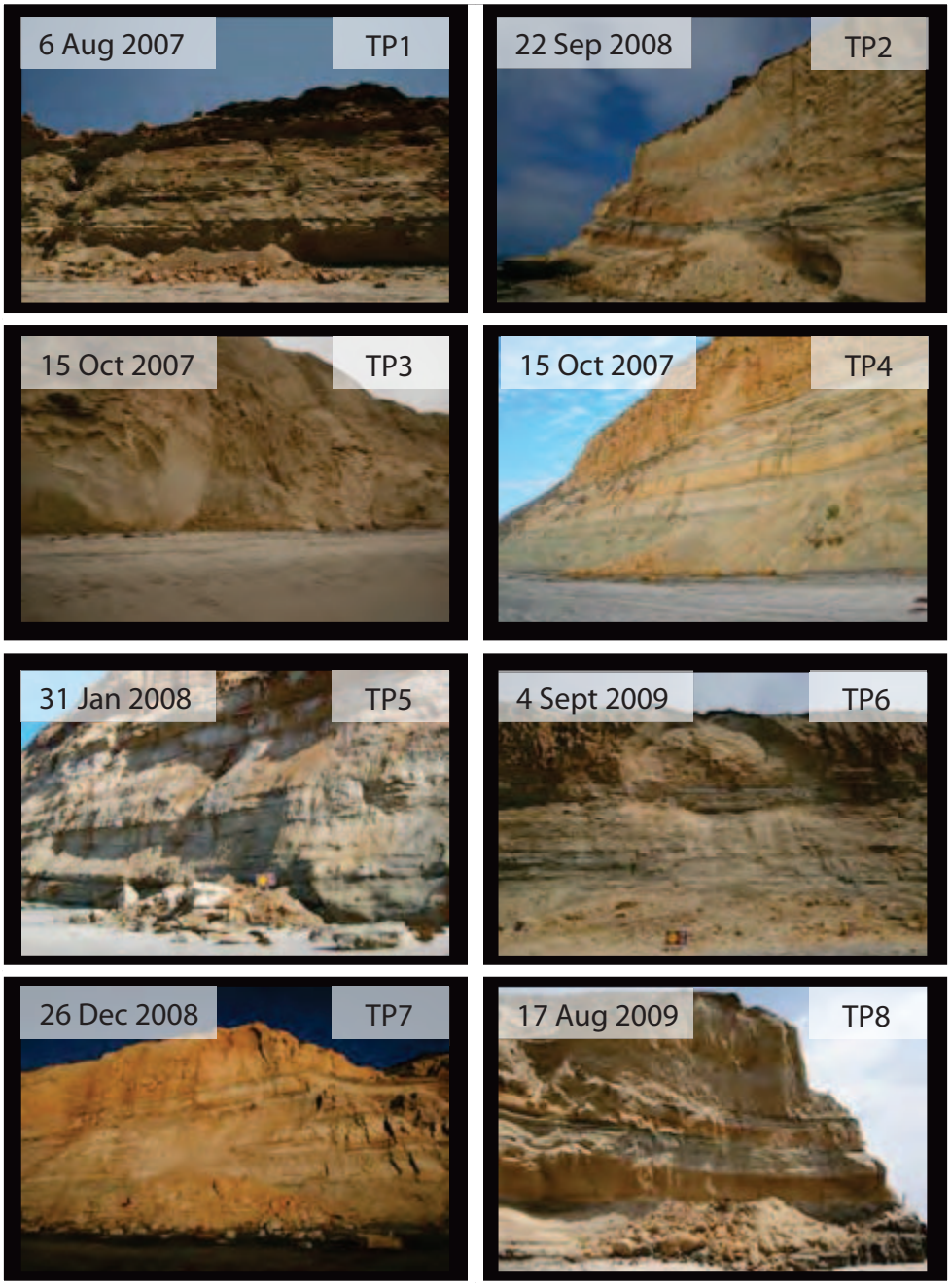

Figure 5-12: Photographs of cliff failures surveyed using Terrestrial Laser Scanning in Torrey Pines State Park.

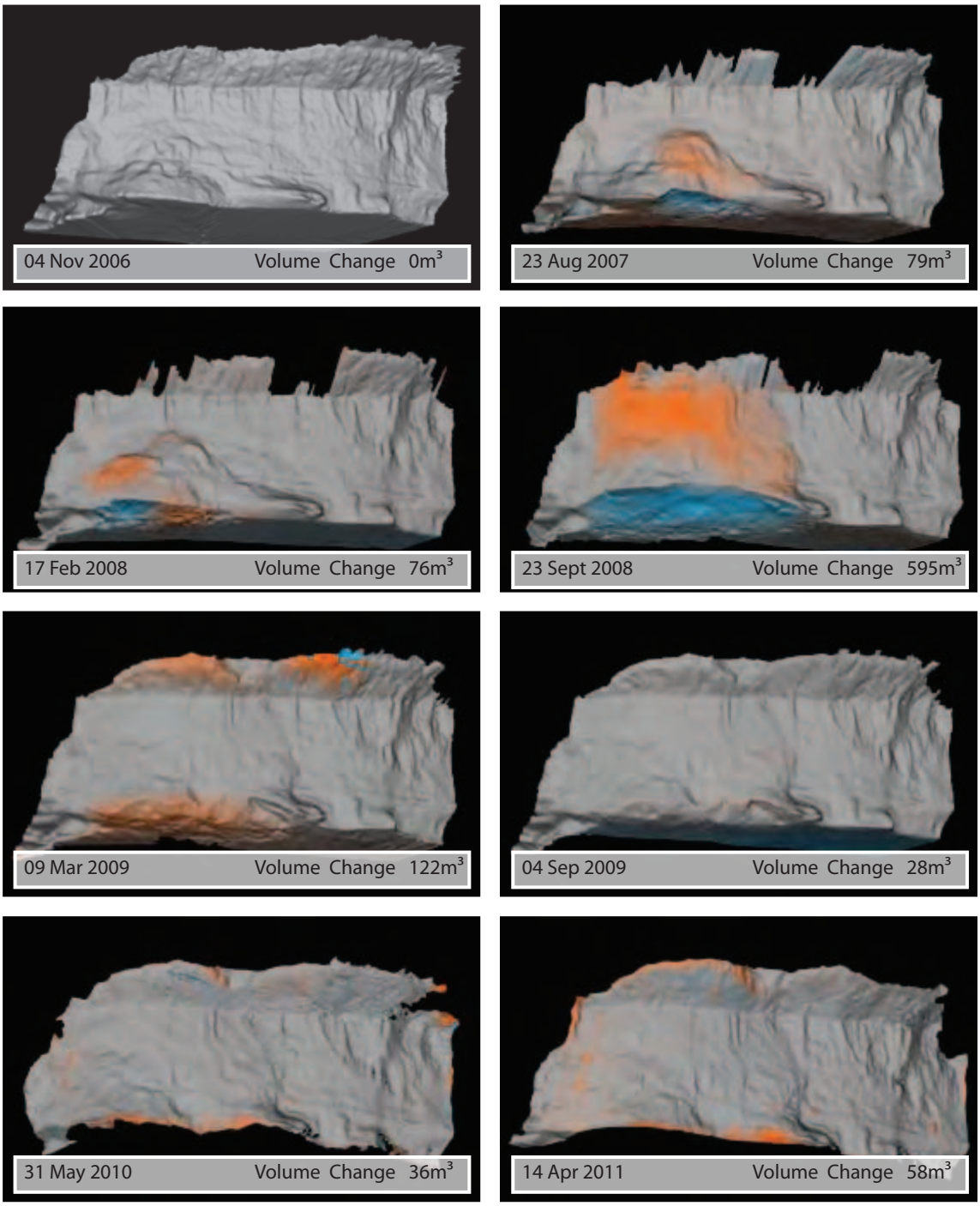

Figure 5-13: Time-series evolution of cliff failure site TP2 imaged in three-dimensional LiDAR models. Lower bar of each image shows date of survey and calculated volume change since last survey. Erosion is depicted in orange shading and accretion in blue. Areas in gray have no change.

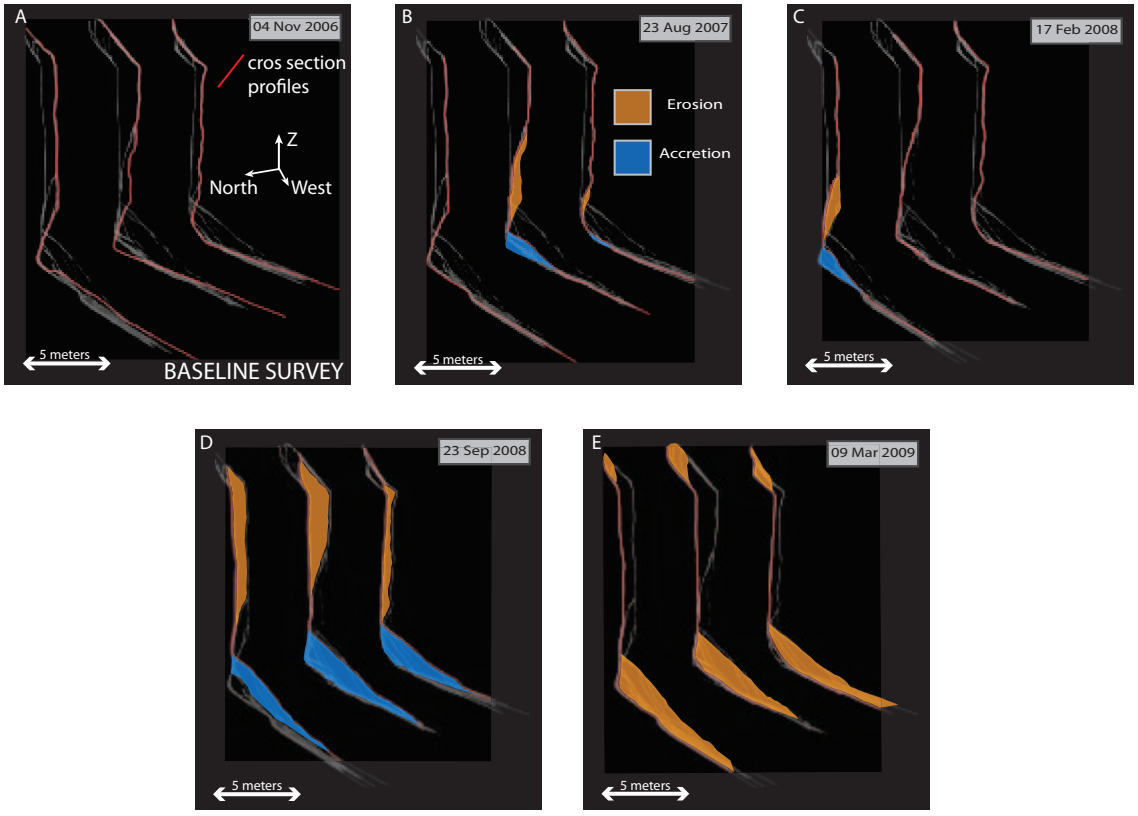

Figure 5-14: Series of cross section profiles of selected adjacent surveys (A-E) at Site TP2 illustrating the evolution of the cliff morphology. Subsequent surveys acquired post collapse events imaged with zones of erosion shown in orange and accretion in blue. Note the large talus from Sept 2008 failure was eroded by winter wave action.

Figure 5-15: Photographs of cliff failures surveyed using Terrestrial Laser Scanning at Scripps Beach.

Figure 5-16: Average cumulative frequency grain size distribution plot for each geological formation in the study area. A littoral cutoff diameter (LCD) of 125 μm (3 Φ) was selected to compare the differences in the contribution of sand from each formation to the littoral sediment budget. The "littoral window" (shaded in gray) denotes the weight percentages of sand above the LCD observed for each geological formation.

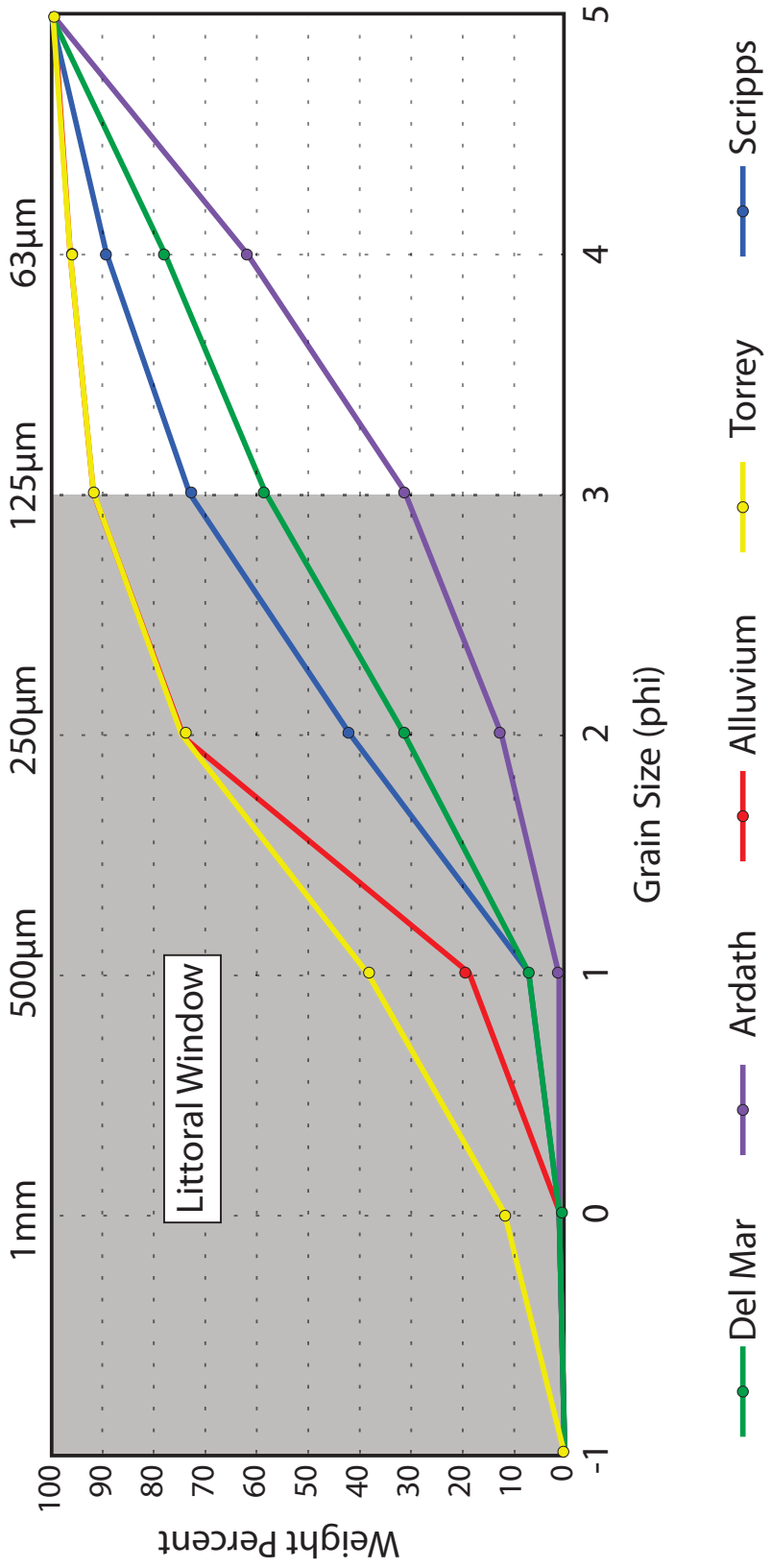
Weight Percent
100
90
80
70
60
50
40
30
20
10
0
1mm
500µm
250µm
125µm
63µm
-1
0
1
2
3
4
5
Grain Size (phi)
Littoral Window
Del Mar
Ardath
Alluvium
Torrey
Scripps

Figure 5-17: Aerial LiDAR digital elevation model of Blacks Beach (top) and Solana Beach (bottom) from 2009. Above 3m is in grayscale and the beach (0-4meter elevation) is shown in color. Red line indicates the location of the 2-D profile for above beach elevation and black line indicates location of 2D profile for beach. Note the vertical and horizontal scale is different for the beach and land profiles.

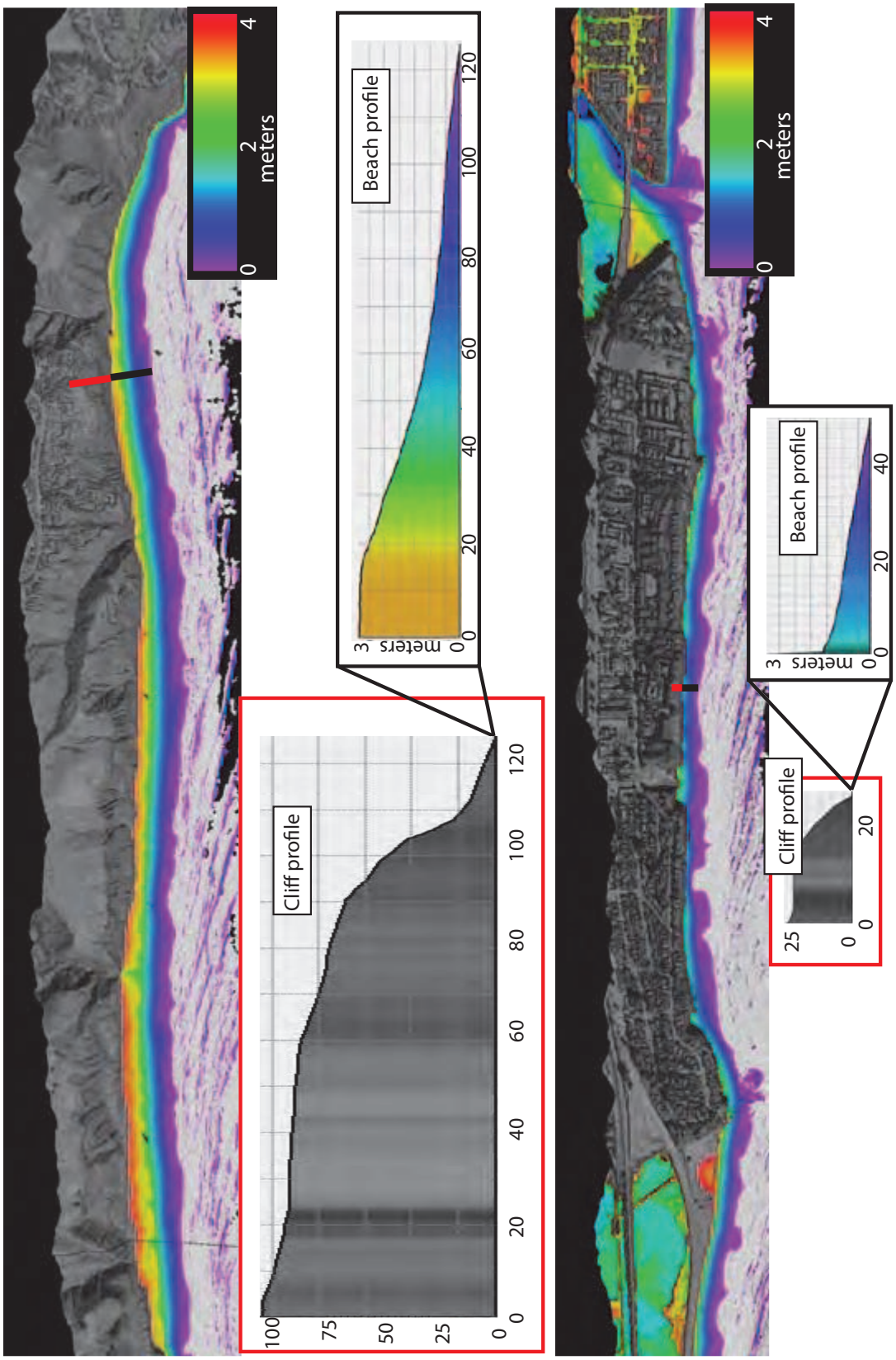
4
2
meters
0
Beach profile
meters
0
20
40
60
80
100
120
Cliff profile
100
75
50
25
0
0
20
40
60
80
100
120
4
2
meters
0
Beach profile
meters
0
20
40
Cliff profile
25
0
0
20

Figure 5-18: A) Merged aerial photographs of sea cliffs in southern Solana Beach taken in 2008 (source: www.californiacoastline.org). Note waves are reaching the base of cliffs and extensive undercutting/ notching is present. B) Aerial LiDAR gridded data of same region acquired in October 2009 (source: http:// www.csc.noaa.gov/digitalcoast/data/coastallidar) with base of cliff digitized in white and visible faults/ joints shown in dashed red lines. C) Photograph of fault controlled cave from region indicated with black lines in Figure 13B. D) Photograph of fault controlled cave from region indicated with black lines in Figure 13B. Note the upper range of cave opening coincides with location of faults.

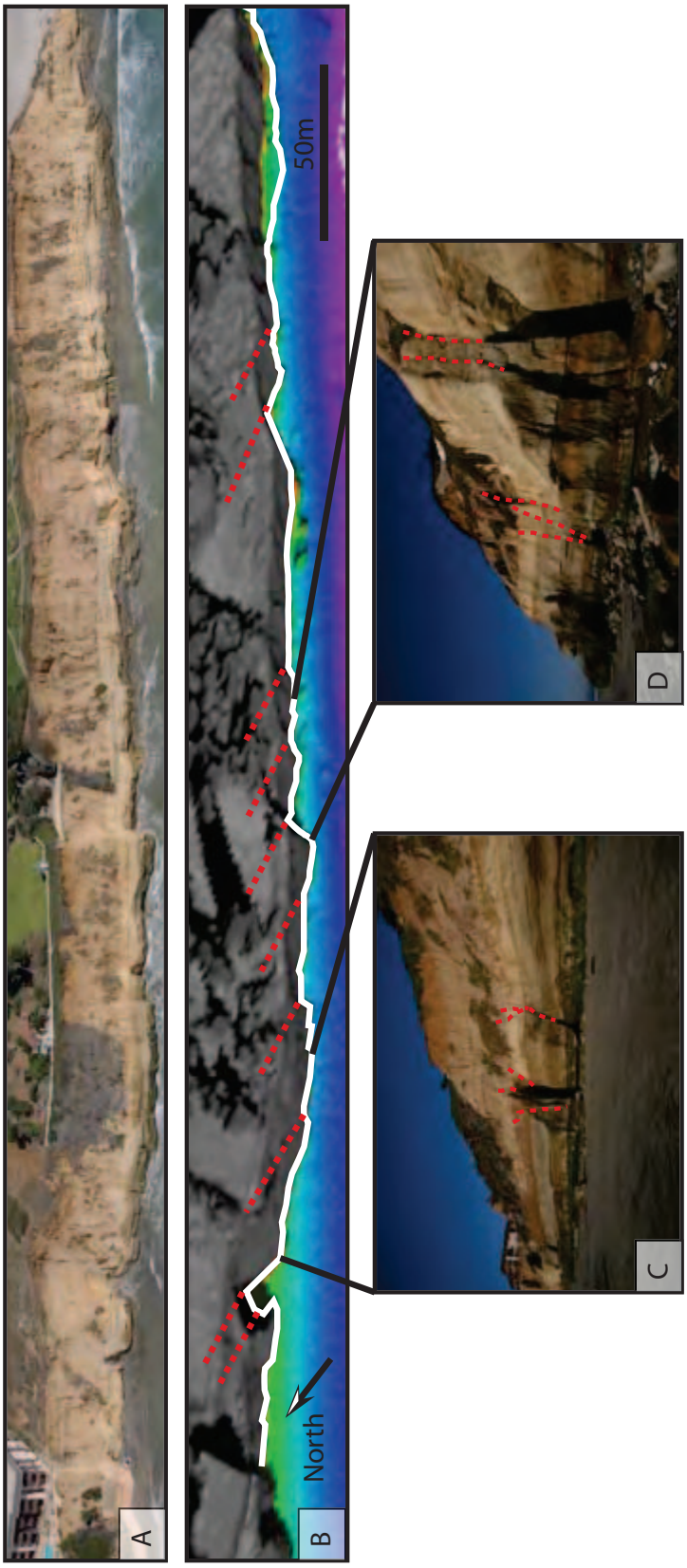
A
B
C
D
50m
North

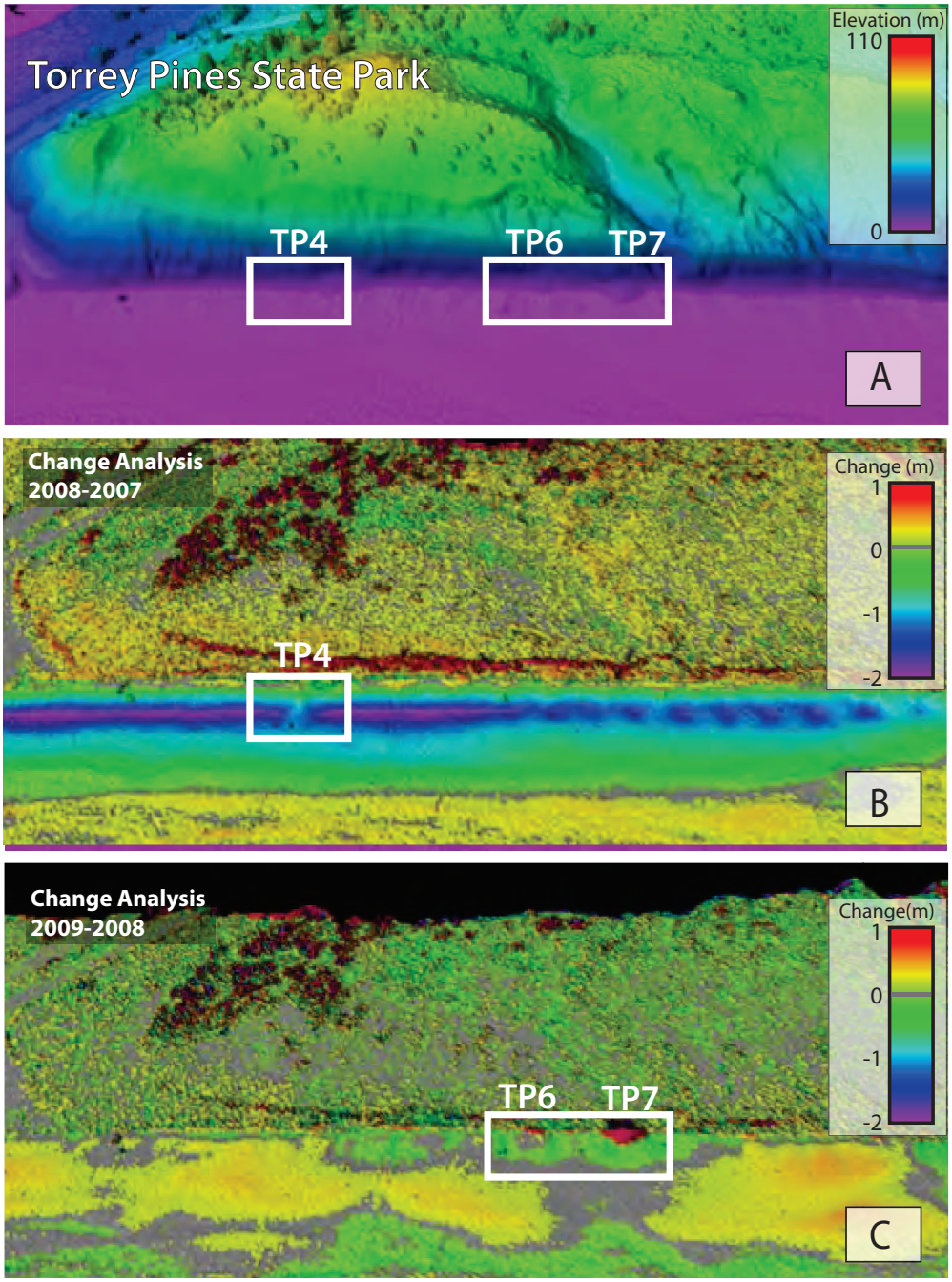

Figure 5-19: A) Aerial LiDAR DEM of north end of Torrey Pines State Park with white box indicating location of large cliff failures. B) Change analysis map of the region between Aerial LiDAR survey in April 2008 and March 2007. Note winter seasonal deflation of beach elevation, except where major cliff failure occured and significant sand was added to the beach material. C) Change analysis map of the region between Aerial LiDAR survey in March 2009 and April 2008. Note where major cliff failure occured significant sand was added to the beach material.

6

CONCLUSIONS

6.1 CONCLUSIONS

This thesis presents research that was conducted to improve our understanding about sediment dispersal systems near continental margins. Geophysical tools were used to acquire significant quantities of interpretable digital data in order to gain insight regarding erosion and deposition of sediments. Sediment acquisition techniques were undertaken to groundtruth datasets and provide lithological and time constraints on observed units. Each preceding chapter presents new data collected by our geological research group at Scripps Institution of Oceanography. The overarching goal of these studies was to improve the state of knowledge in two end-member sediment systems using methods that are repeatable and may be used to understand other similar environments on Earth. The following paragraphs will highlight the major scientific accomplishments of this research.

High-sedimentation rates make the Gulf of Papua (GoP) and ideal location to study the sediment deposition patterns on the continental shelf. As part of the NSF-funded Source-to-Sink (S2S) program, our group studied the subsurface architecture of the mid-shelf clinoform system. By acquiring extensive, high-resolution sub-bottom data, we revealed the presence of three main sediment “lobes” extending from the southern region off the Fly River, to the northern extent near the Purari River. Because these lobes are draining geologically different sediment provenances, the sediment signals were varied in chemical element character. These variations allowed us to distinguish the source of sediment downward through sampled sediment cores, while selected sections were dated with Carbon-14 techniques. The combined effort of interpreting geophysical data with geological sampling and sediment analysis provided evidence that told the story of the modern evolution of this shelf. Our work was complemented by various other research efforts in the adjacent environments from the terrestrial down to the deep sea. This multidisciplinary undertaking revealed how sediments move from source to sink,

with our research making a significant contribution on discovering the Holocene sediment dispersal patterns of a large percentage of the sediments in the system. This research also provided further evidence that supports the modern idea of clinoforms build in complex, three-dimensional patterns that are dependent on the tectonic regime, sediment supply and sea level. Sediment deposition patterns and chemical composition also provide us with scientific clues about the paleoclimate in order to understand the oscillations of Earth's climate and how it affects sediment distribution.

We discovered three main lobes (Southern, Central and Northern) on the mid-shelf in the GoP. The moribound Central lobe is onlapped by the two younger lobes to the north and south. Using seismic imaging and sedimentological chemical analysis to investigate the modern clinoform, we ascertained the modern evolutionary sequence to the sediment deposition in the GoP. The northern Purari River (Type II system) drained the high-relief mountainous region of Papua New Guinea feeding the Central lobe during the mid-Holocene. We postulate during this time, to the south, the Fly River system was depositing its load onshore in the expansive, low gradient coastal plain of the Type I watershed. In the late Holocene a shift in deposition occurred. The northern Purari River sediments abruptly migrated north. What caused these abrupt shifts in deposition isn't fully understood, but we suggest the changes in ITCZ patterns may have altered ocean current conditions. The southern Fly River infilled the onshore accommodation and delivered sediment offshore to form the Southern lobe.

The second study site was the coastal region along the Oceanside Littoral Cell (OCL), in southern California. Beaches backed by steep sea cliffs characterize this coastal environment, and unlike the GoP, this area is sediment starved. Significant development exists along the cliff tops within the study, with the exception of Torrey Pines State Park. Our group established an ongoing time series study of the cliffs beginning in 2006 using terrestrial LiDAR. We acquired high-resolution data of the

terrain in order to create topographic models. The models were then compared to one another to quantify erosion along the cliffs. Our research highlighted the mechanisms that control the erosion patterns and investigated how the sediment was dispersed post collapse. There are two main styles of erosion: subaerial and marine-based. Vulnerability to erosion may also be increased in regions where faulting and jointing exist along the cliff face introducing structural weakness. We also discovered the reworking of the sediments is highly dependent on the beach elevation. Since this physical attribute changes seasonally with alternating wave conditions, the amount of reworking is particularly acute at sites with narrow beaches and lower elevations at the boundary between cliff and the beach. Wave run-up is the controlling factor in dispersing unconsolidated sediments that have been liberated from the cliffs. Therefore, the lower elevation beaches tend to be narrow and exhibited mainly marine-dominated erosion. Subaerial erosion was dominant where there were wide, high beaches. This acts as a positive feedback, since the sediment from subaerial erosion provides more protection from waves to the base of the cliff. Areas that experienced large subaerial failures were buffered from the deflation of the beach and subsequent wave run-up. It was also noted that the sites with armoring (seawalls, riprap, etc) were associated with the narrowest beaches. Without the natural source of sand from the cliffs, the beaches became sediment depleted and were extremely vulnerable to wave attack.

Appendix I: Anatomy and growth of a Holocene clinothem in the Gulf of Papua

JOURNAL OF GEOPHYSICAL RESEARCH, VOL. 113, F01S13, doi:10.1029/2006JF000628, 2008

Anatomy and growth of a Holocene clinothem in the Gulf of Papua

Rudy Slingerland,[1] Neal W. Driscoll,[2] John D. Milliman,[3] Scott R. Miller,[1] and Elizabeth A. Johnstone[2]

Received 6 July 2006; revised 15 April 2007; accepted 8 August 2007; published 5 March 2008.

[1] High-resolution seismic profiles and sedimentological data from grab samples and long cores provide an unprecedented picture of the structure, sedimentology, and late Quaternary development of two Gulf of Papua (GoP) clinothems, one probably Stage 3 and 4 in age and one Holocene in age. The older was partially eroded during Stage 2 and partially covered by the younger clinothem during Stage 1. The younger clinothem consists of three stratigraphic units separated by two surfaces of erosion, bypass, or correlative surfaces of lap. The surfaces were formed by changes in accommodation and sediment supply. The underlying physiography of the older clinothem also appears to play an important role in governing the shape of the younger clinothem. In the northern gulf, oblique clinoforms of the younger clinothem suggest that the rate of sediment supply from the northern rivers outstripped the formation of new accommodation, whereas in the south, sigmoidal clinoforms indicate that accommodation increased faster than sediment supply. The origin of the new accommodation remains uncertain because of limited age constraints. On the basis of sediment thickness, stratal geometry, and acoustic character, off-shelf transport appears to be the dominant sediment transport direction, with preferential accumulation on the promontories and bypass in the valleys. Presently, observed and computed modern flows and complex gyres in shallow water coupled with wave- and current-supported gravity flows or river floods can explain the form, internal clinoform shapes, and mineralogy of the younger Gulf of Papua clinothem.

Citation: Slingerland, R., N. W. Driscoll, J. D. Milliman, S. R. Miller, and E. A. Johnstone (2008), Anatomy and growth of a Holocene clinothem in the Gulf of Papua, *J. Geophys. Res.*, *113*, F01S13, doi:10.1029/2006JF000628.

1. Introduction

[2] Clinothems are the basic building blocks of modern and ancient continental shelves. Seismic and outcrop studies show that at least one-third of modern and ancient shelves have been built by the lateral stacking of such sedimentary packages [*Mitchum et al.*, 1977; *Kuehl et al.*, 1989; *Bartek et al.*, 1991; *Christie-Blick and Driscoll*, 1995; *Nittrouer et al.*, 1995; *Pirmez et al.*, 1998; *Driscoll and Karner*, 1999; *McCormick et al.*, 2000; *Hampson and Storms*, 2003; *Lofi et al.*, 2003; *Deibert et al.*, 2003; *Olariu and Bhattacharya*, 2006; *Cattaneo et al.*, 2004; *Liu et al.*, 2004b]. The lateral stacking patterns exhibit a variety of geometries such as sigmoid, oblique, and parallel (as first classified by *Mitchum et al.* [1977]), but all have in common a lateral translation of a relatively self-similar form. Here we use the term *clinoform* for the chronostratigraphic horizon cutting obliquely through a heterolithic, coarsening upward sequence (as per *Mitchum et al.* [1977]), such as imaged by a single seismic reflector, and the term *clinothem* to indicate a deposit containing such surfaces. We also separate clinothems into two types: those with subaerial topsets (deltas and shorefaces) and those without (subaqueous clinothems).

[3] Subaqueous clinothems, and their evolution through time as reflected in their clinoforms, are thought to be a function of four semi-independent variables: rate of creation of accommodation, type and mass of sediment flux to the shelf, the processes distributing that sediment across the shelf, and stage of development (Figure 1). If we knew the functional relationship between the dependent variables (geometry, facies, and evolution of clinothems), and the independent variables, we could predict better the long-term fate of shelf sediment and hindcast the history of relative sea level, sediment flux, and shelf processes as recorded by clinoforms. Developing this functional relationship has proceeded along the traditional lines of theory (see *Driscoll and Karner* [1999] and *Kostic and Parker* [2003a, 2003b] for reviews), experiment [*Paola et al.*, 2001; *Pratson et al.*, 2004; *Niedoroda et al.*, 2005], and observation.

[4] Observational studies conducted on many modern clinothems around the world provide specific realizations of the functional relationship between clinothem characteristics and the controlling independent variables. The Amazon was the first to be well studied and remains the archetype subaqueous sigmoidal clinothem [*Kuehl et al.*, 1986; *Nittrouer et al.*, 1986; *Nittrouer et al.*, 1995]. Rollover occurs in 40 m water depth over 150 km from the

[1] Department of Geosciences, Pennsylvania State University, University Park, Pennsylvania, USA.
[2] Scripps Institution of Oceanography, La Jolla, California, USA.
[3] School of Marine Science, College of William and Mary, Gloucester Point, Virginia, USA.

0148-0227/08/2006JF000628

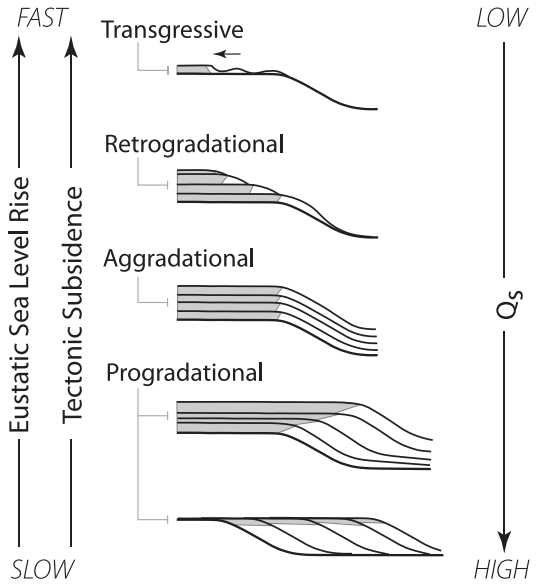

Figure 1. Schematic illustrating the interplay between sediment supply and accommodation in controlling clinoform geometry. Accommodation records both changes in eustatic sea level and tectonic subsidence/uplift. When sediment supply (Q_s) is greater than new accommodation, progradation occurs. Oblique progradation is a special case where no new accommodation is created. Aggradation occurs when sediment supply is equal to accommodation, while backstepping (retrogradational) results when sediment supply is less than accommodation.

coast. Foresets extend to 60 m water depth, dipping relatively steeply (but still less than 1°). *Kuehl et al.* [1986] proposed that sediment-laden buoyant plumes are the delivery mechanism for clinothem growth. Subsequent AmaSeds work [*Kuehl et al.*, 1996; *Nittrouer and DeMaster*, 1996; *Nittrouer et al.*, 1996] showed that the surface low-salinity plume is decoupled from clinoform development and *Kineke et al.* [1996] outlined the importance of hyperpycnal processes on its development.

[5] Quaternary shelves of the Mediterranean show a range of clinothem types from parallel delta/shore clinothems in the Gulf of Lions [*Berne et al.*, 2004] to sigmoidal subaqueous on the Italian Adriatic shelf [*Cattaneo et al.*, 2004]. The late Holocene clinothems are all fine-grained, about 35 m thick with the rollover in about 25 m water depth, and contain clinoform surfaces that dip at less than 1°. Because they extend downdrift for hundreds of kilometers from their parent deltas, it is clear that sediment transport by wind-driven coastal currents with bottom Ekman transport plays a large role in their growth. These geometrical characteristics are remarkably similar to both the Holocene Yellow and Yangtze River clinothems that extend downdrift for hundreds of kilometers along the China coast [*Hori et al.*, 2002b; *Chen et al.*, 2003; *Liu et al.*, 2004a, 2004b].

[6] The Ganges-Brahmaputra subaqueous clinothem rolls over in about 30 m water depth and in most other attributes is similar to the Amazon and Yellow River clinothems [*Kuehl et al.*, 1989, 2005; *Michels et al.*, 1998]. Fine-grained muddy beds of the foreset are thought by *Michels et al.* [1998] to be formed by "slowly moving suspension-rich plumes" (p. 147), decimeter and thicker graded, sand and silt layers by cyclone-generated coastal currents, and acoustically transparent layers by mudflows. It is an interesting point that most modern subaqueous clinothems are built by oblique, along-shelf transport [*Driscoll and Karner*, 1999], even though most conceptual models to date ignore the along-shelf dimension.

[7] These modern studies are supplemented by numerous observations of ancient clinothems. The relationships between form and process can only be broadly inferred, but the geometries provide a useful addition to the database. According to *Steckler et al.* [1999], Miocene subaqueous clinothems of the New Jersey margin were initiated because of increased sediment supply. As they prograded into deeper water they increased in steepness and height, ranging from less than 100 to 700 m [*Poulsen et al.*, 1998]. Other examples include storm-wave-dominated Eocene clinoforms of Spitsbergen [*Deibert et al.*, 2003], reaching heights of 150 m and foreset dips of 4°; and Cretaceous sandy shoreface clinoforms from Utah with heights averaging 20 m and foreset dips less than 1° [*Hampson and Storms*, 2003].

[8] The purpose of this work is to contribute to the growing observational database upon which a definition of the functional relationship between form and process will ultimately depend. Here we present the surface morphology and internal stratigraphy of a modern subaqueous clinothem in the Gulf of Papua on the southeastern coast of Papua New Guinea as imaged by 2-D chirp survey and piston cores. Our observations show that this clinothem is a composite feature built by oblique alongshore stacking of sediment packages as sediment from multiple sources is transported along as well as across-shore, in contradistinction to the standard two-dimensional model of relatively uniform along-strike growth seaward.

2. Study Area

[9] The study area lies on the central shelf of the Gulf of Papua (GoP) (Figure 2), a semicircular embayment off the northern Coral Sea. It is underlain by shelf sediments at depths from 0 to 120 m (mean depth = 50 m) and bordered to the north and west by the mangrove shoreline of Papua New Guinea. It is fed freshwater and sediment by five principal rivers—the Fly, Bamu, Turama, Kikori, and Purari (Table 1 and Figure 2). Their estimated collective freshwater discharge is about 15,000 $m^3\ s^{-1}$ [*Wolanski et al.*, 1995], more or less evenly distributed both seasonally and interannually such that the 100-year floods of the Fly and Purari are only about twice the size of the 2-year floods [*Pickup*, 1984]. Collectively these rivers deliver somewhere around 200 million tons a^{-1} to their respective floodplains, deltas, and the gulf (J. Milliman, unpublished data, 1999). Although the Fly contains by far the largest water discharge, its sediment load is relatively modest because the source rock lithology is limestone-dominated [*Brunskill*, 2004] (Table 1), and the large floodplain still contains unfilled accommodation because of the post-LGM rise in sea level. Approximately 90 percent of the Fly sediment

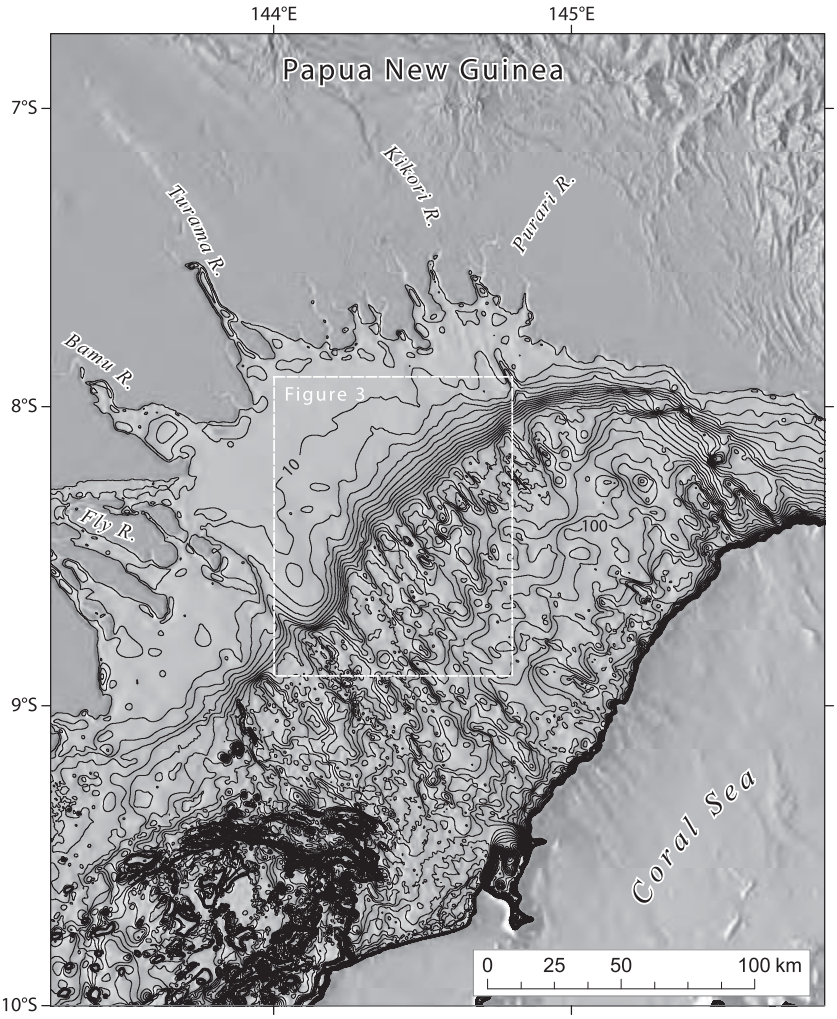

Figure 2. Location of study area (box) showing Gulf of Papua. Bathymetry of shelf in 5 m intervals from 5 to 200 m below sea level (digital data from *Daniell* [2008]). Bathymetry shaded from west.

delivered to the coast is finer than sand size [*Wolanski and Alongi*, 1995]; the sediment is relatively mature with high quartz/feldspar and illite/smectite ratios. The steep northern rivers in contrast, have much higher sediment yields and the sediment is an immature mix of volcaniclastic and other lithic fragments, thereby providing a convenient tracer for sediment transport on the GoP shelf [*Milliman*, 1995; *Brunskill*, 2004]. No estimates of size grading for the northern rivers are available, but the floodplains are narrow and short, suggesting that a greater percentage of sand can be expected to reach the coast.

[10] Sediment delivered to the shelf is thought to be distributed by a combination of tidal, wind-driven, oceanic, and thermohaline currents [*Harris*, 1990; *Wolanski and Alongi*, 1995; *Harris et al.*, 1996; *Walsh et al.*, 2004; *Keen et al.*, 2006; *Ogston et al.*, 2008; *Slingerland et al.*, 2008]. Tides on the shelf in 70 m water depth away from river mouths are mostly semidiurnal [*Wolanski et al.*, 1995; *Ogston et al.*, 2003; *Harris et al.*, 2004; *Ogston et al.*, 2004] and cross-shore. Most of the shelf is mesotidal. Wind-driven currents show two dominant circulation states highly influenced by seasonal monsoon/trade winds [*Wolanski et al.*, 1995; *Hemer et al.*, 2004; *Keen et al.*, 2006; *Slingerland et al.*, 2008]. During the northwest monsoon (December to March) flows on the topset are dominated by tidal variations and river discharge. Net (tidally averaged) flows are generally weak ($\sim$0.01 m s^{-1}) and offshore at the surface, with periods of southerly flow. Flows at the bed are also primarily tidal in nature, and are generally equal in magnitude to flows at the surface, but onshore. Flows over the clinoform face retain a strong tidal signature; however, like the flows on the topset, the net surface flow is weakly ($\sim$0.03 m s^{-1}) offshore. At the toe of the clinothem the SW-directed bottom flows of the outer shelf deflect to the NW as

Table 1. Characteristics of Rivers Draining Into the Gulf of Papua

	Fly	Bamu	Turama	Kikori	Purari	Total
Drainage basin area[a], km^2	62,728	7128	4528	19,800	29,588	123,782
Water discharge[b], $m^3\ s^{-1}$, 1986	6000[c]	2000	2000	2000	3000	15,000
Sediment discharge[d], 10^6 tons a^{-1} [*Wolanski et al.*, 1995]	80	low	low	50	60–70	200–365
Percent carbonate in catchment [*Milliman*, 1995; *Milliman et al.*, 1999]	70	?	?	60	20	
Percent volcaniclastic in catchment [*Brunskill*, 2004]	<5	?	?	30	35	

[a]Estimated by basin analysis of the ETOPO5 DEM.
[b]These values are estimates mainly from *Wolanski et al.* [1984], who provide some data for 1979 for the Kikori River (eight complete months and four part months) and for the Purari River (six part months). Additional data for the Fly are from *Salomons and Eagle* [1990].
[c]Of this amount, 60–80% exits by the southernmost distributary [*Harris et al.*, 2004].
[d]Range reflects uncertainties and estimates by various researchers. Values of individual rivers do not sum to estimated total because estimates for individual rivers are based on the drainage area method of *Harris et al.* [2004].

they climb the face, while maintaining their intensity (0.01 $m\ s^{-1}$). These climbing flows are the source of the upwelling observed on the clinothem topset. The trade wind season (May to November) is marked by surface and bottom flows on the topset that are roughly equal in magnitude to their monsoon counterparts (~0.02 $m\ s^{-1}$), but primarily directed NE. Flows over the clinoform face are parallel to the bathymetric contours and directed NE. These results suggest a sediment dispersal pattern on the modern clinothem topset of offshore surface transport with both SW and NE alongshore components, dependent upon the season. Upwelling on the clinoform face acts to localize deposition there and keep the outer shelf relatively sediment starved [*Moore and MacFarlane*, 1984; *Wolanski and Alongi*, 1995; *Wolanski et al.*, 1995; *Slingerland et al.*, 2008].

[11] Previous work on the GoP clinothem [*Harris et al.*, 1996; *Walsh et al.*, 2004] has demonstrated that discrete, yearly depositional events appear to be the fundamental building unit of the GoP midshelf modern clinothem. According to *Walsh et al.* [2004], the clinoform face is created by fluid mud deposition in response to the transition from trade to monsoon wind conditions, although precisely how this happens in the presence of onshore bottom flows is as yet unknown. Detailed ^{210}Pb and grain-size data indicate that low activities and increased clay contents are associated with discrete decimeter-thick layers that preferentially accumulate on the foresets of the clinothem. Short-term (based primarily on ^{210}Pb) rates of deposition are as high as ~4 cm a^{-1} [*Walsh et al.*, 2004]. Here we extend these observations to the millennial and longer timescales.

3. Methods

3.1. Chirp Data

[12] As part of the NSF MARGINS initiative, more than 6800 km of high-resolution chirp seismic data (2300 km of surface-towed Edgetech and 4500 km of hull-mounted Knudsen) were acquired between September 2003 and March 2004 aboard the RV Melville (cruises VANC22MV and VANC23MV; see http://www.marine-geo.org/margins/ for cruise information). Here we focus on the central portion of the GoP clinothem (Figure 3) over which 670 km of seismic data were collected with penetration 50–100 m below the seafloor. These high-frequency seismic data permit submeter geologic resolution. Basic sequence stratigraphic methods for identifying and interpreting surfaces were employed [e.g., *Christie-Blick and Driscoll*, 1995]. Seismic lines were interpreted on paper and in Seisworks 2D by identifying terminations and then using horizons of terminations to define surfaces. Termination types include onlap, downlap, truncations, and toplap. Surface types include unconformities (local and regional), surfaces of progradation (downlap), retrogradation (onlap), and accretion (onlap and downlap).

[13] Two-way times (TWTs) to the seafloor and various surfaces were converted to depths assuming a seismic velocity in sediment of 1750 $m\ s^{-1}$, a value typical of uncompacted nearshore sediment. The depth difference between the seafloor and a surface yields the thickness of sediment above the surface. The thicknesses were interpolated with an inverse distance weighted method to create an isopach map. For this interpolation, data were resampled at a coarser resolution (one data point every 500 seismic traces rather than one data point per trace) and the closest 50 points were used in the calculation. TWTs to the seafloor varied

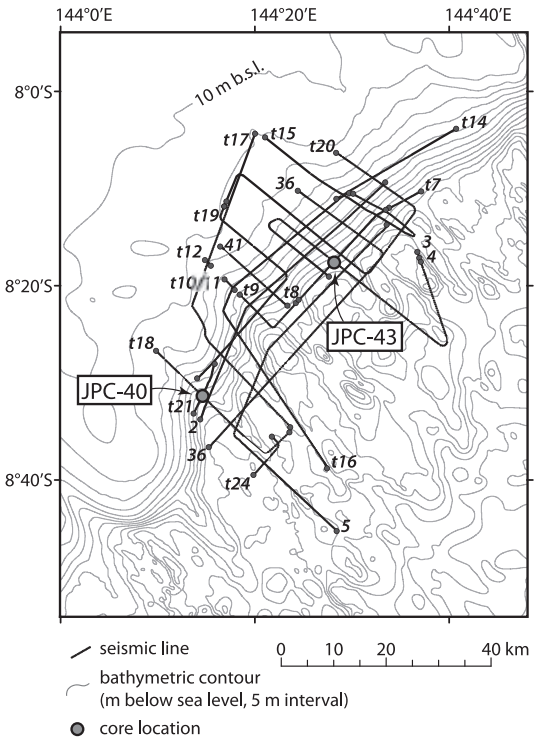

Figure 3. Bathymetric map of the central lobe showing chirp lines used in this study.

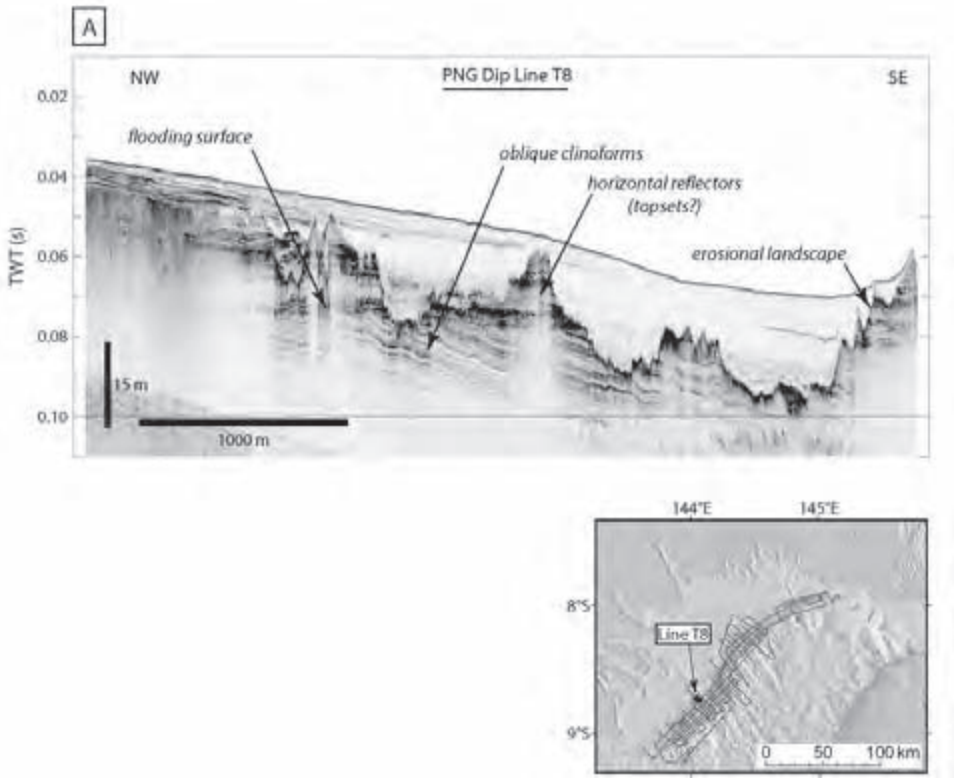

Figure 4a. Chirp subbottom profile Papua New Guinea (PNG) Dipline T8 shows an older clinothem consisting of oblique clinoforms mantled by flat-lying strata above a flooding surface. Above a significant erosional unconformity lies the modern clinothem, here represented by seaward dipping reflectors.

among lines and within lines because the chirp system is deep-towed. Without an independent constraint on the actual seafloor TWT or depth, the TWT or depth to any horizon is not very meaningful. Therefore to create a structure map of a surface, the isopach grid was subtracted from a grid of bathymetry. Reflector dips were determined by measuring apparent dips in two intersecting seismic lines, then solving for true dip as a three-point problem.

3.2. Core Data

[14] Ten piston cores and 7 gravity cores were taken in the study area, and from these, cores JPC-40 (8° 31.4041′ S; 144° 14.7091′ E) and JPC-43 (18° 17.0302′ S; 144° 27.4946′ E) were chosen for radiocarbon dating at the National Ocean Sciences Atomic Mass Spectrometer facility at the Woods Hole Oceanographic Institution, USA, yielding six dates. Figure 3 gives the core locations with respect to the chirp lines.

4. Observations

4.1. General Morphology and Stratigraphy

[15] As first pointed out by *Harris et al.* [1996], the morphology of the GoP shelf consists of two treads separated by a riser (Figure 2). The upper tread is the smooth and gently seaward sloping seabed extending up to 60 km from a mangrove-fringed shoreline to water depths of 20 m where dips increase to 0.2 to 0.8° on the riser. From the toe of the riser in water approximately 80 m deep, the lower tread is the seabed extending seaward 100 km to the shelf edge at 120 m water depth. Unlike the smooth upper tread and riser, the lower tread is corrugated with a NW–SE-trending lineation.

[16] The treads and risers are created by two stacked clinothems—an older deeply eroded clinothem forming the middle (and possibly outer) shelf, and a superjacent younger clinothem extending from the coast offshore forming the inner shelf (Figures 4a–4d). The older, eroded clinothem consists of approximately 30–40 m of generally subhorizontal reflectors lying beneath an erosional surface with marked truncation (Figure 4a). The subhorizontal, concordant reflectors exhibit minimal thickness variations (Figure 4b) and cap a set of obliquely prograding reflectors (Figure 4c) that extend tens of kilometers across the margin. The change in geometry (i.e., oblique progradation to aggradation) allows us to infer the relationship between sediment supply and accommodation (e.g., Figure 1). The oblique clinoforms can be traced across large portions of the GoP shelf and indicate that sediment supply was infilling the available accommodation. The geometry of the overlying aggrading parallel concordant sequence indicates that the creation rate of new accommodation was equal to the rate of sediment supply. In the central gulf

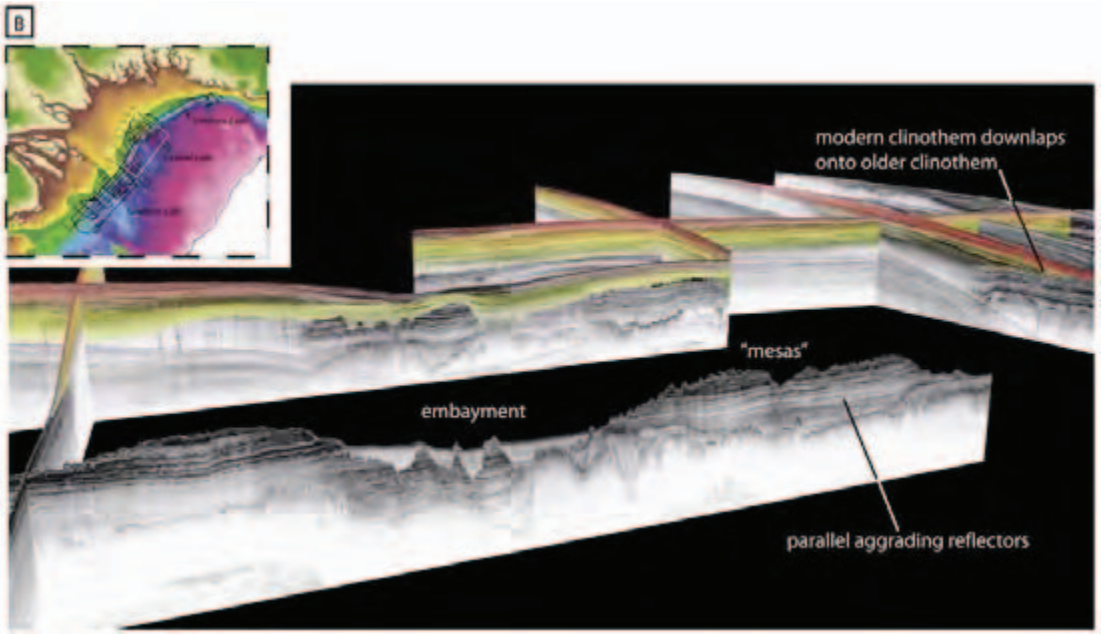

Figure 4b. Chirp fence diagram looking NW along the central lobe on the GoP shelf illustrates the parallel, concordant sequence of the older clinoform. Individual horizons within this sequence can be traced laterally along the margin for great distances with minimal thickness variations. Several valleys or embayments dissect the margin, and intervening highs or erosional "mesas" exhibit marked truncation along their borders. Offshore on the middle and lower tread this erosional morphology outcrops on the seafloor and is only partially infilled in the embayments, which gives rise to the rough corrugated morphology observed in the bathymetry. Landward, the modern clinoform obscures the underlying erosional landscape. Inset shows location of fence diagram.

midshelf region, northeast of the Fly River mouth, this older clinothem has been dissected by six major valleys ranging in width from 10 to 15 km, cut into the subhorizontal strata and separated from one another by "mesas" [*Harris et al.*, 1996] that stand 10–20 m higher than the valleys (Figure 4b). Cut into both the valleys and mesas are numerous channels, mostly less than ~200 m wide but as much as 30–40 m deep (Figure 4d).

[17] The younger clinothem downlaps onto the erosional surface etched into topsets of the older clinothem (Figures 4 and 5). Its face undulates along strike in a series of subtle promontories and reentrants (Figure 2) that correlate with the mesas and paleovalleys etched into the underlying older midshelf clinothem. This erosional landscape creates a variation in accommodation that shapes the overlying sequence. The modern clinoform exhibits both onlap and downlap patterns and these wedges near the base of the clinoform tend to diminish the observed relief. It appears that theses onlapping wedges in Line PNG00-03 (Figure 4c) are recording oblique along-shelf transport. The importance of along-shelf versus across-shelf transport in clinoform development needs to be understood and quantified.

4.2. Description of Stratigraphic Units in the Younger Clinothem

[18] The younger clinothem in the study area consists of three major stratigraphic units (here called Yellow, Orange, and Red) that are separated by two surfaces of erosion or correlative surfaces of down/up/on/off-lap (Figures 5, 6, and 7). The most prominent surface (surface S_1) separates Yellow from the Orange and Red units everywhere in the study area. To the NE it is an erosional unconformity or surface of bypass (e.g., Figure 5); to the SW it is a surface of lap. Below S_1 lies the oldest unit imaged (Yellow in Figure 6), which is present everywhere in the study area. It is acoustically well bedded, prograding (Figure 7), and in places folded, possibly due to soft sediment deformation (Figures 6 and 7).

[19] Above the S_1 surface lie the Orange and Red units. The Orange unit is the older of the two and only occurs in the southern portion of the study area. It is a convex upward body built by accretion beds prograding obliquely both ENE and S. It is acoustically bright and well-bedded. The Red unit drapes both the Orange and Yellow units above a surface of lap (S_2) and is present everywhere in the study area. It is more acoustically transparent and built by up- and down-lapping beds (Figures 6 and 7). Grab samples and cores show that the Red and Orange units consist of three principal facies. By far the most voluminous is Facies 1, a dark gray homogeneous, very fine silty clay (cf. Figures 8 and 9) with occasional well-laminated intervals. Facies 2 consists of very thin interbeds of dark brown very fine sand. Based mostly on correlation with cores taken outside the central study area, Facies 3 consists of muddy fine to very fine sand; superficial iron-stained magnesian-calcitic ooids characterize this facies.

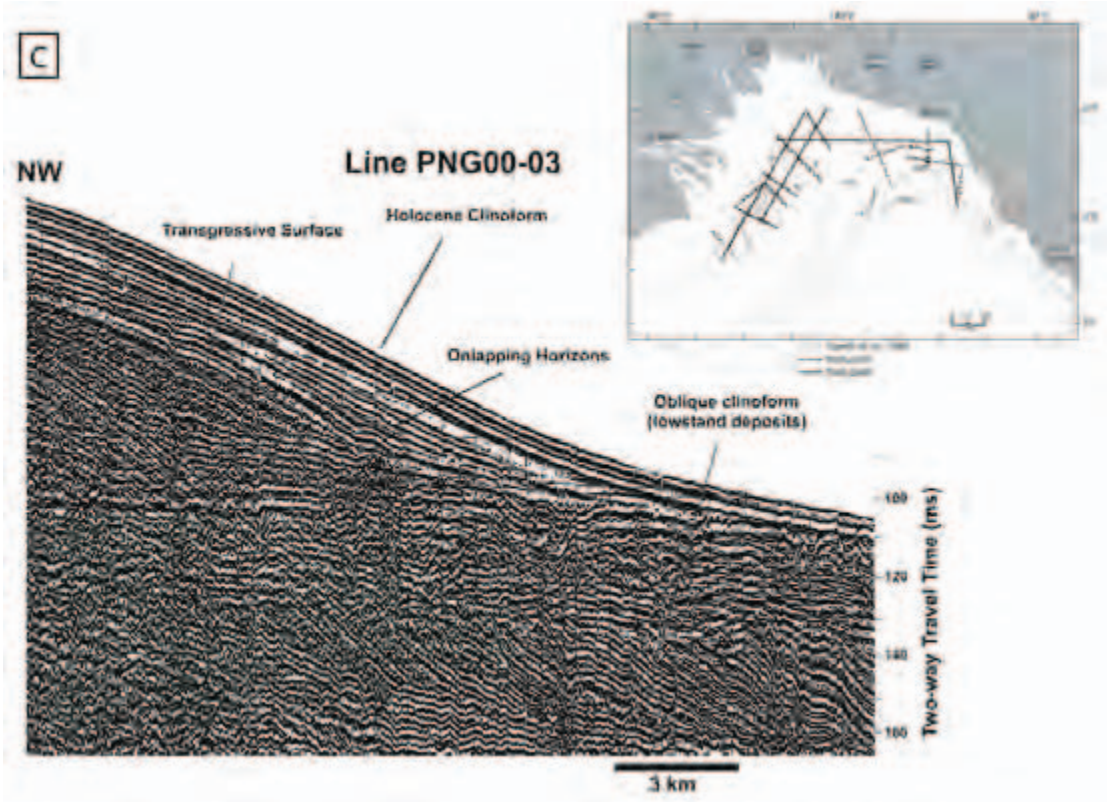

Figure 4c. Sparker profile PNG00-03 acquired in the GoP is roughly coincident with transect H [see *Aller et al.*, 2008] and images the older clinothem. Older clinothem comprises an oblique prograding package mantled by a parallel concordant package. Note that 10 ms is approximately equal to 7.5 m two-way travel time.

[20] The ages of the bounding surfaces are not well constrained. Of the 29 cores taken in the central study area, only one (JPC-40; Figure 8) may have penetrated the Yellow unit, but this core experienced significant flow-in upon extraction. Assuming that all the dated samples come from above S_1, we can say that the S_1 surface must be older than 5.21 ka BP. Core JPC-43 (Figure 9) penetrates 11 m of the Red unit to within 1.5 to 2 meters of S_1. Radiocarbon ages of bulk carbonate from 3, 4.5, and 7 m deep in the core are 1.75, 1.57, and 1.84 ka BP, respectively, yielding a youngest possible age for the S_1 surface of 1.84 ka BP. A core (JPC-02) taken at 7° 58.6841′S; 145° 2.9818′E provides some additional evidence that the S_1 surface is earliest Holocene. An ooid facies in JPC-02 ends abruptly at ~4 m, above which the sediment consists of silty clay. The ooids at 4 m have an age of ~9.5 ka BP, yielding sediment accumulation rates between 4 and 9 m depth in the core of about 2.5 mm a^{-1}. Above ~3.5 m, accumulation rates appear to be <1 mm a^{-1}.

[21] A structure map on the S_1 surface (Figure 10) shows its elevation with respect to sea level. On the whole the reentrants and promontories in the paleobathymetry and modern bathymetry are spatially correlated, indicating that the growth of the clinothem has been roughly self-similar over the last few thousand years. An isopach map created by contouring vertical distances between the structure contour map and the present seabed (Figure 11) shows that the thicknesses of sediment overlying S_1 range from 0 to 38 m. Three depocenters of maximum thickness lie along the upper face of the modern clinothem coincident with the bathymetric promontories. In contrast, on the lower face the depocenters of maximum thickness lie in bathymetric reentrants. Chirp strike lines crossing two promontories in the central region about midway down the clinothem face (Figure 12) show that variations in thickness of the Yellow unit smooth out the paleotopography.

[22] The Orange and Red units overlying S_1 exhibit an interesting constructional character, with the greatest thicknesses on the highs and systematic thinning toward the valleys. In addition, high-amplitude reflectors are preferentially observed within the valleys in the Orange and Red units. Even given these thickness differences, units above and below the S_1 surface show a similarity in reflector dips and dip directions (Figure 13) at a given site. Differences in attitudes are small in comparison to changes among sites, again indicating self-similar growth.

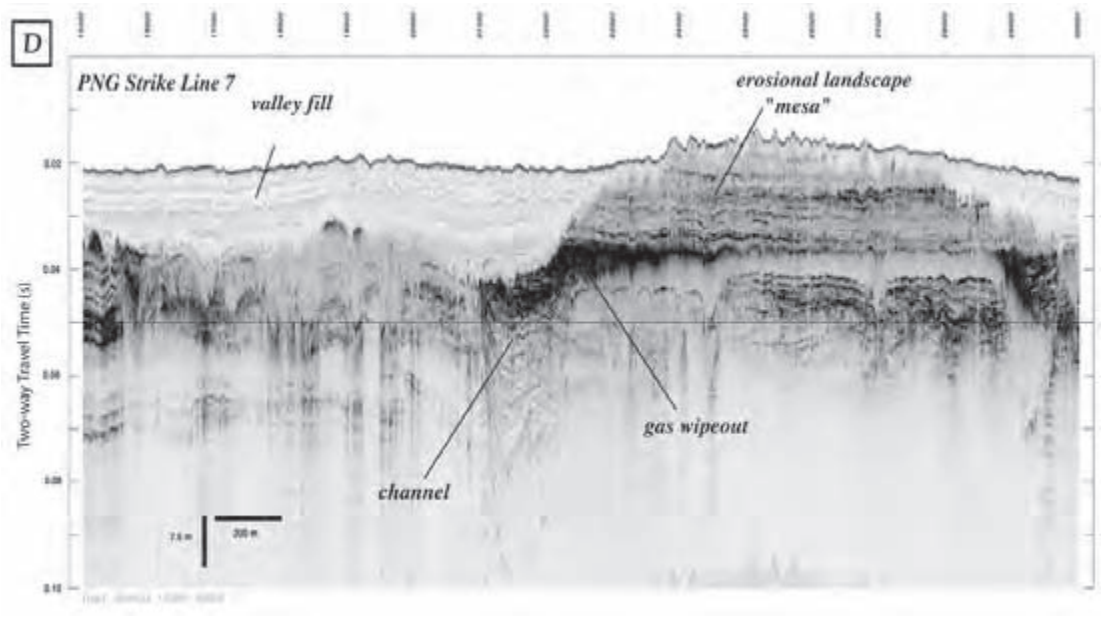

Figure 4d. Chirp profile Line 7 across an erosional mesa and adjacent valley or embayment illustrates the parallel nature of the concordant sequence of the older clinoform and shows erosional truncation and downcutting along the edges of the mesa. Close to the margin the valleys are preferentially filled, and the fill onlaps onto the erosional landscape. Within the valleys are incised channels that are approximately 200 m wide and up to 20–40 m deep.

4.3. Stratal Relations With Adjacent Portions of the Clinothem

[23] Reflectors in the study area are downlapped both to the north and south by younger reflectors (E. A. Johnstone et al., Clinoform architecture in the Gulf of Papua records the interplay between sea level, sediment supply, and climate, submitted to *Geology*, 2008; hereinafter referred to as Johnstone et al., submitted manuscript, 2008),

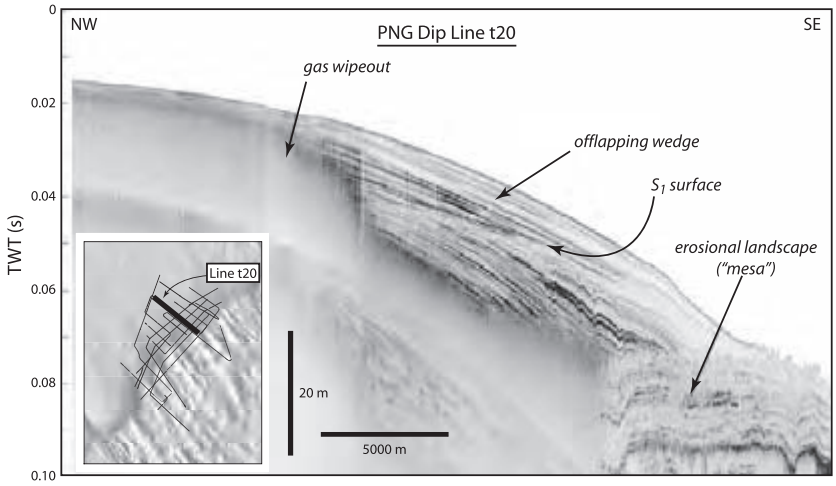

Figure 5. Chirp subbottom profile showing downlapping of younger clinoforms onto topsets of older clinothem (see Figure 2 for location). Surface of erosion or bypass is recorded by the S_1 horizon (see section 4.2 for details).

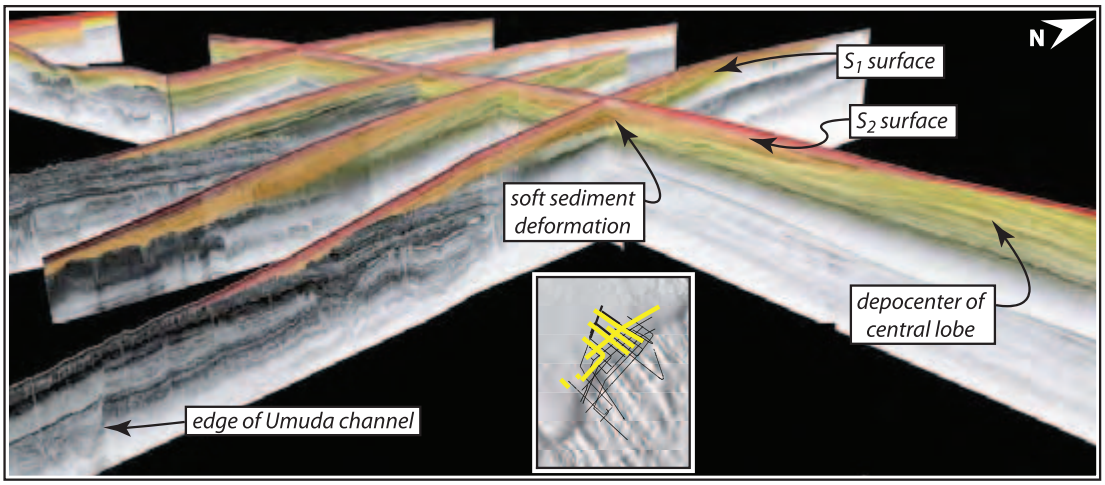

Figure 6. Seismic fence diagram of study area looking southwest along the Holocene clinoform face (see Figure 2 for location). Three stratal units are separated by two surfaces of erosion and lap. Lowest and most regionally extensive surface (S_1) separates an older, more acoustically laminated, obliquely prograding, and in places, folded unit (Yellow unit) from two younger units that are more acoustically transparent, unfolded, and up-building (Orange and Red). Surface S_2 separates a localized acoustically bright unit (Orange) from an acoustically transparent regional drape (Red). (See Johnstone et al., submitted manuscript, 2008, for a more detailed description).

indicating that the standard view of clinothems as two-dimensional prograding bodies is not applicable here. The polygenetic nature of this Holocene clinothem is also indicated by the mineralogy of its surficial sediments. Illite/smectite ratios in the clay fraction (Figure 14) and quartz/feldspar ratios in the 62–90 μm fraction (not shown) can be interpreted to reflect a mixing of subarkosic sands and illite-dominated muds delivered by the Fly River from the south with immature arkosic sands and smectite-dominated muds

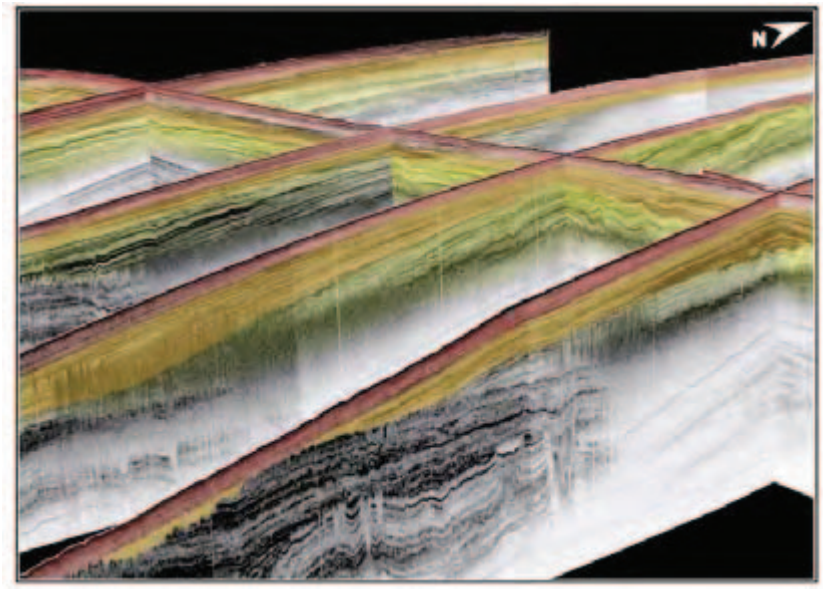

Figure 7. Enlargement of Figure 6 showing the transition from oblique progradation near depocenter to sigmoidal progradation on southern edge of the study area. Also note folds in Yellow unit.

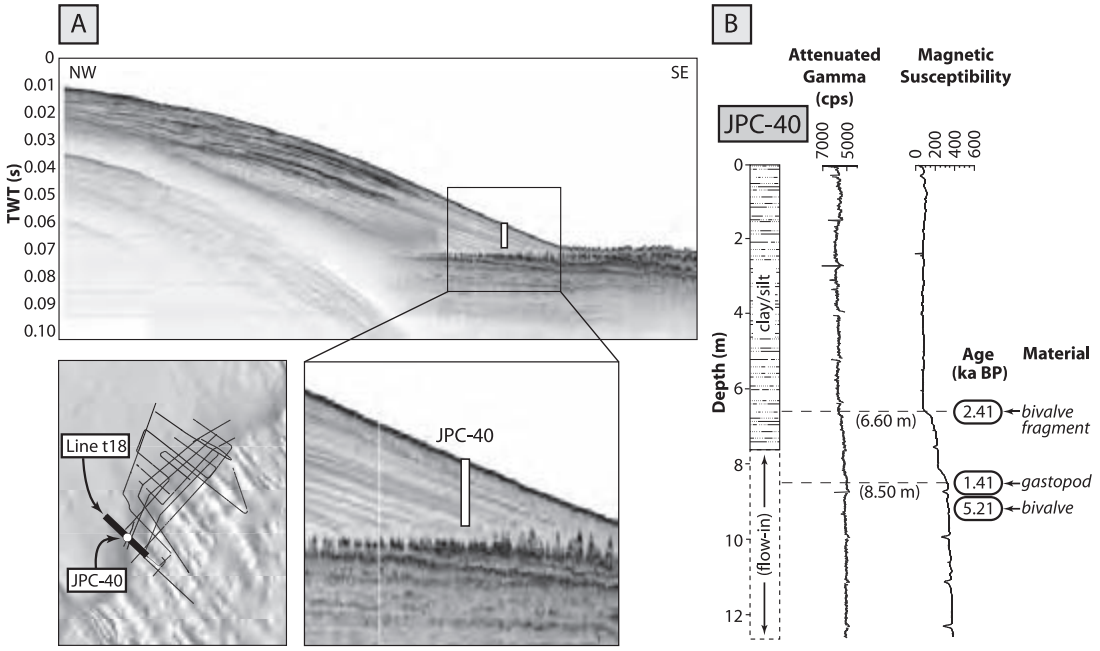

Figure 8. (a) Chirp Track 18 Line 4 showing location of JPC-40. (b) Core lithic log, attenuated gamma and magnetic susceptibility logs, and radiocarbon ages. Sediment below 670 cm in the core was sucked into the core barrel upon extraction, possibly explaining the mixture of radiocarbon ages. Red unit consists of very dark gray homogenous silty clay deposited over the last 5.21 ka.

delivered by the steeper rivers tapping the volcanogenic terrain to the north (Table 1).

5. Interpretation

5.1. Geologic History of the Gulf of Papua Shelf

[24] The upper approximately 100 m of the GoP shelf consists of two stacked clinothems: an older, partially eroded clinothem forming the floor of the middle shelf, and a Holocene clinothem forming the inner shelf. On the basis of the stratal geometry of the older clinothem and its present elevation, we deduce that it prograded two-thirds of the way across the preexisting shelf in response to a relative sea level fall during Stage 4 (Figure 15), when the rate of sediment supply filled the available accommodation. We infer that these oblique clinoforms were deposited during Stage 4 (~55,000–75,000 years BP) because we observe no aggradation during progradation (e.g., Figures 4a and 4c); this requires a rate of eustatic sea level fall that is faster than subsidence. This inference is consistent with a major siliciclastic pulse observed on the slope between 60,000–100,000 years BP [*Mallarino et al.*, 2004].

[25] Above the oblique clinoforms lie parallel reflectors that represent topsets (e.g., Figure 4). Using sequence stratigraphic principles we infer that these topsets formed when the rate of sediment supply equaled the creation of new accommodation (e.g., Figure 1) during Isotope Stage 3 prior to the large sea level fall associated with the LGM (Figure 15). This age is consistent with data from several cores acquired by *Harris et al.* [1996] which recovered Pleistocene sediments from the top of the parallel sequence where exposed at or near the seafloor. Core 37PC11 from the top of an erosional "mesa" yielded a radiocarbon date of 33,850 years BP [*Harris et al.*, 1996] and other cores from the "mesa" features that sampled the parallel, concordant unit (e.g., Fr-93–1PC1, 30PC8) recovered Pleistocene deltaic facies and cohesive reddish brown clays. On the basis of these observations, *Harris et al.* [1996] suggested that the pretransgressive deposits were deposited 50,000–20,000 years BP, consistent with our interpretation. If correct, such a scenario suggests that tectonic subsidence in the region was outpacing the slow eustatic fall during Stage 3 (~1 mm a^{-1}) to create the available accommodation (Figure 15).

[26] This magnitude of differential tectonic subsidence (~1 mm a^{-1} or 10 m/10,000 years) is problematic. Dated coral material acquired from fringing reefs along the Ashmore Trough at 125 m water depth (Core MV-73) suggests there has been little to no tectonic subsidence since the LGM in that region [*Droxler et al.*, 2006]. However, Core MV-73 was acquired south of the peripheral bulge for the GoP foreland basin (Figure 2) and thus might not reflect tectonic subsidence within the foreland. Furthermore, the tectonic subsidence rate demanded by the parallel, concordant topsets observed in the older clinoform is consistent with differential tectonic subsidence rates determined from exploratory wells in the region (e.g., Borabi-1 and Pasca C1; [*Davies et al.*, 1989]). In addition, the transgressive surface formed as a consequence of the rapid

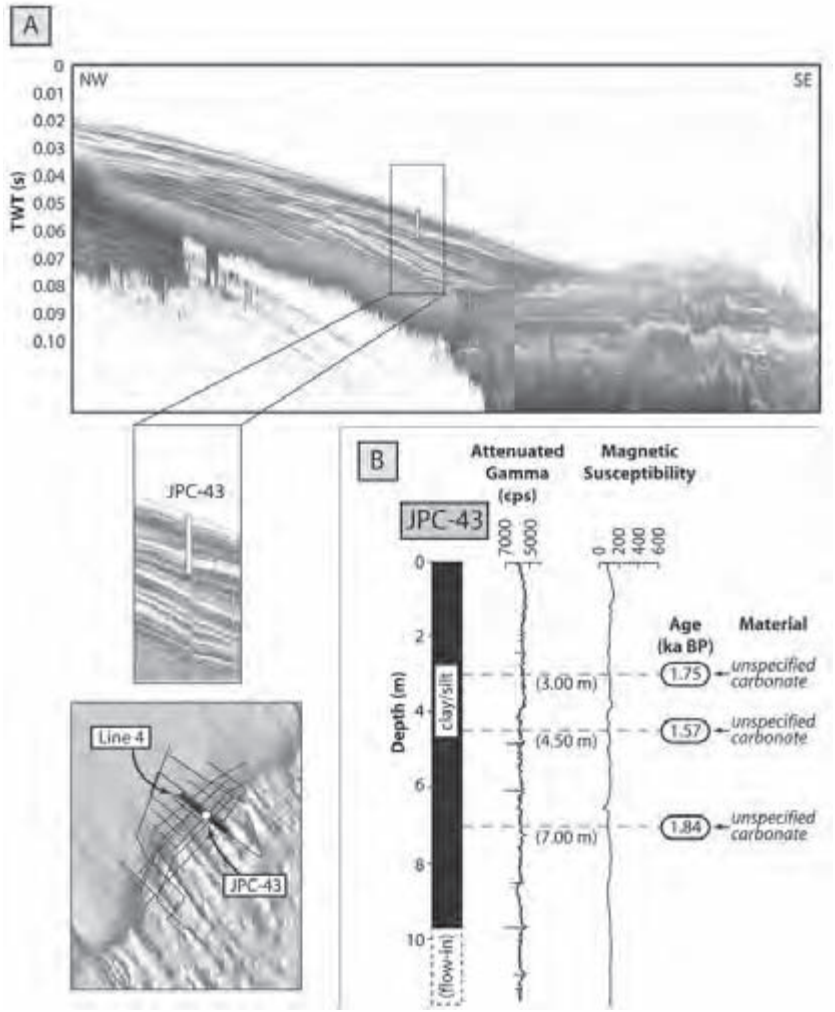

Figure 9. (a) Chirp dip line PNG4L10 near toe of modern clinothem showing location of JPC-43. (b) Core lithic log, attenuated gamma and magnetic susceptibility logs, and radiocarbon ages. Acoustically transparent, very fine silt/clay intervals intercalated with medium thick beds of more reflective very fine sands downlap onto older clinothem. Surface S_1 is the light gray horizon just beyond the bottom of the core.

sea level rise following the LGM exhibits a regional dip toward the northwest. If the transgressive surface had minimal relief when it was formed by wave base erosion, then a dip of this magnitude requires a differential tectonic subsidence rate of $\sim$1 mm a^{-1}. Finally, it is interesting to note that high accumulation rates on the slope between 60,000–100,000 years BP are succeeded by lower rates from $\sim$30,000–55,000 years BP [*Mallarino et al.*, 2004], consistent with an increase of accommodation on the shelf in response to a relative sea level rise produced by tectonic subsidence.

[27] In the central gulf midshelf region NE of the Fly River mouth, the older clinothem has been dissected by six major valleys and numerous channels (cf. Figure 4). We interpret this erosion to be fluvial in origin and to have occurred during the rapid eustatic fall commencing $\sim$25 ka BP (Stage 2) that lowered sea level to $-$125 m. An alternative hypothesis is that they are tidally incised shelf valleys in the manner of *Harris et al.* [2005], but we consider this unlikely given the dendritic nature of the valley systems and the deep channels observed within the valleys (Figure 4d). As eustatic sea level rose from $-$125 to +3 m between 20 and 7 ka BP, the former midshelf river channels within the river valley were partially filled by fluvial and estuarine facies [*Milliman et al.*, 2006]. The transgression was so rapid however, that the valleys themselves remained unfilled except for minimal input from eroding interfluves. Farther landward near the Fly River

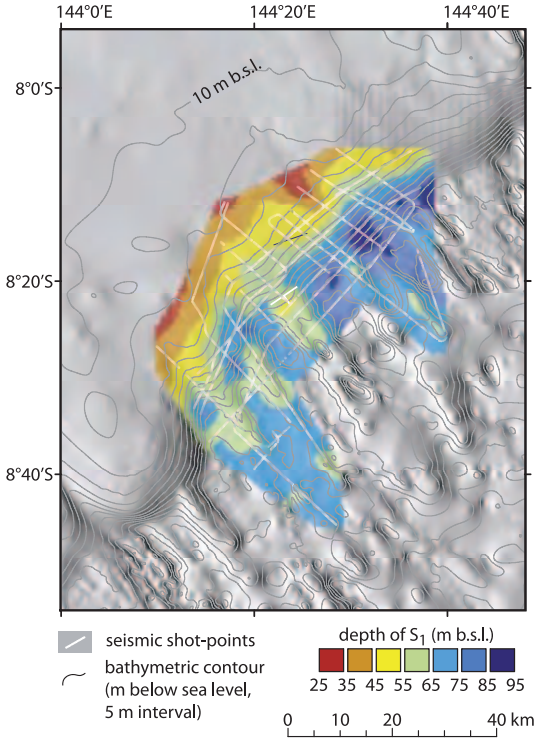

Figure 10. Shaded structure contour map of S_1 surface draped on modern smoothed bathymetric contours. See text for details.

mouth, more of the transgressive systems tract (TST) was preserved [*Harris et al.*, 1996], but even there it remains thin and discontinuous. In most places the sequence boundary, the transgressive surface, and the maximum flooding surface coalesce (e.g., Figure 4a). When and where a Holocene GoP clinothem began advancing seaward remains unknown; the turn around point lies landward of our data. The Holocene clinothem had prograded to within 15 km of its present position by about 4.8 ka BP, although the Yellow unit may be older than 9–9.5 ka BP (i.e., MWP 1C). This early growth produced acoustically high-amplitude reflectors that exhibit oblique progradation at the top of the Yellow unit (Figures 6 and 7), indicating that sediment supply was greater than the creation rate of new accommodation and filled all the available accommodation. Stratal strike profiles show undulations in the clinoform surface caused by the mesas and valleys over which the Holocene clinothem was prograding (Figure 12). The folds in the Yellow unit in the NE corner of the study area appear to record continued downslope soft sediment deformation during clinothem growth. The Orange and Red units downlap onto the S_1 surface and this requires the generation of new accommodation after the deposition of the Yellow unit. Given the uncertainty in the age of S_1, two possible scenarios might explain how the new accommodation was formed. In scenario 1, the oblique clinoforms of the Yellow unit were formed during a eustatic stillstand approximately 9–9.5 ka BP. A subsequent rapid rise in sea level during MWP 1C (dated in the Great Barrier Reef and in southern Asia at 9.1–9.6 ka BP [*Larcombe and Carter*, 1998; *Liu et al.*, 2004b]) produced the S_1 surface and the accommodation in which the finer-grained Orange and Red units came to downlap the Yellow unit (Figures 5 and 6). Alternatively, if the ^{14}C dates from the flow-in of core JPC-40 (Figure 8) come from both above and below S_1, then the age of S_1 lies between 2.41 and 5.2 ka BP. Because there are no known rapid rises of sea level during this interval, S_1 must be due to a rapid decline in the rate of sediment supply at a constant subsidence rate. In scenario 2, the oblique clinoforms are formed during a period of high sediment supply and then the sediment supply is shut off and long-term subsidence accounts for the generation of the new accommodation and formation of the downlap surface. We can find no evidence from other studies to decide between the two scenarios. Longer cores are required to test these two alternatives.

[28] Clinothem growth resumed after the S_1 event as localized sedimentation of the Orange unit in the southern half of the study area. It fills local accommodation, offlapping both to the north and south. By approximately 1.6 ka BP ago, sediments of the Red unit began to blanket the whole study area. These latest sediments consist of an acoustically transparent facies that forms an on- and downlapping toe of the wedge. The thickness of the Red unit

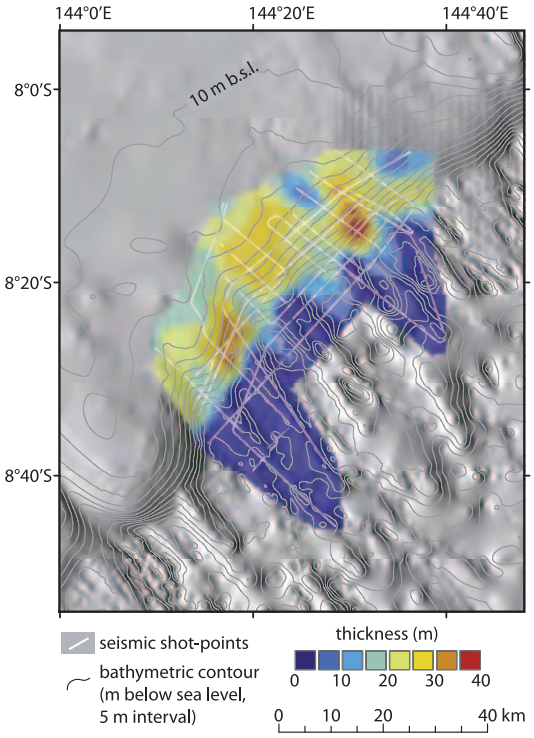

Figure 11. Isopach map of the interval between the S_1 surface and the seafloor, draped over shaded bathymetry. Note that on the upper clinoform face the Orange and Red units are thickest over promontories in underlying landscape, but at the clinoform toe they are thickest in reentrants. See text for details.

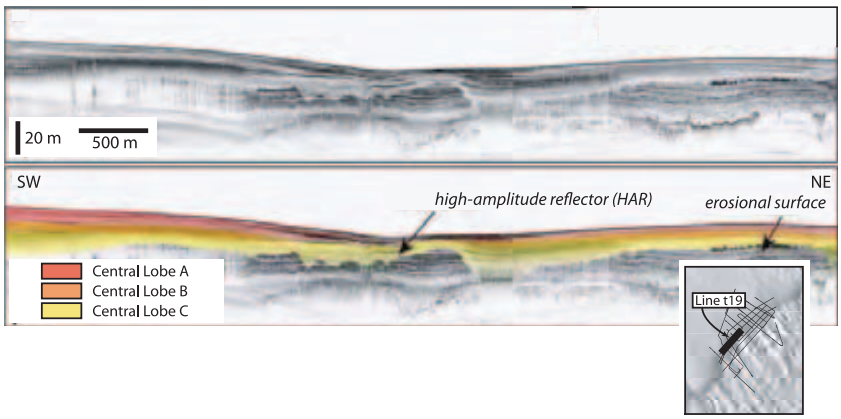

Figure 12. Chirp seismic profile across central lobe illustrating the differential thickness of the upper two units (Orange and Red) being thickest on the promontories and thinnest in the valleys. Note high-amplitude reflectors within the valleys that correlate with sands.

exhibits less variability than the Orange (Figures 6, 7, and 12). This transparent facies appears to be sediment winnowed from upslope strata, suggesting that at present, clinothem progradation may be moribund. The thickness variability observed in the isopachs as well as the high-amplitude reflectors observed in the valleys suggest that the dominant transport is strongly oblique to the isobaths and both northeast and southwest directed.

[29] Mineralogy of the uppermost beds of the Holocene clinothem also indicate significant bidirectional alongshore sediment transport (Figure 14). The Fly River sediment consists of mature illite clay and quartz-rich sands, consistent with its source rock composition and long distance of transport. Sediments of the northern rivers such as the Kikori and Purari consist of immature smectite clays and lithic sands with a strong volcanic component. Sediments of the modern shelf represent a mixture of these two types. This mixed assemblage can only be explained by at least some component of southerly transport along much of the upper tread with a convergence zone just north of the Fly River where sediment is shunted seaward off the shelf.

5.2. Modes of Clinothem Growth

[30] The Holocene GoP clinothem has not formed by simple parallel progradation of topsets over irregular bathymetry. Rather, the clinothem is composed of discrete lobes that formed at separate times. Cross-cutting relationships among the shingled lobes indicate that overall development of the clinothem complex has progressed from the center of the study area outward. These lobes are the fundamental architectural elements of the modern clinothem's stratigraphy. They consist of both onlapping and downlapping reflectors, suggesting that depocenters originated and accreted on the clinothem face, expanding updip and downdip as well as laterally. The pattern of paired onlapping and downlapping is particularly evident in the thickest (central and southwestern) parts of each clinothem segment. This architecture requires a sediment transport process such as sedimentation from suspension or failed

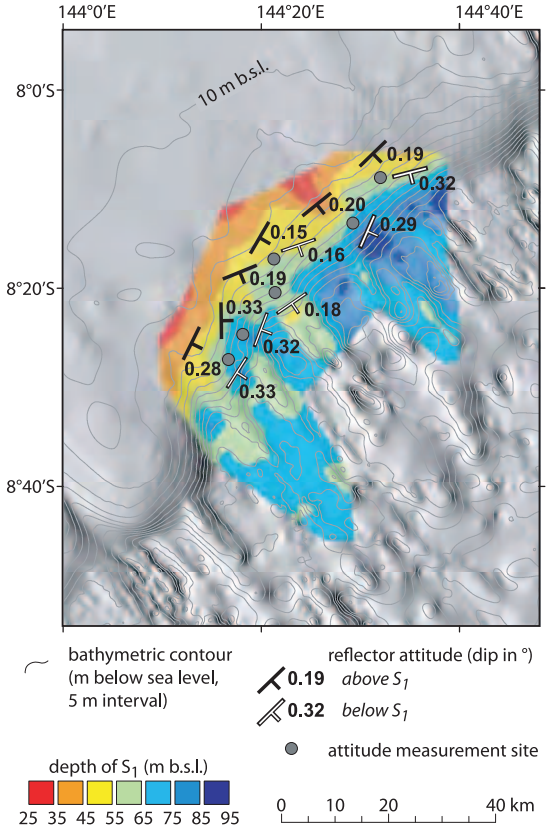

Figure 13. Reflector dips of strata above and below S_1, showing that dip directions are roughly similar indicating self-similar progradation.

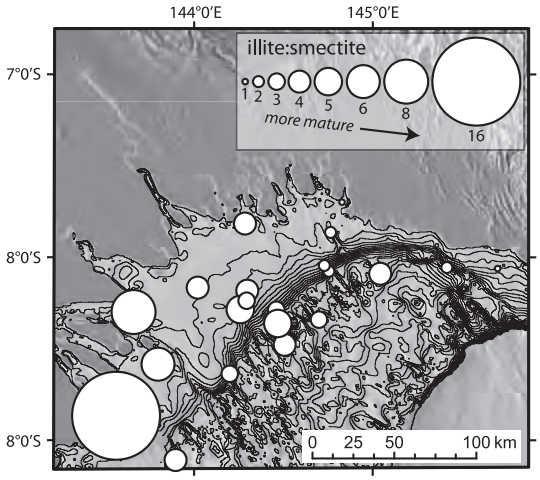

Figure 14. Illite/smectite ratios of the clay size fraction in surface sediments of the Gulf of Papua. Ratio increases systematically from northeast to southwest, indicating smectite-dominated rivers to the northeast contribute a large fraction relative to the illite-dominated Fly River to southwest.

gravity flows that produces initial vertical accretion on the clinoform face and then extension of the locus of deposition both upslope and downslope. The volume of sediment per unit distance along strike deposited since S_1 time can be estimated from the isopach map (Figure 11) to be 420,000 m^2. For a mean vertical thickness above S_1 of 16.2 m and a mean modern clinoform slope of 0.14°, the mean distance of recent clinoform progradation equals 6.6 km, and the mean clinothem vertical sedimentation rate is between 1 and 5 mm a^{-1}. Because the analysis area does not extend completely to the updip end of the clinothem, these values should be considered minimal. This vertical sedimentation rate is smaller by an order of magnitude than short-term sedimentation rates of 1–4 cm a^{-1} reported by *Harris et al.* [1996] and *Walsh et al.* [2004], based on ^{210}Pb and short-core ^{14}C dates, but are consistent with rates of 3 to 4 mm a^{-1} computed using about twenty AMS ^{14}C dates from our cores, which range from a few hundred years to a few thousand years old (see the Marine Geoscience Data System at http://www.marine-geo.org/link/entry.php?id) = VANC23MV for core descriptions and locations). Although it is well known that sedimentation rates calculated using dates spanning greater stratigraphic intervals are always lower [*Gardner et al.*, 1987], this effect cannot explain the magnitude of the discrepancy here over such a relatively young time range of hundreds to a few thousands of years.

[31] Our data indicate that during the formation of the Holocene clinothem, the northern rivers in the Gulf of Papua were supplying much sediment to the midshelf region and filling the available accommodation. Near the Fly River in the southern gulf, sediment input to the region was less than the available accommodation, resulting in the formation of sigmoidal clinoforms.

[32] Can changes in sediment transport patterns explain the S_1 and S_2 surfaces and the shifting loci of deposition? Computed annual circulation of the GoP in response to

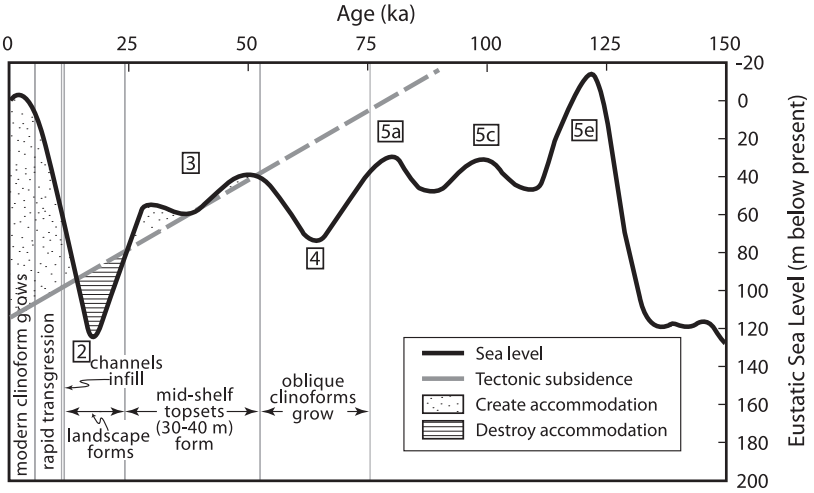

Figure 15. Inferred formation of the Gulf of Papua clinothems. Older, partially eroded clinothem consists of approximately 30–40 m of generally subparallel reflectors mantling a set of obliquely prograding reflectors. Deflection of the transgressive surface from horizontal yields a post-LGM differential subsidence of about 1 mm a^{-1} from the peripheral bulge in the southwest to near the basin depocenter in the northeast. On the basis of the *Lambeck and Chappell* [2001] and *Chappell and Shackleton* [1986] eustatic sea level curve, eustatic sea level fell from ~−40 to ~−65 m between 45 and 25 ka BP. Older clinothem topsets are thought to have accumulated at the end of Stage 3 about 30 ka BP as accommodation space was created by a relative slowing of sea level fall.

trade wind and monsoon conditions shows that the flow fields are significantly different [*Slingerland et al.*, 2008]. Possibly the surfaces and lobes were created by century to millennial-scale changes in the wind fields. This can be a sufficient explanation only if the change in circulation changed the amount of accommodation, because that is the only way to explain oblique offlap changing to aggradation. The most obvious way to do this is to change wave base significantly.

6. Conclusions

[33] The upper 100 m of the Gulf of Papua shelf are composed of two stacked clinothems: an older deeply eroded clinothem forming the middle and outer shelf, and a superjacent younger clinothem extending from the coast offshore forming the inner shelf. The older, partially eroded clinothem was built during Stages 4 and 3, eroded into a series of northwest-southeast trending paleovalleys and mesas during Stage 2, and partially covered by a younger clinothem during Stage 1. The younger clinothem downlaps onto the erosional surface etched into topsets of the older clinothem. It consists of three major stratigraphic units that are separated by two surfaces of erosion or bypass or correlative surfaces of down/up/on/off-lap. The ages and origins of these surfaces are not well known, however the formation of S_1 and its mantle of downlapping strata requires the formation of new accommodation. This stratal geometry cannot be formed by simple lobe switching. We present two scenarios to explain the formation of the new accommodation: changes in the rate of eustatic sea level rise, or changes in the rate of sediment supply with long-term tectonic subsidence.

[34] Isopach patterns, mapped terminations on the regional unconformity, and seismic patterns in the central study area indicate an early phase of clinothem growth below S_1 occurred by oblique progradation of acoustically high-amplitude, well-bedded reflectors on the clinoform face. This phase was succeeded by aggrading onlapping and downlapping acoustically transparent units (Orange and Red). These lithosomes tend to be elongate in the downdip direction and form generally on modern bathymetric promontories. Since formation of S_1, the clinothem has grown vertically by an average of 16 m and advanced shelfward an average distance of 6 km, yielding a mean clinothem vertical sedimentation rate of about 1 to 5 mm a^{-1}. The rates are variable along the present clinoform face. Sediment transport is predominantly off-shelf with the fine-grained material deposited on the highs with bypass and off-shelf transport in the valleys. Off-shelf transport must be oblique across the clinoform face, both NE and SW directed, to account for the directions of lap.

[35] Our study highlights the importance of the underlying physiography in controlling sediment dispersal and accumulation on the Gulf of Papua margin and shows that the Holocene clinothem there is inherently three-dimensional, consisting of lobes within lobes. The observed and computed modern flows and complex gyres in shallow water coupled with wave- and current-supported gravity flows or river floods can explain the form, internal clinoform shapes, and mineralogy of the younger Gulf of Papua clinothem. This knowledge provides a first step toward developing a quantitative understanding of its formation, but the origins of the changes in accommodation remain unknown.

[36] **Acknowledgments.** This research was supported by National Science Foundation awards 0305699, 0305779, and 0305607 under the MARGINS Initiative. Special thanks to the crew of the R/V *Melville*, the Oregon State University Coring Facility, and J. Hill, R. Fenwick, and J. Walsh who participated on the cruise.

References

Aller, R. C., N. E. Blair, and G. J. Brunskill (2008), Early diagenetic cycling, incineration, and burial of sedimentary organic carbon in the central Gulf of Papua (Papua New Guinea), *J. Geophys. Res.*, *113*, F01609, doi:10.1029/2006JF000689.

Bartek, L. R., P. R. Vail, J. B. Anderson, P. A. Emmet, and S. Wu (1991), Effect of Cenozoic ice sheet fluctuations in Antarctica on the stratigraphic signature of the Neogene, *J. Geophys. Res.*, *96*, 6753–6778.

Berne, S., M. Rabineau, J. A. Flores, and F. J. Sierro (2004), The impact of Quaternary global changes on strata formation, *Oceanography*, *17*(4), 92–103.

Brunskill, G. J. (2004), New Guinea and its coastal seas, a testable model of wet tropical coastal processes: an introduction to Project TROPICS, *Cont. Shelf Res.*, *24*(19), 2273–2295.

Cattaneo, A., F. Trincardi, L. Langone, A. Asioli, and P. Puig (2004), Clinoform generation on Mediterranean margins, *Oceanography*, *17*(4), 105–117.

Chappell, J., and N. J. Shackleton (1986), Oxygen isotopes and sea level, *Nature*, *324*(6093), 137–140.

Chen, Z., Y. Saito, K. Hori, Y. Zhao, and A. Kitamura (2003), Early Holocene mud-ridge formation in the Yangtze offshore, China: A tidal-controlled estuarine pattern and sea-level implications, *Mar. Geol.*, *198*(3–4), 245–257.

Christie-Blick, N., and N. W. Driscoll (1995), Sequence stratigraphy, *Annu. Rev. Earth Planet. Sci.*, *23*, 451–478.

Daniell, J. J. (2008), Development of a bathymetric grid for the Gulf of Papua and adjacent areas: A note describing its development, *J. Geophys. Res.*, doi:10.1029/2006JF000673, in press.

Davies, P. J., P. A. Symonds, D. A. Feary, and C. J. Pigram (1989), The evolution of the carbonate platforms of northeast Australia, *Spec. Publ. Soc. Econ. Paleontol. Mineral.*, *44*, 233–258.

Deibert, J. E., T. Benda, T. Loseth, M. Schellpeper, and R. J. Steel (2003), Eocene clinoform growth in front of a storm-wave-dominated shelf, Central Basin, Spitsbergen: No significant sand delivery to deepwater areas, *J. Sediment. Res.*, *73*(4), 546–558.

Driscoll, N. W., and G. D. Karner (1999), Three-dimensional quantitative modeling of clinoform development, *Mar. Geol.*, *154*(1–4), 383–398.

Droxler, A., G. Mallarino, J. M. Francis, J. Dickens, B. N. Opdyke, L. Beaufort, J. Daniell, S. J. Bentley, and L. C. Peterson (2006), Early transgressive establishment of relict upper most Pleistocene barrier reefs on LGM coastal siliciclastic deposits in the Gulf of Papua and Gulf of Mexico: Clue to understand the mid Brunhes global origin of modern barrier reefs, paper presented at Catchments to the Coast, Australian Marine Sciences Association 44th Annual Conference, Soc. of Wetland Scientists, Cairns, Queensland, Australia, 9–14 July.

Gardner, T. W., D. W. Jorgensen, C. Shuman, and C. R. Lemieux (1987), Geomorphic and tectonic process rates: Effects of measured time interval, *Geology*, *15*(3), 259–261.

Hampson, G. J., and J. E. A. Storms (2003), Geomorphological and sequence stratigraphic variability in wave-dominated, shoreface-shelf parasequences, *Sedimentology*, *50*(4), 667–701.

Harris, P. T. (1990), Sedimentation at the junction of the Fly River and the northern Great Barrier Reef, in *Torres Strait Baseline Study Conference*, edited by D. Lawrence and T. Cansfield-Smith, pp. 59–85, Queensland, Australia.

Harris, P. T., C. B. Pattiaratchi, J. B. Keene, R. W. Dalrymple, J. W. Gardner, E. K. Baker, A. R. Cole, D. M. Mitchell, P. Gibbs, and W. W. Schroeder (1996), Late Quaternary deltaic and carbonate sedimentation in the Gulf of Papua foreland basin: Response to sea-level change, *J. Sediment. Res.*, *66*(4), 801–819.

Harris, P. T., M. G. Hughes, E. K. Baker, R. W. Dalrymple, and J. B. Keene (2004), Sediment transport in distributary channels and its export to the pro-deltaic environment in a tidally dominated delta: Fly River, Papua New Guinea, *Cont. Shelf Res.*, *24*(19), 2431–2454.

Harris, P. T., A. Heap, V. Passlow, M. Hughes, J. Daniell, M. Hemer, and O. Anderson (2005), Tidally incised valleys on tropical carbonate

shelves: An example from the northern Great Barrier Reef, Australia, *Mar. Geol.*, *220*, 181–204.

Hemer, M. A., P. T. Harris, R. Coleman, and J. Hunter (2004), Sediment mobility due to currents and waves in the Torres Strait-Gulf of Papua region, *Cont. Shelf Res.*, *24*(19), 2297–2316.

Hori, K., Y. Saito, Q. Zhao, and P. Wang (2002b), Evolution of the coastal depositional systems of the Changjiang (Yangtze) river in response to late Pleistocene-Holocene sea-level changes, *J. Sediment. Res.*, *72*(6), 884–897.

Keen, T. R., D. S. Ko, R. L. Slingerland, S. Riedlinger, and P. Flynn (2006), Potential transport pathways of terrigenous material in the Gulf of Papua, *Geophys. Res. Lett.*, *33*, L04608, doi:10.1029/2005GL025416.

Kineke, G. C., R. W. Sternberg, J. H. Trowbridge, and W. R. Geyer (1996), Fluid-mud processes on the Amazon continental shelf, *Cont. Shelf Res.*, *16*(5–6), 667–696.

Kostic, S., and G. Parker (2003a), Progradational sand-mud deltas in lake and reservoirs. part 1: Theory and numerical modeling, *J. Hydraul. Res.*, *41*(2), 127–140.

Kostic, S., and G. Parker (2003b), Progradational sand-mud deltas in lakes and reservoirs. part 2: Experimental and numerical simulation, *J. Hydraul. Res.*, *41*(2), 141–152.

Kuehl, S. A., D. J. DeMaster, and C. A. Nittrouer (1986), Nature of sediment accumulation on the Amazon continental shelf, *Cont. Shelf Res.*, *6*(1–2), 209–225.

Kuehl, S. A., T. M. Hariu, and W. S. Moore (1989), Shelf sedimentation off the Ganges-Brahmaputra river system; evidence for sediment bypassing to the Bengal Fan, *Geology*, *17*(12), 1132–1135.

Kuehl, S. A., C. A. Nittrouer, M. A. Allison, L. Ercilio, C. Faria, D. A. Dukat, J. M. Jaeger, T. D. Pacioni, A. G. Figueiredo, and E. C. Underkoffler (1996), Sediment deposition, accumulation, and seabed dynamics in an energetic fine-grained coastal environment, *Cont. Shelf Res.*, *16*(5–6), 787–815.

Kuehl, S. A., M. A. Allison, S. L. Goodbred, and H. Kudrass (2005), The Ganges-Brahmaputra Delta, in *River Deltas: Concepts, Models, and Examples*, edited by L. Gosian and J. Bhattacharya, *Spec. Publ. Soc. Econ. Paleontol. Mineral.*, *83*, 413–434.

Lambeck, K., and J. Chappell (2001), Sea level change through the last glacial cycle, *Science*, *292*(5517), 679–686.

Larcombe, P., and R. M. Carter (1998), Sequence architecture during the Holocene transgression: An example from the Great Barrier Reef shelf, Australia, *Sediment. Geol.*, *117*(1–2), 97–121.

Liu, J. P., A. C. Li, Z. S. Yang, K. H. Xu, and J. D. Milliman (2004a), Sediment flux and fate of the Yangtze River sediments delivered to the East China Sea, *Eos Trans. AGU*, *85*(47), Fall Meet. Suppl., Abstract OS23C-1319.

Liu, J. P., J. D. Milliman, S. Gao, and P. Cheng (2004b), Holocene development of the Yellow River's subaqueous delta, north Yellow Sea, *Mar. Geol.*, *209*, 45–67.

Lofi, J., et al. (2003), Plio-Quaternary prograding clinoform wedges of the western Gulf of Lion continental margin (NW Mediterranean) after the Messinian salinity crisis, *Mar. Geol.*, *198*(3–4), 289–317.

Mallarino, G., J. M. Francis, A. W. Droxler, B. N. Opdyke, S. J. Bentley, G. R. Dickens, and L. C. Peterson (2004), Uppermost Pleistocene sea-level transgression across a Last Glacial Maximum mixed carbonate/siliciclastic coastline, modern Gulf of Papua shelf break in the northern Ashmore Trough, *Eos Trans. AGU*, *85*(47), Fall Meet. Suppl., Abstract OS51B-1303.

McCormick, D. S., J. B. Thurmond, J. P. Grotzinger, and R. J. Fleming (2000), Creating a three-dimensional model of clinoforms in the upper San Andres Formation, Last Chance Canyon, New Mexico, paper presented at AAPG Annual Meeting, Am. Assoc. of Pet. Geol., New Orleans, Louisiana, 16–19 April.

Michels, K. H., H. R. Kudrass, C. Huebscher, A. Suckow, and M. Wiedicke (1998), The submarine delta of the Ganges-Brahmaputra: Cyclone-dominated sedimentation patterns, *Mar. Geol.*, *149*(1–4), 133–154.

Milliman, J. D. (1995), Sediment discharge to the ocean from small mountainous rivers: The New Guinea example, *Geo Mar. Lett.*, *15*(3–4), 127–133.

Milliman, J. D., K. L. Farnsworth, and C. S. Albertin (1999), Flux and fate of fluvial sediments leaving large islands in the East Indies, *J. Sea Res.*, *41*, 97–107.

Milliman, J. D., K. Xu, G. J. Brunskill, R. Slingerland, and N. W. Driscoll (2006), Sediment mineralogy on the Gulf of Papua clinoform: New insights into sediment sources and redistribution processes, *Eos Trans. AGU*, *87*(36), Ocean Sci. Meet. Suppl., Abstract OS16A-25.

Mitchum, R. M., Jr., P. R. Vail, and J. B. Sangree (1977), Seismic stratigraphy and global changes of sea level. part 6: Stratigraphic interpretation of seismic reflection patterns in depositional sequences, in *Seismic Stratigraphy: Applications to Hydrocarbon Exploration*, edited by C. E. Payton, pp. 135–143, *Am. Assoc. of Petrol. Geol.*, Tulsa, Okla.

Moore, R., and W. MacFarlane (1984), Migration of ornate rock lobster, *Panulirus ornatus* (Fabricius), in Papua New Guinea, *Aust. J. Mar. Freshwater Res.*, *35*, 197–212.

Niedoroda, A. W., C. W. Reed, H. Das, S. Fagherazzi, J. F. Donoghue, and A. Cattaneo (2005), Analyses of a large-scale depositional clinoformal wedge along the Italian Adriatic coast, *Mar. Geol.*, *222/223*, 179–192.

Nittrouer, C. A., and D. J. DeMaster (1996), The Amazon shelf setting: Tropical, energetic, and influenced by a large river, *Cont. Shelf Res.*, *16*(5–6), 553–573.

Nittrouer, C. A., S. A. Kuehl, D. J. DeMaster, and R. O. Kowsmann (1986), The deltaic nature of Amazon shelf sedimentation, *Geol. Soc. Am. Bull.*, *97*(4), 444–458.

Nittrouer, C. A., S. A. Kuehl, R. W. Sternberg, A. G. Figueiredo Jr., and L. E. C. Faria (1995), An introduction to the geological significance of sediment transport and accumulation on the Amazon continental shelf, *Mar. Geol.*, *125*(3–4), 177–192.

Nittrouer, C. A., S. A. Kuehl, A. G. Figueiredo, M. A. Allison, C. K. Sommerfield, J. M. Rine, L. E. C. Faria, and O. M. Silveira (1996), The geological record preserved by Amazon shelf sedimentation, *Cont. Shelf Res.*, *16*(5–6), 817–841.

Ogston, A. S., J. S. Crockett, R. W. Sternberg, and C. A. Nittrouer (2003), Sediment transport under monsoon conditions on the Fly River clinoform, Papua New Guinea, *Eos. Trans. AGU*, *84*, Fall Meet. Suppl., Abstract OS11A-05.

Ogston, A. S., R. W. Sternberg, C. A. Nittrouer, D. P. Martin, M. A. Goñi, and J. S. Crockett (2004), Factors leading to the spatial heterogeneity of sediment-transport processes on the Fly River clinoform, Gulf of Papua, *Eos Trans. AGU*, *85*(47), Fall Meet. Suppl., Abstract OS44A-03.

Ogston, A. S., J. S. Crockett, M. A. Goni, C. A. Nittrouer, D. P. Martin, and R. W. Sternberg (2008), Sediment delivery from the Fly River tidally dominated delta to the nearshore marine environment and the impact of El Niño, *J. Geophys. Res.*, *113*, F01S11, doi:10.1029/2006JF000669.

Olariu, C., and J. P. Bhattacharya (2006), Terminal distributary channels and delta front architecture of river-dominated delta systems, *J. Sediment. Res.*, *76*(2), 212–233.

Paola, C., et al. (2001), Experimental stratigraphy, *GSA Today*, *11*(7), 4–9.

Pickup, G. (1984), Geomorphology of tropical rivers: I. Landforms, hydrology and sedimentation in the Fly and Lower Purari, Papua New Guinea, *Catena Suppl.*, *5*, 1–17.

Pirmez, C., L. F. Pratson, and M. S. Steckler (1998), Clinoform development by advection-diffusion of suspended sediment: Modeling and comparison to natural systems, *J. Geophys. Res.*, *103*(B10), 24,141–24,157.

Poulsen, C. J., P. B. Flemings, R. A. J. Robinson, and J. M. Metzger (1998), Three-dimensional stratigraphic evolution of the Miocene Baltimore Canyon region: Implications for eustatic interpretations and the systems tract model, *Geol. Soc. Am. Bull.*, *110*(9), 1105–1122.

Pratson, L. F., et al. (2004), Modeling continental shelf formation in the Adriatic Sea and elsewhere, *Oceanography*, *17*(4), 119–131.

Salomons, W., and A. M. Eagle (1990), Hydrology, sedimentology and the fate and distribution of copper in mine-related discharges in the Fly River system, Papua New Guinea, *Sci. Total Environ.*, *97/98*, 315–334.

Slingerland, R., R. W. Selover, A. S. Ogston, T. R. Keen, N. W. Driscoll, and J. D. Milliman (2008), Building the Holocene clinothem in the Gulf of Papua: An ocean circulation study, *J. Geophys. Res.*, doi:10.1029/2006JF000680, in press.

Steckler, M. S., G. S. Mountain, K. G. Miller, and N. Christie-Blick (1999), Reconstruction of Tertiary progradation and clinoform development on the New Jersey passive margin by 2-D backstripping, *Mar. Geol.*, *154*(1–4), 399–420.

Walsh, J. P., C. A. Nittrouer, C. M. Palinkas, A. S. Ogston, R. W. Sternberg, and G. J. Brunskill (2004), Clinoform mechanics in the Gulf of Papua, New Guinea, *Cont. Shelf Res.*, *24*(19), 2487–2510.

Wolanski, E., and D. M. Alongi (1995), A hypothesis for the formation of a mud bank in the Gulf of Papua, *Geo Mar. Lett.*, *15*(3–4), 166–171.

Wolanski, E., G. L. Pickard, and D. L. B. Jupp (1984), River plumes, coral reefs and mixing in the Gulf of Papua and the northern Great Barrier Reef, *Estuarine Coastal Shelf Sci.*, *18*(3), 291–314.

Wolanski, E., A. Norro, and B. King (1995), Water circulation in the Gulf of Papua, *Cont. Shelf Res.*, *15*, 185–212.

N. W. Driscoll and E. A. Johnstone, Scripps Institution of Oceanography, GRD 0244, La Jolla, CA 92093, USA.

S. R. Miller and R. Slingerland, Department of Geosciences, 513A Deike, Pennsylvania State University, University Park, PA 16802, USA.

J. D. Milliman, School of Marine Science, College of William and Mary, 1208 Greate Road, Gloucester Point, VA 23062, USA.

Appendix II: New Automated Point-Cloud Alignment for Ground-Based Light Detection and Ranging Data of Long Coastal Sections

New Automated Point-Cloud Alignment for Ground-Based Light Detection and Ranging Data of Long Coastal Sections

Michael J. Olsen, Ph.D., M.ASCE[1]; Elizabeth Johnstone[2]; Falko Kuester, Ph.D.[3]; Neal Driscoll, Ph.D.[4]; and Scott A. Ashford, Ph.D., M.ASCE[5]

J. Surv. Eng. 2011.137:14-25.

Abstract: This paper presents new techniques with corresponding algorithms to automate three-dimensional point-cloud georeferencing for large-scale data sets collected in dynamic environments where typical controls cannot be efficiently employed. Beam distortion occurs at the scan window edges of long-range scans on near-linear surfaces from oblique laser reflections. Coregistration of adjacent scans relies on these overlapping edges, so alignment errors quickly propagate through the data set unless constraints (origin and leveling information) are incorporated throughout the alignment process. This new methodology implements these constraints with a multineighbor least-squares approach to simultaneously improve alignment accuracy between adjacent scans in a survey and between time-series surveys, which need to be aligned separately for quantitative change analysis. A 1.4-km test survey was aligned without the aforementioned constraints using global alignment techniques, and the modified scan origins showed poor agreement (up to 8 m) with measured real-time kinematic global positioning system values. Further, the effectiveness of the constrained multineighbor alignments to minimize error propagation was evidenced by a lower average, range, and standard deviation of RMS values compared with various single neighbor techniques.

DOI: 10.1061/(ASCE)SU.1943-5428.0000030

CE Database subject headings: Mapping; Topographic surveys; Algorithms; Least squares method; Lasers; Coastal environment.

Author keywords: Terrain mapping; Topographic surveys; Algorithms; Least-squares method; Lasers; LIDAR.

Introduction

Terrestrial laser scanners (TLSs) use Light Detection and Ranging (LIDAR) to generate three-dimensional (3D) models. A laser pulse is emitted and coordinates are determined based on the pulse travel time and angle. Multiple measurements are taken across a scan window, producing a 3D point cloud. TLSs have been proven to be an efficient tool for topographical surveying such as localized seacliff erosion studies (Collins and Sitar 2004; Lim et al. 2005; Rosser et al. 2005; Collins et al. 2007; Young and Ashford 2007). Lim et al. (2005) and Rosser et al. (2005) used external direct georeferencing methods to perform the scan alignment for localized site studies. Collins and Sitar (2004) and Collins et al. (2007) used reflective target registration. Young and Ashford (2007) used structures such as houses and seawalls as common alignment tie points between surveys. These previous techniques can be difficult to implement and can limit data coverage in a dynamic coastal environment where survey work can only be completed during small time windows of low tide. While aerial LIDAR is commonly used for topographical analysis, it tends to have poor coverage on vertical faces, misses complex topography such as caves, and is, therefore, not a viable alternative.

For this seacliff erosion project, multiple time-series surveys consisting of several scans are performed to quantify seacliff erosion for a 20-km segment of coastline in San Diego. Fig. 1 shows how these individual scans are merged to complete a survey without occlusions. To ensure compatibility with other data sets such as aerial LIDAR and photogrammetry, the data sets need to be georeferenced into a real-world coordinate system. While previous work focuses on co-registration of scans in a survey or co-registering different surveys, this new approach seeks to expand such efforts by providing an algorithm that

1. Increases alignment accuracy by using constraints to prevent misalignment propagation;
2. Minimizes error between adjacent scans in a single survey;
3. Decreases error between multiple time-series surveys (demonstrated by Olsen et al. 2009);
4. Provides independent time-series surveys (i.e., one survey is not dependent on another for alignment);
5. Simultaneously georeferences the data to a real-world coordinate system (e.g., Universal Transverse Mercator); and
6. Reduces user-interaction time by automating the alignment procedure.

[1]Assistant Professor, School of Civil and Construction Engineering, Oregon State Univ., 220 Owen Hall, Corvallis, OR 97331 (corresponding author). E-mail: michael.olsen@oregonstate.edu

[2]Ph.D. Candidate, Scripps Institution of Oceanography, Univ. of California San Diego, 9500 Gilman Dr., MC 0244, La Jolla, CA 92093. E-mail: eajohnst@ucsd.edu

[3]Professor, Dept. of Structural Engineering, Univ. of California San Diego, 9500 Gilman Dr., MC 0085, La Jolla, CA 92093. E-mail: fkuester@ucsd.edu

[4]Professor, Scripps Institution of Oceanography, Univ. of California San Diego, 9500 Gilman Dr., MC 0244, La Jolla, CA 92093. E-mail: ndriscoll@ucsd.edu

[5]School Head, School of Civil and Construction Engineering, Oregon State Univ., 220 Owen Hall, Corvallis, OR 97331. E-mail: scott.ashford@oregonstate.edu

Note. This manuscript was submitted on July 13, 2009; approved on February 16, 2010; published online on February 19, 2010. Discussion period open until July 1, 2011; separate discussions must be submitted for individual papers. This paper is part of the ***Journal of Surveying Engineering***, Vol. 137, No. 1, February 1, 2011. ©ASCE, ISSN 0733-9453/2011/1-14–25/$25.00.

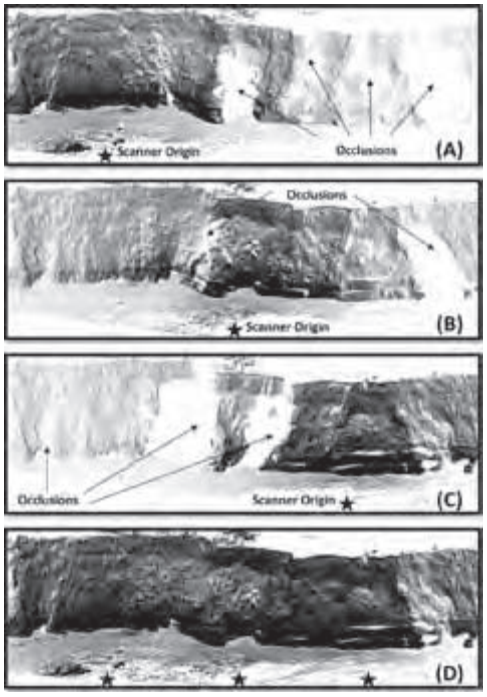

Fig. 1. Occlusions requiring multiple setups: (A) left scan; (B) center scan; (C) right scan; and (D) combined to minimize occlusions

By developing such a methodology, data sets are immediately compatible and comparable to analyze change such as cliff failure volumes and erosion rates. Fig. 2 shows an example of change analysis before and after a collapse using data aligned using PointReg, the algorithm presented in this paper. For accurate change comparison, each survey must be an independent measure and not reliant on a past survey for alignment, otherwise uniform change would be considered error. Such change analysis will provide key insights into many geologic processes occurring on the coastline.

Point-Cloud Alignment Background

Various point-cloud alignment methods exist and several common methods will be discussed in this section, including iterative closest point (ICP), 3D surface, and target. Some methods rely on a fixed reference data set or fixing individual scans as they are aligned. Other methods use a pairwise approach to find the optimal alignment between two scans. These pairwise alignments can then be improved by global optimizations. Several of these methods were developed for manufacturing, reverse engineering, or local site alignments instead of quantitative morphological surveys in a dynamic coastal environment, which necessitates a different approach because error propagation becomes more substantial at a much larger scale. In addition, most processing tools are limited in widespread use by software cost or unavailability.

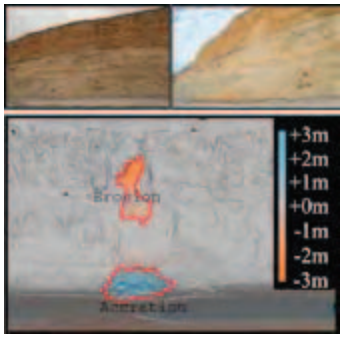

Fig. 2. Example of a failure volumetric and surface change analysis using TLS data aligned using PointReg. Failure site at Torrey Pines State Reserve, Calif.: (A) before failure, October 14, 2007; (B) after failure, October 29, 2007; with (C) failure analysis highlighting area of failure.

The ICP method developed by Besl and McKay (1992) selects random points in one scan, finds a "matching point" for each point in a second scan, and then performs a least-squares analysis to determine the translations and rotations necessary to place the second scan in the same coordinate system as the first. The "matching points" are the closest points found in the second scan respective to points in the first scan and are used to determine the RMS error value. Bernardini and Rushmeier (2002) provided a detailed discussion of several methods developed to improve the ICP method. Zhang (1994) introduced a maximum distance threshold to reduce inconsistent point pair matching.

Least-squares surface registration methods (Gruen and Akca 2004; Yang and Medioni 1992) have been developed to provide a better fit than the traditional ICP methods and were later generalized to allow for multiple registrations (Akca and Gruen 2007) to average the alignment error between neighboring scans. These methods, however, require a proper triangulation of the point clouds prior to the alignment, which can be a tedious task for an unorganized point cloud. While some scanners produce scans that are in a spherical grid structure, some provide raw coordinates without any established relationship between points in the data set.

To reduce the error created from pairwise alignment of scans described above, Pulli (1999) developed a global optimization technique, which can reduce alignment error for the global model by relating a scan to multiple neighboring scans. First, the user performs ICP pairwise alignments for all overlapping scans. Then the global alignment attempts to minimize errors between inconsistencies from pairwise alignments. The methods described by Pulli (1999) and Ikemoto et al. (2003) were designed and work efficiently for features scanned continuously surrounding the target object, such as a statue. Therefore, they are limited in applicability to regional seacliff topography because complete 360° coverage surrounding the seacliffs is not feasible, thereby preventing global error minimization.

An example of an existing software package that readily implements these algorithms is SCANALYZE (2002), which has been used successfully on several projects (e.g., Levoy et al. 2000) to scan objects where surrounding coverage was possible. However, it does not allow degree of freedom (DOF) constraints

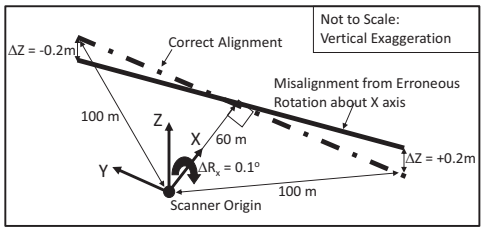

Fig. 3. Illustration showing misalignments from erroneous rotations about *X*- or *Y*-axis

to be defined, requires organized data structures, and works on limited formats, not easily exportable from other software packages, thereby requiring additional conversion steps. Further, these alignment methods are manual and must be tediously applied on a scan by scan basis. For an expert user, several minutes (3–5 min) are generally required to produce a satisfactory initial alignment between two scans. For a novice user, more minutes (10–15 min) are required for data sets with approximately 250,000 points/scan and a point spacing of 5–10 cm.

Target methods are very common and effective, yet time consuming (Collins and Sitar 2004). They are incorporated in proprietary software (e.g., Leica Geosystems 2009; Innovemetric 2009; Riegl 2009). Scans are aligned by setting up three or more common targets between scans or by placing targets over control points. As discussed by Akca and Gruen (2007), these methods are time consuming in the field if targets cannot be permanently placed and, thus, are difficult to use over large areas. Typically, each target can require 15 min to setup, 5 min to scan, and additional field help. Problems can arise if targets are disturbed by settlement in the loose sand, waves, or people. Target methods work well for aligning localized site scans where minimal setup is required (Guarnieri et al. 2005), but implementation requires careful control and spacing of the targets. Schuhmacher and Bohm (2005) discussed comparisons between target-based field methods, surveying control points with a total station, and software-based alignment methods. Also, Lichti et al. (2005) presented an error budget analysis for direct georeferencing.

Misalignment Errors and Beam Distortion Effects in TLS

The accuracy of the final alignment of multiple scans within a survey depends heavily on the quality of the alignments between adjacent scans. Beam distortion errors from oblique measurements can cause misalignments if not accounted for in georeferencing. Incorrect translations and rotations in aligning adjacent scans can then propagate through the data set.

Particularly on a regional scale, slight misalignments between adjacent scans can lead to detrimental global misalignments over a long range. For example, when scans of a linear feature are performed in the *Y*-direction looking toward the *X*-direction (Fig. 3), if a leveled scan is erroneously rotated by 0.1° about the *X*-axis by an algorithm not applying appropriate DOF constraints, and each subsequent scan is then registered to that fixed scan, a misalignment of 0.2 m in the *Z*-direction is introduced at 100 m from the scanner origin as a result of that single misalignment.

Table 1. Percentages of Point Comparisons within Tolerances for Repeat Scans

Deviation (m)	Number of points	Percentage
>0.50	438	0.1
0.25–0.50	5,261	1.5
0.10–0.50	54,253	15.5
0.05–0.10	95,768	27.4
0.01–0.05	151,034	43.2
<0.01	42,821	12.2
Total	349,575	100.0

This then leads to successive misalignments that propagate through the data linked from the original scan, which can be prevented by implementing DOF constraints.

A potential source of these misalignments is beam distortion, where the beam gets skewed when it impacts the surface obliquely, causing an elongation of one of the axes. Scaioni (2005) presented a discussion on theoretical measurement error for a single scan from biases from scanning at nonorthogonal angles because of spot size and shape variations. Laefer et al. (2009) presented a discussion with recommendations for minimizing beam distortion effects by limiting scan angle obliqueness (<45°), spot size by controlling distance to target, and using optimal geometrical configurations when using TLS to detect structural defects.

To illustrate the amount and location of beam distortion that occurs in a scan when scanning linear seacliff features, five repeat scans were performed from the same setup location approximately 35 m from the cliff using an I-Site 4400 laser scanner (nominal accuracy: 2 cm at 50 m under laboratory conditions and 5 cm for a range of 5–500 m for typical field conditions). Because the scanner operates on a repetitive grid format, the laser fires at the same angular increments (0.108° both horizontal and vertical) for each scan. Thus, these multiple scans can be averaged to produce a more accurate point cloud (I-Site 2008), which, for the purposes of this discussion, will be assumed to be the real-world position since it represents the best estimate. Deviations from this averaged value will be assumed to be measurement error. Many other error sources exist; however, this section focuses on measurement errors resulting from the scanning angle and distance. For each grid point, the maximum error of all individual scans compared to the average was evaluated. Table 1 shows the error distribution. Any points that were not on the cliff face were removed prior to the analysis. Note that very few points (<2%) are above a 0.5-m difference threshold and 83% of the points are within 0.1 m. For comparison, typical airborne LIDAR systems are accurate to 0.1–0.4 m (NOAA LDART 2009). Fig. 4 describes the variables used to analyze the measurement distribution, where ψ represents the horizontal angle and ϕ represents the vertical angle of the laser. The range or distance is represented by *r*. The horizontal angles were categorized from −80 to +80° in 5° increments to statistically illustrate the effects of beam distortion.

The average of these maximum errors within each category is plotted in Fig. 5, with error bars representing the standard deviation. Because the scan target surface is roughly a linear feature in the north-south direction, the laser will strike the surface at oblique angles further to the north and south of the scanner location. Fig. 5(A) shows the total error increases with ψ for a linear target surface. Similarly, the standard deviation also increases dramatically for more oblique angles, showing more uncertainty in these

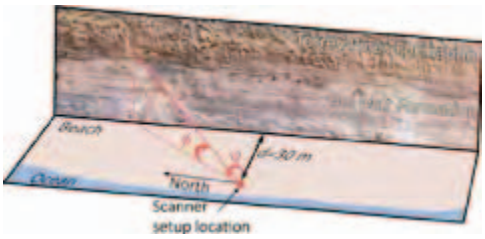

Fig. 4. Definitions of variables used to determine beam distortion effects that occur from scanning at oblique angles shown by repeat scans

measurements taken at oblique angles. Fig. 5(B) shows that at these oblique angles, the majority of the error results from error in the *Y*- (northing) direction. This is because the laser spot is distorted along the *Y*-axis, causing the resulting measurements to be averaged over a larger skewed surface area. Fig. 5(C) shows that the deviation in the *X*-direction is fairly consistent regardless of ψ. This error results from the length of the laser pulse and the measurement accuracy of the scanner rather than the angles. Fig. 5(D) shows that the *Z* values are well resolved and actually tend to be more accurate at more oblique horizontal angles. This occurs because for small *Y* values, the vertical angle, ϕ, is more oblique for the upper cliff and is less oblique for larger *Y* values. Fig. 5(E) shows the increase in error with range. However, much of this error probably results because points at larger ranges were also more oblique. Fig. 5(F) shows the increasing error as a function of vertical angle, which is not as substantial as the influence of ψ. Additionally, note that the beam distortion error is symmetric for the linear seacliffs [Figs. 5(A)–5(D)].

These beam distortion errors create problems during the alignment process because they occur at the scan edges, which contain the overlap necessary for matching in software alignments. Without DOF constraints, this distortion will affect the alignment between adjacent scans and will propagate these errors with each subsequent alignment.

Field Method Overview

To optimize this approach, data collection should follow the field procedure outlined by Olsen et al. (2009), which will be briefly summarized in this section. This field method requires minimal additional field time (approximately 2 min/scan) compared to time required for mobilization (approximately 1.5 h/survey day) and scanning (approximately 6 min/scan). This modest increase in field time translates into a marked reduction in processing time as well as an improved alignment between neighboring scans.

The field method completely constrains five of the six DOFs for data alignment in the field, so the alignment is only dependent on a single DOF, which can be nearly constrained in the field. Translation of the data in the *X*-, *Y*-, and *Z*- (up) directions is accomplished by acquiring real time kinematic (RTK) global positioning system (GPS) coordinates nominally accurate to 2.2 cm to represent the scanner origin. For this study, base corrections to produce accurate RTK GPS measurements were obtained using the network of California Virtual Reference Station (CALVRS) (2008). Occupying known control points or other survey methods can also be used to obtain the coordinates but will require additional setup time. When surveying in dynamic environments such as coastal environments, static control points are difficult, if not impossible, to use. Rotation of the data about the *X*- and *Y*-axes is constrained by a dual axis level/tilt compensator. The final DOF, rotation about the *Z*-axis, is nearly accomplished in the field by backsighting or targeting the scanner to a known point before scanning to calculate a bearing at which to align the data, similar to that done in conventional surveying. In dynamic locations such as sandy coastal beaches without control monuments, it can be difficult to mark a backsight target precisely, thus some rotation about the *Z*-axis is required to minimize error and improve the data fit (see Fig. 6). Thus, this hybrid approach estimating the backsight in the field and then correcting the estimate at the software level by using neighboring scans is employed, as will be discussed in the next section. The approximate backsighting can be performed with a digital compass or quickly estimated by manual rotations in software if the scanner does not have backsighting capabilities.

Processing Methods

Error Metric

Quantifying the accuracy of an alignment of two scans is difficult because both scans will not include points from the same spatial location, and the actual coordinates of the points collected are unknown. However, the most likely fit can be found by least squares. The procedure to calculate the RMS between two scans (Scans A and B) developed for this study is illustrated in Fig. 7 and is shown in pseudocode in Fig. 8. For a complete mathematical discussion of the algorithm, the reader is referred to Appendix I. The points of each scan are divided into cube subsets of user specified dimensions (typically 1 m × 1 m × 1 m) similar to the boxing structure acceleration method discussed by Akca and Gruen (2005). These cube subsets organize the data to decrease computational time and ensure that points are not compared to unrelated distant points. The algorithm finds the cubes containing a sufficient number of user specified points based on the typical scan point density of each scan and selects a subset of the points in these cubes. This ensures that the point selection used to calculate the registration parameters is from areas of dense coverage and is distributed across the point cloud to approximate the overall topography of the entire scan.

The distance from each selected point from Scan A to where that point would correlate with Scan B is calculated by assuming that the point $[p_A=(x_a,y_a,z_a)]$ from Scan A is co-planar with the nearest three points (p_1,p_2,p_3) from Scan B in the same cube. The distance from point, p_A, to the plane formed by the points p_1, p_2, and p_3 is then computed. This is similar to comparing the point to a surface mesh rather than a point cloud, but it does not require the time-consuming process of generating a clean and accurate mesh for each scan prior to alignment. The sum of the squares of the residuals is then used as the RMS measure.

Workflow Overview

Scan alignment requires data preprocessing to ensure that the best points are used for the alignment. The PointReg algorithm automates most procedures required for the scan alignment and thus requires minimal user-guided preprocessing and postprocessing. The workflow is presented in Fig. 8, showing automated steps in boxes and manual procedures in ellipses. Note that all of the

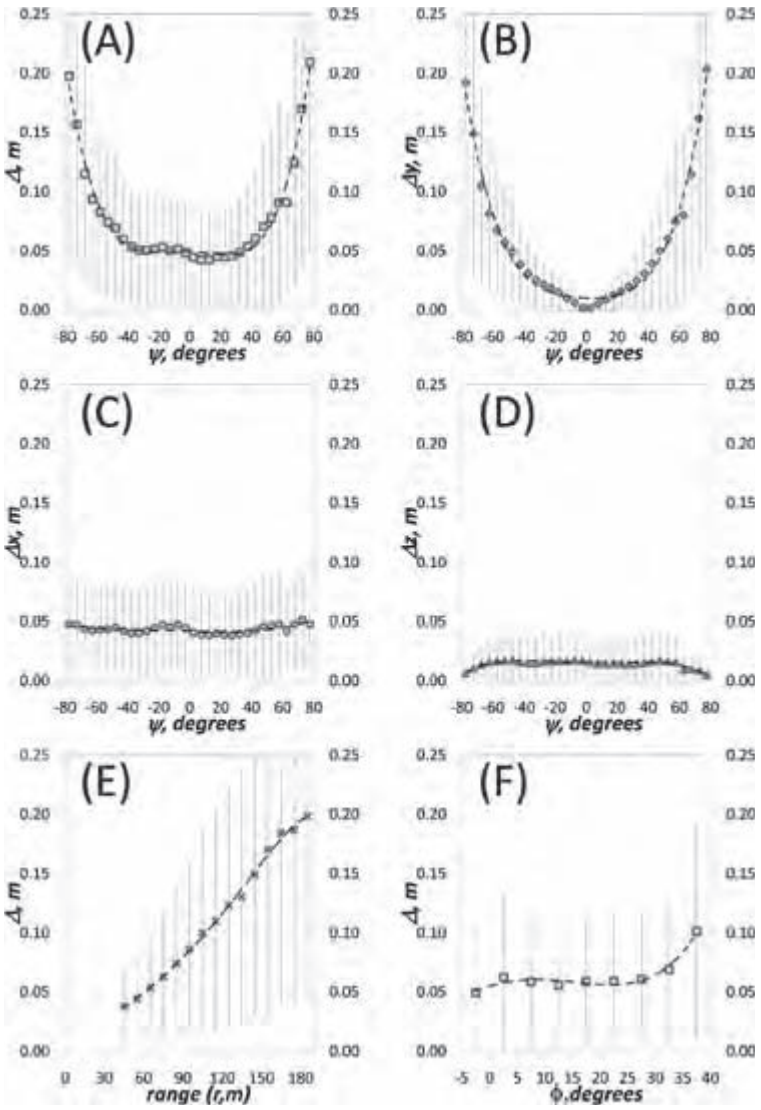

Fig. 5. Error comparisons between repeat scans showing the following: (A) total error; (B) error in *Y*-direction; (C) error in *X*-direction; (D) error in *Z*-direction compared with horizontal angle to surface, ψ; and a comparison of error with (E) range and (F) vertical angle, ϕ. Note that at oblique angles, Δy dominates, whereas at orthogonal angles, Δx dominates

manual procedures in the workflow would be required for adequate results using any registration technique. Major steps of this workflow will be discussed in detail.

Initial Alignment (Steps 1–3)

Most scanners collect data relative to the scanner origin defined as (0,0,0). To translate the data to a global coordinate system, each scan origin is translated by the X,Y,Z coordinates of the setup location, applying any corrections of the height offset from the coordinates obtained from a RTK GPS receiver centered directly above the scanner origin or from another survey technique. Registration and rough alignment of the data by backsight registration can be performed instantaneously for all scans in a survey (e.g., I-Site 2008) by linking scans to relative scanner and backsight coordinates. This rough alignment allows for a quick visual

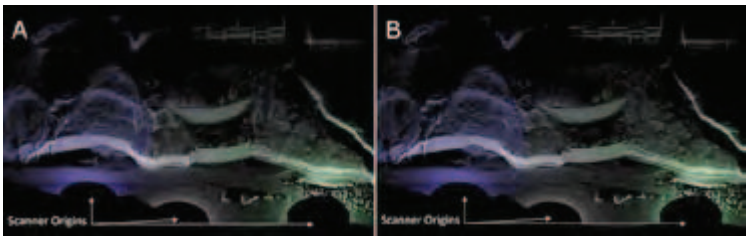

Fig. 6. (A) Three scans aligned using backsight registration only, obtained directly in the field. Note the apparent blurriness from the misalignment. (B) Three scans aligned using PointReg to reduce alignment errors. Note the increased clarity as a result of the alignment.

inspection of the data set and verification that no major errors were incorporated into the data or significant data gaps from overspacing the scans in the field exist.

Scan Editing (Step 4)

To ensure that the registration is performed only on objects consistent between scans, any moving objects in the scans should be eliminated. Beaches are public and heavily frequented locations, thus resulting in people, vehicles, and animals passing in front of the scanner as data are being acquired. Heavy vegetation should be eliminated from the scans because points are reflected off of different parts of the surface, and possible movements of the vegetation between scans can result in significant inconsistencies between acquired points. However, redundant or close points between data sets should only be removed after completion of the registration process. This step can be done before the initial alignment if desired. Further, some of this scan editing can be avoided by using a smaller distance threshold for the registration.

PointReg Algorithm for Point-Cloud Registration (Steps 5–8)

The PointReg algorithm assumes that the scan data only require a minimal rotation ($<5°$) about the Z-axis of the scan origin, is level, and has a coordinate for the origin of each scan. PointReg determines the optimal rotation angle about the Z-axis of a scan based on multiple neighboring scans instead of just one and does not fix any of the scans for reference, so both scans are able to move during the alignment.

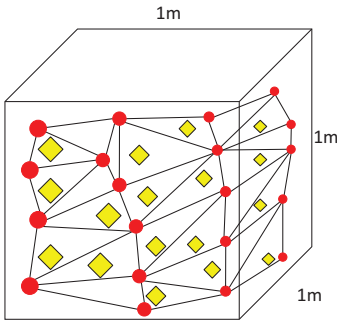

Fig. 7. Schematic illustrating the calculation of the RMS of error between two scans, showing a single cube subset. The selected points from Scan A (diamonds) are compared to triangles formed by the nearest three points in Scan B (circles).

PointReg operates on a simple survey text file of the scanner origin coordinates (X, Y, Z), the scan identification (ID), the scan backsight ID, and a leveling identifier, which can be directly exported from a survey controller. PointReg significantly reduces user-input processing time automatically determining neighboring scans to register together based on the proximity of RTK GPS coordinates. This allows the user to quickly declare a few input parameters and let the program run autonomously in batch mode rather than the user having to manually apply the coregistration to each set of scans. The algorithm progresses from either north to south or east to west (depending on the primary orientation of the target) and registers each scan with the next scan to the south or the east. This ensures that each scan (with the exception of the two boundary scans) is matched against two scans on opposing sides to reduce the propagation of misalignment effects from beam distortion. Further, once a scan has been matched with one neighbor, that rotational angle can be used as a starting point for the match with the second neighbor. An alignment between two scans typically requires 15 s of computational time (Intel Core 2, 2.66 GHz, 4-Gbytes random-access memory) for scans of 250,000 points compared to the time required to apply on a scan by scan basis in common software (3–5 min for expert and 10–15 min for novice user) as discussed in the background section.

PointReg also provides several automated filtering options implemented upon data loading. While loading data, the limiting factor is reading the data from the hard disk, so these filters do not add increased processing time because the processor remains relatively free during data loading. First, PointReg performs basic filtering options by X, Y, Z extents. This is important to seacliff alignment where beach points can be filtered by a minimum Z elevation because they tend to be planar. Second, the data can also be filtered by range to remove points far from the scanner origin. This maximum range is a function of the type of 3D scanner used (power limitations and beam spot size) and the size and amount of topographical features within the line of sight. For this study, the ISITE 4400 scanner has a resolution of approximately 18 cm at 100 m and a spot size of 22 cm at 100 m, so points farther than this were removed because of the large point spacing and hence were less desirable for alignment purposes.

PointReg (see pseudocode in Fig. 8) evaluates the combinations of rotations about the Z-axes of two data sets (Scans A and B) to find the best rotation pair that produces the lowest RMS error. Unfortunately, a direct solution is not possible because both scans must be rotated from their initial positions, as opposed to

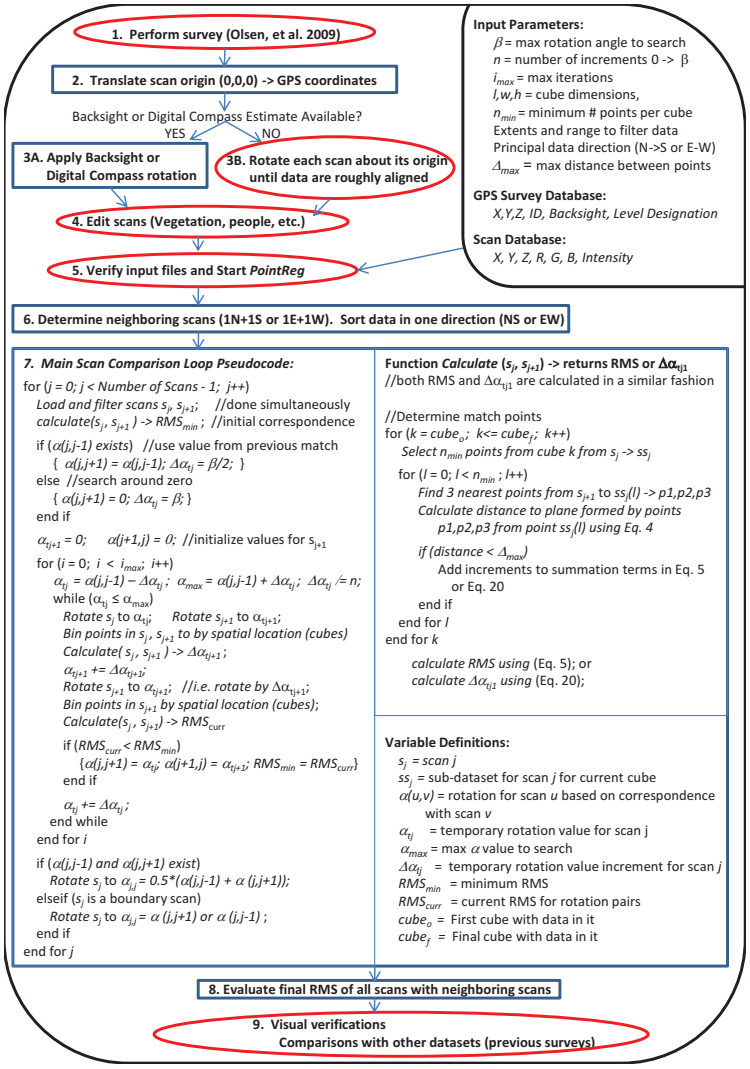

Fig. 8. Workflow diagram and pseudocode for PointReg scan alignment. Manual processes are illustrated by ellipses while boxes represent automated processes.

keeping one scan fixed, as is necessary for least squares. However, an iterative approach can be used to determine the rotational angle, α_A, required for Scan A and then a least-squares technique can be used to determine the optimal rotational angle of Scan B, α_B, given α_A. The detailed math for this least-squares approach is provided in Appendix II. The first scan is rotated about the *Z*-axis centered at its origin from an angle $\alpha_A = -\beta$ (typically 1–2°) to $\alpha_A = +\beta$ in $2n$ increments of $\Delta\alpha_A = \beta/n$. If a value for α_A has already been found for Scan A using another neighboring scan, the search window is reduced to focus around $\alpha_A \pm \beta/2$. At each increment, matching point pairs are updated and the optimal angle, α_B, to rotate Scan B given the current α_A is found. The pair of α_A and α_B that produces the lowest RMS is selected. The user also specifies the number of required iterations. Upon each iteration, the search window and increment steps are refined. This iterative approach allows the solution to converge rapidly; thus, only two to three iterations are required to produce a satisfactory alignment [Fig. 6(B)]. The two rotation angles found for Scan A based on its two neighbors are then averaged for the final rotation angle. While more complex weighting schemes could be implemented, the beam distortion illustrated in Fig. 5 is nearly symmetric, so averaging the rotational angles produces excellent

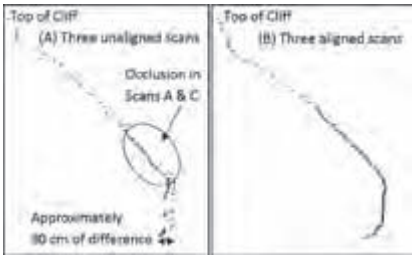

Fig. 9. Verification of alignment through 2D cross-section profiles of the following: (A) three unaligned scans; (B) three aligned scans. See Fig. 1 for description of occlusions.

results, especially since the two rotation angles predicted from the neighboring scans tend to be very similar. PointReg then progresses through the survey data set to ensure that each scan is aligned to two neighboring scans on opposing sides. Once all scans have rotation angles, then PointReg outputs new files with the adjusted scans and evaluates the final error between neighboring scans for the final global model.

Visual Verification (Step 9)

Although results may appear good mathematically, the data still should always be visually inspected for quality control purposes. Long linear structures such as seawalls work well for verification of scan alignments where a misaligned structure can be readily identified from a map perspective. Fig. 6(A) shows an area with a misaligned seawall, stairwell, and buildings that are properly aligned using PointReg in Fig. 6(B). Another visual verification of alignment can be done by comparing RTK GPS points obtained on "fixed structures" appearing in the scans. Comparison of scans to previous surveys or data sets is also an effective method to verify data alignment. Because there are areas in coastal environments that have not undergone significant change between recent surveys, these areas can be compared to confirm that both data sets are in the proper location. Olsen et al. (2009) showed an example of this. While such methods provide an efficient way to quickly detect large misalignments, examination of cross sections (Fig. 9) allows for a finer view of the scan's alignment. A misaligned scan may appear aligned when viewed from a normal 3D view but will appear misaligned in a two-dimensional (2D) cross-section view.

Results and Discussion

Successful application of this algorithm producing repeatable results between multiple coastal surveys has been shown by Olsen et al. (2009). This discussion has been focused on the necessity of several unique features of the PointReg algorithm. First, the magnitude of misalignment propagation from insufficient DOF constraints during alignment was evaluated. Second, the importance of using multiple neighboring scans to minimize alignment error was analyzed. Additionally, the problems associated with algorithms requiring fixed scans for a starting point were also investigated. The test data were obtained from a 1.4-km test section at Torrey Pines, Calif. Data collection was performed facing east (+X) approximately 40 m from the cliffs and marching from north to south (−Y) with approximately 40 m between scans covering a

Fig. 10. Setup for survey used to analyze the effectiveness and necessary steps for the algorithm. The cliff shown is a texture-mapped surfaced model using data from the Torrey Pines survey (September 10–11, 2007) aligned by PointReg.

180° view of the seacliffs. Fig. 10 shows the locations for a section of the survey to illustrate the survey pattern. All scans were edited, filtered to a 100-m range, and had a typical point spacing of 5–10 cm on the cliff. These scans, initially approximately 320,000 points each, were filtered to approximately 200,000 points.

Software Alignment without Constraints Using Global Optimization

Fig. 11 shows the displacement error induced at scan origins after performing a software alignment without any DOF constraints. This error was induced from misalignments created from beam distortion, described previously. Initial scan alignment was performed using GPS information; however, as misalignments grew away from the center, these scans needed to be translated for a better fit with the merged model before the alignment algorithms could be used. The six DOF software alignment was performed by co-registering and then fixing the two center scans to simulate the requisite fixed reference scan for a starting point. Accurate alignment for these scans was verified by comparison to

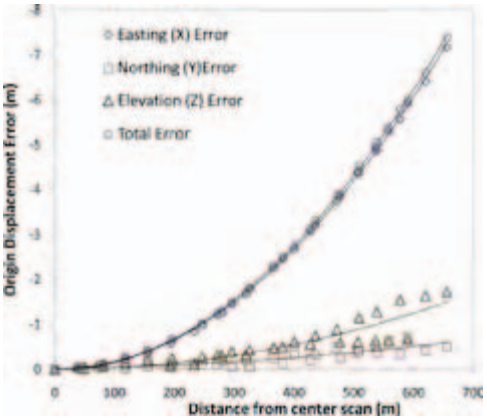

Fig. 11. Comparison of origin displacement error with distance from fixed center scan for scans collected in a north-south sweep and aligned from the center using unconstrained alignment techniques. Note that most of the displacement error is a result displacement in the easting (X)-direction, caused by the propagation of rotational errors about the Z-axis, created by warping biases in each scan. In contrast, because PointReg constrains scan origins, it produces none of these detrimental origin displacement errors.

Table 2. RMS (m) Comparisons for Different Registration Techniques

		Single neighbor alignment		Multiple neighbor alignment	
Scans	Field method	Pair method	Fixed method	ICP method	PointReg method
1 and 2	0.0870	0.0449	0.0455	0.1184	0.0734
2 and 3	0.1210	0.0963	0.0510	0.1144	0.0689
3 and 4	0.1529	0.0509	0.0668	0.1042	0.0586
4 and 5	0.1112	0.1174	0.0609	0.1212	0.0773
5 and 6	0.1803	0.0524	0.0858	0.1158	0.0728
6 and 7	0.0958	0.0799	0.2412	0.1060	0.0598
7 and 8	0.1993	0.0525	0.0728	0.1150	0.0689
8 and 9	0.1685	0.0969	0.0722	0.1301	0.0798
9 and 10	0.1303	0.0598	0.0664	0.1211	0.0736
10 and 11	0.0880	0.0952	0.0742	0.1167	0.0734
11 and 12	0.1116	0.0598	0.0588	0.1054	0.0618
		Summary statistics			
Average	0.1314	0.0733	0.0814	0.1153	0.0699
Maximum	0.1993	0.1174	0.2412	0.1301	0.0798
Minimum	0.0870	0.0449	0.0455	0.1042	0.0586
Standard deviation	0.0386	0.0247	0.0542	0.0078	0.0070

several surveys, guaranteeing that any introduced errors would be a result of the alignment technique itself and not of a poor initial condition.

Pairwise alignments were repeatedly performed multiple times to ensure that the best fit was found between the neighboring scans. Scans were then aligned using a global alignment technique (Pulli 1999), which operates by fixing the scan with the most overlapping scans and adding additional scans outward from the original fixed scan. The postalignment origins of each scan as a result of the translation and rotation during the alignment process were compared to the measured RTK GPS coordinates obtained for the scan origins. The propagating displacement errors shown in Fig. 11 show that current global optimization techniques did not apply the constraints necessary to prevent this error propagation from occurring because they did not initially constrain the scan; they only constrained it relative to its neighbors. Global optimization has succeeded in removing this warping error when it completely surrounds an object, which was impractical for seacliff studies for long coastal sections. Because PointReg constrained the scans to their origins, it did not suffer from these alignment propagations. Additionally, the global alignment technique required substantial user input (3 h) to prealign the data from 36 scans and to reiterate the alignment after the initial pairwise alignments fell victim to localized minima, creating erroneous alignments of up to 20 m. The alignments were visually inspected and produced acceptable RMS errors before comparing origin displacements. PointReg required only 15 min to complete the alignment of this segment (5 min of user time and 10 min of batch processing time).

Fig. 11 also provides insight on how misalignment propagation occurs when attempting to scan over a large region when performing a traditional software alignment. The overwhelming majority of the error resided in incorrect easting values, showing that the major contribution to misalignments was the incorrect rotation about the *Z*-axis, which would lead to large displacements in the easting direction. With the target primarily being scanned in the north-south direction with slight variability in the easting direction, there were limited data to constrain it. The northing direction showed less displacement as a result of substantial data being available along the north-south axis to serve as a constraint. The bifurcation of the *Z*-direction error resulted from larger error in the northern scans compared to the southern scans. The northernmost scans showed more error in the *Z*-direction because the cliffs were taller in the northern direction, which created more uncertainty in the alignment from increased shadowing and complexity.

This bias in the $-X$-(west) direction occurred from scanning a near-linear feature in the north-south direction facing east because of the beam distortion at the edges of the scan window. While for repeat scans, discussed in the section on beam distortion, the measurement error was principally in the *Y*-(north) direction, this measurement error translated into alignment error in the *X*-(east) direction during the alignment process because as points at the overlapping edges of scans were brought closer together to minimize distance, the measurement error in the *Y*-direction causes some incorrect rotation about the *Z*-axis, which, in turn, leads to alignment error in the *X*-direction. Thus, while at an initial glance the results may appear inconsistent, each section is actually discussing a different type of error.

Interestingly, there was no distinguishable bias between the alignment of scans from the center to the north and to the south and shows that averaging the rotation values found from neighboring scans on each side of the scan is effective. With a pairwise alignment with one neighboring scan, these biases will cause a slight incorrect clockwise rotation. Contrarily, the pairwise alignment with the neighboring scan on the other side will cause a slight incorrect counterclockwise rotation. By averaging these rotation angles, PointReg effectively eliminates the misalignment effects caused by this bias error, thus avoiding large global error propagation. Additionally, Fig. 11 shows that these biases were minimized for small distances, thus PointReg effectively constrained and minimized these biases locally by only comparing adjacent scans.

Software Alignment with Constraints (One DOF Solutions)

To contrast the error from software alignments without constraints, Table 2 compares several possible methods using constraints to align the point clouds. Of the filtered scans, the algorithm selected approximately 25,000 points/scan (using the cube subsets) for determining the actual alignment in PointReg. Alignments were performed using scans that were properly field constrained and with only one changing DOF: the rotation about the *Z*-axis. The first column shows the accuracy from the backsighted (estimated) and leveled field data without any software alignment. The effectiveness of single neighbor registration methods was evaluated using both the paired and fixed methods. The paired method consisted of registering each scan with a neighbor. For example, Scans 1 and 2 were registered together and Scans 3 and 4 were registered together and likewise until the end of the linear segment. As shown in Table 2, this produced good agreement between the scans that were co-registered; however, the results are poor for adjacent scans that were not paired together for the registration, such as Scans 2 and 3.

The fixed method fixed a paired registration at each end of the linear segment (Fig. 10) and then registered each adjacent scan to a fixed neighbor until they converged in the center. For example, in this study, Scans 1 and 2 were registered together as in the paired method. Scan 3 was then registered to Scan 2, which re-

mains fixed. This was repeated until the center was reached. On the opposite side, Scans 11 and 12 were registered together and Scan 10 was registered to a fixed Scan 11. This was repeated to the center, where on the left side Scan 6 was registered to Scan 5 and on the right side Scan 7 was registered to Scan 8. This would be similar to performing two separate surveys, one on the north and one on the south. If this method was effective in stopping propagating error, Scans 6 and 7 would have good agreement even though they were not directly registered together. As a result of the previously discussed misalignment propagation, there was considerable error (0.24 m) between Scans 6 and 7 (Table 2). An alternative would have been to fix the center scans (6 and 7) and work outward, which may have produced low RMS values. However, this alternative did not allow for verification of stopping error propagation. Further, because applying this method from the outside scans to the center (similar to merging the results from two independent surveys) propagated error (Table 2), the low RMS did not guarantee an accurate alignment in actual space. This was further validated by comparing the results of multiple repeat surveys aligned using the fixed method from the center, which showed very inconsistent results. The inherent problem with the fixed method was that scan alignment was still reliant on the alignment of all previously aligned scans. Thus, any misalignment between two scans was propagated to all subsequent aligned scans. These results from the single neighbor alignment methods showed that a multiple neighbor registration was needed to distribute the error properly.

The quality of alignment of the multiple neighbor registration was analyzed for the ICP method and the point to plane method used in PointReg. The standard deviations and ranges of the RMS between adjacent scans, shown in Table 2 for these two methods, were much lower than for the single registration method. This showed that the multiple registration method eliminated the misalignment effects caused by beam distortion because they were canceled out between the two neighbors. Further, PointReg ensured that the alignment of a scan was only dependent on correspondence with its neighbors and not the entire scan collection, thereby preventing global error propagation. The ICP method had a higher RMS than the PointReg method because the ICP method assumed that points from different scans were the same point in actuality, which tended to pull points closer together during alignment while trying to minimize error. Thus, it did not achieve as good of an alignment. Note that the average RMS of 7 cm for the PointReg alignment was on par with the nominal accuracies of the scanner (5 cm) and RTK GPS (2.2 cm).

Conclusions

New alignment strategies and tools for point-cloud data sets are available for regional topographic mapping and change analysis in dynamic environments. DOF constraints are crucial for repeat surveys to eliminate misalignment propagation. Additionally, DOF constraints ensure that rates of change between data sets are calculated based on real change and not from misalignments. These misalignments can be much larger than range measurement errors, which tend to include both positive and negative errors, spread throughout, smoothing out the overall error. Additionally, this alignment methodology reduces the potential of beam distortion to cause misalignments by using a multi-neighbor scan alignment, which helps ensure that the error in a scan alignment is averaged between its neighbors instead of fitting one neighbor well and poorly with the other.

The PointReg tool is available for free public use at http://lidarweb.ucsd.edu/coastalstudy/ and operates with unorganized point clouds in a clear-text ASCII file format allowing for straight forward data conversion from arbitrary scanner/software systems. Additionally, parameters can be adjusted for varying typical data set size and point density. Further, because the user is not required to surface or interpolate the data prior to alignment and the PointReg algorithm automatically determines which scans to register together, it can be efficiently implemented in a common survey workflow and can result in substantial time savings to obtain accurate alignments.

Acknowledgments

This research was partially funded via a grant from California Seagrant under Project No. R/OE-39, the Coastal Environmental Quality Initiative (CEQI) under Award No. 04-T-CEQI-06-0046, and the University of California, San Diego Chancellor's Interdisciplinary Collaboratories Fund. The above support is greatly appreciated. The writers also thank Pat Rentz and Jessica Raymond for their assistance in the TLS surveys. The writers also thank Scott Schiele (Maptek I-Site), John Dolan (Maptek I-Site), and Travis Thompson (CALVRS) for their technical assistance and support. We appreciate the reviewers whose thoughtful comments greatly enhanced this paper.

Appendix I: Calculating the RMS Using the Point-to-Plane Technique

After selecting a point from Scan A, the three nearest points from Scan B can be used to obtain the plane. First, the normal ($\mathbf{n}$) of the three points can be calculated by the cross product of the vectors from a point (p_1) in Scan B to the other two points (p_2 and p_3)

$$\vec{n} = (a,b,c) = (p3 - p1) \times (p2 - p1) \tag{1}$$

where a, b, c=components of the normal to the plane. Then, the individual components of the normal can be substituted into the plane equation

$$ax + by + cz + d = 0 \tag{2}$$

where d=constant based on the points in the plane. Using any of the three points and substituting in the x, y, z values of that point and the values of a, b, and c calculated from Eq. (1) into Eq. (2), the constant d is obtained to complete the equation for the plane. The shortest distance from the point (p_A) to the plane is found by projecting point (p_A) onto the plane by taking the dot product of the vector ($\boldsymbol{v}$) formed by the nearest point on that plane [$p_B = (x, y, z)$] to the point p_A and the normalized normal vector of the plane obtained in Eq. (1). This yields

$$D_i = \vec{n} \cdot \vec{v} = \frac{|a(x - x_a) + b(y - y_a) + c(z - z_a)|}{\sqrt{a^2 + b^2 + c^2}} \tag{3}$$

where D_i=minimum distance from the point to the plane. Substituting the plane equation [Eq. (2)] into Eq. (3) yields

$$D_i = \frac{|a(x_a) + b(y_a) + c(z_a) + d|}{\sqrt{a^2 + b^2 + c^2}} \tag{4}$$

For completeness, a point in triangle test can then be implemented to verify that the projection of point p_A is actually in the triangle.

However, testing shows that this verification step only influences the results by <1%. The RMS is obtained by summing up the distances calculated for all n of the selected point pairs using the following equation:

$$\text{RMS} = \sqrt{\left(\sum_{i=1}^{n} D_i^2\right)/n} \tag{5}$$

Appendix II: Least-Squares Approach to Solve for the Optimal α_B for a Given Value of α_A

First, define matrices to represent the 2D coordinates of the matching points of Scans A and B. Because the scan alignment optimization has been reduced to one parameter per scan (rotation about the Z-axis) from the DOF constraints, the other translation and rotation values are not needed. Z values do not affect rotation about the Z-axis, and, thus, they are not included. However, as shown in Appendix I, error in Z is accounted using a full 3D formulation to calculate the RMS. Note that the matching points of Scan A are found by the method described in Appendix I by finding the nearest point on the plane of Scan A to the selected point of Scan B

$$X_A = \begin{Bmatrix} x_{A1} & y_{A1} \\ x_{A2} & y_{A2} \\ \vdots & \\ x_{An} & y_{An} \end{Bmatrix} \quad X_B = \begin{Bmatrix} x_{B1} & y_{B1} \\ x_{B2} & y_{B2} \\ \vdots & \\ x_{Bn} & y_{Bn} \end{Bmatrix} \tag{6}$$

Then, define matrices to represent the 2D coordinates of the origins of Scans A and B

$$X_{A0} = \begin{Bmatrix} X_{A0} & Y_{A0} \\ X_{A0} & Y_{A0} \\ \vdots & \\ X_{A0} & Y_{A0} \end{Bmatrix} \quad X_{B0} = \begin{Bmatrix} X_{B0} & Y_{B0} \\ X_{B0} & Y_{B0} \\ \vdots & \\ X_{B0} & Y_{B0} \end{Bmatrix} \tag{7}$$

Next, define rotational matrices for the rotations of Scans A and B about their respective axes

$$R_A = \begin{bmatrix} \cos\alpha_A & \sin\alpha_A \\ -\sin\alpha_A & \cos\alpha_A \end{bmatrix} \tag{8a}$$

$$R_B = \begin{bmatrix} \cos\alpha_B & \sin\alpha_B \\ -\sin\alpha_B & \cos\alpha_B \end{bmatrix} \tag{8b}$$

Now, define matrices to represent the 2D coordinates of the points of Scans A and B after the rotations have been completed and the scans are at their optimal position. Note that because the rotations are performed about the scan origin, the entire scan must be translated to have an origin at (0,0), perform the rotation, and translate the scan origin back to its original position

$$X_{Af} = (X_A - X_{A0})R_A + X_{A0} \tag{9a}$$

$$X_{Bf} = (X_B - X_{B0})R_B + X_{B0} \tag{9b}$$

Lastly, define the error matrix

$$V = \begin{Bmatrix} v_{x1} & v_{y1} \\ v_{x2} & v_{y2} \\ \vdots & \\ v_{xn} & v_{yn} \end{Bmatrix} \tag{10}$$

Now, formulate the least-squares condition when both scans are rotated to the optimal fit

$$X_{Bf} = X_{Af} + V \tag{11}$$

Two unknown variables α_A and α_B need to be found. An iterative approach can be used to estimate α_A with a least-squares approach to solve directly for the optimal α_B given for each value of α_A. By evaluating the RMS for each pair using the method in Appendix I, the combination that produces the lowest RMS can be selected. Substituting Eq. (9b) into Eq. (11) to include the R_B matrix containing the unknown variable α_B produces

$$(X_B - X_{B0})R_B + X_{B0} = X_{Af} + V \tag{12}$$

Assume the rotation angle is very small ($\cos\alpha \approx 1$ and $\sin\alpha \approx \alpha$) and solve Eq. (12) for V

$$\begin{Bmatrix} v_{x1} & v_{y1} \\ v_{x2} & v_{y2} \\ \vdots & \\ v_{xn} & v_{yn} \end{Bmatrix} = \begin{Bmatrix} x_{B1} - X_{B0} & y_{B1} - Y_{B0} \\ x_{B2} - X_{B0} & y_{B2} - Y_{B0} \\ \vdots & \\ x_{Bn} - X_{B0} & y_{Bn} - Y_{B0} \end{Bmatrix} \begin{bmatrix} 1 & \alpha_B \\ -\alpha_B & 1 \end{bmatrix} + \begin{Bmatrix} X_{B0} & Y_{B0} \\ X_{B0} & Y_{B0} \\ \vdots & \\ X_{B0} & Y_{B0} \end{Bmatrix} - \begin{Bmatrix} x_{Af1} & y_{Af1} \\ x_{Af2} & y_{Af2} \\ \vdots & \\ x_{Afn} & y_{Afn} \end{Bmatrix} \tag{13}$$

Next, calculate the sum of the squares of the errors for the least-squares method

$$V_{SS}^2 = v_{x1}^2 + v_{y1}^2 + v_{x2}^2 + v_{y2}^2 + \cdots + v_{xn}^2 + v_{yn}^2 \tag{14}$$

To minimize the sum of the squares of the errors, differentiate Eq. (14) and set it equal to zero

$$\frac{\partial V_{SS}^2}{\partial \alpha_B} = \frac{\partial v_{x1}^2}{\partial \alpha_B} + \frac{\partial v_{y1}^2}{\partial \alpha_B} + \frac{\partial v_{x2}^2}{\partial \alpha_B} + \frac{\partial v_{y2}^2}{\partial \alpha_B} + \cdots + \frac{\partial v_{xn}^2}{\partial \alpha_B} + \frac{\partial v_{yn}^2}{\partial \alpha_B} = 0 \tag{15}$$

Reducing Eq. (16) for only the ith terms produces

$$\frac{\partial v_{xi}^2}{\partial \alpha_B} + \frac{\partial v_{yi}^2}{\partial \alpha_B} = 0 \tag{16}$$

Looking at the errors from the ith matching pair in Eq. (13) formulates

$$v_{xi} = x_{Bi} - (y_{Bi} - Y_{B0})\alpha_B - x_{Afi} \tag{17a}$$

$$v_{yi} = y_{Bi} + (x_{Bi} - X_{B0})\alpha_B - y_{Afi} \tag{17b}$$

So differentiating v_{xi}^2 and v_{yi}^2 [squaring Eqs. (17a) and (17b)] with respect to α_B

$$\frac{\partial v_{xi}^2}{\partial \alpha_B} = 2(x_{Bi} - (y_{Bi} - Y_{B0})\alpha_B - x_{Afi})(Y_{B0} - y_{Bi}) \qquad (18a)$$

$$\frac{\partial v_{yi}^2}{\partial \alpha_B} = 2[y_{Bi} + (x_{Bi} - X_{B0})\alpha_B - y_{Afi}](X_{Bi} - x_{B0}) \qquad (18b)$$

Substituting the expressions from Eqs. (18*a*) and (18*b*) into Eq. (16) and solving for α_B yield

$$\alpha_B = -\frac{x_{Afi}y_{Bi} - x_{Afi}y_{B0} + x_{Bi}y_{B0} - y_{Afi}x_{Bi} + y_{Afi}x_{B0} - y_{Bi}x_{B0}}{(y_{Bi} - y_{B0})^2 + (x_{Bi} - x_{B0})^2} \qquad (19)$$

Finally, using superposition to expand the solution to use all matching point pairs found in the scans and factoring to minimize computations produce

$$\alpha_B = -\frac{\sum_{i=1}^{n} x_{Afi}y_{Bi} - \sum_{i=1}^{n} y_{Afi}x_{Bi} + y_{B0}\left(\sum_{i=1}^{n} x_{Bi} - \sum_{i=1}^{n} x_{Afi}\right) + x_{B0}\left(\sum_{i=1}^{n} y_{Afi} - \sum_{i=1}^{n} y_{Bi}\right)}{\sum_{i=1}^{n} y_{Bi}^2 + \sum_{i=1}^{n} x_{Bi}^2 - 2\left(y_{B0}\sum_{i=1}^{n} y_{Bi} + x_{B0}\sum_{i=1}^{n} x_{Bi}\right) + n(y_{B0}^2 + x_{B0}^2)} \qquad (20)$$

which represents the optimal rotational angle for Scan B using an assumed value of α_A. Then continue to iterate values of α_A and select the combination which produces the lowest RMS using the method discussed in Appendix I.

References

Akca, D., and Gruen, A. (2005). "Fast correspondence search for 3D surface matching." *Int. Arch. Photogramm. Remote Sens. Spat. Inf. Sci.*, 36(3/W52), 186–191.

Akca, D., and Gruen, A. (2007). "Generalized least squares multiple 3D surface matching." *Int. Arch. Photogramm. Remote Sens. Spat. Inf. Sci.*, 36(3/W52), 1–7.

Bernardini, F., and Rushmeier, H. (2002). "The 3D model acquisition pipeline." *Comput. Graph. Forum*, 21(2), 149–172.

Besl, P. J., and McKay, N. D. (1992). "A method for registration of 3D shapes." *IEEE Trans. Pattern Anal. Mach. Intell.*, 14(2), 239–256.

California Virtual Reference Station (CALVRS). (2008). "CALVRS: A real-time California cooperative." ⟨http://www.calvrs.net⟩ (Aug. 7, 2008).

Collins, B., Kayen, R., Reiss, T., and Sitar, N. (2007). "Terrestrial LIDAR investigation of the December 2003 and January 2007 activations of the Northridge Bluff Landslide, Daly City, California." *Rep. No. 2007-1079*, U.S. Geologic Survey, Menlo Park, Calif.

Collins, B., and Sitar, N. (2004). "Application of high resolution 3D laser scanning to slope stability studies." *Proc., 39th Annual Symp. on Engineering Geology and Geotechnical Engineering*, 79–92.

Gruen, A., and Akca, D. (2004). "Least squares 3D surface matching." *Int. Arch. Photogramm. Remote Sens.* (CD-ROM), 34(5/W16), ⟨http://www.isprs.org/publications/archives.aspx⟩.

Guarnieri, A., Pirotti, F., Pontin, M., and Vettore, A. (2005). "Combined 3D surveying techniques for structural analysis applications." *Int. Arch. Photogramm. Remote Sens.* (CD-ROM), 36(5/W17) ⟨http://www.isprs.org/publications/archives.aspx⟩.

I-Site. (2008). "Maptek I-Site 3D laser scanning." ⟨http://www.isite3d.com⟩ (Aug. 7, 2008).

Ikemoto, L., Gelfand, N., and Levoy, M. (2003). "A hierarchical method for aligning warped meshes." *Proc., 3-D Digital Imaging and Modeling, 3DIM 2003*, IEEE, Los Alamitos, Calif., 434–441.

Innovemetric. (2009). "Polyworks: 3D scanner software." ⟨http://www.innovemetric.com⟩ (July 7, 2009).

Laefer, D. F., Fitzgerald, M., Maloney, E. M., Coyne, D., Lennon, D., and Morrish, S. W. (2009). "Lateral image degradation in terrestrial laser scanning." *Struct. Eng. Int. (IABSE, Zurich, Switzerland)*, 19(2), 184–189.

Leica Geosystems. (2009). "Leica Cyclone—3D point cloud processing software." ⟨http://www.leica-geosystems.com/corporate/en/HDS-Software-Leica-Cyclone_6515.htm⟩ (July 7, 2009).

Levoy, M., et al. (2000). "The digital Michelangelo project: 3D scanning of large statues." *Proc, 27th Annual Conf. on Computer Graphics and Interactive Techniques*, ACM Press, New York/Addison-Wesley Publishing Company, New York, 131–144.

Lichti, D. D., Gordon, S. J., and Tipdecho, T. (2005). "Error models and propagation in directly georeferenced terrestrial laser scanner networks." *J. Surv. Eng.*, 131(4), 135–142.

Lim, M., Petley, D. N., Rosser, N. J., Allison, R. J., and Long, A. J. (2005). "Combined digital photogrammetry and time-of-flight laser scanning for monitoring cliff evolution." *Photogramm. Rec.*, 20(110), 109–129.

NOAA LDART. (2009). "Digital coast—NOAA coastal services center." ⟨http://www.csc.noaa.gov/digitalcoast/index.html/⟩ (Dec. 15, 2009).

Olsen, M. J., Johnstone, E., Ashford, S. A., Driscoll, N., and Kuester, F. (2009). "Terrestrial laser scanning of extended cliff sections in dynamic environments." *J. Surv. Eng.*, 135(4), 161–169.

Pulli, K. (1999). "Multiview registration for large data sets." *Proc., 2nd Int. Conf. on 3D Digital Imaging and Modeling*, IEEE, Los Alamitos, Calif., 160–168.

Riegl. (2009). "RIEGL—RIEGL laser measurement systems." ⟨http//www.riegl.com⟩ (July 6, 2009).

Rosser, N. J., Petlety, D. N., Lim, M., Dunning, S. A., and Allison, R. J. (2005). "Terrestrial laser scanning for monitoring the process of hard rock coastal cliff erosion." *Q. J. Eng. Geol. and Hydrology*, 38, 363–375.

Scaioni, M. (2005). "Direct georeferencing of TLS in surveying of complex sites." *Int. Arch. Photogramm. Remote Sens. Spat. Inf. Sci.* (CD-ROM), 36(5/W17) ⟨http://www.isprs.org/publications/archives.aspx⟩.

SCANALYZE. (2002). "Scanalyze: A system for aligning and merging range data." ⟨http://graphics.stanford.edu/software/scanalyze/⟩ (Sept. 8, 2008).

Schuhmacher, S., and Bohm, J. (2005). "Georeferencing of laser scanner data for applications in architectural modeling." *Int. Arch. Photogramm. Remote Sens. Spat. Inf. Sci.* (CD-ROM), 36(5/W17) ⟨http://www.isprs.org/publications/archives.aspx⟩.

Yang, C., and Medioni, G. (1992). "Object modeling by registration of multiple range images." *Image Vis. Comput.*, 10(3), 145–155.

Young, A. P., and Ashford, S. A. (2007). "Quantifying sub-regional sea-cliff erosion using mobile terrestrial LIDAR." *Shore Beach*, 75(3), 38–43.

Zhang, Z. (1994). "Iterative point matching for registration of free-form curves and surfaces." *Int. J. Comput. Vis.*, 13(2), 119–152.